Received: 4 June 2018
DOI: 10.1002/mop.31578

WILEY

RESEARCH ARTICLE

Novel D SRR-based dual band antenna for WiMAX/C applications

A. Ambika[1] | **C. Tharini**[1] | **M. T. Ali**[2]

[1]Department of Electronics and Communication, B.S. Abdur Rahman Crescent Institute of Science and Technology, Chennai, Tamilnadu, India

[2]Antenna Research Centre (ARC) FKE, Universiti Teknologi MARA, Shah Alam, Malaysia

Correspondence
A. Ambika, Department of Electronics and Communication, B.S. Abdur Rahman Crescent Institute of Science and Technology, Chennai, Tamilnadu, India.
Email: ambika@crescent.education

Abstract

A novel miniaturized D shape split ring resonator (SRR) antenna is proposed for dual band (3.6 GHz and 4.7 GHz) applications. This proposed antenna structure has dimensions of 18 × 20 × 0.8 mm^3 which is built on FR4 dielectric constant (ε_r=4.4). This antenna consists of top and bottom side dual SRR creating dual band resonant frequency which is excited from microstrip line as monopole and slotted partial ground plane for better impedance matching. The microstrip line (monopole) is creating a resonance frequency at 4.7 GHz and the SRR is responsible for creating resonance frequency at the frequency of 3.6 GHz. The parametric study of microstrip line and the position of SRR has been analyzed. The D shape SRR in the monopole is generating another resonating frequency at 3.6 GHz. The metamaterial property of proposed D shape SRR is also verified to validate the resonance frequency. The antenna radiation measurement is carried out in Antenna Research Centre (ARC) FKE, Universiti Teknologi MARA, Malaysia. Both simulated and measured results agreed well. Measured gain achieved with this dual band antenna is around 2-3 dB.

KEYWORDS

D SRR, dual band, microstrip line, miniaturization, monopole

1 | INTRODUCTION

The wireless and mobile devices support multiple radio frequency bands, for that a single antenna has to operate dual or multi band frequencies to reduce its cost and size. The main consideration of any antenna design is that it should occupy less space and the number of components is also to be reduced which may lead to unwanted coupling and other disturbances. For that reason if an antenna is working in dual band then it reduces the usage of separate antenna for the other frequencies. To achieve dual band, different types of antenna designs have been proposed.[1–10] Due to low cost, light weight, and ease of integration, microstrip patch antennas are preferred in many microwave applications. However, there is demand on the reduction of antenna size in particular applications such as some military and commercial wireless communication systems where the system size and profile are a constraint. Over the past few years, significant amount of work has been done to reduce the size of the patch antennas. One of the traditional methods is to use materials with high permittivity which yields a size reduction up to 30%-50%. However, high permittivity substrates lead to high cost and suffer from surface waves which degrade the radiation characteristics of the antenna by increasing significant amount of side lobes. To suppress the surface waves, a number of techniques are proposed. In Ref. 1, the dual band is designed and analyzed in a rectangular printed monopole antenna which used slits and truncated technique; Meander T shape slot antenna, inverted U shape. In Ref. 2, array of square CSRR is etched from ground plane in a conventional patch antenna. Inverted F-micro strip antenna is a kind of dual band which is operated at 2.4 GHz and 5 GHz embedded in L shape slots. In Refs. 3,4, the antenna is designed for about 2.4 GHz-5.2 GHz central frequency which is done by using inverted L shape modified in normal patch antenna. In Ref. 7, the antenna utilizes an H-shape defected ground structure; in Ref. 8, feeding two different length resonant paths with a 50 Ω microstrip line. In Ref. 6,5, the antenna is optimized for dual band by using metamaterial structures such as, circular, hexagonal CSRR, and SRR which exhibits negative permittivity and permeability.

In this work, a D shape SRR based microstrip line monopole antenna is proposed for WiMax (3.45 GHz-3.7 GHz) and C band (4.86 GHz-4.63 GHz) applications.

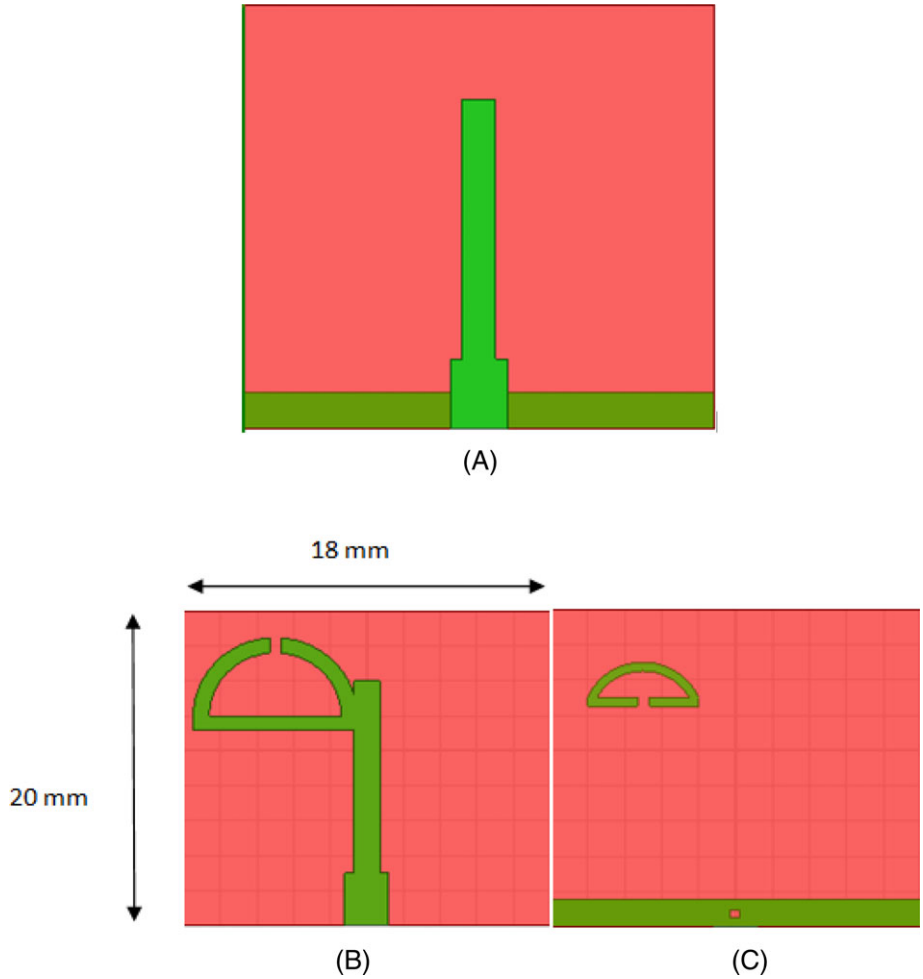

FIGURE 1 (A) Without SRR microstrip line antenna, (B) with dual D SRR with microstrip line top side, and (C) bottom side [Color figure can be viewed at wileyonlinelibrary.com]

A miniaturized dual band was obtained within this compact geometry size.

2 | DESIGN PROCEDURES OF PROPOSED NOVEL SRR DUAL BAND ANTENNA

The Novel D SRR antenna design step is shown in Figure 1. Its design procedure is started from a microstrip line ($l = \lambda_g/4$) which is normally a simple monopole antenna built in FR4 ($\varepsilon_r = 4.4$) dielectric substrate. This microstrip line is connected to a 50 Ω feed line which provides impedance matching along with slotted partial ground structure for both dual frequencies. The dimension of proposed Novel D antenna structure has a compact and high rejection level band-stop filter by using complementary split ring resonator (SRR). The proposed circuit is characterized by compact size, low cost, easy fabrication and its dimensions are listed in Table 1. First, we started designing with microstrip line alone which is acting as a monopole antenna for the resonating frequency of 4.7 GHz by using following mathematical equation:

TABLE 1 Parameters and dimensions of proposed D SRR antenna

Parameters	Dimensions, mm
SRR	
Inner semicircle radius	3.60
Outer semicircle radius	4.65
Outer semicircle	
Strip length, L_0	8.80
Strip length, L_1	7.20
Inner semicircle	
Outer strip length	2.7
Inner strip length	2.2
Outer split gap, S_1	0.90
Inner split gap, S_2	0.50
FR4 substrate	
W_p	20
L_p	18
Height	0.8
Strip line	
Length, ls	11
Width	1.4
Ground	
Length	1.6
Width	20
Slot	0.5 × 0.5

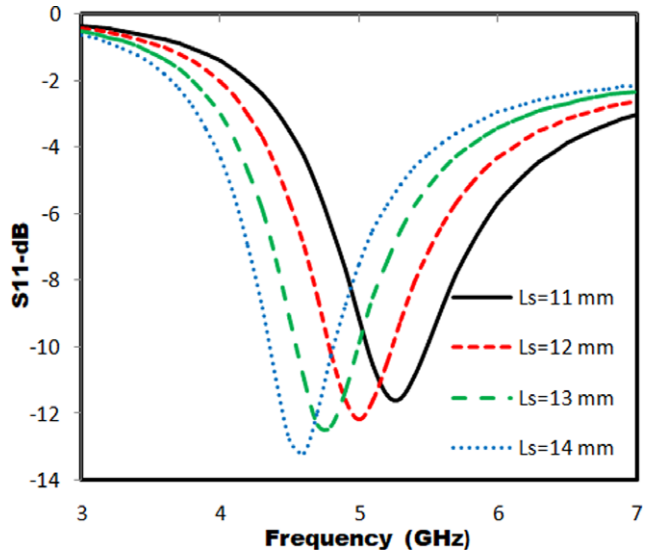

FIGURE 2 Without SRR return loss for various micro strip line lengths [Color figure can be viewed at wileyonlinelibrary.com]

$$l + d = 0.25\lambda, \tag{1}$$

where the design parameters of microstrip line are length, l = 14 mm, width, d = 1.4 mm. For this resonant frequency to find the optimized length, the various length of microstrip line is analyzed in HFSS simulation which is shown in Figure 2. In order to generate dual band D shape SRR is implemented in this design. In general, the electrical behavior of an SRR can be replaced by LC circuit which is acting as a magnetic dipole is excited by an axial magnetic field. In this geometry, proposed D SRR is directly coupled to the microstrip line and its position is optimized by varying its position along the strip line which causes gain variation and slightly affects the monopole resonant frequency but SRR always resonates its designed resonant frequency which is shown. The proposed D SRR is designed for the resonant frequency of 3.6 GHz which is calculated by using the following formula:

$$f_{SRR} = \frac{1}{2\pi\sqrt{L_S C_S}}. \tag{2}$$

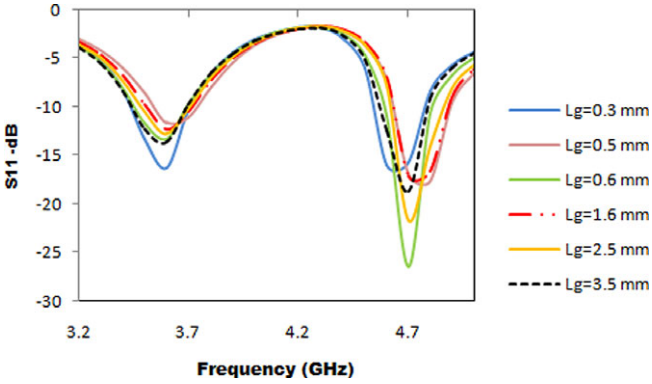

FIGURE 3 Frequency response curve for various partial ground Length 'Lg' [Color figure can be viewed at wileyonlinelibrary.com]

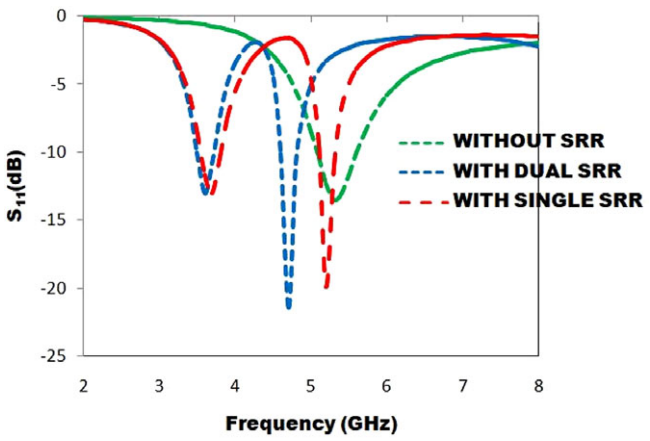

FIGURE 4 Simulated return loss for without and with single and dual SRR [Color figure can be viewed at wileyonlinelibrary.com]

3 | PARAMETRIC ANALYSIS

3.1 | Effects of ground length variations

Parametric analyses have been done in ground length "L_g" for perfect matching. The width of the partial ground "L_g" has been varied from 0.3 mm to 3.5 mm which is shown in Figure 3. Hence the optimized value of Lg is chosen as 1.6 mm and with slot at this 1.6 mm ground length improves the impedance matching at 4.66 GHz frequency. Further increase in "Lg" value makes decrease in impedance.

3.2 | Effects of D SRR

With and without SRR has been analyzed. Without SRR produces resonant frequencies at 5.1 GHz, with single D SRR resonates another frequency at 3.6 GHz along with 5 GHz. Finally, adding small D structure at the bottom side acts as a reflector which emits E field inclined to a normal axis so that improves the effectiveness of radiation at 3.6 GHz resonant frequency which is also able to tuning

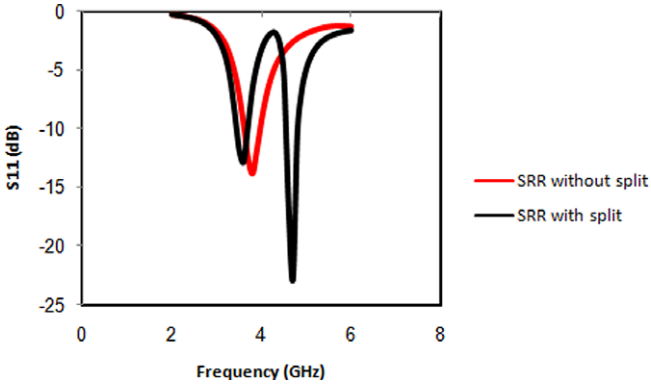

FIGURE 5 Frequency response curve for with and without split of D SRR [Color figure can be viewed at wileyonlinelibrary.com]

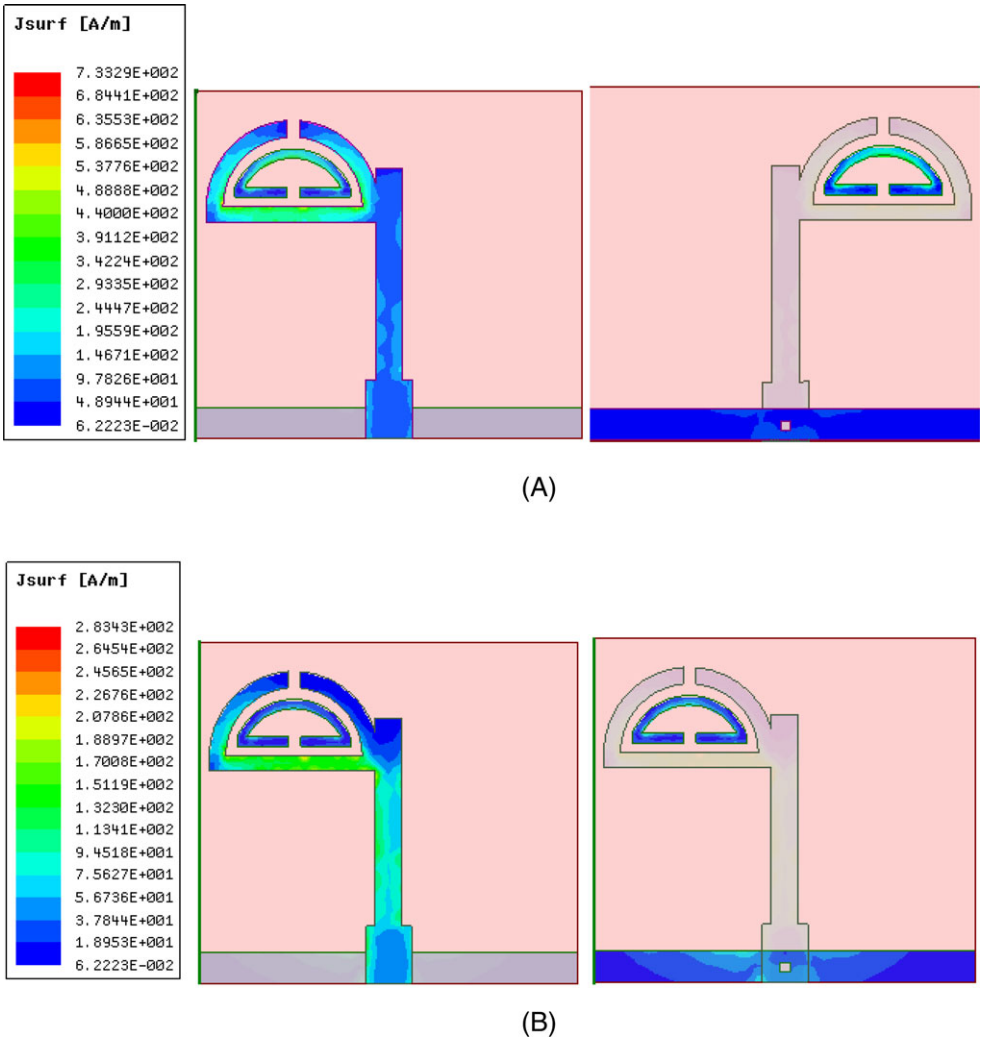

FIGURE 6 (A) Surface current distribution at 4.66 GHz and (B) surface current distribution at 3.56 GHz [Color figure can be viewed at wileyonlinelibrary.com]

higher resonant frequency to 4.7 GHz with this miniaturized proposed antenna. Simulated return loss for without and with single and dual SRR is shown in Figure 4.

3.3 | Effect of split in D SRR

The parameter analysis is also done with the split effect on D SRR and it is found that, SRR without split is not generating resonance at 4.66 GHz. Whereas, split creating a pass band (S_{11}) in S parameter is due to capacitance of SRR formed by split slot and the inductance formed by metal strip length. To pertaining dual band frequency, D SRR position has been analyzed along the microstrip line and hence optimized SRR position at 8.3 mm. Frequency response curve for with and without split of D SRR is shown in Figure 5.

The proposed antenna further analyzed with surface current distribution is shown in Figure 6A,B. The surface current distribution of antenna is analyzed using simulation HFSS software for dual frequencies. In Figure 6A, the current density is more in outer semicircle whereas less current dense is present in inner D shape. So, the outer semicircle is responsible for lower band frequency 3.56 GHz. In Figure 6B, at 4.77 GHz frequency, the surface current density is decreases and increases in outer semicircle which results in inner semicircle controlling the upper band frequency.

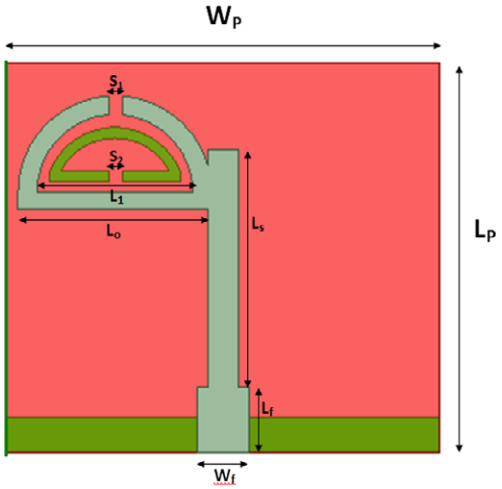

FIGURE 7 Proposed novel D SRR microstrip line monopole antenna [Color figure can be viewed at wileyonlinelibrary.com]

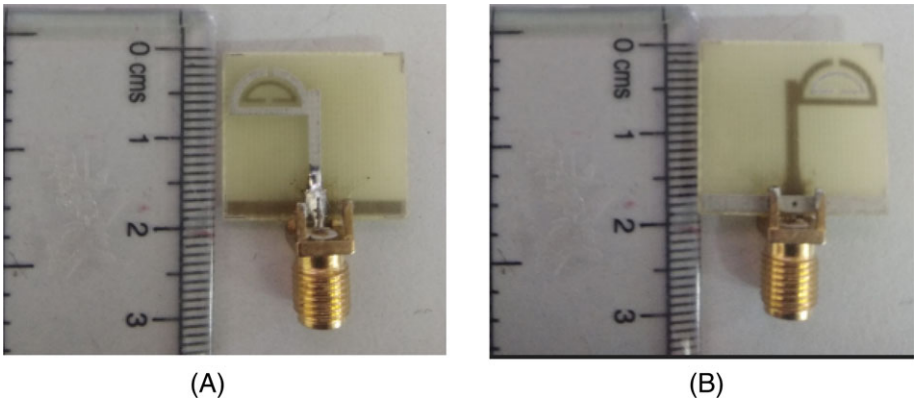

FIGURE 8 Snapshot of proposed antenna. (A) Top view. (B) Bottom view [Color figure can be viewed at wileyonlinelibrary.com]

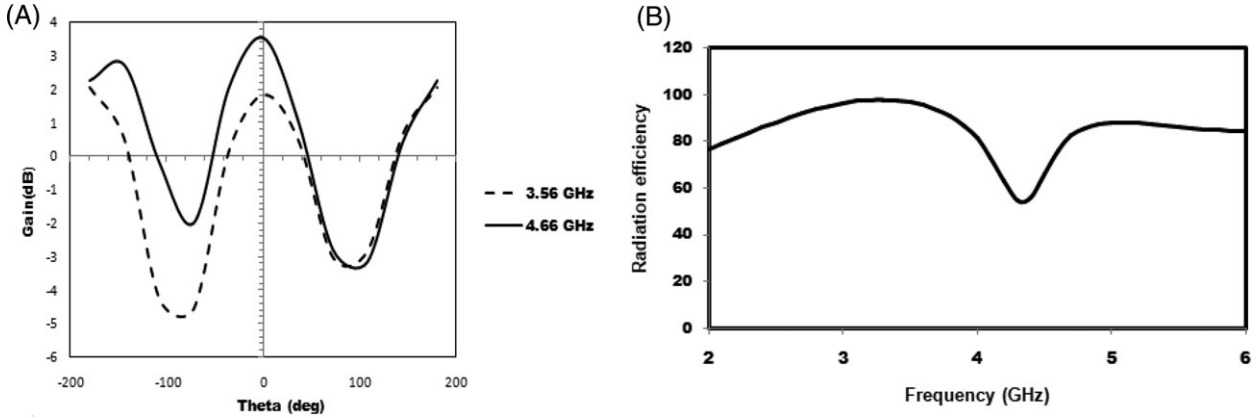

FIGURE 9 (A, B) Simulated gain and efficiency of proposed dual band antenna

4 | RESULTS AND DISCUSSION

The proposed antenna structure simulated on HFSS v.17.0 software is shown in Figure 7. The simulated and fabricated return loss (S_{11}) results were compared and it is observed that measured results provided better results. The obtained bandwidth in simulation and measurement is 300 MHz and 250 MHz respectively for 3.56 GHz and 4.76 GHz. The snapshot of proposed antenna (top and bottom part) is shown in Figure 8A,B. The obtained bandwidth is sufficient for WIMAX and C band applications. The simulated gain and efficiency of the antenna are shown in Figure 9A,B. It produced gain around 2-3 dBat both resonant frequencies and also efficiency is nearly about 80.72% and 79.62% respectively for 3.56 GHz and 4.76 GHz. The Agilent network analyzer is used to measure the return loss of the proposed antenna which is shown in Figure 10. Also simulated and measurement results are listed in Table 2. This dual band antenna has been measured in Antenna Research Centre (ARC), FKE, UiTM. The measurement focuses on measurement of return loss (S_{11}) and radiation pattern. The both simulation and measurements of radiation pattern are shown in

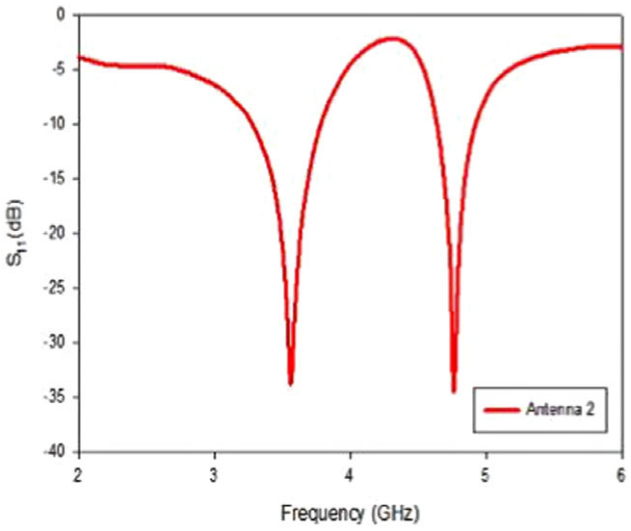

FIGURE 10 Measured return loss (S_{11}) of proposed antenna [Color figure can be viewed at wileyonlinelibrary.com]

TABLE 2 Comparison of simulated and measured values of proposed D-SRR antenna

Proposed dual D-SRR antenna resonant	Frequency, GHz	Return loss, dB	Gain, dB	Radiation efficiency, %
Simulated	3.60	−14.10	1.82	92
	4.66	−26.95	0.13	80
Measured	3.56	−32.69	3.35	80.72
	4.76	−31.23	1.80	79.62

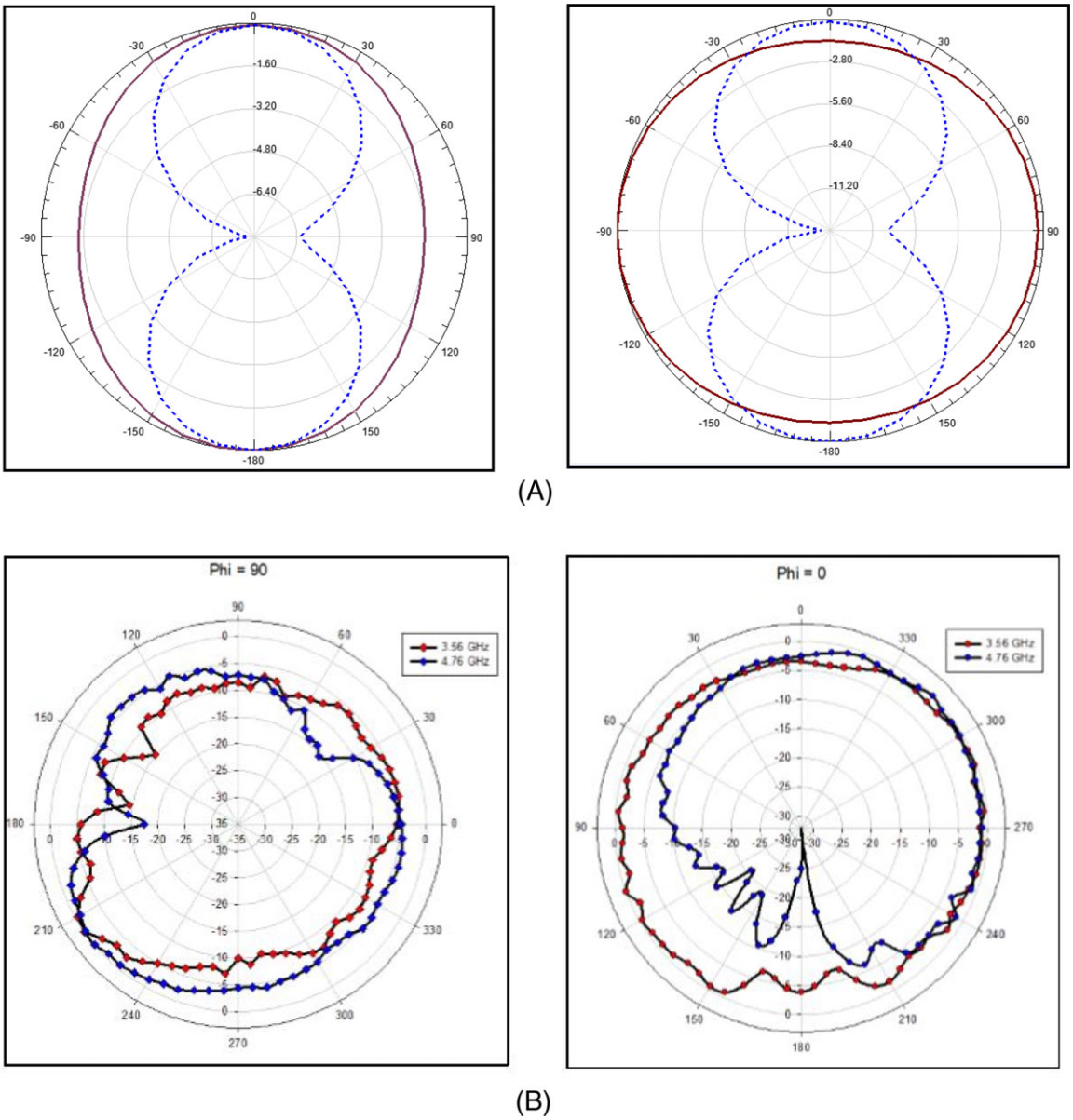

FIGURE 11 (A) Simulated pattern phi = 0°, phi = 90° @ 3.56 GHz and 4.76 GHz. (B) Measured pattern phi = 0°, phi = 90° @ 3.56GHz and 4.76 GHz [Color figure can be viewed at wileyonlinelibrary.com]

Figure 11. Both plots show almost omnidirectional pattern in H plane and bidirectional pattern in E plane at both dual resonant frequencies and due to size constrain slight variation in measured pattern is observed.

5 | CONCLUSION

A very low profile, low cost dual band D shape SRR based antenna only with microstrip line and for D shape SRR is proposed for dual band applications with a size of $20 \times 18 \times 0.8$ mm^3.This antenna is fabricated and measured its return loss, gain, radiation characteristics, and radiation efficiency. The simulated and measured results are validated. This antenna can be designed for any wireless applications just by changing the length of the microstrip line and by varying the SRR radius and strip length. The proposed antenna shows measured frequency responses of 3.56 GHz (3.3 GHz-3.8 GHz) and 4.76 GHz (4.6 GHz-4.85 GHz) and impedance bandwidth around 500 MHz and 250 MHz, respectively. Therefore the proposed miniaturized antenna structure can be utilized for WIMAX and C band applications with low cost.

ACKNOWLEDGMENT

The authors would like to thank Antenna Research Centre (ARC) FKE, Universiti Teknologi MARA, Malaysia, for their help in carrying out measurements of antenna characteristics.

ORCID

A. Ambika https://orcid.org/0000-0002-4959-7392

REFERENCES

[1] Rathore A, Nilavalan R, AbuTarboush HF, Peter T. Compact dual-band (2.4/5.2 GHz) monopole antenna for WLAN applications. *IEEE.* 2010;1-4.

[2] Xie Y, Li L, Zhu C, Liang C. A novel dual-band patch antenna with complementary split ring resonators embedded in the ground plane. *Prog Electromagn Res Lett.* 2011;25:117-126.

[3] Sumathi K. Compact dual-band inverted L shaped monopole antenna for WLAN applications. *ICTACT J Commun Dent Technol.* 2015;6(4):1182-1186.

[4] Sindreu MD, Naqui J, Paredes F, Bonche J, Martin F. Electrically small resonators for planar metamaterial, microwave circuit and antenna design: a comparative analysis. *Appl Sci.* 2012;2:375-395.

[5] Ali T, Biradar RC. A compact hexagonal slot dual band frequency reconfigurable antenna for WLAN applications. *MOTL.* 2017; 59(4):958-964.

[6] Kumar R, Naidu PV, Kamble V. Design of asymmetric slot antenna with meandered narrow rectangular slit for dual band applications. *Prog Electromagn Res B.* 2014;60:111-123.

[7] Mun TY, Kit CY, Chet KV, Islam MT. A novel wideband antenna for dual band WLAN application. In: IEEE International Conference on Communication Systems (ICCS), Singapore; 2010.

[8] Malik J, Kartikeyan MV. A stacked equilateral triangular patch antenna with Sierpinski gasket fractal for WLAN applications. *Prog Electromagn Res Lett.* 2011;22:71-81.

[9] Ming-Tien W, Chuang M-L. Application of transmission-line model to dual-band stepped monopole antenna designing. *IEEE Antennas Wireless Propag Lett.* 2011;10:1449-1452.

[10] Pan C-Y, Horng T-S, Chen W-S, Huang C-H. Dual wideband printed monopole antenna for WLAN/WiMAX applications. *IEEE Antennas and Wireless Propagat Lett.* 2007;6:149-151.

How to cite this article: Ambika A, Tharini C, Ali MT. Novel D SRR-based dual band antenna for WiMAX/C applications. *Microw Opt Technol Lett*. 2018;1–7. https://doi.org/10.1002/mop.31578

Indonesian Journal of Electrical Engineering and Computer Science
Vol. 12, No. 1, October 2018, pp. 393~398
ISSN: 2502-4752, DOI: 10.11591/ijeecs.v12.i1.pp393-398

Intrinsic ZnO/Al-doped ZnO Homojunction: Structural and Optical Properties

A.S. Ismail[1], M.H. Mamat[2], M.F. Malek[3], M.M. Yusoff[4], N.D. Md. Sin[5], S.S. Shariffudin[6], A.S. Zoolfakar[7], A.B. Suriani[8], M.K. Ahmad[9], I. B. Shameem Banu[10], and M. Rusop[11]
[1,2,3,4,5,6,7,11]NANO-ElecTronic Centre (NET), Faculty of Electrical Engineering, Universiti Teknologi MARA (UiTM), 40450 Shah Alam, Selangor, Malaysia
[2,3,11]NANO-SciTech Centre (NST), Institute of Science (IOS), Universiti Teknologi MARA (UiTM), 40450 Shah Alam, Selangor, Malaysia
[8]Nanotechnology Research Centre, Faculty of Science and Mathematics, Universiti Pendidikan Sultan Idris (UPSI), 35900 Tanjung Malim, Perak, Malaysia
[9]Microelectronic and Nanotechnology – Shamsuddin Research Centre (MiNT-SRC), Faculty of Electrical and Electronic Engineering, Universiti Tun Hussein Onn Malaysia (UTHM), Batu Pahat, Johor, Malaysia
[10]Department of Physics, B.S. Abdur Rahman University, Vandalur, Chennai 600 048, India

Article Info

Article history:

Received Jun 1, 2018
Revised Jul 10, 2018
Accepted Jul 25, 2018

Keywords:

Homojunction
Immersion
Structural Properties
Zinc Oxide

ABSTRACT

Intrinsic zinc oxide (ZnO)/Al-doped ZnO (AZO) homojunction film was prepared using two-step immersion processes. The film was characterized using field emission scanning electron microscopy, X-ray diffraction (XRD), Raman spectroscopy, and ultraviolet–visible spectrophotometer to investigate their structural and optical properties. The surface morphology image displays that the ZnO deposited on the nanorod surfaces in layer form with average diameter of nanorods about 95 nm. The structural properties of XRD pattern demonstrate that the film possessed good crystallinity with the preferred orientation at (002) plane. The film also possessed excellent absorption in the ultraviolet (UV) region with optical band gap energy of 3.22 eV. These results indicate that the film has a good potential for optical-based device such a UV sensor.

Corresponding Author:

M.H. Mamat,
NANO-ElecTronic Centre (NET), Faculty of Electrical Engineering,
Universiti Teknologi MARA (UiTM),
40450 Shah Alam, Selangor, Malaysia.
Email: mhmamat@salam.uitm.edu.my

1. INTRODUCTION

Zinc oxide (ZnO) is an n-type which is used in various applications include sensors, solar cells, light emitting diodes, and transistors [1-4]. These wide applications are benefited from its properties such as wide bandgap energy, non-toxic, low cost, and also able to be produced into nanoscale structures. Previous studies reported that ZnO can be produced into various kinds of nanostructures such as nanowires, nanorods, nanospheres, nanoflowers, and nanoflakes. However, one-dimensional structures (nanorod and nanowires) are more promising in device fabrications due to ease of electron transfer and reducing grain boundary-related defect [5]. To date, there are lots of fabrication methods that are used to produce ZnO nanostructures such as metal organic chemical vapour deposition (MOCVD), sputtering, electrodeposition, thermal chemical vapour deposition, and hydrothermal [6]. Among the fabrication methods, water-based preparation is favourable due to simple process and low temperature use. Besides, this method also capable of producing high quality nanostructure films, comparable to the methods which use high temperature and high vacuum conditions.

Based on the previous studies, intrinsic ZnO coating, forming whether homojunction or heterojunction, manage to improve the properties of a film. According to Mamat et al., by coating ZnO nanorod arrays with intrinsic ZnO manage to improve the ultraviolet (UV) sensing performance due to the reduction of dark current [7]. In other study, Jiang et al. reported that the efficiency of $CuIn_{1-x}Ga_xSe_2$ (CIGS) solar cells improved after coated with intrinsic ZnO [8]. In this study, we investigated the effect of ZnO/Al-doped ZnO (AZO) homojunction film in term of structural and optical properties. To the best of our knowledge, detail discussion on such homojunction film is rarely reported. The understanding on their properties is crucial for future implementation in devices.

2. RESEARCH METHOD

The preparation of ZnO/AZO film involved three steps. First is a seed layer preparation. The detail preparation of seed layer has been reported in previous study [9]. For the preparation of AZO, zinc nitrate hexahydrate (0.1 M), hexamethylenetetramine (0.1 M), and aluminum nitrate nonahydrate (0.001M) were used as the main materials. The reagents were combined and then going through sonication process for 30 min (50 °C). Then the solution was stirred for 3h, followed by immersion to grow the nanorod array structures. Finally, the film was annealed for 1 h (500 °C). Then, the second immersion for homojunction layer was conducted by mixing zinc nitrate hexahydrate (0.02 M) and hexamethylenetetramine (0.02M). Similar processes involving sonication, stirring, immersion, and annealing were used, where every parameters for each step were maintained. The illustration for the ZnO/AZO homojunction film preparation is depicted in Figure 1. For structural analyses, field emission scanning electron microscopy (FESEM, JEOL JSM-7600F), X-ray diffraction (PANalytical X'Pert PRO), and Raman spectroscopy (Horiba Jobin Yvon-79 DU420A-OE-325) measurements were conducted. For optical characterizations, ultraviolet–visible (UV–vis) spectrophotometer (Varian Cary 5000) was used.

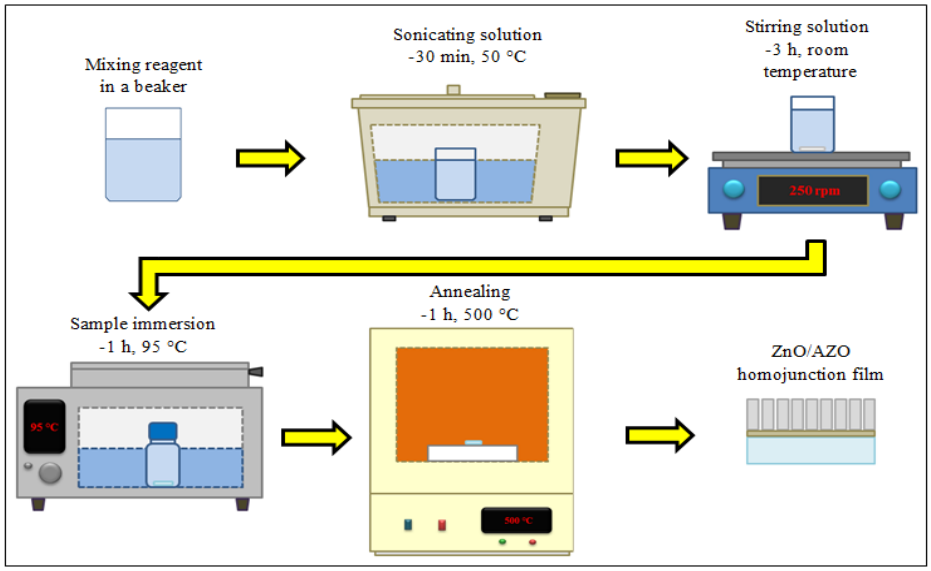

Figure 1. The illustration for the ZnO/AZO homojunction film preparation

3. RESULTS AND ANALYSIS

The FESEM images in Figure 2 depict the surface morphology of the prepared samples. The images were taken at 100,000 × magnifications. Figure 2(a) shows the surface morphology of granular ZnO seed layer film. The average diameter of the grain is about 25 nm. Figure 2(b) demonstrates the AZO film grown on the ZnO seed layer film. The average diameter of the nanorods is about 70 nm. It is observed that the film consist of large pore areas in between the nanorods. Figure 2(c) depicts the ZnO film (0.02 M solution concentration) which was grown on the seed layer film. It is witnessed that only small part of the film is covered by the nanorods. Besides, the diameter of the nanorods is relatively small compared to AZO film, about 35 nm. Other than that, we also observed nanoflake structure appears on the film in addition to the nanorod structures. Figure 2(d) displays the ZnO/AZO homojunction film. Compared to the bare AZO film,

it is witnessed that the nanorod arrays of ZnO/AZO is covered by a slightly light color layer, which is intrinsic ZnO. The average diameter of the film is about 95 nm. Based on the image, it is indicates that the deposition of the intrinsic homojunction layer begin from the side surface, follows by the deposition on the top of the nanorods. This is based on the observation from the FESEM images that shows the less coverage of the intrinsic layer on the top surface of the nanorods. Interestingly, the growth process of the intrinsic ZnO does not develop into any form of nanostructures, but a layer. Such formation occurs may be due to the same crystal structure of ZnO and AZO, which enhances the homoepitaxy growth on the previous crystal (AZO).

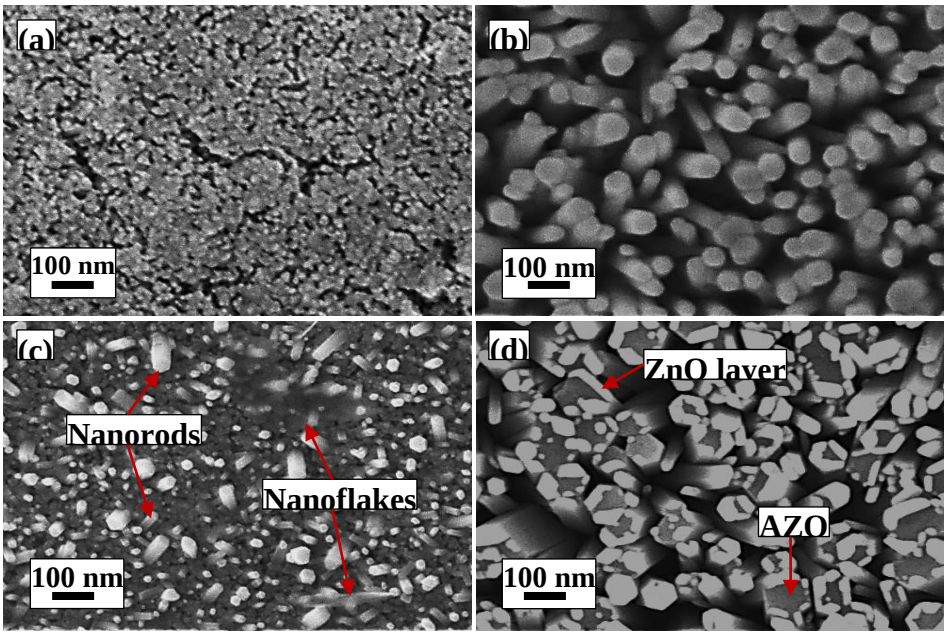

Figure 2. Surface morphology of (a) seed layer, (b) AZO, (c) ZnO, and (d) ZnO/AZO films at 100,000 × magnifications

Figure 3 depicts the XRD pattern of the synthesized films. The diffraction angles measured are from 25° to 60°. The XRD pattern of each film is plotted individually and the intensity of the X-ray is shown in count-per-units (cps) to show the different in the intensity of each film. From the plots, there are several peaks occurred on the pattern, namely; (100), (002), (101), (102), and (110). For AZO film (Figure 3(a)), the dominant diffraction peak is at (002) plane orientation (along *c*-axis). For intrinsic ZnO film (Figure 3(b)), the dominant peak is at (100) and (101) plane orientations. Meanwhile, the growth of ZnO/AZO film also exhibits a preferential growth along *c*-axis (Figure 3(c)). In case of ZnO film, the preferential crystal growth may be dominated by the seed layer film and small number of nanoflake structures (from FESEM images), which preferentially grown along (100) and (101) plane orientations. Once the ZnO layer is grown on the AZO, we can observe that the peak intensity at (100) and (002) slightly increased. The increment of preferential *a*-plane growth may explain the formation of layer on the AZO surface which is expected to originate from the side surface of the nanorods of the AZO film as discussed earlier. Figure 3(d) depicts the magnified image of the XRD patterns at (002) plane orientations. The plot shows the significant increases of peak intensity for the film which was grown with AZO. Comparing both AZO and ZnO/AZO films, only a slight increment to the peak intensity can be detected. Interestingly, no peak shifting can be witnessed after the second growth process, indicating no residual stress forced on the ZnO/AZO film.

To investigate more on the crystal structure, we characterized the films using Raman spectroscopy as shown in Figure 4. The characterization was done under argon (Ar) laser operating at 514 nm as excitation source. Two inherent Raman peaks at 437 and 581 cm^{-1} which correspond to E_2(high) and E_1(LO) mode, respectively [10]. Other insignificant peak can also be observed which situated at 332 cm^{-1}, which represents $2E_2$(M) mode [11]. E_2(high) mode indicates the Raman vibration of hexagonal ZnO structure and the intensity of Raman vibration of E_2(high) increased which shows that better crystalline structure of AZO and ZnO/AZO. This result is in agreement with the previously discussed XRD patterns. Further, the Raman vibration of E_1(LO) mode shifted from 565 cm^{-1} of seed layer and AZO to 581 cm^{-1} of ZnO/AZO. E_1(LO) mode can be related to the lattice defect (oxygen vacancy).

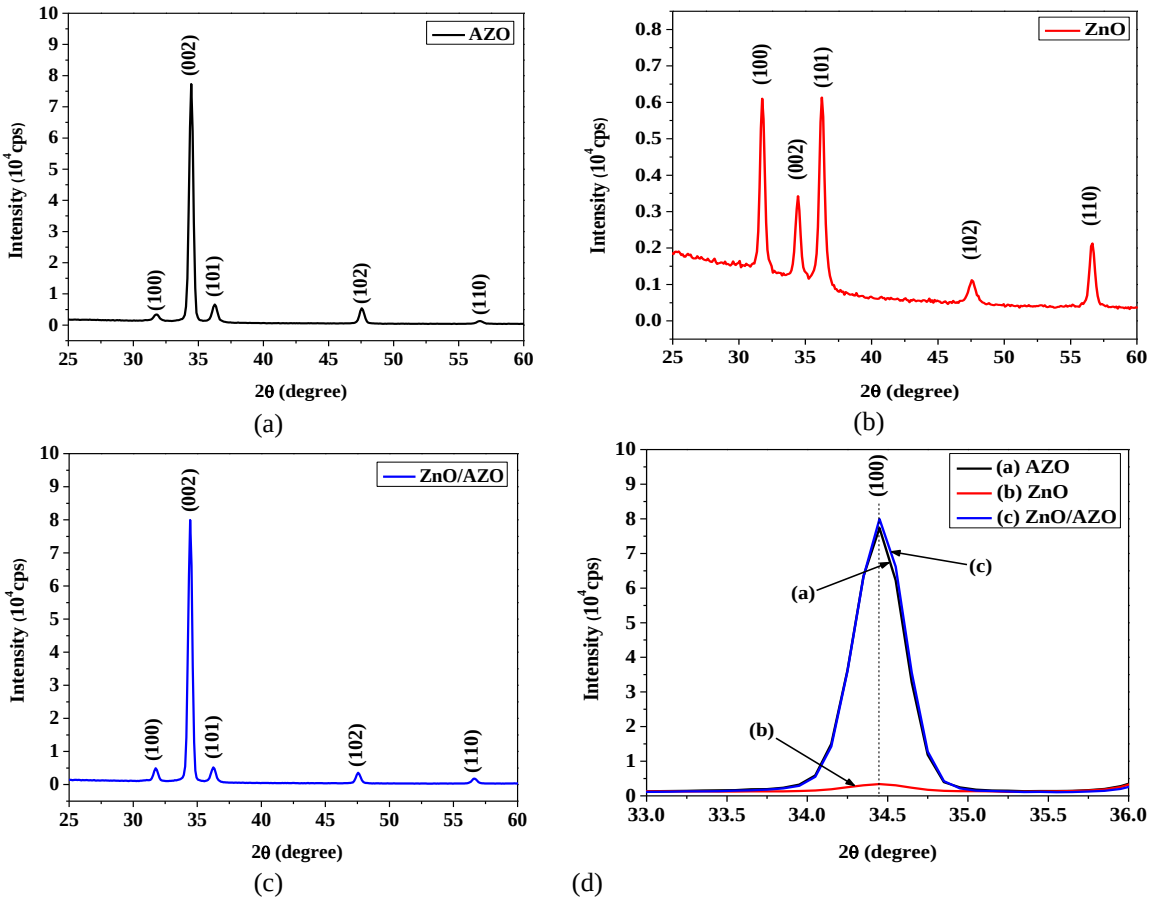

Figure 3. XRD pattern of (a) AZO, (b) ZnO and (c) ZnO/AZO films

The optical properties of the films were measured using UV-vis spectrophotometer in the wavelength range of 350 – 800 nm. Figure 5 depicts the transmittance measurement of the films. All films exhibit good optical transparency in the visible region and steep edge around 380 nm, represent the band gap energy of the ZnO. The average transmittances of each film are 94.4%, 87.8%, and 66.5% for seed layer, AZO and ZnO/AZO homojunction films, respectively. The seed layer film possessed the lowest transmittance may be due to the lowest thickness compared to other films. Similar to other film, the variation of average transmittance is expected from the difference in film thicknesses, which is the cause for optical scattering effect [12].

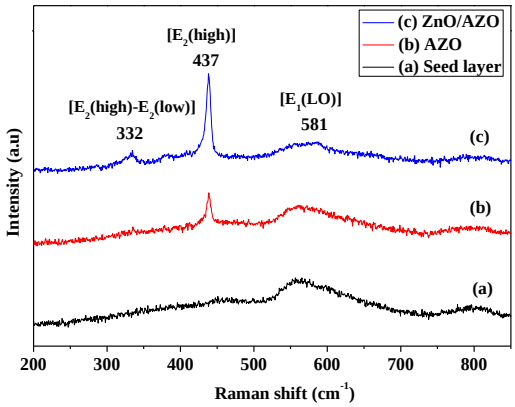

Figure 4. Raman spectra of (a) seed layer, (b) AZO and (c) ZnO/AZO films

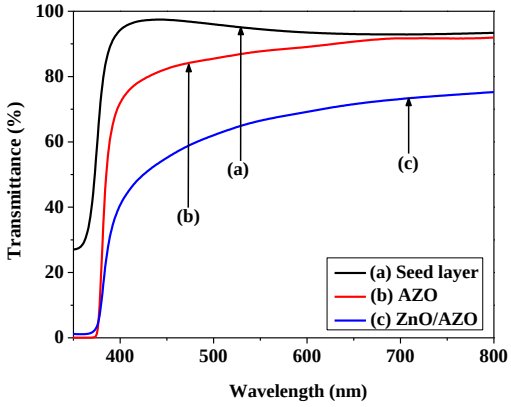

Figure 5. Transmittance spectra of (a) seed layer, (b) AZO and (c) ZnO/AZO films

From the transmittance plot, the absorption coefficient of the films was plotted using the following Equation [13]:

$$a = \frac{1}{t}\ln\left(\frac{1}{T}\right) \quad (1)$$

Here, α is the absorption coefficient, t is the thickness, and T is the transmittance. The absorption coefficient is shown in Figure 6. The films show good absorption at UV region, with ZnO/AZO homojunction film possessed the highest UV absorption compared to other samples. The possible reason which leads to this result is high scattering effect at the homojunction interface which causes more photon trapping in the film.

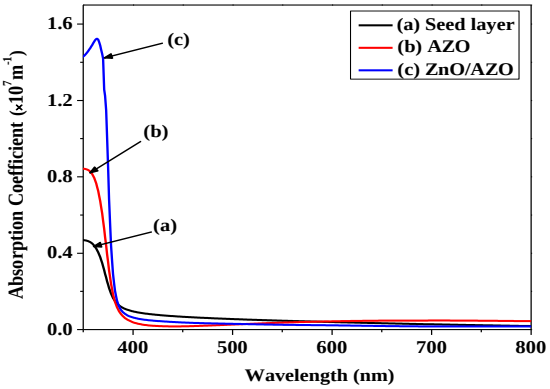

Figure 6. Absorption coefficient of (a) seed layer, (b) AZO and (c) ZnO/AZO films

For direct band gap semiconductor, the optical band gap energy, E_g can be correlated through the given formula [14]:

$$ahv = B\left(hv - E_g\right)^{\frac{1}{2}} \quad (2)$$

Here, B is a constant and hv is the incident photon energy. Figure 7 demonstrates the $(ahv)^2$ versus photon energy for E_g estimation. The E_g of the seed layer, AZO and ZnO/AZO are 3.26, 3.27, and 3.22 eV, respectively. No significant changes to the E_g can be observed. However, one the interesting alteration to the E_g is when the intrinsic ZnO is used on the film. We can see that the E_g shifted to low value for the ZnO/AZO homojunction film. This alteration may be appeared due to the intrinsic nature of ZnO which has E_g value from 3.2 – 3.3 eV [15]. In addition to that, for ZnO/AZO film, the decrement of Eg may be caused by the scattering effect at the interface between the oxide homojunction [16].

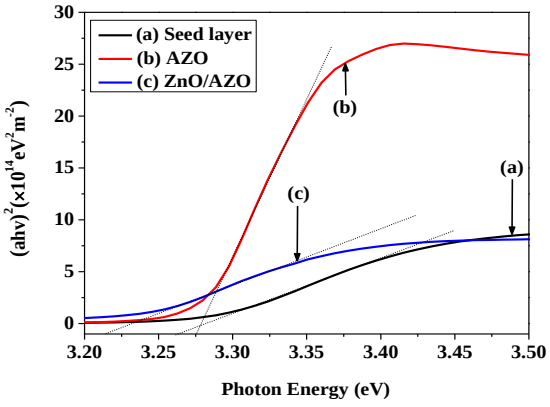

Figure 7. Tauc's plot of (a) seed layer, (b) AZO and (c) ZnO/AZO films

4. CONCLUSION

Intrinsic ZnO/Al-doped ZnO (AZO) homojunction film was prepared using two-step immersion processes. The FESEM images display that the intrinsic ZnO film depositions on the seed layer grew into ZnO nanostructures (nanorods and nanoflakes). However, when the intrinsic ZnO film is deposited on the nanorod surfaces, it just formed a layer which covered the nanorods of AZO film. The average diameter of the ZnO/AZO homojunction also increased up to 95 nm, higher than bare AZO. The XRD patterns demonstrate that the films possessed good crystallinity. AZO and ZnO/AZO homojunction films showed preferred orientation at (002) plane while ZnO film shows preferential growth along (100) and (101) plane orientations. Raman measurement confirms that the films consist of hexagonal ZnO structure with vibration peaks occurred at $2E_2$(M), E_2(high), and E_1(LO). The ZnO/AZO homojunction film possessed excellent absorption at UV region with optical band gap energy of 3.22 eV. These results indicate that the ZnO/AZO homojunction film has a good potential for optical-based device such a UV sensor.

ACKNOWLEDGEMENTS

This work was supported by the ASEAN-India Research & Training Fellowship (IMRC/AISTDF/R&D/P-1/2017). The authors also would like to thank the Faculty of Electrical Engineering of UiTM for their financial support of this research.

REFERENCES

[1] Kokate SK, Supekar AT, Baviskar PK, Palve BM, Jadkar SR, Mohite KC, Pathan HM. CdS sensitized pristine and Cd doped ZnO solar cells: Effect of SILAR cycles on optical properties and efficiency. *Materials Science in Semiconductor Processing*. 2018; 80: 179-183.

[2] Voss T, Waldvogel SR. Hybrid LEDs based on ZnO nanowire structures. *Materials Science in Semiconductor Processing*. 2017; 69: 52-56.

[3] Ismail AS, Mamat MH, Yusoff MM, Malek MF, Zoolfakar AS, Rani RA, Suriani AB, Mohamed A, Ahmad MK, Rusop M. Enhanced humidity sensing performance using Sn-Doped ZnO nanorod Array/SnO2 nanowire heteronetwork fabricated via two-step solution immersion. *Materials Letters*. 2018; 210: 258-262.

[4] Jiang L, Huang K, Li J, Li S, Gao Y, Tang W, Guo X, Wang J, Mei T, Wang X. High carrier mobility low-voltage ZnO thin film transistors fabricated at a low temperature via solution processing. *Ceramics International*. 2018; 44(10): 11751-11756.

[5] Urgessa ZN, Botha JR, Tankio Djiokap SR, Coleman C, Bhattacharyya S. Patterned growth of ZnO nanorods by chemical bath deposition. *Physica B: Condensed Matter*. 2018; 535: 79-83.

[6] Nava Núñez MY, Martínez-de la Cruz A. Nitric oxide removal by action of ZnO photocatalyst hydrothermally synthesized in presence of EDTA. *Materials Science in Semiconductor Processing.* 2018; 81: 94-101.

[7] Mamat MH, Malek MF, Hafizah NN, Md Sin ND, Saurdi I, Suriani A.B, Nafarizal N, Ahmad MK, Rouhi J, Rusop M. Fabrication of Intrinsic Zinc Oxide-Coated, Aluminium-Doped Zinc Oxide Nanorod Array-Based Ultraviolet Photoconductive Sensors. *Applied Mechanics and Materials*. 2015; 773-774: 696-700.

[8] Jiang M, Tang K, Yan X. Characterization of Intrinsic ZnO Thin Film Deposited by Sputtering and Its Effect on CuIn1-xGaxSe2 Solar Cells. *Journal of Photonics for Energy*. 2012; 2(1): 28502.

[9] Mamat MH, Sahdan MZ, Khusaimi Z, Ahmed AZ, Abdullah S, Rusop M. Influence of doping concentrations on the aluminum doped zinc oxide thin films properties for ultraviolet photoconductive sensor applications. *Optical Materials*. 2010; 32(6): 696-699.

[10] Wang M, Ren F, Zhou J, Cai G, Cai L, Hu Y, Wang D, Liu Y, Guo L, Shen S. N Doping to ZnO Nanorods for Photoelectrochemical Water Splitting under Visible Light: Engineered Impurity Distribution and Terraced Band Structure. *Sci. Rep.* 2015; 5: 12925.

[11] Chanda A, Gupta S, Vasundhara M, Joshi SR, Mutta GR, Singh J. Study of structural, optical and magnetic properties of cobalt doped ZnO nanorods. *RSC Advances*. 2017; 7(80): 50527-50536.

[12] Ismail AS, Mamat MH, Md. Sin ND, Malek MF, Zoolfakar AS, Suriani AB, Mohamed A, Ahmad MK, Rusop M. Fabrication of hierarchical Sn-doped ZnO nanorod arrays through sonicated sol−gel immersion for room temperature, resistive-type humidity sensor applications. *Ceramics International*. 2016; 42(8): 9785-9795.

[13] Lee S-M, Joo Y-H, Kim C-I. Influences of film thickness and annealing temperature on properties of sol–gel derived ZnO–SnO2 nanocomposite thin film. *Applied Surface Science*. 2014; 320: 494-501.

[14] Mohamed R, Mamat MH, Ismail AS, Malek MF, Zoolfakar AS, Khusaimi Z, Suriani AB, Mohamed A, Ahmad MK, Rusop M. Hierarchically assembled tin-doped zinc oxide nanorods using low-temperature immersion route for low temperature ethanol sensing. *J Mater Sci: Mater Electron*. 2017; 28(21): 16292-16305.

[15] Ahmed MAM, Mwankemwa BS, Carleschi E, Doyle BP, Meyer WE, Nel JM. Effect of Sm doping ZnO nanorods on structural optical and electrical properties of Schottky diodes prepared by chemical bath deposition. *Materials Science in Semiconductor Processing*. 2018; 79: 53-60.

[16] Yu S, Ding L, Zheng H, Xue C, Chen L, Zhang W. Electrical and photoelectric properties of transparent Li-doped ZnO/ZnO homojunctions by pulsed laser deposition. *Thin Solid Films*. 2013; 540: 146-149.

S.M. et al. BMC Complementary and Alternative Medicine (2018) 18:104
https://doi.org/10.1186/s12906-018-2165-1

BMC Complementary and Alternative Medicine

RESEARCH ARTICLE Open Access

Gelidiella acerosa inhibits lung cancer proliferation

Fazeela Mahaboob Begum S.M.[1], Kalai Chitra[2], Benin Joseph[2], Raji Sundararajan[3] and Hemalatha S.[1*]

Abstract

Background: Lung adenocarcinoma is the most common subtype of Non small cell lung cancer in which the PI3K/Akt cascade is frequently deregulated. The ubiquitous expression of the PI3K and the frequent inactivation of PTEN accounts for the prolonged survival, evasion of apoptosis and metastasis in cancer. This has led to the development of PI3K inhibitors in the treatment of cancer. Synthetic PI3K inhibitors undergoing clinical and preclinical studies are toxic in animals. Hence, there is a critical need to identify PI3K inhibitor(s) of natural origin.
The current study aims to explore the efficacy of the red algae *Gelidiella acerosa*on inhibition of cell proliferation, migration and the expression of cell survival genes in lung adenocarcinoma cell line A549.

Methods: The phytoconstituents of *Gelidiella acerosa* were extracted sequentially with solvents of different polarity, screened qualitatively and quantitatively for secondary metabolites and characterized by GC-MS. The in-vitro studies were performed to check the efficacy of the extract on cell proliferation (MTT assay), cell invasion (scratch assay and colony formation assay), apoptosis (fluorescent, confocal microscopy and flow cytometry) and expression of apoptosis and cell survival proteins including PI3K, Akt and GSK3β and matrix metalloproteinase MMP2 and MMP9 by Western blot method. The antitumor activity of GAE was analyzed in a tumor model of Zebrafish.

Results: The outcomes of the in vitro analysis showed an inhibition of cell proliferation, induction of apoptosis, inhibition of cell migration and colonization by the crude extract. The analysis of protein expression showed the activation of caspases 3 and Pro apoptotic protein Bax accompanied by decreased expression of Bcl-2 and Bcl-XL. On the other hand, subsequent activation of GSK3β and down regulation of PI3K, Akt were observed. The decreased expression of MMP2 correlated with the antimetastatic activity of the extract. The in vivo studies showed an inhibition of tumor growth by GAE in Zebrafish.

Conclusion: The phytoconstituents of algal extract contributed to the anticancer properties as evidenced by in vitro and in vivo studies. These phytoconstituents can be considered as a natural source of PI3K/Akt inhibitor for treatment of cancers involving the PI3K cascade.

Keywords: *Gelidiella acerosa*, PI3K, Akt, GSK3β, Caspase 3, Bax, Bcl-2, Bcl-XL, Tumor model of zebrafish

Background

Lung cancer is a heterogeneous disease which has taken a death toll of 1.6 million in 2015 [1]. The two major classes of lung cancer are Non Small cell lung cancer (NSCLC) and Small cell lung cancer. Of these, the NSCLC accounts for 85% of lung cancer cases. Histologically, NSCLC includes three subclasses, namely small cell carcinoma, large cell carcinoma and adenocarcinoma. Among these, the lung adenocarcinoma constitutes 40% of NSCLC cases [2]. The 5-year survival rate of NSCLC varies from 1 to 45%, depending on the extent of metastasis. Molecular profiling studies have identified the PI3K/Akt cascade as a frequently targeted pathway in NSCLC [3, 4].

The phosphoinositide kinases 3 (PI3Ks) are groups of proteins that regulate cell growth, survival, metabolism and glucose homeostasis [5]. Recent studies have shown that PI3K and its components are frequently mutated in human cancers which in turn contribute to the aberrant activation of the PI3K/AKT/mTOR pathway in cancer. Hence, the PI3K cell survival pathway became the most

* Correspondence: hemalatha.sls@bsauniv.ac.in
[1]School of Life Sciences, B.S. Abdur Rahman Crescent University, Chennai 600048, India
Full list of author information is available at the end of the article

targeted candidates for anticancer therapy [5, 6]. Further, the aberrant expression of PI3K confers multidrug resistance, thus contributing to poor prognosis [7, 8]. Targeting the PI3K signaling cascade with small molecule inhibitors could be an effective means of treating cancer [9, 10]. Current PI3K inhibitors that are available in the market act either by inhibiting PI3K or any of its downstream components [7–11]. The first generation PI3K inhibitors including Wortmannin and LY294002 were discontinued due to their toxicity in animals [12, 13]. Several PI3K inhibitors are being developed in both the pharmaceutical industries and academic institutions. These include the Dactolisib, Umralisib, Buparlisib, Serabelisib, IP1–549, SF-253, GDC-0326and Alpelisib which are undergoing different phases of clinical trials [14–22]. The recent approval of Idelalisib, the first oral PI3K inhibitor by the FDA for the treatment of chronic lymphocytic leukemia [23], has triggered the drug industry to search for new PI3K inhibitors that act efficiently and selectively without any side effects. Hence, the current study was intended to identify natural bioactives which can target PI3K or its components and without any cytotoxicity.

Natural products are used worldwide for the treatment of various diseases. Recent studies have shown that 47% of anticancer drugs are developed from natural products [24]. According to the World Health Organisation, 80% of the world's population relies on natural products for health care. Over the past 40 years, the marine environment has drawn special attention due to the discovery of numerous lead compounds and drugs with unique structures [25]. Among the marine organisms, algae and sponges are widely utilized as sources of novel drugs. Marine red algae are rich in bioactive metabolites with varied therapeutic properties [26, 27]. They are widely exploited for the production of agar, alginates and carrageenan worldwide [28]. The marine red algae *Gelidiella acerosa* (*G.acerosa*) (Order: *Gelidiales*, Family: *Gelidiellaceae*, Genus: *Gelidiella*) is abundantly found in the intertidal zones of the Gulf of Mannar, South India. It is widely utilized by the Food and Pharma industries for its high-quality agar [29]. Studies conducted earlier have reported the antimicrobial, antioxidant, antifungal, anticoagulant, antifertility, anticholinesterase, anticancer and post-coital contraceptive activities of *G.acerosa* [30–40]. Although, the anticancer activity of the algae was reported previously [39] the phytocompounds and their mechanism of action were not reported. Our current research is focused on discovering the bioactive molecules from *G.acerosa*, which can target PI3K pathway and its components without inducing any cytotoxicity. Although enough medical advancement is achieved in the management of lung cancer, the survival rate is highly disappointing [41]. The frequent deregulation of PI3K and its components accounts for progression of lung cancer [42]. The over-activation of PI3K confers resistance to the current anticancer therapies. Hence there is a critical need to identify a suitable drug which acts by inhibiting PI3K, Akt expression. In the current study, the phytoconstituents of *G.acerosa* are analyzed for their efficacy to inhibit cell proliferation, invasion and tumor formation, induction of apoptosis and regulation of cell survival cascade PIK3, Akt, GSK3β under in vitro conditions using the adenocarcinoma lung cancer cell line A549.

As per FDA regulations, acute and chronic toxicity studies are essential for compounds which are intended for human use. As most of the compounds which are effective under in vitro conditions, failed in toxicity analysis and in vivo studies, the current research was focused on determining the in vivo toxicity in adult Zebrafish (*Danio rerio*) and confirming the results through a novel Tissue-Chip technology.

Methods

Seaweed collection, processing and characterization

Marine red algae *G.acerosa* was collected from the Mandapam coast, Tamil Nadu, India after identification and authentication by Dr. Raju Saravanan, Scientist, Center for Marine Fisheries Research Institute (CMFRI), Mandapam, India. A specimen of the seaweed was deposited at CMFRI (accession number: MMM-CMFRI17002). The seaweed was washed, shade dried, milled and the dry powder was used for sequential extraction [43] and analyzed for the presence of various phytoconstituents [44, 45]. The total polyphenol and flavonoids content of the extracts were estimated [46, 47]. The ethyl acetate extract of *G.acerosa* (GAE) was subjected to HPLC analysis [48] in Shimadzu HPLC 9A with LC 20 AD binary gradient pump, SPD- M20A Diode array detector and RF-Fluorescence detector. The identification of functional groups, covalent bonds in GAE was carried out through Fourier Transformation Infrared spectroscopy [49, 50]. The GC MS analysis of GAE was done in JOEL GCMATE II GCMS advanced mass spectroscopy system. The sample was analyzed as per the manufacturer's protocol and the emerging fragment ions were collected. The probable structure based on the ion fragmentation pattern was derived from the NIST14 (National Institute of Standards and Technologies) library search.

Determination of antioxidant activity

2, 2 Di phenyl – 1-Picrylhydrazyl (DPPH) radical scavenging assay

The efficacy of the algal extracts to scavenge the free radicals generated in the form of (DPPH) was assessed as previously described [51].

In vitro analysis of cell viability

A549 cells, procured from National Facility for Animal Tissue and Cell Culture, Pune, India, were used for the study. The cells were subcultured in DMEM containing 10% heat-inactivated FBS and 1% antibiotic cocktail (GIBCO, USA). The cell viability assay was carried out [52]. Briefly, 2 × 105 cells were seeded in 96 well plates and allowed to adhere. The cells were exposed to different concentrations of GAE (0.1–2 mg/ml) for 24 h and the cell viability was assessed by MTT assay.

Analysis of apoptosis

The hallmarks of apoptosis were analyzed by fluorescent and confocal microscopy. In brief, 2 × 105 cells were seeded in 6 well plates and allowed to become 80% confluent. The cells were exposed to 1.5 mg of GAE for 24 h. The cells were washed with ice-cold PBS twice and fixed with 70% ice-cold methanol and stained with DAPI (5 μl) for 5 min in darkness. The cells were observed for nuclear fragmentation under the inverted fluorescent microscope (Zeiss1.0). The same procedure was followed for staining with propidium iodide (5 mg/ml) and AnnexinV (5 μl). For Flow cytometry analysis, 5 × 103 cells were seeded in 35 mm Petri dishes and treated with 1.5 mg of GAE for 6 h. The cells were trypsinized and treated with 5 μl of DAPI (5 min) and analyzed for apoptosis, cell cycle arrest and changes in DNA content in Beckman Coulter Moflo [53, 54]. The cells which were not exposed to GAE served as the control group.

Immunoblot analysis

The cells at a concentration of 5×10^5cells/ml were seeded in 100 mm Petri dishes and incubated to attain confluence. The cellswere exposed to the inhibitory concentration of GAE (1.5 mg/ml) for 24 h. The cells without GAE treatment represented the control group. The medium was removed and the cells were washed twice with ice-cold PBS and lysed with RIPA buffer. The cell lysate was centrifuged (14,000 rpm, 10 min) and the supernatant was stored at − 20 °C till further use. The protein content of the cell lysate was quantified by Lowry's method. 50 μg of protein was separated in 10% SDS- PAGE and the proteins were transferred onto a nitrocellulose membrane (BioRad, USA) and blocked with 5% skim milk (BioRad, USA). Following this, the membrane was exposed to primary antibodies (4 °C, 24 h) against Bax (1:500 Abcam, USA) ,Bcl-2(1:500 Abcam, USA), Bcl-XL (1:500 Abcam, USA), Caspase 3 (1:200 Abcam, USA), PI3K (1:500 Abcam, USA), p PI3k(1:1000 Abcam, USA), Akt(1:500 GenetexBio, USA), p Akt(1: 1000 GenetexBio, USA) and β actin (1:1000 1:1000 Abcam, USA). The membrane was then incubated with HRP-conjugated anti-mouse (1:2500) and anti-rabbit (1:2000) secondary antibodies for 1 h (RT) with continuous shaking. The protein bands were visualized using an ECL staining kit (Amersham Pharmacia Biotech, Sweden).

Scratch assay

In order to analyze the effect of GAE on cell migration, the wound healing assay was carried as previously described [55]. In brief, cells were grown in 12-well culture plates until they became 90% confluent. Following this, the cells were exposed to serum-free medium for 12 h. The monolayers of cells were scratched with a fine micropipette tip to create a wound. The cellular debris was removed by PBS, and the cells were exposed to serum-free medium containing different concentrations of GAE (0.1–1.5 mg/ml). The migrated cells were fixed (cold 75% methanol, 30 min) and washed with ice-cold PBS. The migration of cells into the wounded area was imaged at 0 and 24 h.

Clonogenic assay

The ability of single cells to retain their reproducing ability to develop as a colony was analyzed by the classical clonogenic assay as described earlier [56]. In brief, the cells were grown in 6 well plates until they became confluent. The cells were then exposed to different concentrations of GAE (0.1–1.5 mg/ml) for 24 h. The medium was removed and the cells were trypsinized to obtain a single cell suspension. Five hundred cells, exposed and unexposed to GAE were seeded in 6 well plates and fresh medium was added. The plates were left undisturbed for 7 days. Later, the medium was removed and the cells were washed with PBS, stained with Trypan blue and observed under the microscope.

Immunoblot analysis of MMP expression

To determine the antimetastatic activity of GAE, the expression of matrixes, MMP2 and MMP9 were analyzed by western blot. In brief, the cells were grown in 6 well plates, treated with GAE (1 mg/ml) for 24 h. The cells that were not exposed to GAE represented the control. The cells were lysed as mentioned previously, and the protein was isolated. The protein was analyzed for the expression of MMP2 and MMP9 in the treated and control cells.

Statistical analysis

For in vitro analysis, all experiments were done in triplicate and the data represents the mean ± SD.

Analysis of antitumor activity of GAE on A549 tumor-induced zebrafish

Adult male Zebrafishes (2.5 ± 0.2 cm long, 1.5 ± 0.5 g) were induced to develop tumors as described previously with slight modifications [57]. In brief, adult Zebrafishes were injected with 5 μl of A549 cells in the muscle

region to develop tumors. After 14 days interval, the second dose of A549 cells (5 μl) was injected. The fishes were maintained in a 21-l water tank, 14/10 h light and dark cycles, under normal feed for 60 days to develop tumors. The development of tumors was confirmed by dissecting the tumor-induced fish. The tumor-induced Zebrafishes were fed with GAE (15, 30, 45 and 60 μg/day) for a period of 10 days. Following this treatment, the fishes were dissected and analyzed for parameters including muscle anatomy, tumor anatomy and pathology. The experiment was done in triplicate with two fishes per group for each dosage. A control without GAE treatment was also maintained.

Acute and chronic toxicity analysis in zebrafish

Adult *Danio rerio* were housed in pairs. Different concentrations of GAE (100,250,500 μg/day) were administered orally along with the fish feed. The fishes were observed for behavioral changes and for acute and chronic toxicity. The experiment was done in triplicate and a control group was maintained.

Novel Tissue-Chip for drug screening

The novel lab-on-chip technology was used to screen the efficacy of the algal extract. The Tissue -Chip is a novel platform to replace the use of animal models. In Tissue-Chip, (Refer Additional file 1) the major organs like heart, liver, skeletal muscle and brain cells are grown in a fully closed circulatory system with active physiological hormonal balance; hence the Tissue-Chip mimics the whole animal system. Further, the Tissue-Chip enables the rapid screening of compounds (24–48 h), reduces the volume of compounds for analysis, is cost-effective, non-laborious and the results are comparable to whole animal models. Currently, the toxicology analysis, drug screening, kinetics, and bioequivalence are carried out independently. However, all these processes can be integrated into a single step in the Tissue-Chip platform. Therefore, in one step, ADMET (Absorption, Distribution, Metabolism, Excretion and Toxicity), drug screening and elimination of false positives can be done.

The Tissue-Chip (Pentagrit, Chennai) used for the current drug screening is a 3D scaffold which allows growing cells from different organs in a single chip. Adult male Zebrafish were euthanized as per guidelines. The liver, heart, muscle and brain were dissected and isolated using dissection needle. The organs were teased to obtain a single cell suspension, centrifuged at 9000 rpm for 15 min. The cell pellet obtained was mixed well to get a single cell suspension.5 μl of the cells from each organ was loaded to the separate scaffold provided in the Tissue-Chip and the Cells were cultured in DMEM (without glucose and with 0.01% tetracycline) along with different concentrations of GAE (100,250,500 μg/ml) at 37 °C for 48 h.The tissue developed was removed and stained with Hematoxylin and Eosin stain and observed under the microscope for cell viability.

Results

GAE is rich in polyphenols and flavonoids

G. acerosa was extracted sequentially with solvents of varying polarity. Phytochemical analysis showed the abundance of compounds in ethyl acetate extract (GAE). Table 1 shows the phytochemical analysis of different solvent extracts of *G.acerosa* and the presence of various phytoconstituents at different concentration in the extracts.

Total polyphenols (61.2 μg/100 mg) and flavonoids (13 μg/100 mg) were highest in GAE (Fig. 1a and b). HPLC analysis confirmed the presence of 4 compounds in GAE with retention times of 15.083, 16.70, 18.086, 19.588 min (Fig. 1c). FTIR analysis revealed the presence of a carbonyl group (1733 cm^{-1}), C-O, stretching of alcohol (1045 cm^{-1}), C-O, stretching of ether (1244 cm^{-1}), and C-O, stretching of acid groups (2977 cm^{-1}) in GAE (Fig. 1d). The GC-MS analysis (Fig. 2) revealed the presence of fourteen compounds in GAE (Table 2).

The abundance of phytoconstituents suggested that ethyl acetate is the best- suited solvent for the extraction of algal bioactives. The results of the DPPH assay (Fig. 1e) showed that GAE has a higher antioxidant efficiency (381%) than ascorbic acid. The antioxidant assay showed that GAE is more effective in scavenging free radicals when compared to standard ascorbic acid.

GAE induces cytotoxicity in A549 cells in vitro

In order to determine the antiproliferative activity of GAE, A549 cells were treated with increasing concentration of GAE for 24 h and cell death induced was measured by MTT assay. GAE induced cell death was concentration dependent. Cell viability decreased at concentrations >1 mg/ml. The inhibitory concentration, IC50 which induced 50% cell death was identified as 1.5 mg/ml (Fig. 3a). Hence this concentration was used for further studies.

GAE induces apoptosis

In order to investigate whether the antiproliferative activity was mediated through the induction of apoptosis, A549 cells, treated with GAE (1.5 mg/ml, 6 h) were observed for changes in nuclear morphology by DAPI, PI and Annexin V staining. The characteristic features of apoptosis-like nuclear fragmentation, sub-lobed nuclei and exposure of Phosphatidyl serine were observed in GAE treated cells through fluorescent and confocal microscopy (Fig. 3b and c). As the apoptotic hallmarks were observed morphologically, flow cytometric determination of apoptosis was done with DAPI staining. The DAPI staining revealed the presence of a diploid peak,

Table 1 Phytochemical analysis of *G.acerosa*

Phytochemical	Hexane	DCM	Ethyl Acetate	Ethanol	Methanol	Water
Tannins	-	+	+++	++	+++	-
Alkaloids	+++	++	++	-	-	-
Flavonoids	+	+	+++	+++	++	++
Saponins	-	-	-	-	-	-
Phytosterol	-	+++	+++	+++	+++	-
Glycoside	+++	+++	+++	+++	+++	+
Oils & Fats	++	++	+++	++	++	-
Protein	-	+	+	+++	+++	++
Carbohydrates	-	-	+	+++	+++	+++
Resins	-	-	-	++	++	-
Coumarins	-	+	+++	++	++	+
Terpenoids	-	-	+++	+++	+++	-

+ Weak (< 3 μg/ml), ++ Moderate (5–7 μg/ml), +++ Strong (> 8 μg/ml), - Absent

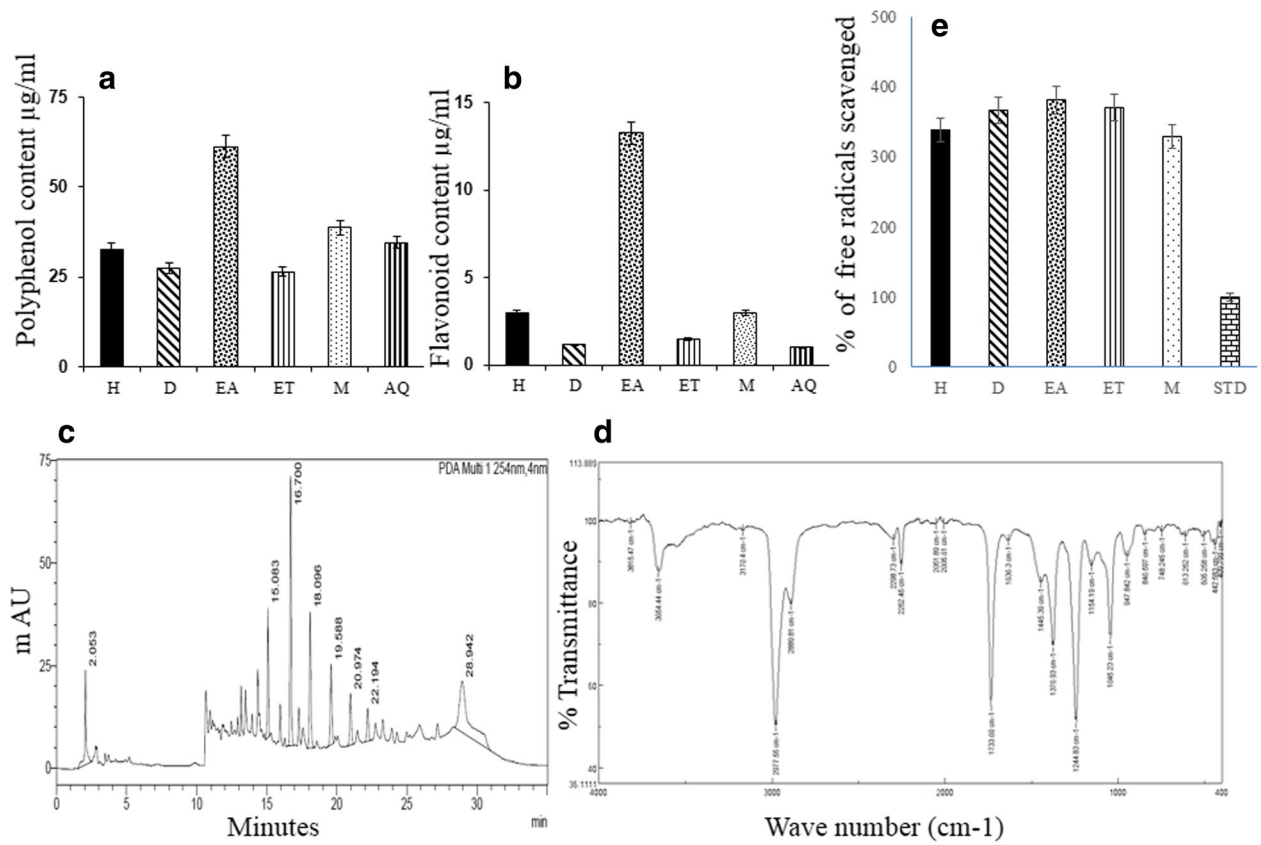

Fig. 1 Characterization of algal phytoconstituents. **a** and **b** Quantification of polyphenols and flavonoids in algal extracts reveals maximum concentration in ethyl acetate extract. **c**. HPLC analysis of ethyl acetate extract shows the presence of 4 compounds with retention time. **d** FTIR analysis of ethyl acetate extract showing presence of functional groups. **e** Analysis of antioxidant activity by DPPH assay reveals maximum antioxidant efficiency of ethyl acetate extract. Values expressed are Mean ± S.D. (H- hexane, D- Dichloromethane, EA- ethyl acetate, ET- ethanol, M- methanol, AQ - aqueous, STD- Ascorbic acid)

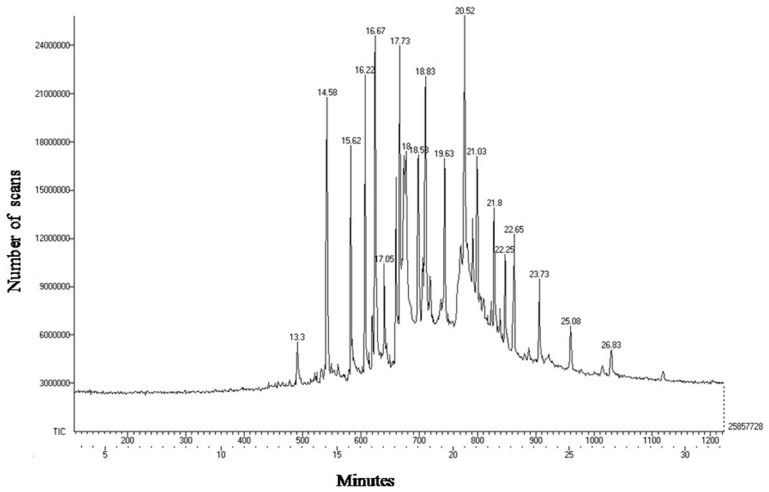

Fig. 2 GC-MS profile of GAE. The GC-MS analysis revealed the presence of various compounds with differing retention time

representing cells with fragmented DNA in the treated group (Fig. 3d). The FACS analysis thus confirmed the arrest of the cell cycle through the induction of apoptosis.

GAE stimulates caspase activation

The role of the caspase cascade in apoptosis isestablished through several studies. In order to investigate whether the induction of apoptosis is caspase-dependent, the expression of caspase-3 and 8 were analyzed in A549 cells treated with GAE. The results showed that caspase-3 was activated as evidenced by the cleaved forms of caspase-3, whereas caspase-8 expression was unaltered (Fig. 4a). The data prompts the involvement of caspase-3 rather than caspase-8 in the induction of apoptosis by GAE.

GAE increases Bax/Bcl2 ratio

Followed by the observation of caspase-3 in GAE induced apoptosis, the role of apoptosis regulators, namely Bax, Bcl2 and Bcl-XL was further investigated. As evidenced by western blot, the GAE treatment up-regulated the expression of the pro-apoptotic protein Bax and down-regulated the expression of anti-apoptotic proteins Bcl2 and Bcl-XL (Fig. 4a). The result strongly suggests that GAE induces apoptosis by altering the Bax/Bcl-2 ratio.

Table 2 GC-MS profile of *G.acerosa* ethyl acetate extract

S. No	Retention Time (Minutes)	PubChem CID	Name of the compound	Molecular formula	Molecular weight
1	15.62	8217	1-octadecene	$C_{18}H_{36}$	252.486
2	16.22	10,408	6,10,14-trimethyl Pentadecan-2-one	$C_{18}H_{36}O$	268.485
3	17.05	8181	Methyl Palmitate	$C_{17}H_{34}O_2$	270.457
4	19.63	545,651	1-Heneicosyl formate	$C_{22}H_{44}O_2$	340.592
5	21.80	12,403	Heneicosane	$C_{21}H_{44}$	296.583
6	22.25	71,750,792	Mono(2-ethyl-6-(tetrahydropyranoxy)hexyl) Phthalate	$C_{21}H_{30}O_6$	378.465
7	22.65	12,592	Tetracosane	$C_{24}H_{50}$	338.664
8	23.73	8222	Eicosane	$C_{20}H_{42}$	282.556
9	26.83	5,365,995	5 Methyl-Z,5-docosene	$C_{23}H_{46}$	322.621
10	18.00	985	Palmitic acid	$C_{16}H_{32}O_2$	256.43
11	13.30	12,395	1-Hexadecene	$C_{16}H_{32}$	224.432
12	14.58	12,398	n-Heptadecane	$C_{17}H_{36}$	240.475
13	25.08	283,510	2-Methyl tricosane	$C_{24}H_{50}$	338.664
14	16.67	3,072,462	Methyl(((2-nitro-4- (phenylmethoxy)phenyl)amino) thioxomethyl)carbamate	$C_{16}H_{15}N_3O_5S$	361.372

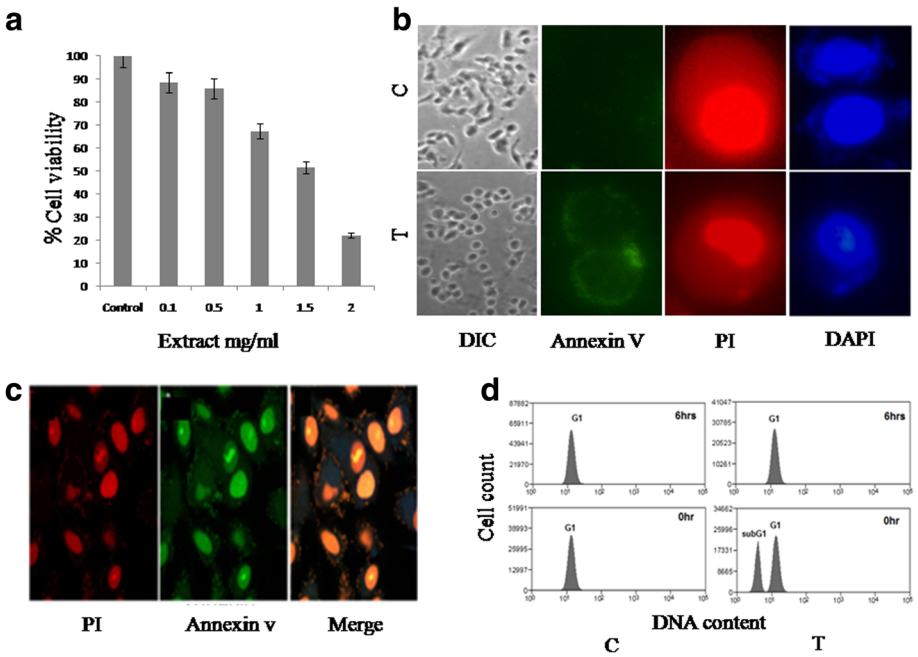

Fig. 3 In vitro analysis of anticancer activity in A549 cells. **a** Cytotoxicity analysis in A549 cells identifies IC50 as1.5 mg/ml of GAE. **b** Fluorescent imaging with Annexin, Propidium iodide and DAPI revealed the translocation of Phosphatidyl serine to the cell membrane and nuclear fragmentation in GAE treated cells. **c** Confocal imaging of GAE treated cells showing nuclear fragmentation. **d** FACS analysis of Apoptosis by DAPI staining shows the emergence of apoptotic peak after 6 h of GAE treatment. All experiments were done in triplicate. The values represent Mean ± SD. C-control, T-treated

GAE activates GSK3β

In order to determine the molecular mechanism behind the alteration of Bax/Bcl-2 ratio, the expression level of GSK3β, a major regulator of apoptotic proteins was analyzed in GAE treated A549 cells. The results revealed that GAE treatment decreased the phosphorylation of GSK3β, thus preventing the inactivation of GSK3β (Fig. 4a). The expression of the active form of GSK3β directly correlates to the increased Bax and decreased Bcl-2 levels.

GAE affects PI3K/Akt expression

In order to explore the underlying mechanism that contributes to the activation of GSK3β, its direct upstream regulators, namely PI3K and Akt expression were investigated. In most human cancers the pro-survival kinase signaling pathway PI3K/Akt is activated accompanied by the inactivation of GSK3β.Hence the expression of PI3K and Akt in GAE treated cells was analyzed. The results showed a decrease in the phosphorylation of both the upstream targets PI3K and Akt (Fig. 4a) which in turn coincides with the increased expression of GSK3β. These findings indicate that GAE induces apoptosis, activates GSK3β through the suppression of PI3K/Akt cascade in A549 cells. The protein levels were quantified and shown in Fig. 5.

GAE inhibits cell migration

In order to analyze the invasive potency of GAE, the wound healing assay was carried out. The cells treated with GAE were observed for their ability to invade into the wounded area. The results of the assay showed that the untreated cells were more efficient in closing the created wound compared to the GAE treated cells. Thus, GAE (1 mg/ml) decreased the number of cells invading the wound. The concentrations less than 1 mg/ml were not effective (Fig. 4b).

GAE treatment suppresses colonization

Metastasis is a multi-step process, involving the digestion of the ECM (Extracellular Matrix), migration and colonization of cells to distant sites. As GAE inhibited cell migration and cell proliferation, the ability of GAE on colony formation was analyzed by the clonogenic assay. The results showed that GAE inhibited the ability of individual cells to form colonies at 1 mg/ml in A549 cells, whereas the concentrations less than 1 mg/ml did not have any effect on colonization. (Fig. 4c).

GAE suppresses MMP2 level

In order to determine the antimetastatic activity of GAE, the protein from the cells was analyzed for the expression patterns of matrix metalloproteinases. The results of Western blot showed decreased expression of MMP2

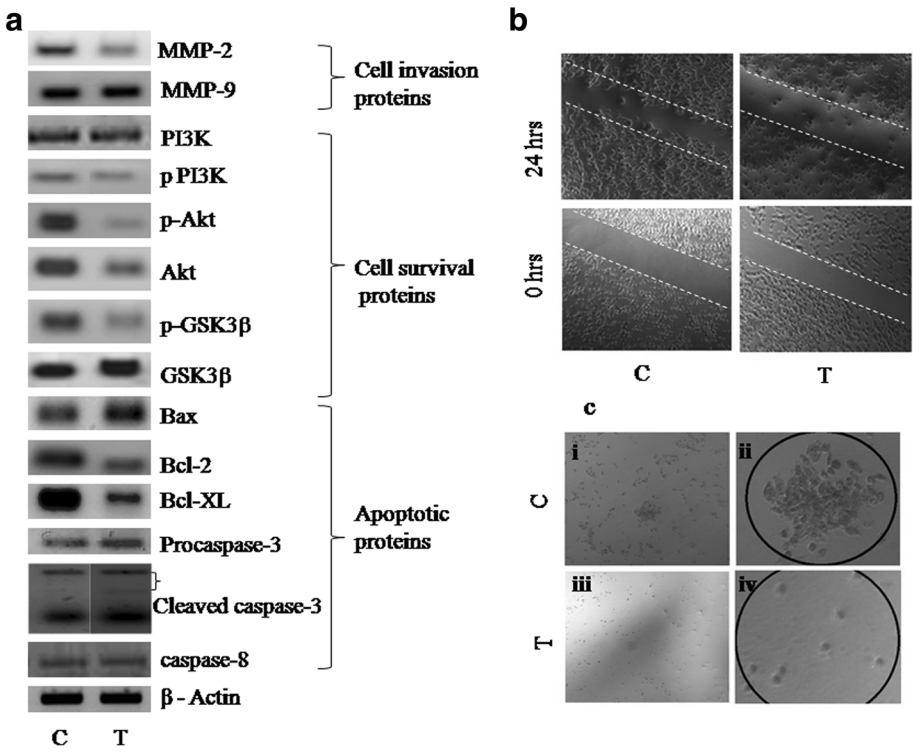

Fig. 4 Analysis of protein expression. **a** Western blot analysis of procaspase-3, cleaved caspase3, caspase-8, Bax, Bcl-2 and Bcl-XL, p-Akt, Akt, p-GSK3β and GSK3β, PI3K, p-PI3K, MMP2 and MMP9. βactin was used to check equal loading. **b** The scratch assay shows the inhibition of cell invasion into the wound region after 24 h of GAE treatment (1 mg/ml). **c** The clonogenic assay result shows the inability of single cells to proliferate as a colony after GAE treatment (1 mg/ml). (i) Colony formed in control cells after 7 days, (ii) magnified colony of control cells, (iii) Treated cells after 7 days, (iv) treated cells magnified. C-control, T-treated

in GAE treated cells when compared to the control (Fig. 4a) however, MMP9 expression was not altered.

Thus, the results of in vitro analysis confirmed the efficiency of GAE in regulating cell proliferation through PI3K cascade and also in controlling metastasis and tumor formation in A549 cells.

GAE is not toxic in vivo and in vitro

The outcomes of the in vivo toxicology analysis showed that the major organs, including the brain, heart, muscle and liver were normal at the dosages of GAE used, both in acute and chronic studies (Fig. 6). These results were confirmed by the lab-on-chip assay where the tissues of brain, heart, liver and muscles regenerated normally till the highest dosage used (500 μg). Both the in vitro and in vivo toxicology studies proved that GAE is not toxic to animals (Fig. 7).

GAE inhibits tumor proliferation in vivo

The antitumor activity of GAE was determined in vivo, using the tumor model of zebrafish. The tumor anatomy, tumor pathology and muscle pathology were analyzed by H & E stain. The results of the histological analysis showed that the tumor control exhibited swollen muscle pathology (Fig. 8a), loss of normal cell architecture with the irregular nucleus (Fig. 8c) whereas the GAE treated group showed normal muscle pathology (Fig. 8d) and lysing tumor cells (Fig. 8f). An increase in the normal cell population was observed in the treated group (60 μg) as compared to the tumor control. The other treated groups (15, 30 & 45 μg) did not show any consistent change. The tumor anatomy showed a decrease in the extent of angiogenesis in the treated group as compared to the control group (Fig. 8b & e).

Discussion

Oxidative damage by reactive oxygen species plays a major role in cancer. Intake of antioxidants can protect from oxidative stress. In the current study, GAE has exhibited higher antioxidant efficiency than ascorbic acid. An earlier study has shown that the methanol fraction of *G.acerosa* exhibited comparative antioxidant activity as that of Butylated Hydroxyl Toluene [58]. The current study has revealed the superiority of GAE over the methanol fraction in scavenging free radicals. Phenolics and flavonoids are excellent free radical scavengers [59]. The current study has revealed a positive correlation between the flavonoid, phenolic and antioxidant efficiency.

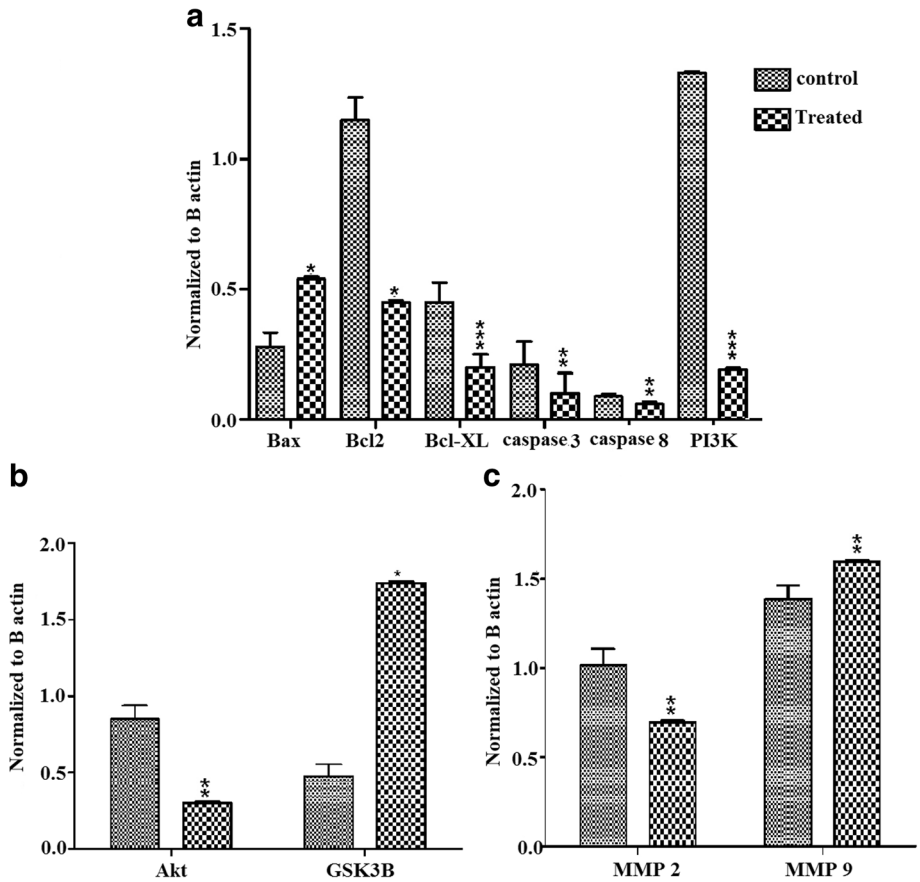

Fig. 5 Analysis of protein expression. Histogram shows the optical density of (**a**) Bax, Bcl2, Bcl-XL, Caspase 8, Caspase 3 and ratio of phospho to total PI3K. **b** Histogram shows the optical density of phospho to total Akt, GSK3β. **c** Histogram shows the optical density of MMP2 and MMP9. Relative expression of protein was normalized to β actin. The density was analyzed by ImageJ software. Values represent mean ± SD.*$p < 0.1$, **$p < 0.05$, ***$p < 0.001$ compared to control group. C-control, T-treated

Hence it can be concluded that these components confer free radical scavenging ability to GAE.

Further, the results of the study coincide with similar studies which have reported a positive correlation between antioxidant activity, flavonoids and phenolic content [60].

Lung adenocarcinoma is the major subtype that contributes to 40% of NSCLC cases when compared to other subtypes [61]. For the current study, the A549 cells (Adenocarcinoma epithelial cells) were used to investigate the efficacy of GAE, as the A549 cells are well characterized among human lung cancer cells and serve as an established research tool to analyze the anticancer drug efficacy, permeability, immunotoxicity, apoptosis and protein expression under in vitro conditions. The anticancer activity of GAE was analyzed against different types of cancer cell lines (results are not shown) and the current study discusses the anticancer activity of GAE in A549 adenocarcinoma cell line.

The MTT assay showed that GAE exerted growth inhibitory activity in A549 cells in a concentration-dependent way. A concentration of 1.5 mg/ml induced 50% cell death, which was identified as the inhibitory concentration (IC50). The results of the current study are comparable with a previous study, where the methanol extract of *G.acerosa* was shown to affect the viability of A549 cells [37–39]. Additionally, the benzene extract of *G.acerosa* was reported as non-cytotoxic in PBMC and did not induce mutagenicity and genotoxicity [62]. The results of these previous studies show that the algal extract is not toxic to normal cells, but can affect the viability of cancer cells.

The observation of the hallmarks of apoptosis, as documented by fluorescent, confocal microscopy and the appearance of the sub-diploid peak as evidenced from FACS analysis in GAE treated cells confirmed that cytotoxicity exerted by GAE is through the induction of apoptosis. Apoptosis or programmed cell death is activated by two major pathways [63], one involving the activating caspase-8 and the other involving the execution caspase-3. In the current study, treatment with GAE activated Caspase-3 and altered the Bax/Bcl2 ratio, which suggests that apoptosis is induced by the mitochondria -

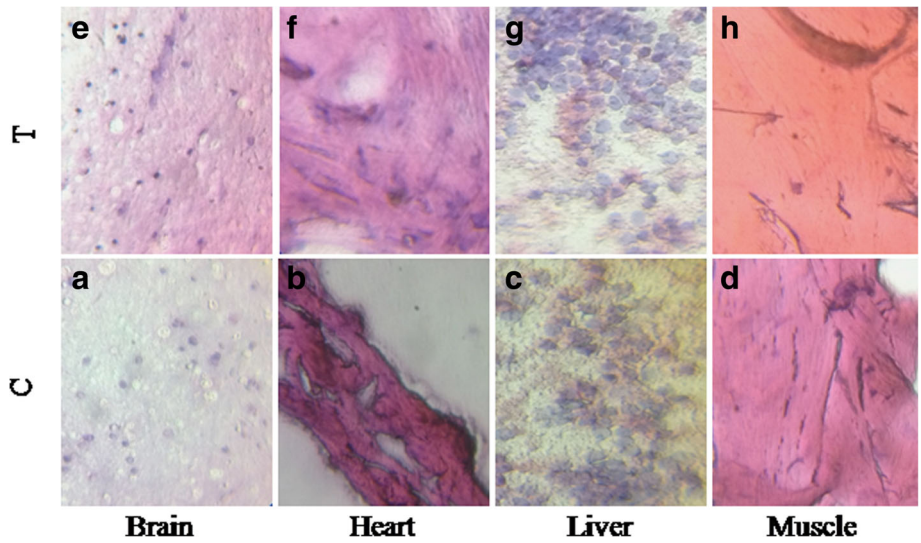

Fig. 6 In vivo chronic toxicology analysis. **a**, **e** Shows the unaltered brain pathology of control and GAE treated Zebrafish. **b**, **f** Shows the pathology of heart muscles in control and GAE treated Zebrafish. **c**, **g** Shows the unaltered muscle pathology of control and GAE treated Zebrafish. **d**, **h** Shows the pathology of liver cells in control and GAE treated Zebrafish. The pathology results confirm that GAE is not toxic to these major organs under chronic conditions. C-control, T-treated

mediated pathway. The alteration of the pro-apoptotic to anti-apoptotic protein levels strongly confirmed the involvement of GSK3β in the apoptotic pathway. As GSK3β regulates the expression of proteins in Bcl-2 family [64, 65], it plays a pivotal role in cell death and survival. Further, the imbalance between pro and anti-survival factors is associated with malignancy, the expression levels of GSK3 in correlation with them were investigated. The results of the current study showed that treatment with GAE inhibited the inactivation of GSK3β, which in turn up-regulated the Bax expression, activated caspase-3 and induced apoptosis. As the activation of GSK3 is strictly regulated by its immediate upstream targets PI3K and Akt [66], the study further investigated the expression of these pro-survival components. The results of the analysis showed that PI3K and Akt are down-regulated by GAE treatment which directly contributed to the activation of GSK3β. The results

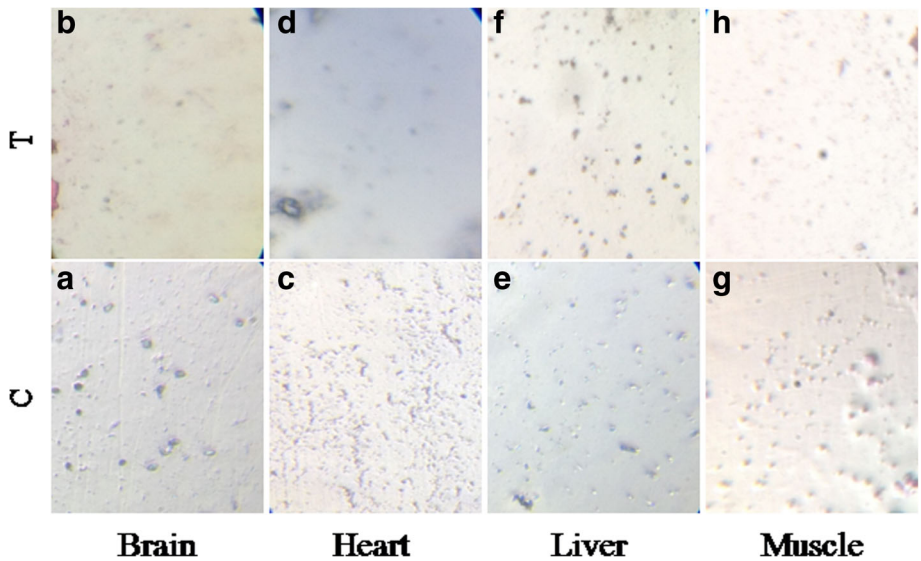

Fig. 7 Toxicology analysis in Tissue-Chip. The pathology studies of vital organs namely brain, heart, liver and muscle were analyzed in both control (**a**, **c**, **e**, **g**) and in treated (**b**, **d**, **f**, **h**) tissue chip. The treatment with algal extract 500 μg did not affect the tissue architecture. The results of tissue chip analysis also support GAE to be safe without toxicity. These tissues were developed and analysed for toxicity in Tissue-Chip Pentagrit, Chennai. C-control, T-treated

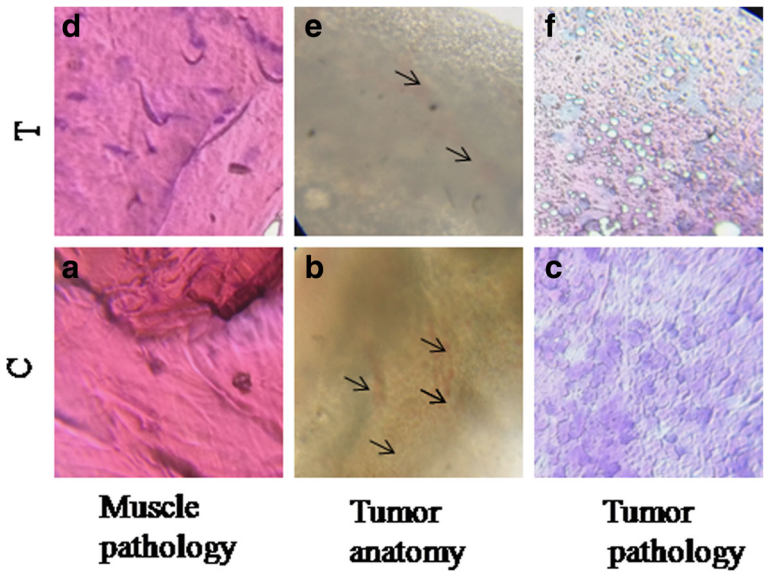

Fig. 8 In vivo analysis of antitumor activity. **a**, **b**, **c** Histopathological analysis of muscle and tumor of tumor induced zebrafish. **d**, **e**, **f** Histopathological analysis of muscle and tumors from GAE treated tumor induced zebrafish. C-control, T-treated

of the current study are in correlation with a previous study, where the inhibition of PI3K/Akt is reported to enhance apoptosis [67]. As the constitutive expression of PI3K pathway causes inactivation of GSK3β and inhibition of apoptosis, GAE treatment is shown to decrease PI3K/Akt expression, activate GSK3β and promote apoptosis. Further, the level of GSK3β is considered as a probe for analyzing PI3K/Akt activity [68]. The findings of the study strongly confirm the down-regulation of PI3Kand Akt which suggests that GAE possess bioactive compounds that can serve as effective PI3K inhibitors.

Although previous studies have reported on the antiproliferative property of *G acerosa*, ours is the first study to report on the antimetastatic property of *G.acerosa*. Metastasis is the major cause of cancer deaths and poor prognosis [69]. It is a complex process involving the degradation of extracellular matrix and invasion of cells into the circulation [70]. Metastasis in cancers of the lung, breast, prostate and ovary are marked by an increased expression of Matrixins or Matrix metalloproteinases (MMPs) [71–73]. MMPs play a vital role in tumor growth, proliferation, angiogenesis and invasion. The secretion and activation of MMP2 and MMP9 are linked with the degradation of ECM and promotion of tumor metastasis [74, 75]. The cell migration assay and colony formation assays revealed the efficiency of the algal bioactives to inhibit cell invasion and prolonged proliferation and correlated with the expression of MMPS. The results revealed a significant decrease in the expression level of MMP2 in the GAE treated cells. Thus the investigation showed that the algal compounds regulate metastasis through the inhibition of MMP2 rather than MMP9. Previous studies have reported the increased levels of MMP2 in NSCLC population and that the level of MMP2 served as an indicator of the extent of tumor metastasis [76–80]. Thus the findings of the current study are in correlation with the previous studies which have shown an increased MMP2 expression in NSCLC. Hence the outcomes of our study confirmed that the algal compounds effectively inhibited not only cell survival, but also cell migration and colonization which are the key challenges in the treatment of cancer.

Following the results of in vitro analysis, the anticancer activity of *G.acerosa* was determined *invivo* in tumor model of zebrafish. The results of the histological analysis showed an increase in the normal cell population in the treated group (60 μg). The observation of lysing cells in the treated group further emphasized the antitumor efficacy of GAE. The outcomes of the in vivo study which are in correlation with the in vitro results suggested the antiproliferative activity of GAE.

The activation of Akt through PI3K is reported to confer resistance to cancer therapy and contribute to poor prognosis in cancer [81] hence down regulation of PI3K and its components are crucial in controlling cell survival and proliferation. Thus the current study has enabled toexplore the molecular mechanism by which the algal compounds can induce apoptosis and regulate the PI3K pathway in cancer. These findings may pave new ways for the effective utilization of seaweeds in the development of PI3K/Akt inhibitors for the management of cancer.

Since GAE exhibited antitumor activity in vitro, the analysis of acute and chronic toxicity was carried out.

The results of in vivo toxicology analysis (both acute and chronic) showed that the compounds of GAE were nontoxic at the concentration used. The major organs including the brain, heart, liver and muscles showed a normal morphology as the control. Similarly in vitro toxicology analysis in Zebrafish Tissue-Chip also revealed the ability of brain, heart, liver and muscles to develop normally without any deformities. Thus the toxicology analysis further supports our study that GAE can induce apoptosis only in tumor cells by targeting PI3K without inducing any toxicity.

In addition, in the current study, the bioactives of GAE were not isolated and analyzed individually. The outcomes of the study are the combined effect of the bioactives, which can be analyzed further for their individual effects. This correlates well with the concept of traditional medicine, which indicates that the synergistic effect of all the components of an extract contributes to the maximum therapeutic effect. As natural products are multitargeted, they have good bioavailability and can neutralize any adverse effects, and hence are widely used in treating multitargeted diseases. In recent years combination therapy has gained importance in the treatment of various diseases like diabetes, cancer and cardiovascular disease, and our study is in line with this.

Conclusion

Overallthe results of the current investigation revealed the antitumor efficacy of GAE phytochemicals which need to be isolated and characterized for further development of potent PI3K inhibitors for the efficient management of cancer. The current investigations pave way for the improved utilization of marine resources which still remain as an untapped reservoir of biotherapeutics.

Additional file

Additional file 1: Image of tissue chip. (JPEG 62 kb)

Abbreviations

ADMET: Absorption, distribution, metabolism, excretion and toxicity; DAPI: 4′,6-diamidino-2-phenylindole; DMEM: Dulbecco's modified eagle medium; FACS: Fluorescence-activated cell sorting; GAE: *Gelidiella acerosa ethyl acetate extract*; PI: Propidium Iodide; PI3K: Phoshhotidyl inositol-3-kinase

Acknowledgements

The Research Scholar, S.M.Fazeela Mahaboob Begum would like to thank B.S.Abdur Rahman Crescent University for providing Junior Research Fellowship for her. We are thankful to Dr. Raju Saravanan, Scientist, Center for Marine Fisheries Institute, Mandapam, India for his constant support in collection and authentication of the seaweed used for the study.

Funding

The study did not receive any research funding from any agency.

Availability of data and materials

The datasets used and analyzed during the current study are available from the corresponding author on reasonable request.

Authors' contributions

SMF performed the experiment, collected and analyzed the data, KC & BJ designed the Zebrafish work, RS edited the manuscript, SH designed and conceived the study. All the authors wrote and edited the manuscript. All authors read and approved the final manuscript.

Ethics approval

The Ethical clearance was granted by the Institutional Animal Ethics Committee of Pentagrit, where the work was carried out (IAEC study No: 213/GO06/IAEC).

Consent for publication

Not applicable.

Competing interests

The authors declare that they have no competing interests.

Publisher's Note

Author details

[1]School of Life Sciences, B.S. Abdur Rahman Crescent University, Chennai 600048, India. [2]Pentagrit, Chennai 600100, India. [3]School of Engineering Technology, Purdue university, West Lafayette, IN 47907, USA.

Received: 18 August 2017 Accepted: 9 March 2018
Published online: 20 March 2018

References

1. Kumar R. A phase 1b trail of the combination of an all- oral regimen of capecitabine and erlotinib in advanced non small cell lung cancer in Caucasian patients. Cancer ChemotherPharmacol. 2016;77:375–83.
2. Travis WD, Brambilla E, Noguchi M, Nicholson AG, Geisinger KR, Yatabe Y, et al. International association for the study of lung cancer/american thoracic society/european respiratory society: international multidisciplinary classification of lung adenocarcinoma. J Thorac Oncol. 2011;8(2):381–5.
3. Dacic S. Molecular diagnostics of lung carcinomas. Arch Pathol Lab Med. 2011;135(5):622–9.
4. RapariaK VC, DeCamp MM, Patel JD, Mehta MP. Molecular profiling in non–small cell lung cancer :a step toward personalized medicine. Arch Pathol Lab Med. 2013;137:481–91.
5. Fruman DA, Meyers RE, Cantley LC. Phosphoinositide kinases. Annu Rev Biochem. 1998;67:481–507.
6. Thorpe LM, Yuzugullu H, Zhao JJ. PI3K in cancer: divergent roles of isoforms, modes of activation and therapeutic targeting. Nat Rev Cancer. 2015;15(1):7–24.
7. Li L, Wei XH, Pan YP, Li HC, Yang H, He QH, Pang Y, Shan Y, Xiong FX, Shao GZ, Zhou RL. LAPTM4B: anovel cancer-associated gene motivates multidrug resistance through efflux and activating PI3K/AKT signaling. Oncogene. 2010;29:5785–95.
8. Choi BH, Kim CG, Lim Y, Shin SY, Lee YH. Curcumin down-regulates the multidrug-resistance mdr1b gene by inhibiting the PI3K/Akt/NF kappa B pathway. Cancer Lett. 2008;259:111–8.
9. Foster JG, Blunt MD, Carter E, Ward SG. Inhibition of PI3K signaling spurs new therapeutic opportunities in inflammatory/ autoimmune diseases and hematological malignancies. Pharmacol Rev. 2012;64:1027–54.
10. Barrett D, Brown VI, Grupp SA, Teachey DT. Targeting the PI3K/AKT/mTOR signaling axis in children with hematologic malignancies. Paediatr Drugs. 2012;14:299–316.
11. Sheppard K, Kinross KM, Solomon B, Pearson RB, Phillips WA. Targeting PI3 kinase/AKT/mTOR signaling in cancer. Crit Rev Oncog. 2012;17:69–95.
12. Knight ZA, Shokat KM. Chemically targeting the PI3K family. Biochem Soc Trans. 2007;35:245.
13. Marone R, Cmiljanovic V, Giese B, Wymann MP. Targeting phosphoinositide 3-kinase: moving towards therapy. Biochim Biophys Acta. 2008;1784:159–85.
14. Serra V, Markman B, Scaltriti M, Eichhorn PJA, Valero V, Guzman M, Botero ML, Llonch E. NVP-BEZ235, a dual PI3K/mTOR inhibitor, prevents PI3K signaling and inhibits the growth of Cancer cells with activating PI3K mutations. Cancer Res. 2008;68(19):8022–30.

15. Fruman DA, Cantley LC. Idelalisib — A PI3Kδ Inhibitor for B-Cell Cancers. N Engl J Med. 2014;370(11):1061-2. https://doi.org/10.1056/NEJMe1400055.
16. Ando Y, Inada-Inoue M, Mitsuma A, Yoshino T, Ohtsu A, Suenaga N, et al. Phase Idose-escalation study of buparlisib (BKM120), an oral pan-class IPI3K inhibitor, in Japanese patients with advanced solid tumors. Cancer Sci. 2014; 105:347–53.
17. Massacesi C, Di Tomaso E, Urban P, et al. PI3K inhibitors as new cancer therapeutics: implications for clinical trial design. OncoTargets Ther. 2016;9: 203-10. https://doi.org/10.2147/OTT.S89967.
18. Juric D, de Bono JS, LoRusso PM, Nemunaitis J, Heath EI, Kwak EL, MacarullaMercadé T, Geuna E, Jose de Miguel-Luken M, Patel C, Kuida K, Sankoh S, Westin EH, Zohren F, Shou Y, Tabernero J. A first-in-human, phase I, dose-escalation study of TAK-117, a selective PI3Kα isoform inhibitor, in patients with advanced solid malignancies. Clin Cancer Res. 2017;23(17):5015–23.
19. Evans CA, Liu T, Lescarbeau A, Nair SJ, Grenier L, Pradeilles JA, Glenadel Q, Tibbitts T, Rowley AM, DiNitto JP, Brophy EE, O'Hearn EL, Ali JA, Winkler DG, Goldstein SI, O'Hearn P, Martin CM, Hoyt JG, Soglia JR, Cheung C, Pink MM, Proctor JL, Palombella VJ, Tremblay MR, Castro AC. Discovery of a selective p hosphoinositide-3-kinase (PI3K)-γ inhibitor (IPI-549) as an immuno-oncology clinical candidate. ACS Med ChemLett. 2016;7(9):862–7.
20. Carlino L, Rastelli G. Dual kinase-Bromodomain inhibitors in anticancer drug discovery: a structural and pharmacological perspective. Med Chem. 2016; 59(20):9305–20.
21. Heffron TP, Heald RA, Ndubaku C, Wei B, Augistin M, Do S, Edgar K, Eigenbrot C, Friedman L, Gancia E, Jackson PS, Jones G, Kolesnikov A, Lee LB, Lesnick JD, Lewis C, McLean N, Mörtl M, Nonomiya J, Pang J, Price S, Prior WW, Salphati L, Sideris S, Staben ST, Steinbacher S, Tsui V, Wallin J, Sampath D, Olivero AG. The rational design of selective Benzoxazepin Inhibitors of the α-isoform of phosphoinositide 3-kinase culminating in the identification of (S)-2-((2-(1-isopropyl-1H-1,2,4-triazol-5-yl)-5,6-dihydrobenzo[f]imidazo[1,2-d][1,4]oxazepin-9-yl)oxy) propanamide (GDC-0326). J Med Chem. 2016;59(3):985–1002.
22. Rugo HS, Vidula N, Ma C. Improving response to hormone therapy in breast cancer: new targets, new therapeutic options. Am Soc Clin Oncol Educ Book. 2016;35:e40–54.
23. Burger JA, Tedeschi A, Barr PM, Robak T, Owen C, et al. Ibrutinib as initial therapy for patients with chronic lymphocytic leukemia. N Engl J Med. 2015; 373:2425-37. https://doi.org/10.1056/NEJMoa1509388.
24. Newman DJ, Cragg GM. Natural products as sources of new drugs over the 30 years from 1981 to 2010. J Nat Prod. 2012;75(3):311–35.
25. Haefner B. Drugs from the deep: marine natural products as drug candidates. Drug Discov Today. 2003;8(12):536–44.
26. Cragg GM, Newman DJ. Plants as a source of anti-cancer agents. J Ethnopharmacol. 2005;100:72–9.
27. Harada H, Yamashita U, Kurihara E, Fukushi E, et al. Antitumor activity of palmitic acid found as a selective cytotoxic substance in marine red algae. Anticancer Res. 2002;22:2587–90.
28. Taskin E, Ozturk M, Taskin E, Kurt O. Antibacterial activities of some marine algae from the Aegean Sea (Turkey). Afr J Biotechnol. 2007;6(24):2746–51.
29. Prasad K, Siddhanta AK, Ganesan M, Ramavat BK, Jha B, Ghosh Pushpito K, et al. Agars of *Gelidiella acerosa* of west and southeast coasts of India. Bioresour Technol. 2007;98(10):1907–15.
30. Pandima Devi K, Suganthy N, Kesika P, Pandian SK. Bioprotective properties of seaweeds: in vitro evaluation of antioxidant activity and antimicrobial activity against food borne bacteria in relation to polyphenolic content. BMC Complement Altern Med. 2008;8-38:1–11.
31. Suganthy N, Nisha SA, Pandian SK, Devi KP. Evaluation of *Gelidiella acerosa*, the red algae inhabiting south Indian coastal area for antioxidant and metal chelating potential. Biomed Prev Nutr. 2013;3(4):399–406.
32. Nobel Surya Pandidurai R, Kalavathi K, Perumal P. Studies on antibacterial activity of seaweeds, *Enteromorphaintestinalis*(Linnaeus) and *Gelidiella acerosa* (Forsskal) from Puducherry and Rameswaram (southeast coast of India). Int J Pharma Bio Sci. 2014;5(1):(B)1139–47.
33. Vivek M, Kumar PS, Steffi S, Sudha S. Biogenic silver nanoparticles by *Gelidiella acerosa* extract and their antifungal effects. Avicenna J Med Biotechnol. 2011;3:43–8.
34. Queiroz INL, Rodrigues JAG, Quinderé ALG, Holanda ML, Pereira MG, Benevides NMB, et al. Inhibition of coagulation proteases and thrombosis and sub-chronic toxicological study of a sulfated polysaccharidic fraction from the red alga *Gelidiella acerosa*. Maringá,v. ActaScientiarum. Biological Sci. 2014;36-4:393–401.
35. Naqvi SWA, Solimabi S, Kamat SY, Fernandes L, Reddy CVG, Bhakuni DS, et al. Bot Mar. 1980;23:51.
36. Syad AN, Shunmugiah KP, Pandima Devi K. Assessment of anticholinesterase activity of *Gelidiella acerosa*: implications for its therapeutic potential against Alzheimer's disease. Evidence-Based Complement Altern Med. 2012;497242:1-8.
37. Lakmal HHC, Samarakoon KW, Lee WW, Lee JH, Abeytunga DTU, Lee HS, et al. Anticancer and antioxidant effects of selected Sri Lankan marine algae. J Natl Sci Found. 2014;42(4):315–23.
38. Duraikannu K, Shameem Rani K, Anithajothi R, Umagowsalya G, Ramakritinan CM. In- vivo anticancer activity of red algae (*Gelidiella acerosa* and *Acanthophoraspicifera*). Int J Pharm Sci Res. 2014;5(8):3347–52.
39. Murugan K, Iyer VV. Differential growth inhibition of cancer cell lines and antioxidant activity of extracts of red, brown, and green marine algae. In Vitro Cell Dev Biol Anim. 2013;49:324–34.
40. Ratnasooriya WD, Premakumara GA, Tillekeratne LM. Post-coital contraceptive activity of crude extracts of Sri Lankan marine red algae. Contraception. 1994;50(3):291–9.
41. Demedts IK, Vermaelen KY, Van Meerbeeck JP. Treatment of extensive-stage small cell lung carcinoma: current status and future prospects. Eur Respir J. 2010;35:202–15.
42. Memmott RM, Dennis PA. The role of Akt/MTOR pathway in tobacco carcinogen – induced lung tumorogenesis. Clin Cancer Res. 2010;16:4–10.
43. Pathmanathan MK, Uthayarasa K, Jeyadevan JP, Jeyaseelan EC. In vitro antibacterial activity and phytochemical analysis of some selected medicinal plants. Int J Pharm Biol Arch. 2010;1(3):291–9.
44. Evans WC, Saunders WB. Trease and Evan's Pharmacognosy Tokyo; 2001. p. 1–579.
45. Harborne JB. Phytochemical methods: a guide to modern technique of plant analysis. London: Chapman and Hall Ltd.; 1973. p. 49–188.
46. Singleton VL, Rossi JA. Colorimetry of total phenolics with phosphomolybdic-phosphotungstic acid reagents. Am J Enol Vitic. 1965;16:144–58.
47. Zhishen I, Mengcheng T, Jianming W. The determination of flavanoids contents in mulberry and their scavenging effects on super radicals. Food Chem. 1999;64:555–9.
48. Gurav N, Kardani K, Solanki B, Patel B. Quantification of phenolic compound gallic acid in polyherbal ranger capsule by high performance chromatographic method. Int J Pharm Sci Rev Res. 2014;25(31):183–7.
49. Packialakshmi N, Naziya S. Fourier transform infrared spectroscopy analysis of various solvent extracts of *Caralluma fimbriyata*. Asian J Biom Pharm Sc. 2014;4(36):20-5.
50. Ashok kumar R, Ramaswamy M. Phytochemical screening by FTIR spectroscopic analysis of leaf extracts of selected Indian medicinal plants. Int J Curr Microbiol App Sci. 2014;3(1):395–406.
51. Blois MS. Antioxidant determination by the use of a stable free radical. Nature. 1958;181:1199–200.
52. Mossman T. Rapid colorimetric assay for cellular growth and survival: application to proliferation and cytotoxicity assays. J Immunol Methods. 1983;65:55–63.
53. Nicoletti L, Migliorati G, Pagliacci MC, Grignani F, Riccardi C. A rapid and simple method for measuring thymocyte apoptosis by propidium iodide staining and flow cytometry. J Immunol Meth. 1991;139:271–9.
54. Dimmick I. Multiple flow cytometry applications: use of DAPI. BioMed Sci. 2011;541-3.
55. Park SY, Kim JH, Lee YJ. Surfactin suppresses TPA-induced breast cancer cell invasion through the inhibition of MMP-9 expression. Int J Oncol. 2013;42:287–96.
56. Rafehi H, Orlowski C, Georgiadis GT, et al. Clonogenic Assay: Adherent Cells. Jove. 2011;49:2573. https://doi.org/10.3791/2573.
57. Stoletov K, Klemke R. Catch of the day: zebrafish as a human cancer model. Oncogene. 2008;27:4509–20.
58. Devi KP, Suganthy N, Kesika P, Karutha Pandian S. Bioprotective properties of seaweeds: In vitro evaluation of antioxidant activity and antimicrobial activity against food borne bacteria in relation to polyphenolic content. BMC Complement Altern Med. 2008;8:38.
59. Wu C, Huang M, Lin Y, Ju H, Ching H. Antioxidant properties of *Cortex fraxini*and its simple coumarins. Food Chem. 2007;104:1464–71.
60. Bouba A, Njintang YN, Scher J, Mbofung CMF. Phenolic compounds and radical scavenging potential of twenty Cameroonian spices. Agric Biol J N Am. 2010;1(3):213–24.
61. Alberg AJ, Ford JG, Samet JM. Epidemiology of lung cancer: ACCP evidence based clinical practice guidelines (2nd edition). Chest. 2007;132:29S–55S. PMID: 17873159

62. Arif Nisha S, Pandima Devi K. Assessment of mutagenic effect of *G. acerosa* and *S. wightii* in *S. typhimurium*(TA 98, TA 100, and TA 1538 strains) and evaluation of their cytotoxic and genotoxic effect in human mononuclear cells: a non-clinical study. Biomed Res Int. 2014:1–8. https://doi.org/10.1155/2014/313942
63. David R. McIlwain D, Berger T, Mak T. Caspase functions in Ccell death and disease. Cold Spring Harb Perspect Biol. 2013;5:a008656. https://doi.org/10.1101/cshperspect.a008656.
64. Anagnostou V, Lowery F, Zolota V, Tzelepi V, Gopinath A, Liceaga C, et al. High expression of BCL-2 predicts favorable outcome in non-small cell lung cancer patients with non squamous histology. BMC Cancer. 2010;10:186.
65. Maurer U, Preiss F, Brauns-Schubert P, Schlicher L, Charvet C. GSK-3 – at the crossroads of cell death and survival. J Cell Sci. 2014;127:1369–78.
66. Jope RS, Yuskaitis CJ, Beurel E. Glycogen synthase kinase-3 (GSK3): inflammation, diseases, and therapeutics. Neurochem Res. 2007;32:577–95.
67. Kurosu T, Nagao T, Wu N, Oshikawa G, Miura O. Inhibition of the PI3K/Akt/GSK3 pathway downstream of BCR/ABL, Jak2-V617F, or FLT3-ITD downregulates DNA damage-induced Chk1 activation as well as G2/M arrest and prominently enhances induction of apoptosis. PLoS ONE. 2013;8(11):e79478. https://doi.org/10.1371/journal.pone.0079478.
68. Kitagishi Y, Nakanishi A, Ogura A, Matsuda S. Dietary regulation of PI3K/*AKT*/GSK-3β pathway in Alzheimer's disease. Alzheimers Res Ther. 2014;6:35.
69. Mehlen P, Puisieux A. Metastasis: a question of life or death. Nat Rev Cancer. 2006;6:449–58.
70. John A, Tuszynski G. The role of matrix metalloproteinases in tumor angiogenesis and tumor metastasis. Pathol Oncol Res. 2001;7:14–23.
71. Ohbayashi H. Matrix metalloproteinases in lung diseases. Curr Protein Pept Sci. 2009;3:409–21.
72. Kim SJ, Rabbani ZN, Dewhirst MW, Vujaskovic Z, Vollmer RT, Schreiber EG, Oosterwijk E, Kelley MJ. Expression of HIF-1, CA IX, VEGF, and MMP-9 in surgically resected non-small cell lung cancer. Lung Cancer. 2005;49:325–35.
73. Schmalfeldt B, Prechtel D, Harting K, Spathe K, Rutke S, Konik E, Fridman R, Berger U, Schmitt M, Kuhn W, Lengyel E. Increased expression of matrix metalloproteinases MMP-2, MMP-9, and the urokinase-type plasminogen activator is associated with progression from benign to advanced ovarian cancer. Clin Cancer Res. 2001;7:2396–404.
74. Sheen-Chen SM, Chen HS, Eng HL, Sheen CC, Chen WJ. Serum levels of matrix metalloproteinase 2 in patients with breast cancer. Cancer Lett. 2001;173:79–82.
75. Coussens LM, Fingleton B, Matrisian LM. Matrix metalloproteinase inhibitors and cancer: trials and tribulations. Science. 2002;295:2387–92.
76. Egeblad M, Werb Z. New functions for the matrix metalloproteinases in cancer progression. Nat Rev Cancer. 2002;2:161–74.
77. Iniesta P, Moran A, Juan C, Gomez A, Hernando F, Garcia-Aranda C, Frias C, Antonio Diaz-Lopez A, Rodriguez-Jimenez F, Balibrea J, Benito M. Biological and clinical significance of MMP-2, MMP-9, TIMP-1 and TIMP-2 in non-small cell lung cancer. Oncol Rep. 2007;17:217–23.
78. CB G, Wang S, Deng C, Zhang DL, Wang FL, Jin XQ. Relationship between matrix metalloproteinase 2 and lung cancer progression. Mol Diagn Ther. 2007;11(3):183–92.
79. Zhang L, Li N, Yan HC, Jiang H, Fang XJ. Expression of novel CD44st and MMP2 in NSCLC tissues and their clinical significance. Oncol Res Treat. 2017;40:192–6.
80. Leinonen T, Pirinen R, Böhm J, Johansson R, KosmaVM. Increased expression of matrix metalloproteinase-2 (MMP-2) predicts tumour recurrence and unfavourable outcome in non-small cell lung cancer. Histol Histopathol. 2008;23(6):693–700.
81. Sarbassov DD, Guertin DA, Ali SM, Sabatini DM. Phosphorylation and regulation of Akt/PKB by the Rictor-mTOR complex. Science. 2005;307:1098-101. https://doi.org/10.1126/Science.1106148.

Nanocarnation-like nickel oxide thin film: Structural and optical properties

Article · January 2018

CITATIONS
0

READS
42

7 authors, including:

Norfarariyanti Parimon
Universiti Malaysia Sabah (UMS)
25 PUBLICATIONS **34** CITATIONS
SEE PROFILE

M. H. Mamat
Universiti Teknologi MARA
368 PUBLICATIONS **1,225** CITATIONS
SEE PROFILE

Mohamad Rusop
Universiti Teknologi MARA
166 PUBLICATIONS **538** CITATIONS
SEE PROFILE

Wan Rosmaria Wan Ahmad
Universiti Teknologi MARA
21 PUBLICATIONS **7** CITATIONS
SEE PROFILE

International Journal of Engineering & Technology, 7 (4.18) (2018) 103-106

International Journal of Engineering & Technology

Website: www.sciencepubco.com/index.php/IJET

Research paper

Nanocarnation-like Nickel Oxide Thin Film: Structural and Optical Properties

N. Parimon[1,3,*], M. H. Mamat[1,2,*], M. A. R. Abdullah[1], A. S. Ismail[1], W. R. W. Ahmad[1], I. B. Shameem Banu[4], and M. Rusop[1,2]

[1]NANO-ElecTronic Centre (NET), Faculty of Electrical Engineering, Universiti Teknologi MARA (UiTM), 40450 Shah Alam, Selangor, Malaysia

[2]NANO-SciTech Centre (NST), Institute of Science (IOS), Universiti Teknologi MARA (UiTM), 40450 Shah Alam, Selangor, Malaysia

[3] Faculty of Engineering, Universiti Malaysia Sabah, 88400 Kota Kinabalu, Sabah, Malaysia

[4]Department of Physics, B.S. Abdur Rahman Crescent Institute of Science & Technology, Vandalur, Chennai, 600 048, India

**Corresponding author E-mail: fara2012@ums.edu.my, mhmamat@salam.uitm.edu.my*

Abstract

Herein, the structural and optical properties of highly porous nanocarnation-like nickel oxide (NiO) thin film in possibility of sensing applications were reported. The highly porous nanocarnation-like NiO was grown on indium tin oxide (ITO) glass substrates by using sonicated sol-gel immersion process. The grown film was characterized in details to examine the structural and optical properties using field emission scanning electron microscopy (FESEM), X-ray diffraction (XRD), Raman spectroscopy, and ultraviolet–visible–near infrared (UV-vis-NIR) spectroscopy, respectively. The XRD pattern reveals that the grown nanocarnation-like NiO film has crystalline NiO with a cubic structure. The UV-vis-NIR spectrum demonstrates that the average transmittance value of the sample in the visible region is approximately 48 % transmission. The results showed that, in view of highly porous nanocarnation-like NiO structure exhibited a great influence on its possibility for sensing applications.

Keywords: *Nickel oxide (NiO); Thin Film; sol-gel; Structural Properties; Optical Properties*

1. Introduction

Some metal oxides with semiconductor properties of n-type or p-type such as ZnO, TiO_2, Fe_2O_3, WO_3, CuO and NiO has been discussed extensively to be utilized as outstanding electron mediator for sensing membranes [1]. From previous researches, metal oxides have attained excellent consideration because of its terrific surface properties like high surface area, large pore volume, pore diameter, well-ordered pore channels and capillaries [2]. For example, the porous structures of metal oxides can be seen their utilization in wide sensing applications [3] including for gas [1, 4-7] and humidity [8, 9]. In addition, metal oxides have other important advantages such as low cost preparation, easy integration in electronic circuit, and controllable preparation process.

Meanwhile, the reports on p-type metal oxides semiconductors are relatively rare. Among all the p-type metal oxides, nickel oxide (NiO) which has a wide band gap (3.6 - 4.0 eV) is most preferable for widely used in various sensing applications because of the excellent chemical stability and high optical transparency [3]. In addition, NiO nanomaterial possess magnificent electrical conductivity, distinctly electro-active nature, low synthesis cost and a high surface to volume ratio [1]. Meanwhile, the sensing properties based on p-type oxide semiconductor materials are relatively poor compare to the n-type oxide semiconductor materials if both materials share similar morphologies and size [10]. This is based on the equation of $S_p = (S_n)^{1/2}$, where S_P and S_N are the chemical or gas sensitivities of the p-type and n-type oxide semiconductors, respectively. This equation evidently reveals that the fabrication of p-type oxide semiconductor materials for high performance sensor applications remains a huge challenge. Therefore, the details study on fabrication processes and properties of nanostructured NiO provide interesting tasks toward improving the properties of p-type materials as a sensing membrane.

Although many techniques such as hydrothermal [1, 5, 6], chemical spray pyrolysis (CSP) and chemical bath deposition (CBD) [7], electrospinning [8, 9], and sol-gel [11] have been put widely into the synthesis of NiO nanostructures, it remains rare for researchers using a facile route of sonicated sol-gel immersion method. In addition to simple techniques, it is important because the design and preparation of nanostructured metal oxides with various morphologies can effectively improve the sensing properties due to their high surface area [12]. Accordingly, this NiO thin film was prepared on indium tin oxide (ITO) glass substrates in the present study for possibility in sensing applications.

2. Experimental Details

For this work, nanocarnation-like NiO thin film was successfully prepared on ITO glass substrates. The fabrication involved sonicated sol-gel immersion method using a precursor solution of nickel nitrate hexahydrate. Prior to the growth process, ITO glass was cleaned using solutions of ethanol, acetone, and de-ionized (DI) water in the ultrasonic bath (Hwasin Technology PowerSonic 405, 40k Hz) for 15 minutes each. Furthermore, the ITO glass is blown using nitrogen gas for drying. To grow nanocarnation-like NiO thin film, a solution consisting of 0.2M nickel (II) nitrate

hexahydrate ($Ni(NO_3)_2.6H_2O$) and 0.2M hexamethylenetetramine (HMT) ($C_6H_{12}N_4$) were prepared in a beaker filled with 200 ml DI water. The solution then went through sonication process using ultrasonic bath for 30 minutes. Next, the solution was stirred for 45 minutes at constant speed of 300 rpm in ambient. Then, the solution was transferred to the Schott bottle, where the ITO glass substrate was positioned at the bottom. Afterward, the bottle was immersed in water bath instrument for 2 hours at temperature of 95 ºC. After the immersion process, the ITO glass deposited with NiO thin film was taken out from the bottle and rinsed with DI water. The sample was further blown with nitrogen gas for drying process. Then, the sample was pre-baked in a furnace for 15 minutes at 150 ºC followed by annealing process at temperature of 500 ºC for 1 hour.

The sample was characterized using field emission scanning electron microscopy (FESEM, JEOL JSM-7600F) for the surface morphological studies. The crystallinity of the sample was investigated using X-ray diffraction (PANalytical X'Pert PRO). The structural analysis of the sample was also conducted by using Raman spectroscopy (Horiba Jobin Yvon-79 DU420A-OE-325). The Raman measurement was conducted using an excitation source of 514 nm Ar^+ ion laser. The optical properties of the grown sample were characterized using ultraviolet–visible-near infrared (UV–vis-NIR) spectrophotometer (Varian Cary 5000). Summarization of the experiment processes in a flow chart is shown in Fig. 1.

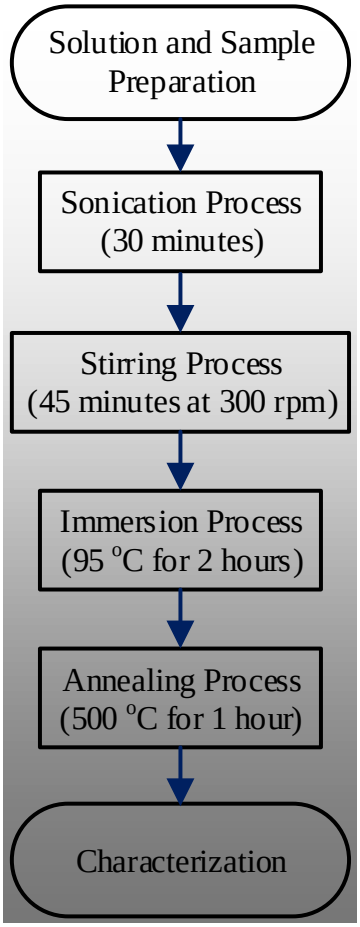

Fig. 1: A general procedure showing various steps for the synthesizing of nanocarnation-like NiO thin film.

3. Results and Analysis

3.1. FESEM observation

The surface morphology images and micro structural features of NiO film on ITO-coated glass substrates were investigated in detail by FESEM. As depicted in Fig. 2, (a), (b), (c), and (d) the panoramic FESEM images are arranged according to the magnification of 10,000×, 30,000×, 50,000× and 100,000×, respectively. As observed from the FESEM images in Fig. 2(a), the films exhibit unique structures called nanocarnation-like NiO with high porous channel densities. These films reveal porous structure of well-connected particles to form nanocarnation-like structure. We can see that the microstructure of pure NiO is highly porous nanosheets. The diameter of individual nanocarnation-like NiO is approximately 1.5µm. The FESEM images in Fig. 2(b) and 2(c) revealed that the nanocarnation-like NiO was constructed from NiO nanolayers. The nanocarnation-like NiO was assembled by a plenty of two-dimensional curving NiO nanolayers forming a highly porous microsphere. Meanwhile, the two-dimensional nanolayer was fabricated from NiO nanocrystallite chains, which form unique and porous network layers as can be observed in Fig. 2(d).

The chemical reactions for the formation of nanocarnation-like NiO using sonicated sol-gel immersion method can be described by the following equations [1]:

$$(CH_2)_6N_4 + 6H_2O \rightarrow 6HCHO + 4NH_3 \quad (1)$$

$$NH_3 + H_2O \rightarrow NH_4^+ + OH^- \quad (2)$$

$$Ni(NO_3)_2 \cdot 6H_2O \rightarrow Ni^{2+} + 2NO_3^- + 6H_2O \quad (3)$$

$$Ni^{2+} + 2OH^- + \chi H_2O \rightarrow Ni(OH)_2 \cdot \chi H_2O \quad (4)$$

$$Ni(OH)_2 \cdot \chi H_2O \rightarrow NiO + (\chi + 1)H_2O \quad (5)$$

Preliminary, the HMT decomposes into formaldehyde (HCHO) and ammonia (NH_3) in the water medium as described in Eq. 1. These chemical substances provide an alkaline environment to the solution, which enhance the growth of nanostructures. Besides, these reagents also act as the surfactant agent to the Ni^{2+} ions for polymerization process.

According to Jiang et al., NH_3 forms a complex molecules with Ni^{2+} ions, which subsequently reduces the concentration of Ni^{2+} ions in the solution [13]. Therefore, the growth rate of the crystal is reduced, which enables the formation of thin two-dimensional nanolayers. The HMT undergoes a hydrolysis process as the reaction proceeds, which produces more OH^- ions in the solution. This condition is favorable for the formation of two-dimensional $Ni(OH)_2$ on the ITO glass. This hydrolysis process of the HMT can be described in Eq. 2, where the by-product of Eq. 1 in form of NH_3 reacts with water to produce NH_4^+ and OH^- ions in the process. Therefore, HMT acts as a pH buffer in the solution by providing NH_3 at a slow rate and in controlled supply. Simultaneously, the $Ni(NO_3)_2.6H_2O$ decomposes into Ni^{2+} ion, NO_3^- ion, and water in the solution as presented in Eq. 3. Successively, the Ni^{2+} ion reacts with NO_3^- ion and water molecules in the presence of thermal energy to form $Ni(OH)_2{\cdot}\chi H_2O$ in the process, which then condenses on the ITO glass.

The reaction is shown in Eq. 4. The remaining HMT, which are not involved in the NH_3 decomposition, may adsorbed on (001) plane of $Ni(OH)_2{\cdot}\chi H_2O$. This condition inhibited the growth of $Ni(OH)_2{\cdot}\chi H_2O$ at (001) plane to form thin two-dimensional nanolayers. To minimize the overall surface energy, the thin two-dimensional $Ni(OH)_2{\cdot}\chi H_2O$ nanolayers would self-aggregate to form nanocarnation-like structure. Subsequently, some of the $Ni(OH)_2{\cdot}\chi H_2O$ structures on ITO glass decomposes into NiO nanostructure as described in Eq. 5 due to the supplied thermal energy during immersion process. Upon annealing process at 500ºC, a complete conversion of $Ni(OH)_2{\cdot}\chi H_2O$ into NiO is occurred as a result of sufficient thermal energy supplied to the system. This conversion into NiO crystal was confirmed by the XRD data.

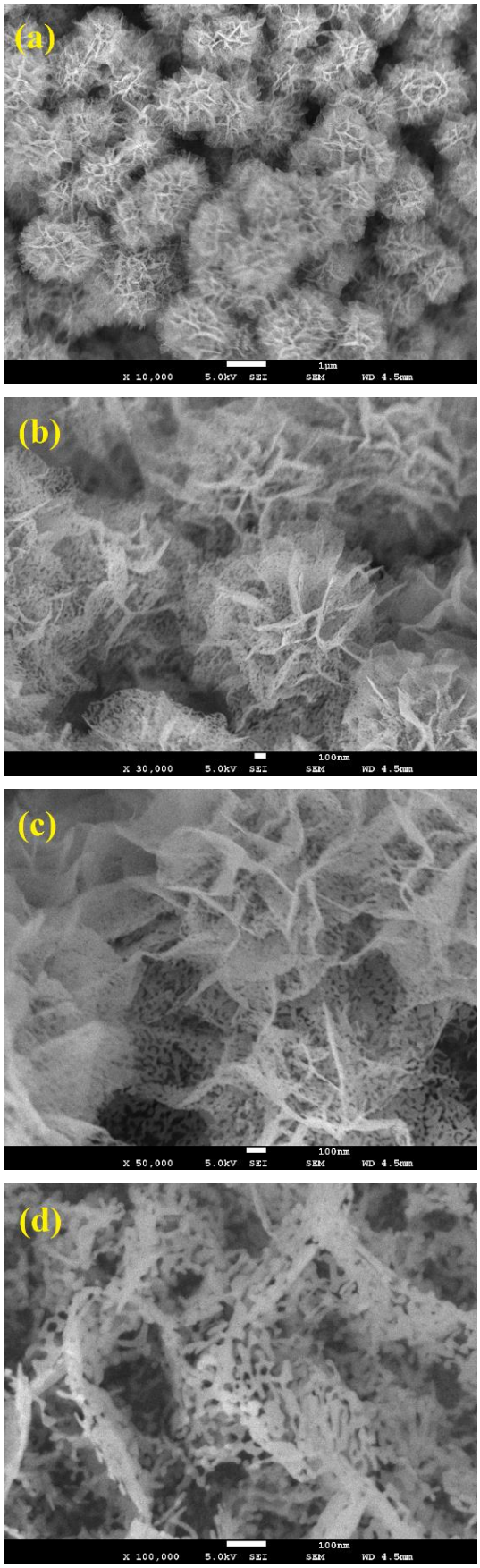

Fig. 2: The FESEM images of nanocarnation-like NiO thin film with different magnification of (a) 10,000× (b) 30,000× (c) 50,000×, and (d) 100,000×.

3.2. XRD analysis

The XRD pattern for nanocarnation-like NiO film grown on ITO glass substrates is shown in Fig. 3. The XRD pattern indicates that NiO film displays polycrystalline structure, which can be indexed to the cubic type of β-NiO (JCPDS NO.47-1049). The diffraction patterns revealed that NiO film shows peaks at 2θ values of approximately 37.7°, 43.7°, 63.4°, 75.8° and 79.7° which were indexed to (111), (200), (220), (311), and (222) crystal planes, respectively. Meanwhile, the diffraction peaks labelled with diamond belong to SnO_2 peaks from the ITO. The XRD examination confirmed that the results indicate the crystalline of NiO structure during immersion at 95 °C and calcination at 500 °C. The XRD pattern also reveals that no other diffraction peaks associated with $Ni(OH)_2$ or other phases were observed in the pattern. This result further confirmed that the grown NiO film consists of pure NiO structure and prove that the $Ni(OH)_2{\cdot}\chi H_2O$ was completely converted into NiO. The impurity from other substance except the contribution from the ITO substrate is not significant and could not be detected in the pattern up to the detection limit of the X-ray diffraction equipment. According to Dam et al., the hydroxide groups were completely detached from NiO film when the heat treatment was applied at temperature of 270 °C [14].

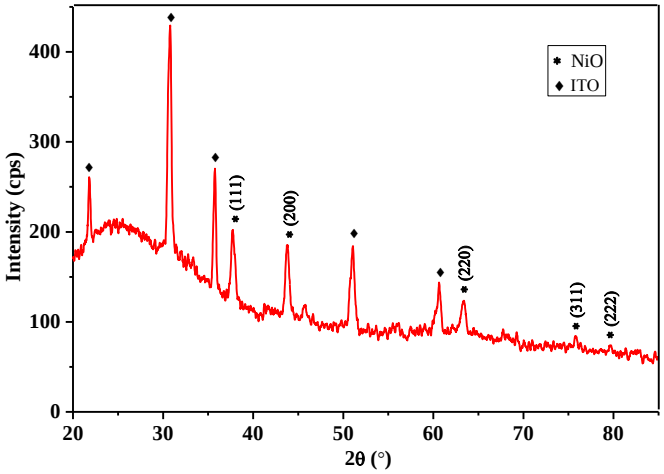

Fig. 3: The XRD pattern of nanocarnation-like NiO film.

3.3. Raman spectroscopy

The Raman measurement was conducted in order to further investigate the structural properties of nanocarnation-like NiO film. The Raman spectrum of nanocarnation-like NiO film is shown in Fig. 4. The spectrum was dominated by numerous of NiO characteristic peaks. The first vibrational band of NiO, assigned to one-phonon (1P) transverse optical (TO) and 1P longitudinal optical (LO) modes were observed at Raman shift of approximately 463 cm^{-1} and 492 cm^{-1} [15]. The vibrational peak at 554 cm^{-1} is assigned to the Ni-O stretching mode, which involves Ni^{2+} and O^{2-} species that are not linked to a proton [16]. The presence of these first order Raman scattering peaks indicate that structural imperfection of NiO occurs, which contributed from the structural disorder by nickel interstitial, oxygen vacancies, and surface effects [17-19]. Also, there is a strong 2LO phonon mode located at 1093 cm^{-1} due to the vibration of Ni-O bond. In between, there is two-phonon (2P) two transverse optical (2TO) stretching mode at 810 cm^{-1} with low intensities. In the present study, two magnons (2M) excitation peak, which normally located at 1550 cm^{-1} [20, 21], was not observed in the Raman spectrum to indicate that the prepared nanocarnation-like NiO film does not has antiferromagnetic properties at room temperature. This result also indicate that the nanocarnation-like NiO film exhibits super-paramagnetic properties due to the small crystallite size and high density of structural disorder [18].

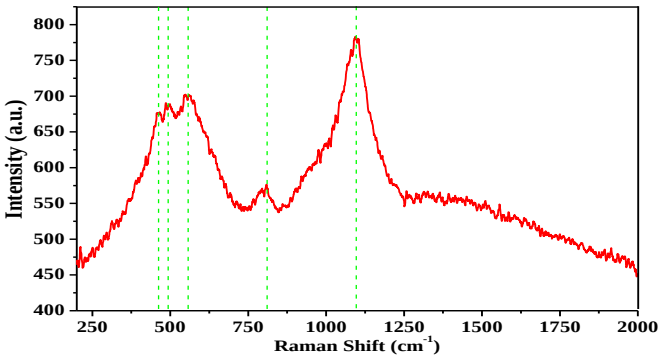

Fig. 4: Raman spectrum of nanocarnation-like NiO film

3.4. UV-vis-NIR spectroscopy

Fig. 5 demonstrates optical transmittance of the nanocarnation-like NiO thin film prepared using sonicated sol-gel immersion method. The optical transmittance measurement was carried out in the ranges of wavelength from 300 nm to 1000 nm. From the transmittance plot, we can clearly observe that the nanocarnation-like NiO exhibit moderate transparency. The transmittance extends to 50 % or less in the ultraviolet (UV) and visible regions. The average transmittance value of the film in the visible region (400 - 800 nm) was estimated to be 48 %. This lower transmittance percentage may be depending on the thickness of nanocarnation-like NiO film. In addition, the optical scattering occurrence in the nanocarnation-like NiO film may be one of the factors to this transmittance result.

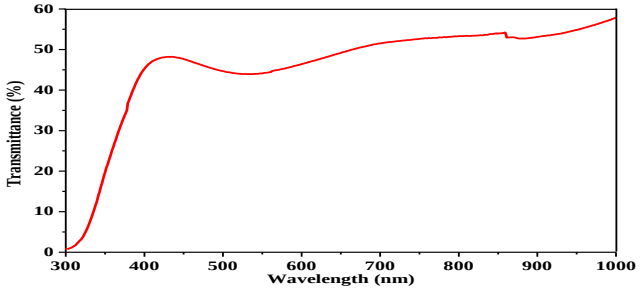

Fig. 5: The transmittance properties of NiO in the UV visible regions

4. Conclusion

The synthesis of porous morphology nanocarnation-like NiO has been successfully conducted via sonicated sol-gel immersion method. The highly porous nanocarnation-like NiO was characterized by various techniques which confirmed the formation of well-crystalline cubic phase, pure, and high density growth of nanocarnation-like NiO. The XRD pattern reveals that the grown NiO sample has NiO polycrystalline structure. The Raman analysis shows that nanocarnation-like NiO film has pure NiO characteristic peaks, which support the XRD data. The transmittance plot shows that the transparency of highly porous nanocarnation-like NiO is approximately 48 % in the visible region. In summary, the exposure of high surface area nanocarnation-like NiO thin film with high porosity represent a valuable way for producing high performance and sensitivity sensing applications in the future.

Acknowledgement

This work is financially supported by REI grant (600-IRMI/REI 5/3 (017/2018)). The work is also supported by ASEAN-India Research & Training Fellowship (IMRC/AISTDF/R&D/P-1/2017). The authors would like to thank Ministry of Higher Education, Malaysia, Faculty of Electrical Engineering and Research Management and Innovation (IRMI) of UiTM for their support of this research.

References

[1] Z. Qu, U. Ahmad, S. E. Mehdi, A. Aziz, X. Lingna, G. Yingang, A. I. Ahmed, K. Rajesh & S. Baskoutas (2018), Fabrication and characterization of highly sensitive and selective sensors based on porous NiO nanodisks. *Sensors and Actuators B: Chemical* 259, 604-615.

[2] D. Ahirwar, M. Bano, I. Khan, M. U.-D. Sheikh, M. Thomas & F. Khan (2018), Fabrication of hierarchically mesoporous NiO nanostructures and their role in heterogeneous photocatalysis and sensing activity. *Journal of Materials Science: Materials in Electronics* 29, 5768-5781.

[3] S. Akinkuade, B. Mwankemwa, J. Nel & W. Meyer (2018), Structural, optical and electrical characteristics of nickel oxide thin films synthesised through chemical processing method. *Physica B: Condensed Matter* 535, 24-28.

[4] S. Leonardi (2017), Two-Dimensional Zinc Oxide Nanostructures for Gas Sensor Applications. *Chemosensors* 5, 17, 28.

[5] Y. Lu, Y. Ma, S. Ma & S. Yan (2017), Hierarchical Heterostructure of Porous NiO Nanosheets on Flower-like ZnO Assembled by Hexagonal Nanorods for High-performance Gas Sensor. *Ceramics International* 43, 7508-7515.

[6] R. Miao, W. Zeng & Q. Gao (2017), Hydrothermal synthesis of novel NiO nanoflowers assisted with CTAB and SDS respectively and their gas-sensing properties. *Materials Letters* 186, 175-177.

[7] M. M. Gomaa, G. RezaYazdi, M. Rodner, G. Greczynski, M. Boshta, M. B. S. Osman, V. Khranovskyy, J. Eriksson & R. Yakimova (2018), Exploring NiO nanosize structures for ammonia sensing. *Journal of Materials Science: Materials in Electronics* 29, 11870-11877.

[8] D. Li, Y. Li, F. Li, J. Zhang, X. Zhu, S. Wen & S. Ruan (2015), Humidity sensing properties of MoO3-NiO nanocomposite materials. *Ceramics International* 41, 4348-4353.

[9] P. Pascariu, A. Airinei, N. Olaru, I. Petrila, V. Nica, L. Sacarescu, F. Tudorache (2016), Microstructure, electrical and humidity sensor properties of electrospun NiO–SnO2 nanofibers. *Sensors and Actuators B: Chemical* 222, 1024-1031.

[10] M. Hübner, C. E. Simion, A. Tomescu-Stănoiu, S. Pokhrel, N. Bârsan & U. Weimar (2011), Influence of humidity on CO sensing with p-type CuO thick film gas sensors. *Sensors and Actuators B: Chemical* 153, 347-353.

[11] L. G. Teoh & K.-D. Li (2012), Synthesis and Characterization of NiO Nanoparticles by Sol-Gel Method. *Materials Transactions* 53, 2135-2140.

[12] H. Gao, D. Wei, P. Lin, C. Liu, P. Sun, K. Shimanoe, N. Yamazoe & G. Lu (2017), The design of excellent xylene gas sensor using Sn-doped NiO hierarchical nanostructure. *Sensors and Actuators B: Chemical* 253, 1152-1162.

[13] H. Jiang, T. Zhao, C. Li & J. Ma (2011), Hierarchical self-assembly of ultrathin nickel hydroxide nanoflakes for high-performance supercapacitors. *Journal of Materials Chemistry* 21, 11, 3818-3823.

[14] D. T. Dam, X. Wang & J.-M. Lee (2013), Mesoporous ITO/NiO with a core/shell structure for supercapacitors. *Nano Energy*, 2, 6, 1303-1313.

[15] P. Bose, S. Ghosh, S. Basak & M. K. Naskar (2016), A facile synthesis of mesoporous NiO nanosheets and their application in CO oxidation. *Journal of Asian Ceramic Societies*, 4, 1, 1-5.

[16] S. Deabate, F. Fourgeot & F. Henn (2000), X-ray diffraction and micro-Raman spectroscopy analysis of new nickel hydroxide obtained by electrodialysis. *Journal of Power Sources*, 87, 1, 125-136.

[17] N. P. Kiran, M. P. Deshpande, C. Krishna, R. Piyush, S. Vasant, P. Swati & S. H. Chaki (2017), Synthesis, structural and photoluminescence properties of nano-crystalline Cu doped NiO. *Materials Research Express* 4, 10, 105027.

[18] P. Ravikumar, B. Kisan & A. Perumal (2015), Enhanced room temperature ferromagnetism in antiferromagnetic NiO nanoparticles. *AIP Advances*, 5, 8, 087116.

[19] S. Liu, J. Jia, J. Wang, S. Liu, X. Wang, H. Song and X. Hu (2012), Synthesis of Fe-doped NiO nanofibers using electrospinning method and their ferromagnetic properties. *Journal of Magnetism and Magnetic Materials* 324, 13, 2070-2074.

[20] F. T. Thema, E. Manikandan, A. Gurib-Fakim & M. Maaza (2016), Single phase Bunsenite NiO nanoparticles green synthesis by Agathosma betulina natural extract. *Journal of Alloys and Compounds* 657, 655-661.

[21] M. Ben Amor, A. Boukhachem, A. Labidi, K. Boubaker, and M. Amlouk (2017), Physical investigations on Cd doped NiO thin films along with ethanol sensing at relatively low temperature. *Journal of Alloys and Compounds* 693, 490-499.

J Mater Sci: Mater Electron (2018) 29:2363–2371
DOI 10.1007/s10854-017-8155-0

Synthesis, luminescent properties and energy transfer in Tb^{3+} and Eu^{3+} co-doped $Li_3Ba_2Gd_3(MoO_4)_8$ phosphors for W-LED's

Saravana Kumar Jaganathan[1,2,3] · John Peter Anthuvan[4] · I. B. Shameem Banu[5]

Received: 15 August 2017 / Accepted: 27 October 2017 / Published online: 9 November 2017

Abstract For the first time, single phase monoclinic $Li_3Ba_2Gd_3(MoO_4)_8$: 0.08 Tb^{3+},yEu^{3+} (0, 0.005, 0.02, 0.04, 0.06, 0.08 and 0.10 mol) nano phosphors were prepared by the simple mechanochemically assisted direct solid state reaction method at room temperature. Their crystal structures, luminescence properties, energy transfer mechanism and life time were studied in detail. At the excitation wavelength of 378 nm, the emission spectra of $Li_3Ba_2Gd_3(MoO_4)_8$: 0.08 Tb^{3+},yEu^{3+} (0, 0.005, 0.02, 0.04, 0.06, 0.08 and 0.10 mol) phosphors exhibit the characteristic emissions of Tb^{3+} and Eu^{3+} ions at around 545, 594 and 615 nm due to energy transfer from Tb^{3+} ions to Eu^{3+} ions. It is confirmed from the results that electric dipole–dipole interaction phenomena is the main cause for having energy transfer from Tb^{3+} to Eu^{3+} ions in $Li_3Ba_2Gd_3(MoO_4)_8$ host. The CIE coordinates of the prepared nano phosphors illustrate that by changing the ratio of Eu^{3+} ions the white light emission can be realized from $Li_3Ba_2Gd_3(MoO_4)_8$ phosphor and it coexist very close to an ideal white chromaticity coordinates (0.33, 0.33). All properties show that $Li_3Ba_2Gd_3(MoO_4)_8$: 0.08 Tb^{3+}, 0.005 Eu^{3+} nano phosphor is a promising material for single-phase phosphor based white light emitting diodes.

✉ Saravana Kumar Jaganathan
quantajohn@gmail.com

John Peter Anthuvan
quantajohn@gmail.com

1 Department for Management of Science and Technology Development, Ton Duc Thang University, Ho Chi Minh City, Vietnam

2 Faculty of Applied Sciences, Ton Duc Thang University, Ho Chi Minh City, Vietnam

3 IJN-UTM Cardiovascular Engineering Centre, Department of Clinical Sciences, Faculty of Biosciences and Medical Engineering, Universiti Teknologi Malaysia, 81300 Skudai, Johor, Malaysia

4 Department of Physics, St. Anne's College of Engineering and Technology, Panruti, Tamilnadu, India

5 Department of Physics, B. S. Abdur Rahman University, Vandalur, Chennai, Tamilnadu, India

1 Introduction

Nowadays, the phosphor based white light-emitting diodes (WLEDs) are well thought-out as next age bracket of solid state lighting owing to their environmental friendliness, stability, extensive lifetimes, consistency, and low power consumption [1–5]. In broad-spectrum, there are a range of methods to pile up the white LEDs. A usual way is to mix up a blue emitting LED in the midst of a yellow-emitting phosphor, as $Y_3Al_5O_{12}$: Ce^{3+} [6]. In view of the fact that, this route is about easy, the device has been used for commercial purpose applications. On the other hand, the white light produced by this route has feeble CRI due to the color deficiency occurs in the red and green region of the spectrum. On the road to get the better of its shortcomings, the arrangement of near-ultraviolet (n-UV) LEDs emitting at 370–410 nm with a red Y_2O_2S: Eu^{3+}, green ZnS: Cu^+, Al^{3+}, and blue ZnS: Ag^+ phosphor combination has been demonstrated [7]. This type of white LED can pay for first-rate color homogeny and a sky-scraping color-rendering index. However, for the present tri color commercially available phosphor mixtures, the well-built re-absorption and nonuniformity of luminescence problems stay alive, this outcome en route for the failure of luminescence efficiency, properties, and tricolor emitting points. In recent times, it is demonstrated that judge against among phosphor mixtures, a single-phased white light emitting phosphor with UV/NUV chips has more advantages and prevail over the

existing problems of tricolor phosphors due to their excellent Ra values and color stability. So, a single-phased white light emitting phosphor is delighted as a very promising material for W-Led applications. One of the approaches for producing white light from single-phased phosphors is by codoping sensitizer and activator into the same host [8–11]. A short time ago, the host $Li_3Ba_2Gd_3(MoO_4)_8$ has received a grand deal of interest as a prospective optical system owing to its stable crystalline structure, multifariousness and chemical stability [12–15].

In continuation to our previous work on the red luminescent $Li_3Ba_2Gd_3(MoO_4)_8$: Eu^{3+} [16] and green luminescent $Li_3Ba_2Gd_3(MoO_4)_8$: Tb^{3+} [17] phosphors for various lighting applications, in the present work we prepare single-phased Tb^{3+} and Eu^{3+} co doped $Li_3Ba_2Gd_3(MoO_4)_8$ white light emitting phosphor by mechanochemically assisted direct solid state reaction method at room temperature and study its crystal structure, the mechanism of energy transfer from sensitizer Tb^{3+} ion to activator Eu^{3+} ion, photoluminescence properties, life time and color tunability in detail.

2 Experimental method

2.1 Preparation of phosphors

The single-phase nano phosphors of $Li_3Ba_2Gd_3(MoO_4)_8$: 0.08 Tb^{3+},yEu^{3+} (y = 0.005, 0.02, 0.04, 0.06, 0.08 and 0.10 mol) were prepared by mechanochemically assisted direct solid state reaction method at room temperature by using AR grade LiCl, $BaCl_2$,$GdCl_3$, Na_2MoO_4, $EuCl_3$ (99.9%) and $TbCl_3$ (99.9%) as the preliminary materials. The right stoichiometric mixtures of LiCl, $BaCl_2$, $GdCl_3$, Na_2MoO_4, $TbCl_3$ and $EuCl_3$ were mixed and were pulverized for a period of 2 h (optimized) inside a planetary ball mill Pulverisette- 7 (FRITSCH). Milling was through two grinding vials (tungsten carbide) of 15 cm volume containing balls (tungsten carbide) each with a diameter of 12 mm. The number of milling balls and the rotation speed of the planetary system of milling device were optimized. The resulting powder was rinsed many times by distilled water to remove sodium chloride which was the byproduct of the reaction and then dried at 80 °C for 3 h in air atmosphere and sieved [16, 17].

2.2 Characterization

X-ray powder diffraction (XRD) analysis was done using Pan Analytical X'pert pro x-ray diffractometer with Cu K-alpha radiation (λ = 1.5406 Å) at a scanning rate of 0.02° per second. The XRD patterns were received in the range of $0° \le 2\theta \le 70°$ and were compared with the standard JCPDS data. Fourier Transform infrared spectroscopy (FTIR) measurements were done in the wavelength range of 400–4000 cm^{-1} with a Nicolet 6700 FTIR set with a deuterated triglycine sulfate detector. The morphology and dimension of the product were monitored and taken by Tecnai G20 (FEI Corporation of Holland) transmission electron microscopy using an accelerating voltage of 200 kV.The measurements of PL and photoluminescence excitation (PLE) spectra were performed by a Jobin Yuvon Flurolog-3-11 Spectroflurometer at room temperature with 450W xenon lamp. All spectroscopic measurements of the phosphors were carried out at room temperature.

3 Results and discussion

3.1 XRD and size distribution characterization

XRD patterns of $Li_3Ba_2Gd_3(MoO_4)_8$, $Li_3Ba_2Gd_3(MoO_4)_8$: 0.08 Eu^{3+}, $Li_3Ba_2Gd_3(MoO_4)_8$: 0.08 Tb^{3+} and $Li_3Ba_2Gd_3(MoO_4)_8$:0.08Tb^{3+},0.08Eu^{3+} nano phosphors synthesized by mechanochemically assisted direct solid state reaction method at room temperature is exhibited in Fig. 1. It is observed that all diffraction patterns of the un doped and doped samples are fit very well with standard JCPDS 77-0830 standard data of $Li_3Ba_2Gd_3(MoO_4)_8$. The patterns in the XRD spectra are narrow and strong presenting that a

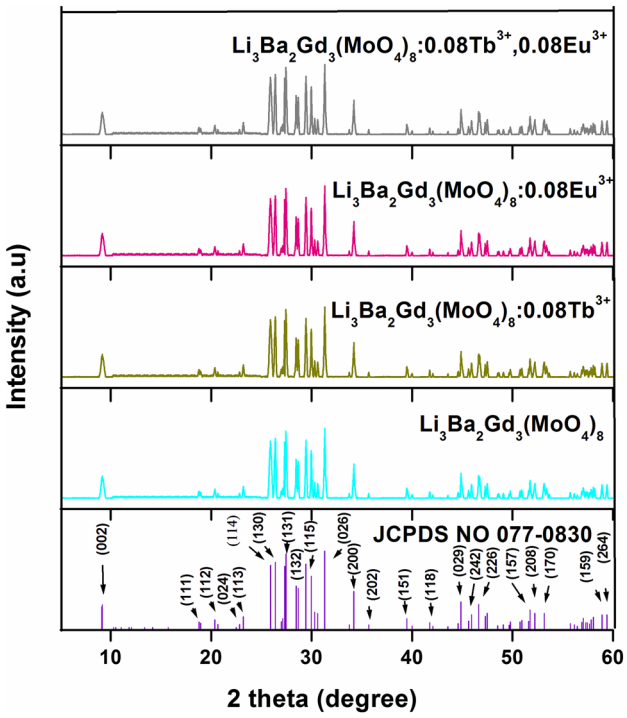

Fig. 1 Powder XRD patterns of $Li_3Ba_2Gd_3(MoO_4)_8$,$Li_3Ba_2Gd_3(MoO_4)_8$: 0.08 Tb^{3+}, $Li_3Ba_2Gd_3(MoO_4)_8$: 0.08 Eu^{3+} and $Li_3Ba_2Gd_3(MoO_4)_8$: 0.08 Tb^{3+}, 0.08 Eu^{3+} phosphors

well crystalline single-phase of $Li_3Ba_2Gd_3(MoO_4)_8$ phosphors with the monoclinic structure of space group C2/c had been effectively produced by mechanochemically assisted solid state reaction at room temperature. No added or impurity peaks were monitored in the diffraction patterns due to the presence of Tb^{3+}, Eu^{3+} ions in the host [16, 17].

The probable particle size of the system is deliberate from a strong (131) peak by using Debye–Scherrer's equation:

$$D = 0.89\lambda/(\beta \cos\theta)$$

where D is the average grain size, λ denotes Cu Kα wavelength of 0.1542 nm and β is the half-width of the peak with Bragg angle θ. The calculated outcomes demonstrate that the average crystallite sizes of $Li_3Ba_2Gd_3(MoO_4)_8$:$0.08Tb^{3+}$,$0.08Eu^{3+}$ are in the region of 62 nm. In view of the fact that the ionic radius of Eu^{3+} ($r = 1.066$ Å, $CN = 8$, where CN is the coordination number of the metal ions) and the ionic radius of Tb^{3+} ($r = 1.066$ Å, $CN = 8$) are nearer to that of Gd^{3+} ($r = 1.053$ Å, $CN = 8$) compared with Ba^{2+} ($r = 1.61$ Å, $CN = 12$) and Mo^{6+} ($r = 0.59$ Å, $CN = 6$), we therefore consider that doped Tb^{3+} and Eu^{3+} ions are preferred to engage the Gd^{3+} sites [18]. These outcomes demonstrate that the doped Tb^{3+} and Eu^{3+} ions exclusively occupied the Gd^{3+} sites. This is in harmony with Vegard's law, which states that on the way to have a solid system the cations of two systems should contain ionic radii within ±15% of each other [18]. The particle size distribution of $Li_3Ba_2Gd_3(MoO_4)_8$:$0.08Tb^{3+}$,$0.08Eu^{3+}$ nano phosphor is illustrated in Fig. 2a. The particles show a fine range of distribution at the average diameter of 64 nm which illustrates that the particles are fit for the fabrication of solid state lighting devices.

3.2 EDX analysis

Figure 2c represents EDX spectrum of $Li_3Ba_2Gd_3(MoO_4)_8$:$0.08Tb^{3+}$,$0.08Eu^{3+}$ phosphors. The EDX spectrum of the $Li_3Ba_2Gd_3(MoO_4)_8$:$0.08Tb^{3+}$,$0.08Eu^{3+}$ validates the presence of lithium (Li),barium (Ba), oxygen (O), molybdenum (Mo), europium (Eu), terbium (Tb), Gadolinium (Gd). The study of EDX spectrum confirms that $Li_3Ba_2Gd_3(MoO_4)_8$:$0.08Tb^{3+}$,$0.08Eu^{3+}$ phosphor have been prepared successfully by mechanochemically assisted direct solid state reaction at room temperature.

3.3 TEM

The structures of $Li_3Ba_2Gd_3(MoO_4)_8$:$0.08Tb^{3+}$,$0.08Eu^{3+}$ nano particles are clearly demonstrated by TEM image, as shown in Fig. 2b. The powder particles tend to appear highly crystalline, spherical and distributed homogenously in the system. No significant differences were exhibited in the TEM images of the powder samples by varying Tb^{3+}/Eu^{3+} ratios. The average grain size of the nano particles is about 65 nm which is in full agreement with the data received from the XRD patterns.

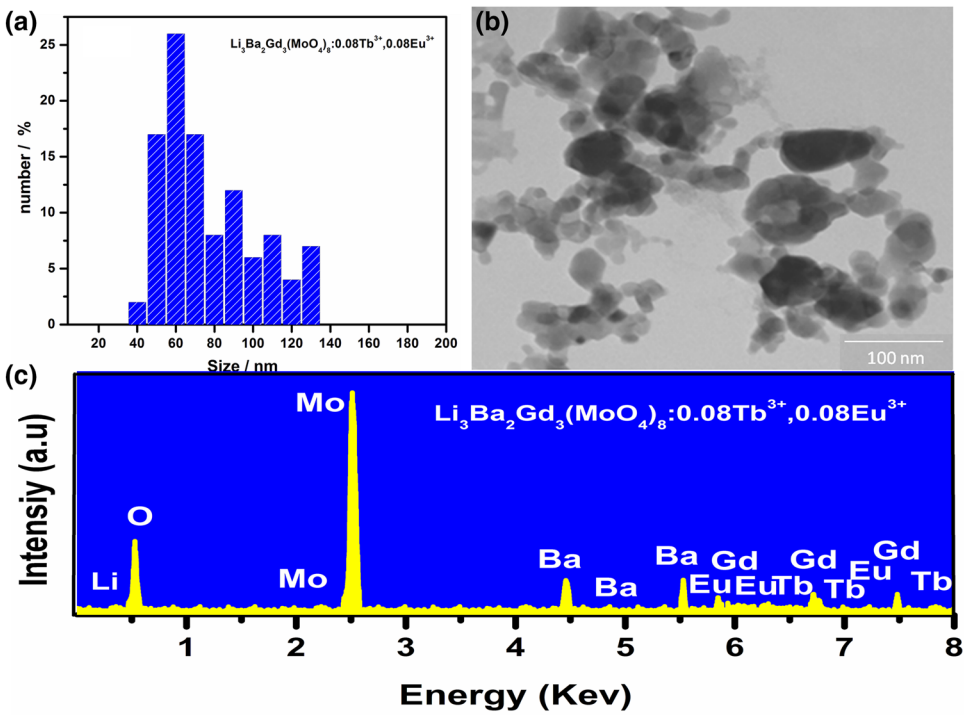

Fig. 2 **a** Particle size distribution of $Li_3Ba_2Gd_3(MoO_4)_8$: 0.08 Tb^{3+}, 0.08 Eu^{3+} phosphor. **b** EDX spectrum of $Li_3Ba_2Gd_3(MoO_4)_8$: 0.08 Tb^{3+}, 0.08 Eu^{3+} phosphor. **c** TEM image of $Li_3Ba_2Gd_3(MoO_4)_8$: 0.08 Tb^{3+}, 0.08 Eu^{3+} phosphor

3.4 FTIR analysis

The FT-IR spectra of $Li_3Ba_2Gd_3(MoO_4)_8$: 0.08 Eu^{3+}, $Li_3Ba_2Gd_3(MoO_4)_8$:0.08 Tb^{3+} and $Li_3Ba_2Gd_3(MoO_4)_8$:0.08Tb^{3+},0.08Eu^{3+} nano phosphors are shown in Fig. 3.The bands at 3400–3450 and 1600–1650 cm^{-1} are consigned to O–H stretching vibrations and H–O–H bending vibrations of water molecules from air physically absorbed on the material surface, which is entirely unlike from coordinated water in compounds [19, 20]. The very strong absorption peaks at 820, 829 and 842 cm^{-1} which are consigned to stretching vibration of O–Mo–O in MoO_4^{2-} tetrahedron [19].

3.5 Photoluminescence properties

The excitation spectra at the emission wavelength of 616 nm and emission spectra at the emission wavelength of 394 nm of $Li_3Ba_2Gd_3(MoO_4)_8$: 0.08 Eu^{3+} phosphor is illustrated in Fig. 4. Due to intra configurational f–f transitions of ($^7F_0 \rightarrow {}^5D_4$, $^7F_0 \rightarrow {}^5G_3$, $^7F_0 \rightarrow {}^5L_6$ and $^7F_0 \rightarrow {}^5D_2$) Eu^{3+}, a strong and narrow peaks were monitored in the excitation spectra at the wavelengths of 364, 380, 394 and 464 nm, respectively [16]. The PL emission spectra exhibits strong narrow lines with wavelength ranging from 530 to 710 nm, which are related to $^5D_0 \rightarrow {}^7F_J$ (J = 1, 2, 3, 4) transitions of the excited Eu^{3+} ions to the ground energy state. The transitions due to $^5D_0 \rightarrow {}^7F_2$ at 615 nm is the most prominent among the other transitions of Eu^{3+} such as, $^5D_0 \rightarrow {}^7F_1$, $^5D_0 \rightarrow {}^7F_3$, and $^5D_0 \rightarrow {}^7F_4$ located in the range of 530–710 nm [21]. The emission intensity of $^5D_0 \rightarrow {}^7F_2$ transition was found to be much stronger than $^5D_0 \rightarrow {}^7F_1$ transition suggesting that the Eu^{3+} ions are situated in a distorted (or asymmetric) cation surroundings and indicates that Eu^{3+} ions occupy the sites of Gd [16, 22].

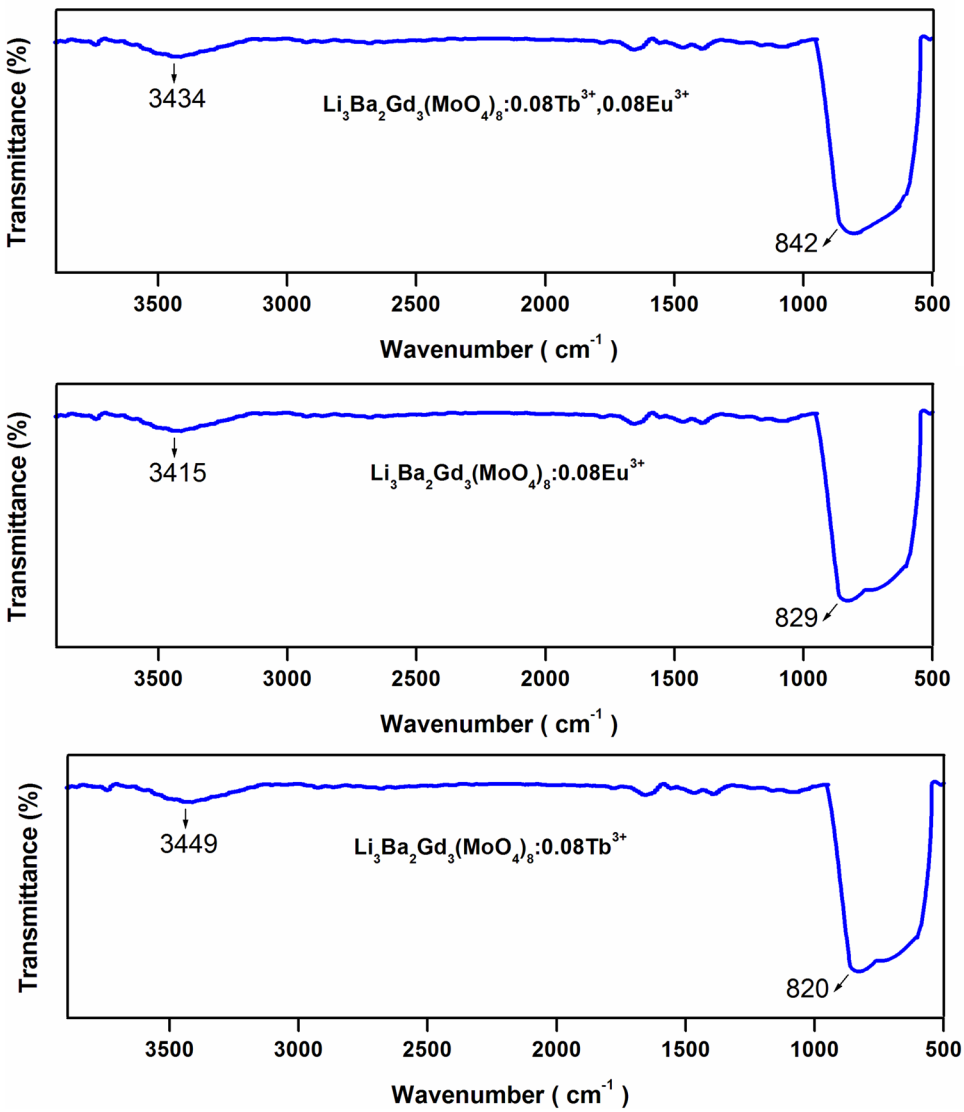

Fig. 3 FTIR spectrum of $Li_3Ba_2Gd_3(MoO_4)_8$: 0.08 Tb^{3+}, $Li_3Ba_2Gd_3(MoO_4)_8$: 0.08 Eu^{3+} and $Li_3Ba_2Gd_3(MoO_4)_8$: 0.08 Tb^{3+}, 0.08 Eu^{3+} phosphors

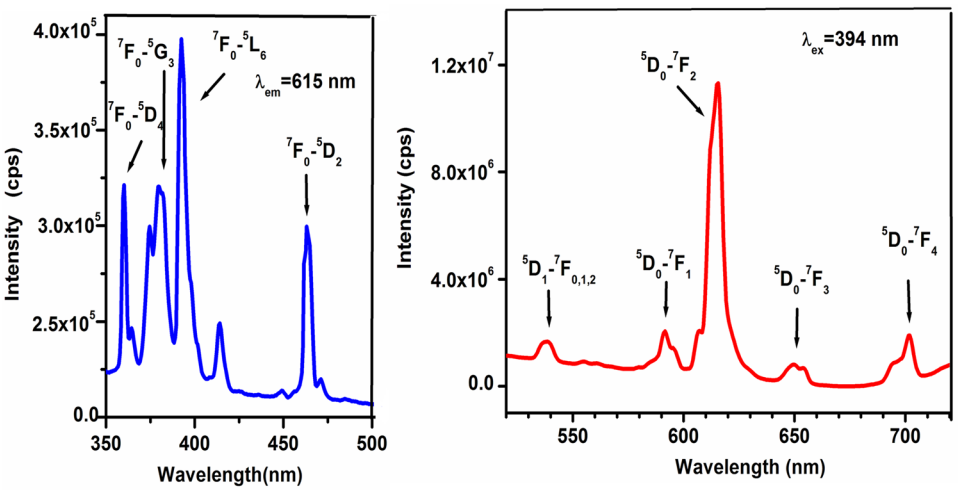

Fig. 4 Excitation and emission spectra of $Li_3Ba_2Gd_3$ $(MoO_4)_8$: 0.08 Eu^{3+} phosphor

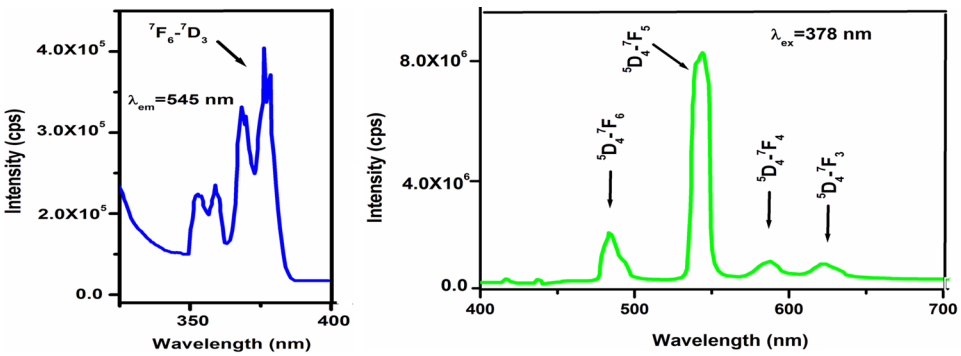

Fig. 5 Excitation and emission spectra of $Li_3Ba_2Gd_3$ $(MoO_4)_8$: 0.08 Tb^{3+} phosphor

Figure 5 shows the excitation spectra at the emission wavelength of 545 nm and emission spectra at the excitation spectra of $Li_3Ba_2Gd_3$ $(MoO_4)_8$: 0.08 Tb^{3+}. In the excitation spectra, Many strong and narrow peaks due to intra configurational f–f transitions of Tb^{3+} ions were monitored. The strongest peak is observed at the wavelength of 378 nm due to the transitions of $^7F_6 \rightarrow {}^5D_3$ [16]. Under the excitation of 378 nm, the emission spectrum has the characteristic emission peaks of Tb^{3+} at 489, 545, 587, and 620 nm corresponding to the transitions of $^5D_4$ energy level to $^7F_6$, $^7F_5$, $^7F_4$, and $^7F_3$ energy levels, respectively [17, 23, 24].

Since the emissions of Tb^{3+} due to $^5D_4 \rightarrow {}^7F_j$ transitions are very well overlapped with the $^7F_0 \rightarrow {}^5D_{0,1,2}$ absorption transitions of Eu^{3+}, thus energy transfer from Tb^{3+} to Eu^{3+} ions would be considered as efficient [25].

Figure 6 illustrates the emission spectra of $Li_3Ba_2Gd_3$ $(MoO_4)_8$: 0.08 Tb^{3+}, yEu^{3+} (y = 0.005, 0.02, 0.04, 0.06, 0.08 and 0.10 mol) samples monitored at the excitation wavelength of 378 nm. It is observed that the codoped Eu^{3+} and doped Tb^{3+} ions in $Li_3Ba_2Gd_3$ $(MoO_4)_8$ host demonstrate not only the characteristics emission of Tb^{3+} ($^5D_4 \rightarrow {}^7F_{6,5,4,3}$) ions but also the characteristics emission of Eu^{3+} ions ($^5D_0$–$^7F_{1,2}$) [25].

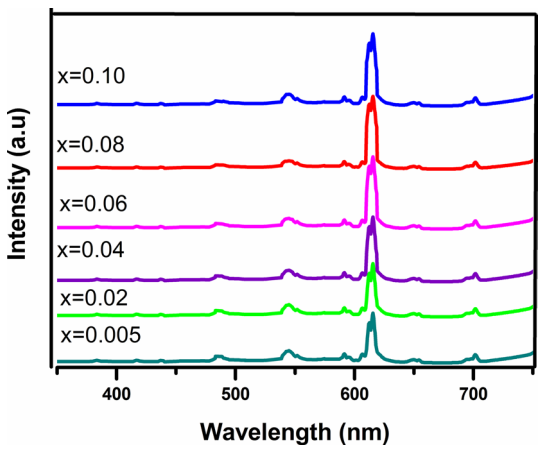

Fig. 6 The emission spectra of $Li_3Ba_2Gd_3$ $(MoO_4)_8$: 0.08 Tb^{3+}, yEu^{3+} (y = 0.005, 0.02, 0.04, 0.06, 0.08 and 0.10 mol) samples at the excitation wavelength of 378 nm

If the doping concentration of Eu^{3+} increases, the emission intensity at 615 nm ($^5D_0$–$^7F_2$) of Eu^{3+} are enhanced and reaches the maximum at y = 0.08 and then decreases owed to concentration quenching effect, meanwhile the emission

intensity of Tb^{3+} is gradually decreased which demonstrates an energy transfer occurs from Tb^{3+} to Eu^{3+} ions. It is observed that photoluminescence colors were tuned by simply adjusting the doping concentrations of Eu^{3+} $Li_3Ba_2Gd_3$ $(MoO_4)_8$: 0.08 Tb^{3+} in the host [16].

The energy-transfer efficiency from a sensitizer to an activator, η_{ET} can be obtained as the following equation: [9, 26]

$$\eta_{ET} = 1 - \frac{I_s}{I_{so}}$$

where I_{so} is the intrinsic luminescent intensity of Tb^{3+}, I_s is the luminescent intensity of Tb^{3+} in the presence of Eu^{3+}. Figure 7 exhibits the energy transfer efficiencies from Tb^{3+} to Eu^{3+} excited at 378 nm .As illustrated in figure, the energy transfer efficiency of $Li_3Ba_2Gd_3$ $(MoO_4)_8$: 0.08 Tb^{3+}, y Eu^{3+} increases as the concentration of Eu^{3+} increases from 0.005 to 0.08 mol and it gradually decreases with the increase of Eu^{3+} concentration. The energy transfer efficiency from Tb^{3+} to Eu^{3+} were calculated to be 76, 80.92, 82.41, 85.06, 88.34 and 83% for $Li_3Ba_2Gd_3$ $(MoO_4)_8$: 0.08 Tb^{3+}, y Eu^{3+} (y = 0, 0.005, 0.02, 0.04, 0.06, 0.08 and 0.10 mol, respectively) samples, respectively. It indicates that the energy transfer from Tb^{3+} to Eu^{3+} is very proficient.

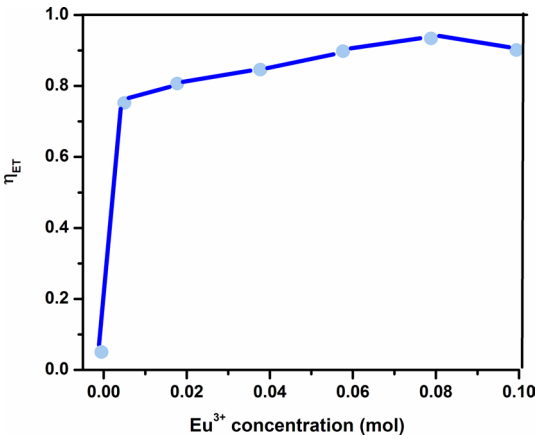

Fig. 7 Dependence of energy transfer efficiency with increase of Eu^{3+} concentration

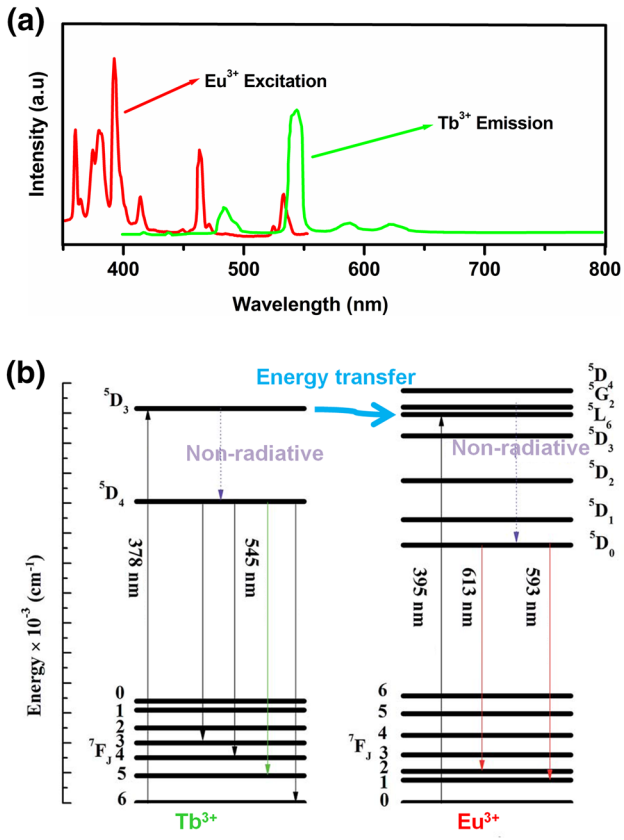

Fig. 9 **a** Overlap spectral profile of Tb^{3+} emission (λ_{exci} = 378 nm) and Eu^{3+} excitation (λ_{em} = 618 nm). **b** Energy levels of Tb^{3+} and Eu^{3+} in $Li_3Ba_2Gd_3$ $(MoO_4)_8$ phosphor

In general, there are two mechanisms which could occur during the energy transfer from a sensitizer to an activator [21, 27, 28].

i. Exchange interaction, whenever the typical critical distance is shorter than 5 A^o exchange interaction occurs.
ii. Multipolar interaction,whenever the typical critical distance is longer than 10 A^o multipolar interaction occurs.

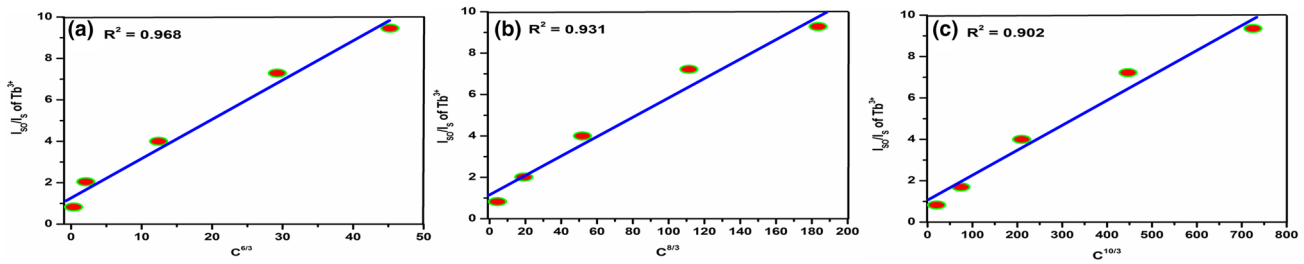

Fig. 8 Dependence of $\frac{I_{so}}{I_s}$ of Tb^{3+} on $C^{6/3}$, $C^{8/3}$ and $C^{10/3}$

According to Blasse's theory, the critical distance R_c from Tb^{3+} to Eu^{3+} ions for energy transfer can be established from the following equation [29–31].

$$R_C = 2\left[\frac{3V}{4\pi xN}\right]^{1/3}$$

here, V is the volume of the unit cell. x is the critical concentration at which the luminescence intensity of the sensitizer (Tb^{3+}) is half that in the sample in the absence of activator (Eu^{3+}). N is the coordinate number of molecules in the unitcell. For $Li_3Ba_2Gd_3(MoO_4)_8$, V = 2046.73 $A^{0\,3}$, N = 3and x = 0.085. The critical distance Rc was determined to be 24.6 A°. It is much longer than 5 A°, which indicates that energy transfer through exchange interaction is not possible. It implies that the energy transfer between Tb^{3+} ions and Eu^{3+} ions happen only in the way of electric multipolar interaction phenomena.

Dexter's energy transfer for electric multipolar interaction and Reisfeld's approximation are calculated by using the following equation [32–34],

$$\frac{\eta_{SO}}{\eta_S} \alpha\, C^{(\alpha/3)}$$

The luminescent quantum efficiency of Tb^{3+} in the absence and presence of Eu^{3+} is denoted as η_{SO} and η_S.C is the concentration of Eu^{3+} ions. Based on equation x, when

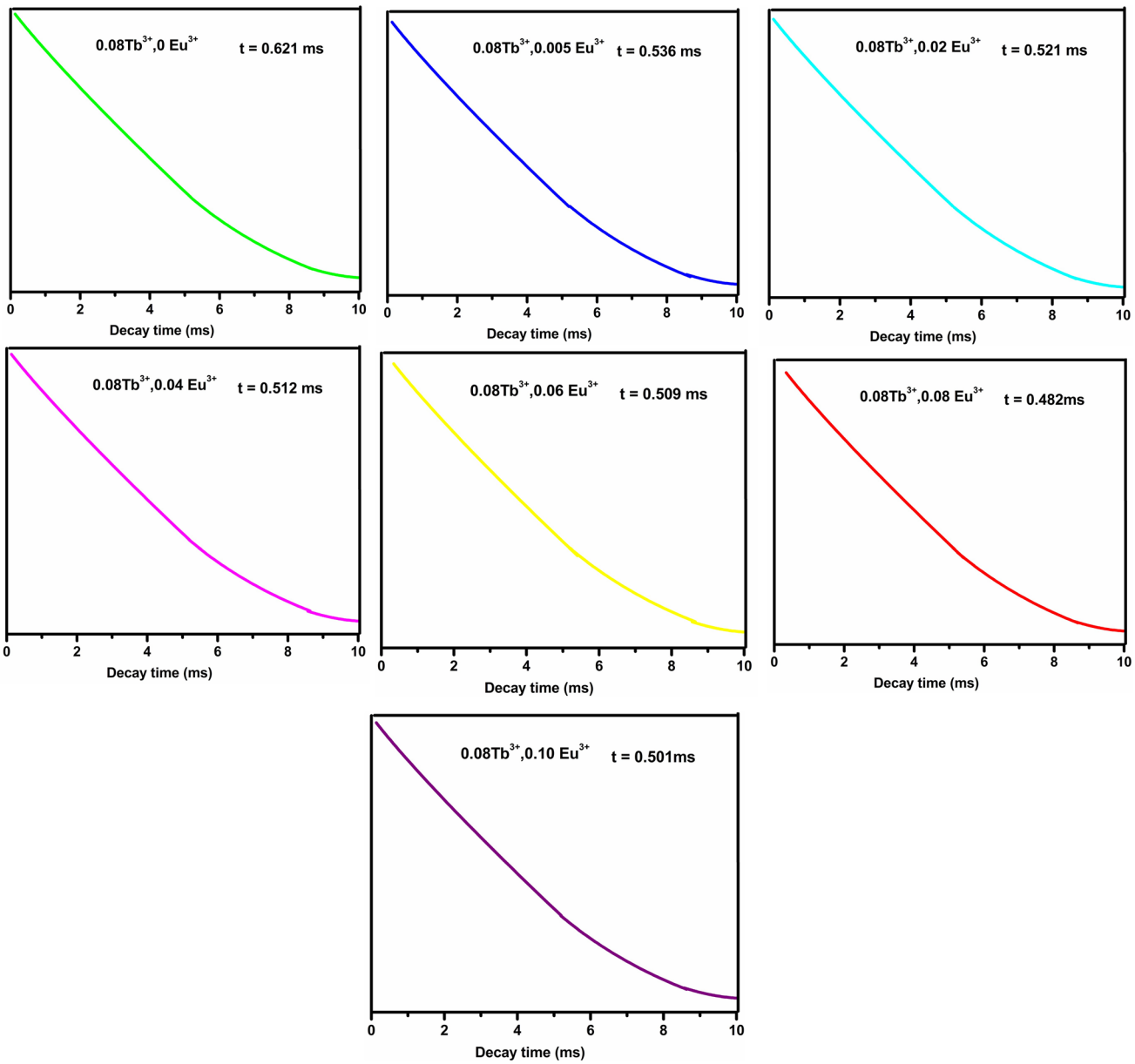

Fig. 10 Fluorescent decay curve of the as-prepared of $Li_3Ba_2Gd_3(MoO_4)_8$: 0.08 Tb^{3+}, x Eu^{3+} phosphor samples (λ_{ex} = 378 nm)

$\alpha = 6$, It corresponds to electric dipole- dipole interactions. When $\alpha = 8$, It corresponds to electric dipole-quadrupole interactions. When $\alpha = 10$, It corresponds to electric quadrupole -quadrupole interactions, respectively. Figure 8 exhibits the $\frac{I_{SO}}{I_S} \propto C^{\propto/3}$ ($\propto = 6,8,10$) plots for $Li_3Ba_2Gd_3(MoO_4)_8$: 0.08 Tb^{3+}, y Eu^{3+} when monitored at the excitation wavelength of 378 nm. It is observed that the $\frac{I_{SO}}{I_S}$ value follows the linear growth law at $\propto = 6$ and it is very well fit and comfort than when $\propto = 8$ or $\propto = 10$. So, it is observed that the energy transfer from Tb^{3+} to Eu^{3+} occurs only due to electric dipole–dipole interaction mechanism [25].

Figure 9a indicates the overlap spectral profile of Tb^{3+} emission ($\lambda_{exci} = 378$ nm) and Eu^{3+} excitation ($\lambda_{em} = 618$ nm) and implies the possibility of energy transfer phenomena from Tb^{3+} ions to Eu^{3+}ions [35]

Figure 9b exhibits the mechanism of energy transfer process from Tb^{3+} ions to Eu^{3+} ions. At the excitation wavelength of 378 nm, Tb^{3+} ions are excited and they reach higher energy level through $^7F_6$–$^5D_3$ transitions. Once life span is over, the Tb^{3+} ions relaxed and reach lower energy levels through $^5D_3$–$^7F_{5,4,3}$ Transitions. These transitions are non radiative in nature. Some of Tb^{3+} ions reaches lower lying energy level described as metastable state ($^5D_4$).Once life span is over at the metastable state they reach lower energy levels through $^5D_4$–$^7F_{5,4,3}$ transitions. These transitions are radiative in nature. Some of the Tb^{3+} ions at the energy level $^5D_3$ transfer their energy to the Eu^{3+} ions and thus, the Eu^{3+} ions could reach higher energy level through $^7F_0$–$^5G_2$. By undergoing a fast non radiative transition, the Eu^{3+} ions reaches lower energy levels radiatively through $^5D_0$–^7F_J (J = 0–6 transitions).Thus, the characteristic emission of Eu^{3+} at 615 nm was enhanced due to energy transfer process.

Figure 10 represents the photoluminescence decay curves and lifetime of Tb^{3+} ($\lambda_{ex} = 378$ nm) in the as-prepared $Li_3Ba_2Gd_3(MoO_4)_8$: 0.08 Tb^{3+}, y Eu^{3+} (y = 0, 0.005, 0.02, 0.04, 0.06, 0.08 and 0.10 mol, respectively) phosphor samples by mechanochemically assisted direct solid state reaction at room temperature. This can be fitted by a single-exponential function as $I = Aexp(-t/\tau)$ (τ is the life time of rare earth ion), and the value of lifetime of co-activated samples have been shown decrement while compared with life time of singly activated Tb^{3+} ions and thus due to energy transfer of excitation energy of Tb^{3+} ions to Eu^{3+} ions in the system [36–38]. The result shows that the lifetime is short enough for prospective applications in lighting.

Figure 11 exhibits the CIE chromaticity coordinates diagram $Li_3Ba_2Gd_3(MoO_4)_8$: 0.08 Tb^{3+}, $Li_3Ba_2Gd_3(MoO_4)_8$: 0.08 Tb^{3+}, y Eu^{3+} (y = 0, 0.005, 0.02, 0.04, 0.06, 0.08 and 0.10) and $Li_3Ba_2Gd_3(MoO_4)_8$: 0.08 Eu^{3+} phosphors. In accordance with the emission spectra, the values of CIE

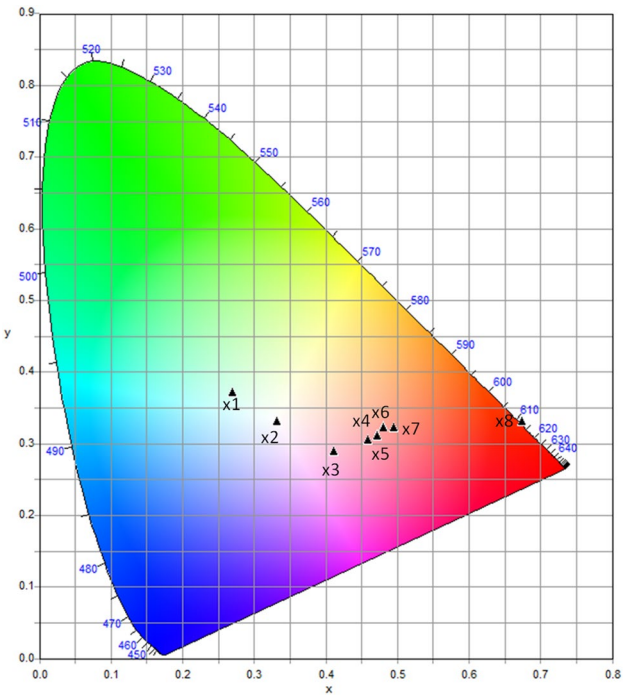

Fig. 11 CIE coordinates of the of $Li_3Ba_2Gd_3(MoO_4)_8$: 0.08 Tb^{3+}, yEu^{3+} (y = 0, 0.005, 0.02, 0.04, 0.06, 0.08 and 0.10 mol) and $Li_3Ba_2Gd_3(MoO_4)_8$: 0.08 Eu^{3+} phosphors

Table 1 CIE chromaticity coordinates of the $Li_3Ba_2Gd_3(MoO_4)_8$: 0.08 Tb^{3+}, y Eu^{3+} (y = 0, 0.005, 0.02, 0.04, 0.06, 0.08 and 0.10 mol) and $Li_3Ba_2Gd_3(MoO_4)_8$: 0.08 Eu^{3+} phosphors

Point	Sample ($\lambda_{ex} = 378$ nm)	CIE (x,y)
x1	$Li_3Ba_2Gd_3(MoO_4)_8$: 0.08 Tb^{3+}, 0 Eu^{3+}	(0.269, 0.369)
x2	$Li_3Ba_2Gd_3(MoO_4)_8$: 0.08 Tb^{3+}, 0.005Eu^{3+}	(0.332, 0.329)
x3	$Li_3Ba_2Gd_3(MoO_4)_8$: 0.08 Tb^{3+}, 0.02 Eu^{3+}	(0.411, 0.287)
x4	$Li_3Ba_2Gd_3(MoO_4)_8$: 0.08 Tb^{3+}, 0.04 Eu^{3+}	(0.458, 0.303)
x5	$Li_3Ba_2Gd_3(MoO_4)_8$: 0.08 Tb^{3+}, 0.06 Eu^{3+}	(0.472, 0.309)
x6	$Li_3Ba_2Gd_3(MoO_4)_8$: 0.08 Tb^{3+}, 0.08Eu^{3+}	(0.480, 0.321)
x7	$Li_3Ba_2Gd_3(MoO_4)_8$: 0.08 Tb^{3+},0.10 Eu^{3+}	(0.495, 0.320)
x8	$Li_3Ba_2Gd_3(MoO_4)_8$: 0.08 Eu^{3+} ($\lambda_{ex} = 394$ nm)	(0.674, 0.329)

parameters of the synthesized nano phosphors with various doping concentrations are summarized in Table 1. At the excitation wavelength of 378 nm, it is observed that varying the ratio of Eu^{3+} and Tb^{3+} concentrations the phosphors can be tuned from blue green (point x1) to white (point x2), yellow (point x3, x4, x5, x6, x7) and atlast to the orange red (point x8).The CIE chromaticity coordinates (x,y) of $Li_3Ba_2Gd_3(MoO_4)_8$: 0.08 Tb^{3+}, 0.005 Eu^{3+} (x = 0.358 and y = 0.305) which is very close to an ideal white chromaticity coordinates (0.33, 0.33).Thus the obtained results exhibit that the as prepared $Li_3Ba_2Gd_3(MoO_4)_8$: 0.08 Tb^{3+},

$0.005Eu^{3+}$ is a promising single-phase white light emitting phosphor material for White LEDs.

4 Conclusion

In summary, uniform spherical like Tb^{3+} and Eu^{3+} codoped $Li_3Ba_2Gd_3(MoO_4)_8$ nanoarchitectures has been prepared for the first time by mechanochemically assisted solid state reaction at room temperature. The $Li_3Ba_2Gd_3(MoO_4)_8$: 0.08 Tb^{3+}, yEu^{3+} phosphors can be effectively excited at 378 nm and have several emission peaks due to Tb^{3+} and Eu^{3+} ions centered at 545, 594 and 615 nm. The energy transfer from Tb^{3+} to Eu^{3+} in The $Li_3Ba_2Gd_3(MoO_4)_8$ was demonstrated to be electric dipole–dipole interaction phenomena. The value of energy transfer efficiency in Tb^{3+}–Eu^{3+} was calculated to be 88.34% at $Li_3Ba_2Gd_3(MoO_4)_8$: 0.08 Tb^{3+}, 0.08 Eu^{3+} phosphor. The CIE coordinates of the phosphors demonstrates that as prepared nanophosphors can be tuned from blue-green to white, yellow and finally to the orange-red by varying the concentrations of Eu^{3+} ions. All these favorable results indicate that $Li_3Ba_2Gd_3(MoO_4)_8$: 0.08 Tb^{3+}, 0.005 Eu^{3+} is a promising single-composition phosphor for application involving white-light NUV LEDs.

References

1. Z.Y. Hou, G.G. Li, H.Z. Lian, J. Lin, J. Mater. Chem. **22**, 5254 (2012)
2. M.M. Shang, C.X. Li, J. Lin, Chem. Soc. Rev. **43**, 1372 (2014)
3. S. Nizamoglu, G. Zengin, H.V. Demir, Appl. Phys. Lett. **92**, 1 (2008)
4. C.C. Lin, Y.S. Zheng, H.Y. Chen, C.H. Ruan, G.W. Xiao, R.S. Liu, J. Electrochem. Soc. **157**, 900 (2010)
5. H.A. Hoppe, Angew. Chem. Int. Ed. **40**, 3572 (2009)
6. M. Xu, L. Wang, D. Jia, H. Zhao, J. Am. Ceram. Soc. **98**, 1536 (2015)
7. T. Nishida, T. Ban, N. Kobayashi, Appl. Phys. Lett. **82**, 3817 (2003)
8. G.G. Li, Y. Zhang, D.L. Geng, M.M. Shang, C. Peng, Z.Y. Cheng, J. Lin, ACS Appl. Mater. Interfaces **4**, 296 (2012)
9. W. Lu, N. Guo, Y.C. Jia, Q. Zhao, W.Z. Lv, M.M. Jiao, B.Q. Shao, H.P. You, Inorg. Chem. **52**, 3007 (2013)
10. C.C. Sun, W.T. Chien, I. Moreno, C.T. Hsieh, M.C. Lin, S.L. Hsiao, Opt. Express **18**, 6137 (2010)
11. I. Moreno, C.C. Sun, Opt. Express **16**, 1808 (2008)
12. R.F. Klevtsova, A.D. Vasil'ev, L.A. Glinskaya, A.D. Kruglik, N.M. Kozhevnikova, V.P. Korsun, Zh. Strukt. Khim **33**, 126 (1992)
13. M. Rico, X. Han, C. Cascales, F. Esteban-Betegon, C. Zaldo, Opt. Express **19**, 7640 (2011)
14. M. Song, L. Zhang, G. Wang, J. Alloys Compd. **480**, 839 (2009)
15. A. Garcia-Cortes, C. Cascales, Chem. Mater. **20**, 3884 (2008)
16. A.J. Peter, I.B. Shameem Banu, J. Mater. Sci.: Mater. Electron. **26**, 2045 (2015)
17. A.J. Peter, I.B. Shameem Banu, J. Appl. Sci. Eng. **19**, 409 (2016)
18. R.D. Shannon, Acta Crystallogr. A **32**, 751 (1976)
19. L.J. Burcham, I.E. Wachs, Spectrochim. Acta A **54**, 1355 (1998)
20. A. Kato, S. Oishi, T. Shishido, M. Yamazaki, S. Lida, J. Phys. Chem. Solids **66**, 2079 (2005)
21. M. Shang, D. Geng, D. Yang, X. Kang, Y. Zhang, J. Lin, Inorg. Chem. **52**, 3102 (2013)
22. A.J. Peter, I.B. Shameem Banu, J. Thirumalai, S.P. David, J. Mater. Sci.: Mater. Electron. **24**, 4503 (2013)
23. X. Zhang, L. Zhou, J. Shi, M. Gong, Mater. Lett. **137**, 32 (2014)
24. A.J. Peter, I.B. Shameem Banu, J. Mater. Sci.: Mater. Electron. **25**, 2771 (2014)
25. B. Wang, Q. Ren, O. Hai, X. Wu, RSC Adv. **7**, 15222 (2017)
26. C.H. Huang, T.M. Chen, J. Phys. Chem. C **115**, 2349 (2011)
27. P. Blasse, Res. Rep. **24**, 131 (1969)
28. M.M. Shang, G.G. Li, X.J. Kang, D.M. Yang, D.L. Geng, J. Lin, ACS Appl. Mater. Interfaces **3**, 2738 (2011)
29. S.P. Lee, T.S. Chan, T.M. Chen, ACS Appl. Mater. Interfaces **7**, 40 (2014)
30. S.P. Lee, C.H. Huang, T.S. Chan, T.M. Chen, ACS Appl. Mater. Interfaces **6**, 7260 (2014)
31. G. Blasse, Phys. Lett. **28**, 444 (1968)
32. G. Zhu, Y. Wang, Z. Ci, B. Liu, Y. Shi, S. Xin, J. Lumin. **132**, 531 (2012)
33. D.L. Dexter, J. Chem. Phys. **21**, 836 (1953)
34. R. Reisfeld, J. Chem. Phys. **56**, 1698 (1972)
35. L.-M. Shao, X.-P. Jing, J. Lumin. **131**, 1216 (2011)
36. M. Abdelaziz, M.M. Ghannam, Physica B **405**, 958 (2010)
37. J. Olesiak-Banska, M. Nyk, D. Kaczmarek, K. Matczyszyn, K. Pawlik, M. Samoc, Opt. Mater. **33**, 1419 (2011)
38. H. Jiu, J. Ding, Y. Sun, J. Bao, C. Gao, Q. Zhang, J. NonCrystal. Solids **352**, 197 (2006)

Journal of Materials Science: Materials in Electronics (2018) 29:12076–12088
https://doi.org/10.1007/s10854-018-9314-7

Modulation of Sn concentration in ZnO nanorod array: intensification on the conductivity and humidity sensing properties

A. S. Ismail[1] · M. H. Mamat[1,2] · I. B. Shameem Banu[3] · M. F. Malek[2,4] · M. M. Yusoff[1] · R. Mohamed[1,5] · W. R. W. Ahmad[1] · M. A. R. Abdullah[1] · N. D. Md. Sin[1] · A. B. Suriani[6] · M. K. Ahmad[7] · M. Rusop[1,2]

Received: 7 April 2018 / Accepted: 17 May 2018 / Published online: 21 May 2018

Abstract
Tin (Sn)-doped zinc oxide (ZnO) nanorod arrays (TZO) were synthesized onto aluminum-doped ZnO-coated glass substrate via a facile sonicated sol–gel immersion method for humidity sensor applications. These nanorod arrays were grown at different Sn concentrations ranging from 0.6 to 3 at.%. X-ray diffraction patterns showed that the deposited TZO arrays exhibited a wurtzite structure. The stress/strain condition of the ZnO film metamorphosed from tensile strain/compressive stress to compressive strain/tensile stress when the Sn concentrations increased. Results indicated that 1 at.% Sn doping of TZO, which has the lowest tensile stress of 0.14 GPa, generated the highest conductivity of 1.31 S cm^{-1}. In addition, 1 at.% Sn doping of TZO possessed superior sensitivity to a humidity of 3.36. These results revealed that the optimum performance of a humidity-sensing device can be obtained mainly by controlling the amount of extrinsic element in a ZnO film.

1 Introduction

The influence of humidity level in the environment has been a major concern of moisture-sensitive fields, such as weather forecasting, chemical production area, agriculture, and inflammable gas inspection [1]. Recent studies on humidity sensors mostly focused on high sensitivity over a wide range of humidity levels, fast response time, good reproducibility, negligible temperature dependence, low cost, ease of fabrication, and long term stability [2–4]. Through intensive studies, metal oxides, such as titanium dioxide (TiO_2), tin oxide (SnO_2), zinc oxide (ZnO), and iron oxide (Fe_2O_3), were found to meet the criteria required to produce high-quality humidity sensors [5–8]. Among the metal oxides, ZnO has the highest potential in humidity sensor owing to its wide energy bandgap (~ 3.3 eV) of *n*-type semiconductor, non-toxicity, high chemical/physical stability, and unique electrical and optical properties [9–11]. ZnO is an important material in sensors, light emitting diode, and solar cells [12–14]. One-dimensional nanostructure films, such as nanorods, yield excellent performance because of its high surface-to-volume ratio, offering a direct pathway for charge transport along the axes of nanostructure arrays and significantly reducing the rate of electron–hole pair recombination [15–17]. Currently, ZnO nanorod arrays are synthesized through solution-based processes [12, 18–20], chemical vapor deposition (CVD) [21], sputtering [22], and metalorganic CVD [23]. The solution-based method is frequently preferred because of its simple preparation, low cost, and capability for high-quality ZnO nanorod array productions.

Nevertheless, high resistivity and low free carrier concentrations result in lagging changes in resistance values at high relative humidity (RH), thereby limiting the use

✉ M. H. Mamat
mhmamat@salam.uitm.edu.my

1 NANO-ElecTronic Centre (NET), Faculty of Electrical Engineering, Universiti Teknologi MARA (UiTM), 40450 Shah Alam, Selangor, Malaysia

2 NANO-SciTech Centre (NST), Institute of Science (IOS), Universiti Teknologi MARA (UiTM), 40450 Shah Alam, Selangor, Malaysia

3 Department of Physics, B.S. Abdur Rahman University, Vandalur, Chennai 600 048, India

4 Faculty of Applied Sciences, Universiti Teknologi MARA (UiTM), 40450 Shah Alam, Selangor, Malaysia

5 Faculty of Applied Sciences, Universiti Teknologi MARA (UiTM), 26400 Bandar Jengka, Pahang, Malaysia

6 Nanotechnology Research Centre, Faculty of Science and Mathematics, Universiti Pendidikan Sultan Idris (UPSI), 35900 Tanjung Malim, Perak, Malaysia

7 Microelectronic and Nanotechnology – Shamsuddin Research Centre (MiNT-SRC), Faculty of Electrical and Electronic Engineering, Universiti Tun Hussein Onn Malaysia (UTHM), 86400 Batu Pahat, Johor, Malaysia

of pristine ZnO as sensing element for humidity sensors [24–26]. The properties of pristine ZnO, particularly its crystal properties, catalytic behavior, and conductivity, can be enhanced through doping with metal elements, such as gallium (Ga) [27], copper (Cu) [28], sodium (Na) [29], and tin (Sn) [30]. Among these metal elements, we focused use on Sn because it can enhance conductivity through its double-ionized donors, which provide extra carriers and improve water adsorption for humidity sensing applications [31–33]. However, controlling the ratio of doping element in the ZnO structure is vital because an optimum amount of dopant atoms can significantly enhance crystal properties and device performances. For instance, Luo et al. found that 15 at.% of Sn doped to ZnO, which was prepared using hydrothermal method, demonstrated high sensitivity to ethanol owing to surface area improvement and electron concentration increment [34]. Chahmat et al. reported that 4% Sn doping concentration improves the crystalline, structural, and transmittance properties of ZnO films [35]. Furthermore, controlling the level of doping in ZnO-based humidity sensors is exceptionally crucial. Hong et al. investigated the effects of different concentrations of Ga-doped ZnO seed layer on ZnO nanorods and on their humidity sensing performance [26]. They observed that Ga concentration increment in ZnO seed layer leads to nanorod size decrement and increase in nanorod length, thereby improving the surface areas of the sensors and humidity sensing capabilities of the films. Zhu et al. reported the effects of Fe concentrations to hydrothermally grown ZnO nanorod array-based and self-powered humidity sensors [36]. Fe concentration increment increased the diameter of the nanorod array, and 1% of Fe doping produced the highest response to humidity. The effects of Sn concentrations on the properties and performance levels of ZnO-based humidity sensors were investigated. Ates et al. fabricated Sn-doped ZnO-based quartz crystal microbalance humidity sensor, where the Sn concentrations varied at 0, 0.1, 1, and 2% [37]. They found that Sn doping increased the sizes of the particles, consequently decreasing the surface volume ratio. This effect reduced the adsorption of water molecules. Although reports on the effects of Sn doping on ZnO properties already exist, detailed investigation on the effect of Sn concentrations to the structural, optical, and electrical characteristics of ZnO, especially the correlation between stress/strain, band gap energy, conductivity, and humidity sensing performance are rarely discussed in previous studies. Furthermore, ZnO humidity sensors in a resistive configuration have not been widely studied. Therefore, this particular topic is of particular interest for understanding effect of Sn doping concentrations to the ZnO behavior in terms of structural, optical and electrical properties, as well as their resulting humidity sensing performance.

In this study, Sn-doped ZnO nanorod array (TZO)-based humidity sensors were prepared by varying the Sn concentrations via a facile sonicated sol–gel immersion method and fabricated for the detection of humidity at room temperature. Structural, optical, and electrical characterizations were conducted for the evaluation of sensor properties.

2 Experimental procedure

Prior to the deposition of TZO-based humidity sensors, ZnO seed layer film was first deposited using spin coating method. The detail processes have been reported elsewhere [38]. For the preparation of TZO films, aqueous solutions which consist of (0.1 M) zinc nitrate hexahydrate ($Zn(NO_3)_2{\cdot}6H_2O$; 98.5% purity; Riendemann Schmidt), (0.1 M) hexamethylenetetramine ($C_6H_{12}N_4$; 99% purity; Sigma-Aldrich), and (0.6, 1, 2, and 3 at.%) tin (IV) chloride pentahydrate ($SnCl_4{\cdot}5H_2O$; 98% purity; Sigma-Aldrich) were sonicated in a water bath sonication tank for 30 min and then aged for 3 h at room temperature. The solutions were immersed at 95 °C for 2 h. The samples were then cleaned and heated at 150 °C for 10 min and annealed at 500 °C for 1 h. The corresponding process is shown in Fig. 1. For comparison, an undoped ZnO (0 at.%) film was prepared using the same procedure. Subsequently, 60 nm-thick Au contacts were sputtered on the samples as electrodes using a sputter coater (Emitech K550X).

Field emission scanning electron microscope (JEOL JSM-7600F) and X-ray diffraction (XRD) with PANalytical X'Pert PRO were used to evaluate the structural and crystalline properties of the film. Ultraviolet–Visible spectrophotometer (Varian Cary 5000) was used for optical analysis of the samples. The current–voltage (I–V) characteristics were measured by using a 2-probe I–V measurement system (I–V, Advantest R6243). Humidity sensing performance of the sensors was investigated using humidity measurement system (ESPEC-SH261).

3 Result and discussion

3.1 Structural and morphological characteristics

Figure 2 shows the surface morphologies of the TZO films at different Sn concentrations. The nanorods were densely and uniformly deposited on the seed layer-coated glass substrate. The hexagonal nanorods had an average diameters of 112, 105, 99, 95, and 91 nm at Sn concentrations of 0, 0.6, 1, 2, and 3 at.%, respectively. The cross-sectional images of the TZO films at different Sn concentrations are depicted in Fig. 3. The cross-sectional images indicate that the TZO growth was perpendicular to the substrate or along

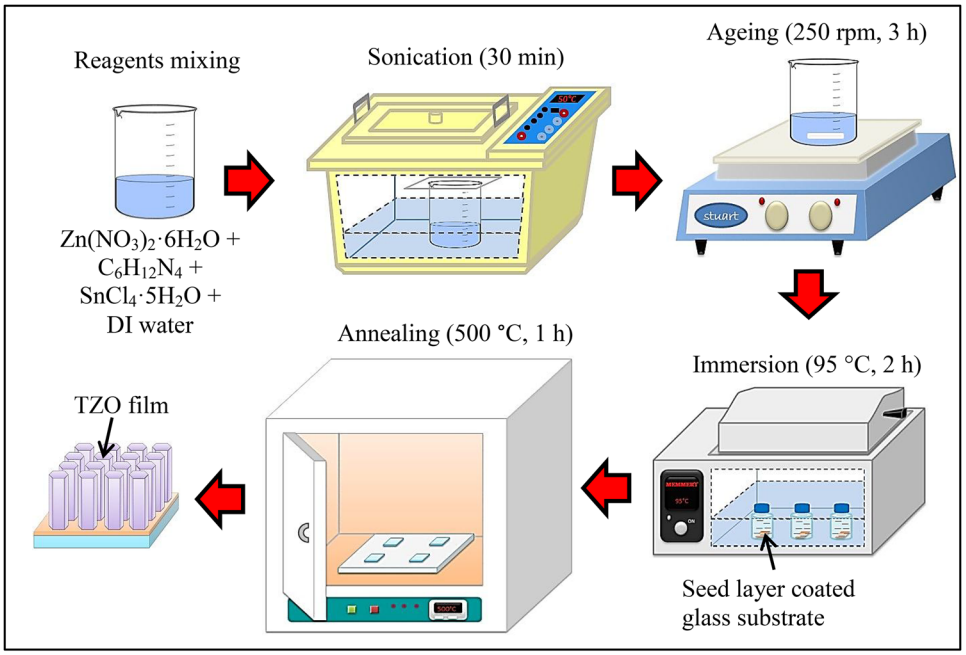

Fig. 1 Synthesis of TZO thin film via sol–gel immersion method

the *c*-axis orientation. The thicknesses of the film were 1.10, 0.98, 0.93, 0.84, and 0.71 μm when the samples were doped with 0, 0.6, 1, 2, and 3 at.% Sn, respectively. The results suggested that the average diameters and thicknesses of the samples were reduced when Sn doping concentrations were increased. This condition may be due to the decreased ionic radii of Sn^{4+} (0.69 Å) ions replacing the Zn^{2+} (0.74 Å) ions [39]. This phenomenon was also observed by Wang et al. [40], who prepared Sn-doped ZnO nanostructures via polyol-mediated precipitation method. According to them, the substitution of Sn element into ZnO crystal causes the reduction of ZnO growth rate. Supatutkul et al. [30] pointed out that a doped ZnO crystal structure yields higher formation energy than an undoped ZnO. Notably, the reaction between O species with Zn species at (002) orientation is closely related to the formation energy between the two elements. Owing to the appearance of Sn atoms, the enhancement of lattice distortion was inevitable and led to the increment of formation energy in the growth system. As an enhanced formation energy was required because of the increased Sn concentration, the growth rate of ZnO crystal at (002) plane was reduced. The reduction may have decreased the thicknesses of the nanorod arrays. Aside from the reduction in diameter and thickness, no other significant change in the surface morphology of the nanorods could be observed.

The crystalline properties of the films were analyzed from the XRD plot as depicted in Fig. 4. The appeared peaks were matched with the standard diffraction pattern of a polycrystalline hexagonal wurtzite ZnO crystal (JCPDS #36-1451). No peak corresponded to SnO_2 and SnO or other formation of crystal structure can be detected. The peak of (002) plane exhibited the highest intensity. Under thermodynamic equilibrium condition, (002) plane exhibited higher surface energy than the other planes [41]. Thus, crystal structure formation mostly occurred along the *c*-axis orientation or perpendicular to the substrate [42]. The appearance of other weak peaks may correspond to the imperfect nanorods alignment on the substrate [43]. To investigate the effect of doping on TZO crystallinity, we monitored the (002) diffraction peak. The diffraction peaks showed that the intensity of the preferred *c*-axis orientation was slightly reduced at 0.6 and 1 at.% of Sn in contrast to that in undoped ZnO. The peak intensity was strongly affected when Sn concentration was increased to 2 and 3 at.%. This trend clearly demonstrated the necessity to examine the lattice properties of these TZO films. The calculation of lattice constant (c_{film}), which corresponds to the (002) plane orientation can be expressed as [24, 44]:

$$c_{film} = \frac{\lambda}{\sin\theta} \quad (1)$$

Here, λ and θ are the X-ray wavelength (1.54 A) and diffracting angle associated with (002) plane orientation, respectively. The calculated values are recorded in Table 1. The diffracting angle of (002) peak showed a slight shift towards a higher angle, verifying the substitutions of Sn atoms into Zn sites and the lowering of the lattice parameter of ZnO. This shifting was elucidated by Navale et al. when they prepared Sn-doped ZnO nanotetrapods film via thermal evaporation [45]. Besides, the c_{film} values of the TZO films contracted when the Sn concentrations increased. This outcome may be ascribed to the variations in the crystallographic properties

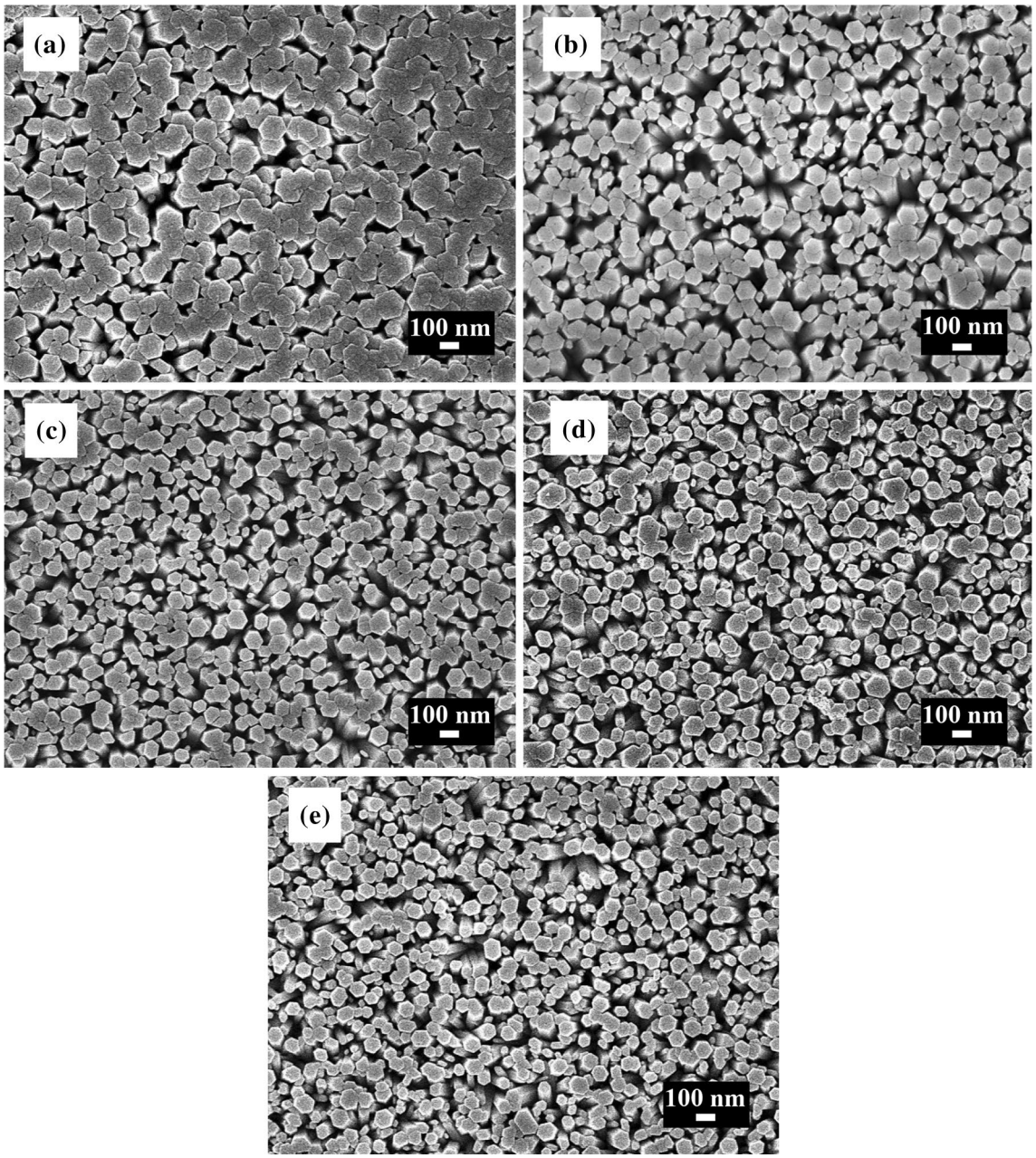

Fig. 2 The surface images of **a** undoped ZnO (0 at.%) and TZO prepared using **b** 0.6, **c** 1, **d** 2, and **e** 3 at.% Sn concentrations

of the films. These variations resulted from the difference between the ionic radii of the Sn^{4+} and Zn^{2+} ions. According to Khuili et al. [46], when ZnO is doped by atoms with an ionic radius smaller than that of Zn^{2+}, its diffraction peaks shift toward higher diffraction angles. This observation is in agreement with the present study and those reported by other researchers [45, 47].

Furthermore, the peak shifting can be envisaged to the strain/stress variation in the film. The lattice strain (ε_{zz}) along the *c*-axis can be expressed as below [48]:

$$\varepsilon_{zz} = \frac{c_{film} - c_{bulk}}{c_{bulk}} \times 100\% \quad (2)$$

where c_{film} and c_{bulk} are the lattice parameters for the synthesized and standard bulk (or powder) ZnO, respectively. In case of tensile strain, positive strain value is observed. Meanwhile, negative strain value is emerged for compressive strain [42, 49]. For residual stress estimation, the following equation is used [50]:

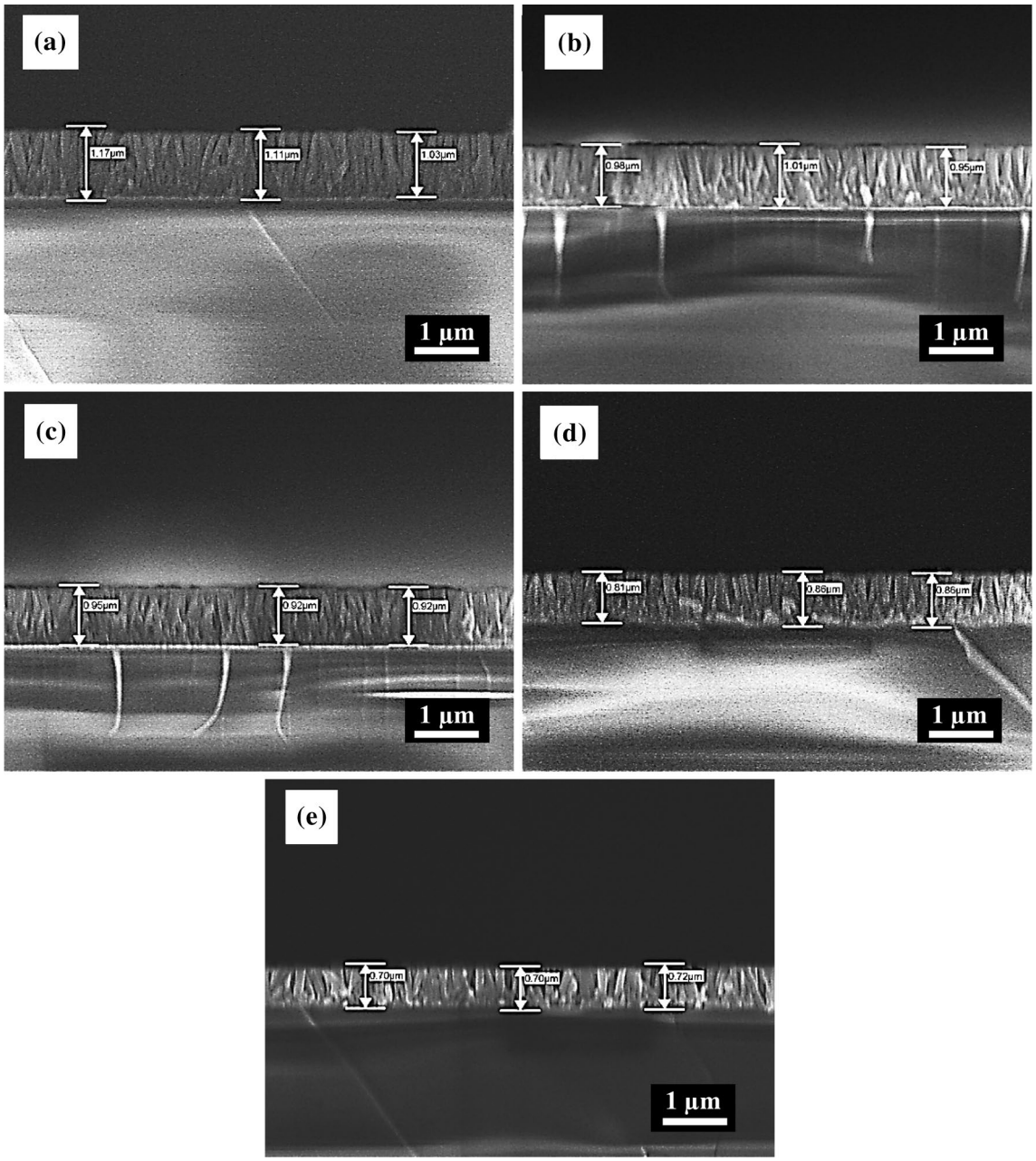

Fig. 3 The cross-sectional images of **a** undoped ZnO (0 at.%) and TZO prepared using **b** 0.6, **c** 1, **d** 2, and **e** 3 at.% Sn concentrations

$$\sigma_{film} = \frac{2C_{13}^2 - C_{33}(C_{11} + C_{12})}{2C_{13}}\varepsilon_{zz} \tag{3}$$

C_{ij} is the elastic stiffness constants of bulk ZnO where C_{11}, C_{12}, C_{13}, and C_{33} hold the values of 208.8, 119.7, 104.2, and 213.8 GPa, respectively, and ε_{zz} represent the lattice strain along *c*-axis. Similar to strain, tensile stress exhibits positive stress value while compressive stress shows negative stress value [42]. The estimated strain/stress of the samples is displayed in Table 1. On the basis of the estimated data, the low Sn concentration sample (0.6 at.%) yielded tensile strain/compressive stress, whereas the strain/stress metamorphosed to compressive strain/tensile stress at higher Sn concentrations (1–3 at.%). Sn^{4+} doping changes the crystal structure because the ionic radius of Sn^{4+} is smaller than that of Zn^{2+} [35]. As additional Sn atoms occupied the ZnO lattice, the direction of strain/stress during the growth process deviated from tensile strain/compressive stress to compressive strain/tensile stress. Moreover, when Sn concentration was increased to 2 and 3 at.%, the residual stress of the films significantly increased. Such finding may have resulted from lattice

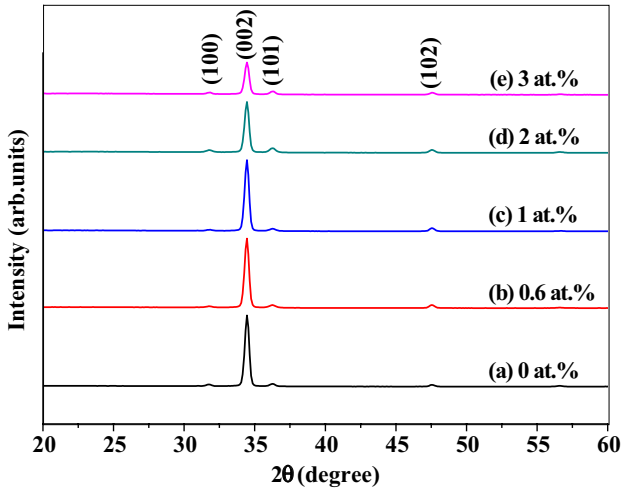

Fig. 4 The XRD patterns of undoped ZnO and TZO films

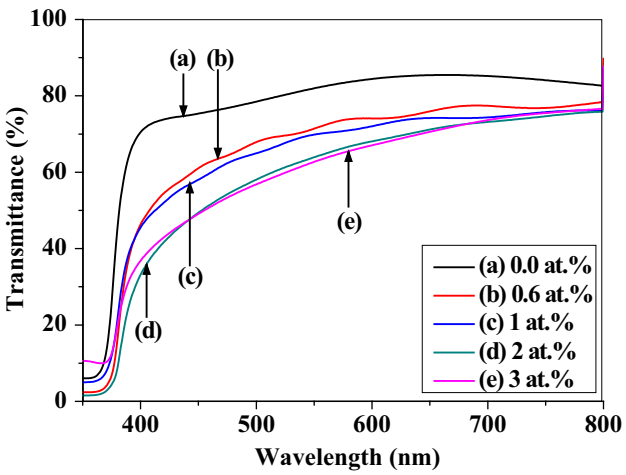

Fig. 5 Transmittance spectra of undoped ZnO and TZO films

structure deterioration due to the excessive substitution of Sn into the ZnO nanorod array structure. This behavior explained the significant reduction of the peak intensity of the film at (002) orientation produced by the 2 and 3 at.% samples.

3.2 Optical properties

In this segment, the optical properties of the undoped ZnO and TZO such as transmittance and absorption coefficient were determined. The measurement wavelength ranged between 350 and 800 nm. Figure 5 depicts the transmittance spectra of the films. At transmission wavelength around 380 nm, the transmittance rapidly drop which persuaded by the band gap energy of ZnO. The average transmittance of the films apparently decreased when doped with Sn, as shown in Table 2. The undoped ZnO film had the highest average transmittance (79%) as of its structural homogeneity and highly crystalline film, which resulted in a low optical scattering effect. The 3 at.% Sn had the lowest average transmittance (64%). Figure 6 depicts the absorption coefficient spectra of the films which were obtained from the Lambert's law [51]:

$$\alpha = \frac{1}{t}\ln\left(\frac{1}{T}\right) \tag{4}$$

Here, t is the film thickness which was estimated from cross-sectional images and T is the measured transmittance. The films exhibited high UV absorption properties at <400 nm wavelength. The change in optical band gap energy (E_g) reflected the effect of Sn doping to the optical properties of ZnO nanorod array film. The value of E_g can be obtained from Tauc's relation as expressed below [52]:

$$ahv = B\left(hv - E_g\right)^{\frac{1}{2}} \tag{5}$$

where α is the absorption coefficient, hv is the photon energy, E_g is the optical band gap energy, and B is an energy-independent constant [53]. Figure 7 depicts the Tauc's plot and the estimated E_g are provided in Table 2. The E_g values were slightly dependent on Sn concentration, and E_g was escalated when ZnO was doped with Sn up to 1 at.%. When the concentrations of Sn were further increased to 2 and 3 at.%, the E_g values were decreased. This result is in agreement with those of previous reports [37, 54]. The increased in E_g from 0 to 1 at.% Sn concentrations could be explained by the Burstein–Moss effect [55], where E_g rises because of band filling, which causes the Fermi level to move higher than the band edge. The Pauli exclusion principle indicates that states cannot be doubly occupied. Thus, electrons from a valence band acquires additional energy to be excited to

Table 1 Diffraction angle, lattice parameter, strain, and stress of undoped ZnO and TZO films

Concentration (at.%)	Diffraction angle, 2θ (°)	Lattice parameter c_{film} (Å)	Strain (%)	Stress (GPa)
0 (undoped)	34.38	5.2108	0.081	− 0.19
0.6	34.38	5.2108	0.081	− 0.19
1	34.43	5.2034	−0.061	0.14
2	34.47	5.1976	−0.173	0.40
3	34.48	5.1961	−0.202	0.47

Table 2 Average transmittance, optical band gap energy, Urbach energy, and conductivity of undoped ZnO and TZO films

Concentration (at.%)	Average transmittance, T (%)	Optical band gap energy, E_g (eV)	Urbach energy, E_u (meV)	Conductivity, σ (S cm^{-1})
0 (Undoped)	79	3.21	95	0.015
0.6	70	3.23	105	0.733
1	68	3.23	109	1.310
2	63	3.22	133	0.701
3	63	3.20	171	0.057

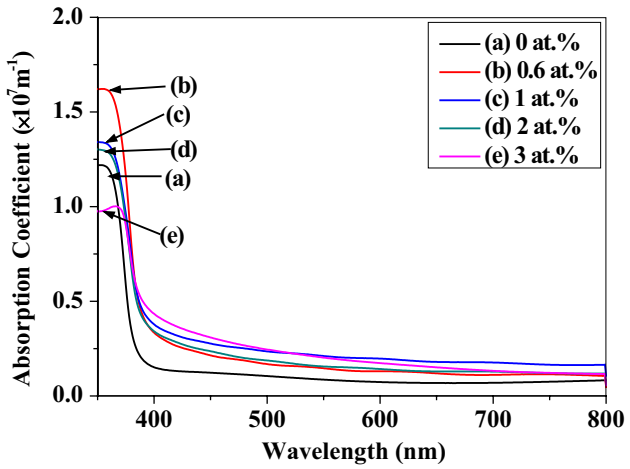

Fig. 6 Plot of absorption coefficient of undoped ZnO and TZO films

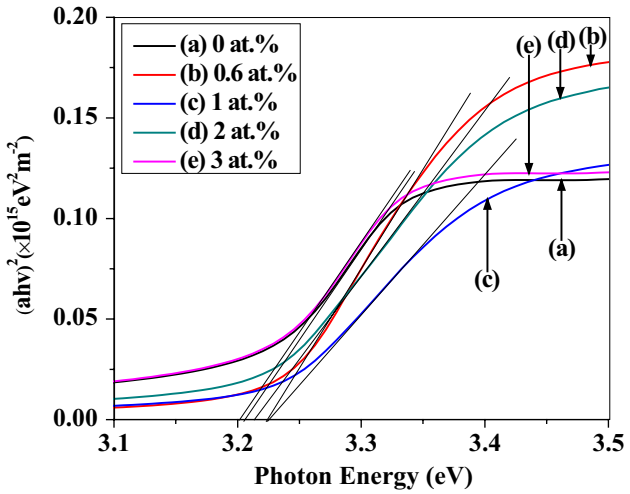

Fig. 7 Estimation of the optical band gap energy, E_g, undoped ZnO, and TZO films by using Tauc's plot

the next energy states in the conduction band, leading to broader energy gap formation [56]. However, the reduction in E_g when Sn concentrations reached 2–3 at.% was related to the increase of additional band tail states [57, 58]. This increase led to the shrinkage of the band gap when doping was performed above the threshold concentration. Thus, the

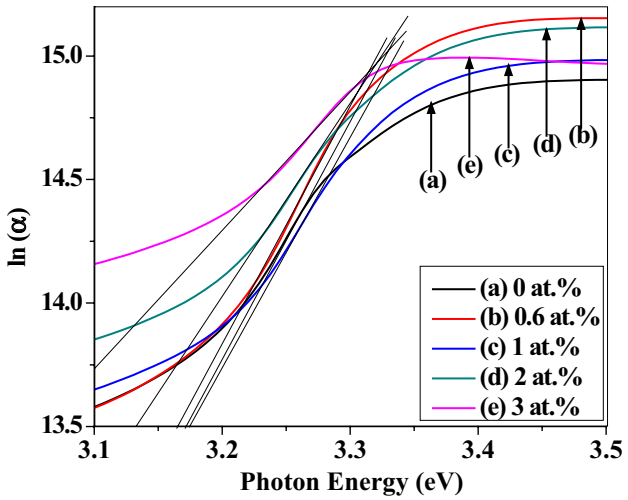

Fig. 8 Plot of ln (α) versus photon energy for undoped ZnO and TZO films for Urbach energy estimation

reduction in E_g was linked to the increased lattice disorders induced by doping. Dopants generally play an important role in determining the electrical and optical properties of materials due to the presence of localized levels/bands or lattice disorder in the band gap of the materials. Thus, studying the relation of lattice disorder with the increased/decreased E_g due to doping is remarkable.

Disorder formation in the film can be represented by Urbach energy (E_u), where E_u is the width of the available localized states in the optical band gap of the films. The enhancement of E_u is associated with band bending, which occurs depending on the structural defect [51]. The variable E_u can be determined by using the following equation [59]:

$$\alpha = \alpha_0 \exp\left(\frac{hv}{E_u}\right) \tag{6}$$

where α is the absorption coefficient, α_0 is the pre-exponential factor, hv is the photon energy, and E_u is the Urbach energy. Figure 8 represents the Urbach plot of TZO at different Sn concentrations. The E_u values of the undoped ZnO and TZO films are presented in Table 2. The E_u values

slightly increased from 0 to 1 at.% Sn concentrations but significantly increased as Sn concentrations were further increased to 2 and 3 at.%, reflecting the enhancement of structural disorder. Such behavior reinforced the significant reduction in crystallinity of 2 and 3 at.% samples based on XRD spectra and the shrinking of E_g. The increased E_u at high concentrations of Sn-doping was also observed in previous studies [60, 61]. Furthermore, the increment of lattice disorder may be the reason for the average transmittance reduction, as summarized in Table 2. This finding was also observed by other researchers [62].

3.3 Conductivity and resistivity measurement

Figure 9 displays the I–V characteristics of the undoped ZnO and TZO films. The I–V curves indicate that the nanorod arrays exhibited ohmic behavior. The result also indicates that the current is enhanced with increasing supplied voltage for the nanorod arrays. The conductivity of the film (σ) was determined using the following equation [42]:

$$\sigma = \frac{1}{\rho} \tag{7}$$

where ρ is the resistivity, which can be expressed as:

$$\rho = \left(\frac{V}{I}\right)\frac{wt}{l} \tag{8}$$

where V is the supplied voltage, I is the measured current, t is the film thickness, w is the electrode width, and l is the length between the electrodes. The active area of the thin films was 3×10^{-6} m^2. The σ of the undoped ZnO and TZO films are listed in Table 2. The lowest conductivity was obtained for undoped ZnO. Conductivity gradually increased with the incorporation of Sn dopants. The highest

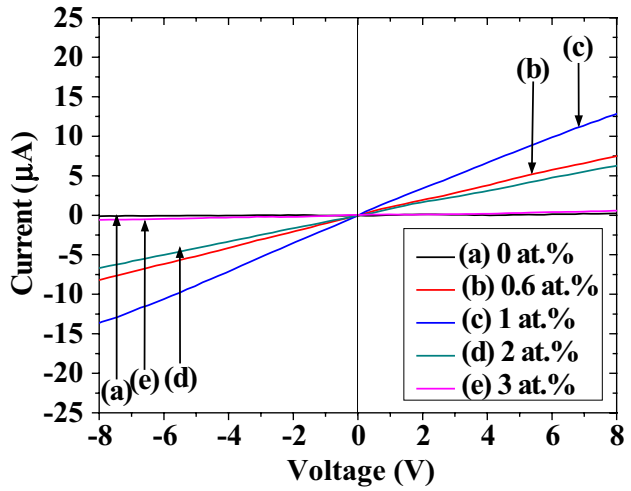

Fig. 9 I–V characteristics of undoped ZnO and TZO films

conductivity was noted at 1 at.%. However, when the Sn doping concentrations were increased up to 2 and 3 at.%, the conductivity of the films was significantly reduced. The conductivities were expected to increase due to the generation of free carriers, as expressed in the following equation [63]:

$$SnO_2 \rightarrow Sn_{Zn}^{\cdot\cdot} + V_{Zn}'' + V_o^x + O_{2(g)} + 2e^- \tag{9}$$

where Sn atoms substitute the Zn sites in ZnO lattice and dispense two extra electrons to the conduction band. The conductivity enhancement after doping might also due to the contribution of extrinsic impurity states around ZnO Fermi level [64]. Theoretically, the addition of increased Sn dopants to ZnO increases the concentrations of free carriers. This increase was not observed in our results. Upon further increase in Sn concentrations (2–3 at.%), the excessive substitution of Sn atoms in the ZnO lattice structure induced the deterioration of the ZnO crystal structure rather than providing additional carrier concentration. Salam et al. reported that excessive doping of ZnO structure generates increased strain to the crystal structure and reduces the electron mobility, leading to enhanced resistivity [65]. Yildiz et al. mentioned that conductivity reduction at high Sn concentrations (> 2 at.%) may be associated with carrier traps at grain boundaries [66]. Shelke et al. reported that doping at a certain amount of dopant may form a film with less compressive stress and enhanced conductivity [67]. This finding was in agreement with the previously discussed XRD, bandgap energy, and conductivity data.

3.4 Humidity sensing performance

Figure 10 reveals the humidity sensing responses of TZO films prepared at different Sn concentrations. A commercial humidity chamber (ESPEC-SH261) was used for the measurement purpose with varies humidity level (40–90% RH) and at room temperature. RH was initially maintained at 40%. After 300 s, the RH was altered from 40 to 90% to observe the absorption of humidity, and then decreased from 90 to 40% RH to investigate the desorption behavior. The current signal was very stable at the initial 40% RH. The current signals were observed to increase steadily until reaching 90% RH. When humidity was reduced to 40% RH, the current signals dropped slowly until it achieved the minimum current.

The performance of the fabricated humidity sensors were analyzed based on their sensitivity where sensitivity is given by [68]:

$$S = \frac{R_a}{R_{rh}} \tag{10}$$

where S is sensitivity, R_a represents the resistance at initial humidity level (40% RH), and R_{rh} is the resistance of the varied humidity levels. The resistance values were attained

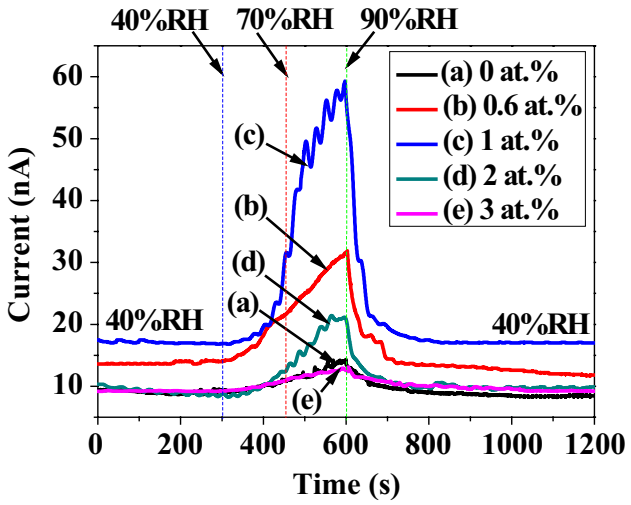

Fig. 10 Humidity sensor responses of undoped ZnO- and TZO-based humidity sensors

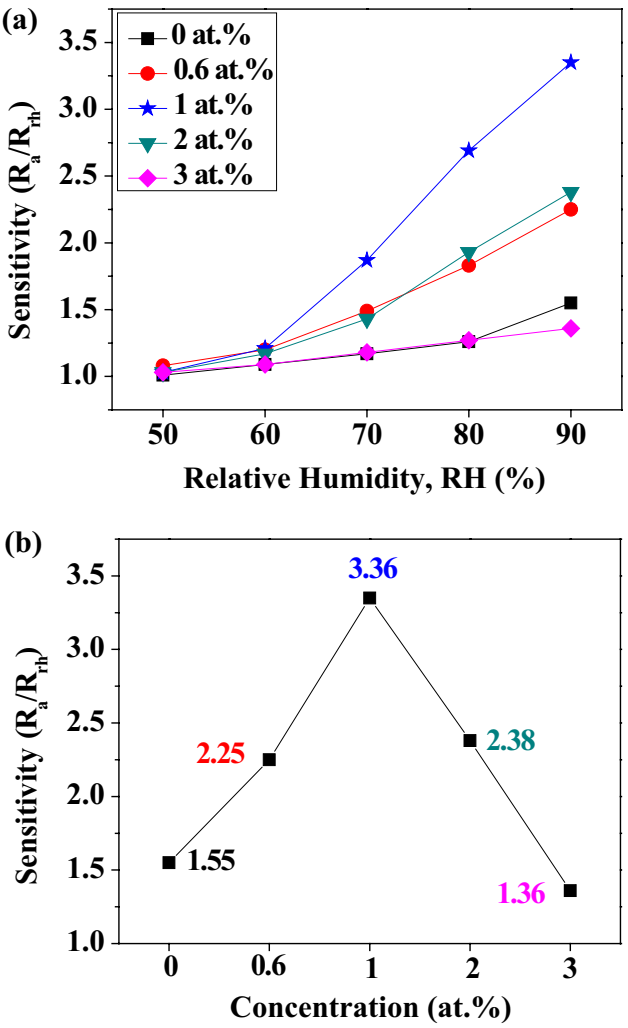

Fig. 11 **a** Sensitivity plot of undoped ZnO and TZO-based humidity sensors at different humidity level. **b** Plot of sensitivity variation at 40–90% RH of undoped ZnO and TZO-based humidity sensors induced by the alteration of Sn doping concentrations

from current values of the response curves using Ohm's law (V = IR). The values of R_a, R_{rh}, and sensitivity of the humidity sensors from 40 to 90% RH are presented in Table 3. The sensitivity of the humidity sensor increased from 1.55 to 3.36 when doped with Sn up to 1 at.%. However, the sensitivity value dropped to 1.36 once the doping concentration reached 3 at.%. The sensitivity plots at different humidity levels in Fig. 11a revealed the excellent performance of 1 at.% sample. The sensitivity plot from 40 to 90% RH in Fig. 11b indicated an obvious enhancement of sensitivity persuaded by the 1 at.% Sn doping. The correlation between residual stress, conductivity, and sensitivity of the sensors are plotted in Fig. 12, which illustrates that the TZO-based humidity sensor prepared at 1 at.% Sn possessed superior sensitivity compared with other fabricated sensors. This condition might be associated with the highest conductivity of the 1 at.% film. Ye et al. reported that the electron transport capacity in high charge carrying density film is enhanced [69]. Zhu et al. demonstrated that the increment in free carrier density induces strong electric field at the film surface [36]. Thus, the amount of ionized water molecules on the TZO surface was enhanced. Another possible explanation for this result is that the low stress film of 1 at.% Sn was expected to become the key factor to assist efficient electron transfer on the nanorod surface, enhancing the adsorption and desorption of water molecules, as observed in residual stress plot in Fig. 12.

Table 3 Resistance and sensitivity of undoped ZnO- and TZO-based humidity sensors

Concentration (at.%)	Resistance (MΩ)		Sensitivity
	40% RH	90% RH	
0 (undoped)	543	350	1.55
0.6	355	158	2.25
1	296	88	3.36
2	572	240	2.38
3	541	397	1.36

The working mechanism of the humidity sensors is illustrated in Fig. 13. At low RH (40% RH), oxygen from ambient is able to be attracted to the sensor surface. This attraction is aided by the strong electrostatic force on the ZnO surface. This lead to the electron trapping as given in the following relation [70–72]:

$$O_2 + e^- \rightarrow O_2^- \quad (11)$$

The reaction of oxygen molecules with electron formed adsorbed oxygen ion (O_2^-). As a consequence of this electron

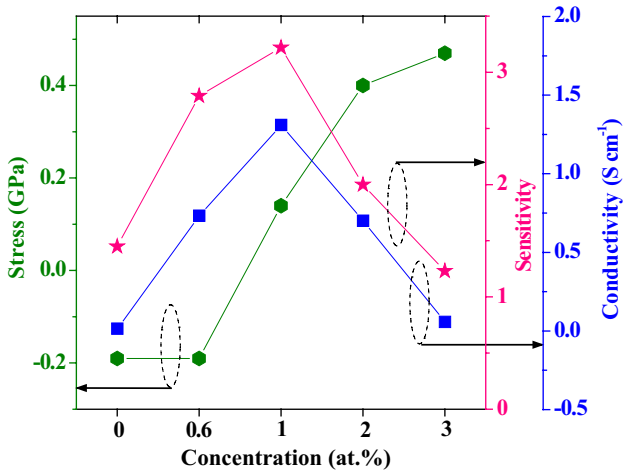

Fig. 12 Correlation of stress, conductivity, and sensitivity of undoped ZnO and TZO films

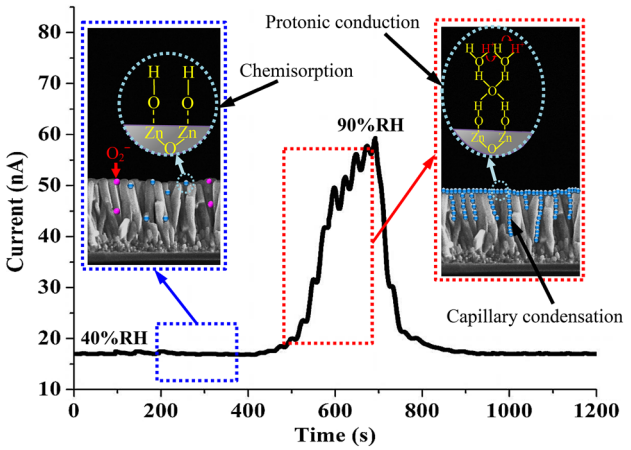

Fig. 13 Conduction mechanism on ZnO nanorod array surfaces at different humidity levels

trapping, the concentration of free carriers in the film reduced. Zhang et al. [73] mentioned that the introduction of Sn^{4+} ions into ZnO, which produces two free electrons in the process, increasing the density of adsorbed oxygen molecules on the ZnO surface. At the regions in which the water molecules are adsorbed the reaction happened is as followed:

$$2H_2O + O_2^- \rightarrow 2H_2O_2 + e^- \quad (12)$$

The chemisorption of water molecules released the trapped electron back to the film. Before we increased the RH level higher than 40% RH, the electron trapping and water molecules adsorption reactions happened at the same reaction rate. Thus, the current signal at that moment is stable. Once the RH level was elevated, the adsorption process gradually increased and formed physisorbed water layers. Due to high electrostatic force in the chemisorbed layer, the physisorbed water layer dissociates into H_3O^+ and OH^- ions. At this moment, the dominant electrical conduction is based on the protonic conduction (Grotthuss chain) in which the H^+ ions is released from H_3O^+ ions while accepting another neighboring H^+ ions [74]. According to the I–V analysis, 1 at.% doping may produce the highest free carriers which give rise to high water molecule adsorptions, leading to large ratio of minimum to maximum current change. At certain water level (high % RH), water molecules begin to condense between the pore channels of the film. This condensation of water molecules allowed the maneuver of conducting ions freely across each individual nanorods. This conduction mechanism is called capillary condensation [75, 76]. Both of this simultaneous electrical conduction mechanism caused a rapid current signal changed after the humidity level was elevated higher than 40% RH. In case of low stress film, the mobility of conducting ions may be better than that of high stress film, producing film with better humidity sensing performance.

Figure 14 shows the repeated response cycles of the TZO-based humidity sensor at 1 at.% Sn in order to observe the stability of the sensor. The responses were very stable and identical to each other which indicate that the sensor possesses good repeatability behavior.

4 Conclusion

TZO was successfully deposited on a seed layer-coated glass substrate by using a sonicated sol–gel immersion method at different Sn concentrations. The XRD patterns showed that the films exhibited wurtzite structures with preferred (002) plane orientation. Sn concentration increment led to

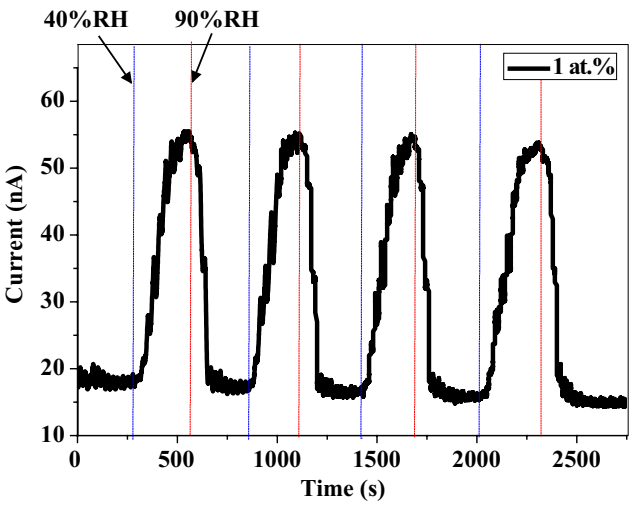

Fig. 14 The repeatability behavior of TZO-based humidity sensor at 1 at.% Sn concentration

small crystallite size, diameter, and thickness. The stress/strain of the ZnO film changed from tensile strain/compressive stress to compressive strain/tensile stress when the Sn concentrations in ZnO increased. The TZO films showed good transmittance properties at a visible region with a band gap of ~3.2 eV. The Urbach energy of the TZO films was increased when Sn concentration was increased, which was in parallel with the dislocation density increment, reflecting the enhanced defects and lattice disorders. Our results showed the highest conductivity of 1.31 S cm^{-1} produced by 1 at.% Sn doping of TZO, which exhibited the lowest tensile stress. The TZO-based humidity sensor at 1 at.% Sn doping of TZO possessed superior sensitivity of 3.36 compared to the other samples. All of these results indicated that TZO exhibited a high potential for humidity-sensor applications, and controlling the concentrations of doping element is critically important.

Acknowledgements This work was supported by the ASEAN-India Research & Training Fellowship (IMRC/AISTDF/R&D/P-1/2017). The authors also would like to thank the Institute of Research Management and Innovation (IRMI) of UiTM and the Ministry of Higher Education of Malaysia for their financial support of this research.

References

1. T.A. Blank, L.P. Eksperiandova, K.N. Belikov, Recent trends of ceramic humidity sensors development: a review. Sens. Actuator B-Chem. **228**, 416–442 (2016)
2. K. Narimani, F.D. Nayeri, M. Kolahdouz, P. Ebrahimi, Fabrication, modeling and simulation of high sensitivity capacitive humidity sensors based on ZnO nanorods. Sens. Actuator B-Chem. **224**, 338–343 (2016)
3. L. Gu, K. Zheng, Y. Zhou, J. Li, X. Mo, G.R. Patzke, G. Chen, Humidity sensors based on ZnO/TiO_2 core/shell nanorod arrays with enhanced sensitivity. Sens. Actuator B-Chem. **159**, 1–7 (2011)
4. J. Herrán, I. Fernández, E. Ochoteco, G. Cabañero, H. Grande, The role of water vapour in ZnO nanostructures for humidity sensing at room temperature. Sens. Actuator B-Chem. **198**, 239–242 (2014)
5. S.S. Batool, Z. Imran, M. Israr Qadir, M. Usman, H. Jamil, M.A. Rafiq, M.M. Hassan, M. Willander, Comparative analysis of Ti, Ni, and Au electrodes on characteristics of TiO_2 nanofibers for humidity sensor application. J. Mater. Sci. Technol. **29**, 411–414 (2013)
6. V.K. Tomer, S. Duhan, A facile nanocasting synthesis of mesoporous Ag-doped SnO2 nanostructures with enhanced humidity sensing performance. Sens. Actuator B-Chem. **223**, 750–760 (2016)
7. E. Modaresinezhad, S. Darbari, Realization of a room-temperature/self-powered humidity sensor, based on ZnO nanosheets. Sens. Actuators B **237**, 358–366 (2016)
8. G. Neri, A. Bonavita, S. Galvagno, N. Donato, A. Caddemi, Electrical characterization of Fe_2O_3 humidity sensors doped with Li^+, Zn^{2+} and Au^{3+} ions. Sens. Actuator B-Chem. **111–112**, 71–77 (2005)
9. M.H. Mamat, M.F. Malek, N.N. Hafizah, M.N. Asiah, A.B. Suriani, A. Mohamed, N. Nafarizal, M.K. Ahmad, M. Rusop, Effect of oxygen flow rate on the ultraviolet sensing properties of zinc oxide nanocolumn arrays grown by radio frequency magnetron sputtering. Ceram. Int. **42**, 4107–4119 (2016)
10. S.T. Navale, V.V. Jadhav, K.K. Tehare, R.U.R. Sagar, C.S. Biswas, M. Galluzzi, W. Liang, V.B. Patil, R.S. Mane, F.J. Stadler, Solid-state synthesis strategy of ZnO nanoparticles for the rapid detection of hazardous Cl^2. Sens. Actuator B-Chem. **238**, 1102–1110 (2017)
11. N. Irawati, H.A. Rahman, H. Ahmad, S.W. Harun, A PMMA microfiber loop resonator based humidity sensor with ZnO nanorods coating. Measurement **99**, 128–133 (2017)
12. M.H. Mamat, M.F. Malek, N.N. Hafizah, Z. Khusaimi, M.Z. Musa, M. Rusop, Fabrication of an ultraviolet photoconductive sensor using novel nanostructured, nanohole-enhanced, aligned aluminium-doped zinc oxide nanorod arrays at low immersion times. Sens. Actuator B-Chem. **195**, 609–622 (2014)
13. C.-Y. Huang, J.-H. Lai, Efficient polymer light-emitting diodes with ZnO nanoparticles and interpretation of observed sub-bandgap turn-on phenomenon. Org. Electron. **32**, 244–249 (2016)
14. R.K. Chava, M. Kang, Improving the photovoltaic conversion efficiency of ZnO based dye sensitized solar cells by indium doping. J. Alloy. Compd. **692**, 67–76 (2017)
15. C.J. Lin, S.-J. Liao, L.-C. Kao, S.Y.H. Liou, Photoelectrocatalytic activity of a hydrothermally grown branched Zno nanorod-array electrode for paracetamol degradation. J. Hazard. Mater. **291**, 9–17 (2015)
16. Y. Dou, F. Wu, C. Mao, L. Fang, S. Guo, M. Zhou, Enhanced photovoltaic performance of ZnO nanorod-based dye-sensitized solar cells by using Ga doped ZnO seed layer. J. Alloy. Compd. **633**, 408–414 (2015)
17. M.M. Yusoff, M.H. Mamat, M.F. Malek, A.B. Suriani, A. Mohamed, M.K. Ahmad, S.A.H. Alrokayan, H.A. Khan, M. Rusop, Growth of titanium dioxide nanorod arrays through the aqueous chemical route under a novel and facile low-cost method. Mater. Lett. **164**, 294–298 (2016)
18. Z. Yu, H. Li, Y. Qiu, X. Yang, W. Zhang, N. Xu, J. Sun, J. Wu, Size-controllable growth of ZnO nanorods on Si substrate. Superlattices Microstruct. **101**, 469–479 (2017)
19. R. Taheri Ghahrizjani, M.H. Yousefi, Effects of three seeding methods on optimization of temperature, concentration and reaction time on optical properties during growth ZnO nanorods. Superlattices Microstruct. **112**, 10–19 (2017)
20. A.S. Ismail, M.H. Mamat, M.M. Yusoff, M.F. Malek, A.S. Zoolfakar, R.A. Rani, A.B. Suriani, A. Mohamed, M.K. Ahmad, M. Rusop, Enhanced humidity sensing performance using Sn-Doped ZnO nanorod Array/SnO_2 nanowire heteronetwork fabricated via two-step solution immersion. Mater. Lett. **210**, 258–262 (2018)
21. E.S. Babu, S.K. Hong, Effect of indium concentration on morphology of ZnO nanostructures grown by using CVD method and their application for H_2 gas sensing. Superlattices Microstruct. **82**, 349–356 (2015)
22. M.H. Mamat, N.N. Hafizah, M. Rusop, Fabrication of thin, dense and small-diameter zinc oxide nanorod array-based ultraviolet photoconductive sensors with high sensitivity by catalyst-free radio frequency magnetron sputtering. Mater. Lett. **93**, 215–218 (2013)
23. B. Wu, Y. Zhang, Z. Shi, X. Li, X. Cui, S. Zhuang, B. Zhang, G. Du, Different defect levels configurations between double layers of nanorods and film in ZnO grown on c-Al_2O_3 by MOCVD. J. Lumines. **154**, 587–592 (2014)
24. A.S. Ismail, M.H. Mamat, N.D. Md., M.F. Sin, A.S. Malek, A.B. Zoolfakar, A. Suriani, M.K. Mohamed, M. Ahmad, Rusop, Fabrication of hierarchical Sn-doped ZnO nanorod arrays through sonicated sol–gel immersion for room temperature, resistive-type humidity sensor applications. Ceram. Int. **42**, 9785–9795 (2016)

25. T. Zhao, Y. Fu, Y. Zhao, L. Xing, X. Xue, Ga-doped ZnO nanowire nanogenerator as self-powered/active humidity sensor with high sensitivity and fast response. J. Alloy. Compd. **648**, 571–576 (2015)
26. H.-S. Hong, G.-S. Chung, Controllable growth of oriented ZnO nanorods using Ga-doped seed layers and surface acoustic wave humidity sensor. Sens. Actuator B-Chem. **195**, 446–451 (2014)
27. C. Moditswe, C.M. Muiva, A. Juma, Highly conductive and transparent Ga-doped ZnO thin films deposited by chemical spray pyrolysis. Optik **127**, 8317–8325 (2016)
28. R. Shabannia, Synthesis and characterization of Cu-doped ZnO nanorods chemically grown on flexible substrate. J. Mol. Struct. **1118**, 157–160 (2016)
29. Z. Ye, T. Wang, S. Wu, X. Ji, Q. Zhang, Na-doped ZnO nanorods fabricated by chemical vapor deposition and their optoelectrical properties. J. Alloy. Compd. **690**, 189–194 (2017)
30. C. Supatutkul, S. Pramchu, A.P. Jaroenjittichai, Y. Laosiritaworn, Density functional theory investigation of surface defects in Sn-doped ZnO. Surf. Coat. Technol. **298**, 53–57 (2016)
31. K. Soonjae, N. Sekwon, J. Haseok, K. Sunho, L. Byunghoon, Y. Jaehyun, K. Hyoungsub, L. Hoo-Jeong, Effects of Sn doping on the growth morphology and electrical properties of ZnO nanowires. Nanotechnology **24**, 065703 (2013)
32. X. Zhou, T. Lin, Y. Liu, C. Wu, X. Zeng, D. Jiang, Y. Zhang, T. Guo, Structural, optical, and improved field-emission properties of tetrapod-shaped Sn-doped ZnO nanostructures synthesized via thermal evaporation. ACS Appl. Mater. Interfaces **5**, 10067–10073 (2013)
33. A.A. Hendi, R.H. Alorainy, F. Yakuphanoglu, Humidity sensing characteristics of Sn doped Zinc oxide based quartz crystal microbalance sensors. J. Sol-Gel. Sci. Technol. **72**, 559–564 (2014)
34. S. Luo, Y. Shen, Z. Wu, M. Cao, F. Gu, L. Wang, Enhanced ethanol sensing performance of mesoporous Sn-doped ZnO. Mater. Sci. Semicond. Process. **41**, 535–543 (2016)
35. N. Chahmat, T. Souier, A. Mokri, M. Bououdina, M.S. Aida, M. Ghers, Structure, microstructure and optical properties of Sn-doped ZnO thin films. J. Alloy. Compd. **593**, 148–153 (2014)
36. D. Zhu, T. Hu, Y. Zhao, W. Zang, L. Xing, X. Xue, High-performance self-powered/active humidity sensing of Fe-doped ZnO nanoarray nanogenerator. Sens. Actuator B-Chem. **213**, 382–389 (2015)
37. T. Ates, C. Tatar, F. Yakuphanoglu, Preparation of semiconductor ZnO powders by sol–gel method: humidity sensors. Sens. Actuator A-Phys. **190**, 153–160 (2013)
38. M.H. Mamat, M.Z. Sahdan, Z. Khusaimi, A.Z. Ahmed, S. Abdullah, M. Rusop, Influence of doping concentrations on the aluminum doped zinc oxide thin films properties for ultraviolet photoconductive sensor applications. Opt. Mater. **32**, 696–699 (2010)
39. M. Ajili, M. Castagné, N.K. Turki, Study on the doping effect of Sn-doped ZnO thin films. Superlattices Microstruct. **53**, 213–222 (2013)
40. H. Wang, R. Bhattacharjee, I.M. Hung, L. Li, R. Zeng, Material characteristics and electrochemical performance of Sn-doped ZnO spherical-particle photoanode for dye-sensitized solar cells. Electrochim. Acta **111**, 797–801 (2013)
41. R. Deng, X. Zhang, E. Zhang, Y. Liang, Z. Liu, H. Xu, S. Hark, Planar defects in Sn-doped single-crystal ZnO nanobelts. J. Phys. Chem. C **111**, 13013–13015 (2007)
42. M.F. Malek, M.H. Mamat, Z. Khusaimi, M.Z. Sahdan, M.Z. Musa, A.R. Zainun, A.B. Suriani, N.D. Md Sin, S.B. Abd Hamid, M. Rusop, Sonicated sol–gel preparation of nanoparticulate ZnO thin films with various deposition speeds: The highly preferred c-axis (002) orientation enhances the final properties. J. Alloy. Compd. **582**, 12–21 (2014)
43. M.F. Malek, M.Z. Sahdan, M.H. Mamat, M.Z. Musa, Z. Khusaimi, S.S. Husairi, N.D. Md Sin, M. Rusop, A novel fabrication of MEH-PPV/Al:ZnO nanorod arrays based ordered bulk heterojunction hybrid solar cells. Appl. Surf. Sci. **275**, 75–83 (2013)
44. T. Jan, J. Iqbal, M. Ismail, Q. Mansoor, A. Mahmood, A. Ahmad, Eradication of multi-drug resistant bacteria by Ni doped ZnO nanorods: structural, raman and optical characteristics. Appl. Surf. Sci. **308**, 75–81 (2014)
45. S.C. Navale, I.S. Mulla, Photoluminescence and gas sensing study of nanostructured pure and Sn doped ZnO. Mater. Sci. Eng. C **29**, 1317–1320 (2009)
46. M. Khuili, N. Fazouan, H.A. El Makarim, G. El Halani, E.H. Atmani, Comparative first principles study of ZnO doped with group III elements. J. Alloy. Compd. **688**, 368–375 (2016)
47. A.D. Acharya, S. Moghe, R. Panda, S.B. Shrivastava, M. Gangrade, T. Shripathi, D.M. Phase, V. Ganesan, Growth and characterization of nano-structured Sn doped ZnO. J. Mol. Struct. **1022**, 8–15 (2012)
48. M. Gao, X. Wu, J. Liu, W. Liu, The effect of heating rate on the structural and electrical properties of sol–gel derived Al-doped ZnO films. Appl. Surf. Sci. **257**, 6919–6922 (2011)
49. R. Ghosh, D. Basak, S. Fujihara, Effect of substrate-induced strain on the structural, electrical, and optical properties of polycrystalline ZnO thin films. J. Appl. Phys. **96**, 2689–2692 (2004)
50. D. Fang, K. Lin, T. Xue, C. Cui, X. Chen, P. Yao, H. Li, Influence of Al doping on structural and optical properties of Mg–Al co-doped ZnO thin films prepared by sol–gel method. J. Alloy. Compd. **589**, 346–352 (2014)
51. M.F. Malek, M.H. Mamat, M.Z. Musa, T. Soga, S.A. Rahman, S.A.H. Alrokayan, H.A. Khan, M. Rusop, Metamorphosis of strain/stress on optical band gap energy of ZAO thin films via manipulation of thermal annealing process. J. Lumines. **160**, 165–175 (2015)
52. M. Jlassi, I. Sta, M. Hajji, H. Ezzaouia, Effect of nickel doping on physical properties of zinc oxide thin films prepared by the spray pyrolysis method. Appl. Surf. Sci. **301**, 216–224 (2014)
53. E.A. Davis, N.F. Mott, electrical and transparent properties of amorphous semiconductor. Philos. Mag. **22**, 903–920 (1970)
54. A. Yildiz, T. Serin, E. Öztürk, N. Serin, Barrier-controlled electron transport in Sn-doped ZnO polycrystalline thin films. Thin Solid Films **522**, 90–94 (2012)
55. S.D. Senol, O. Ozturk, C. Terzioğlu, Effect of boron doping on the structural, optical and electrical properties of ZnO nanoparticles produced by the hydrothermal method. Ceram. Int. **41**, 11194–11201 (2015)
56. S. Aydemir, S. Karakaya, The effect of Al on structure, morphology and optical properties of network texture ZnO thin films synthesized using the sol–gel method. Optik **126**, 1735–1739 (2015)
57. F.Z. Bedia, A. Bedia, N. Maloufi, M. Aillerie, F. Genty, B. Benyoucef, Effect of tin doping on optical properties of nanostructured ZnO thin films grown by spray pyrolysis technique. J. Alloy. Compd. **616**, 312–318 (2014)
58. S.K. O'Leary, S. Zukotynski, J.M. Perz, Disorder and optical absorption in amorphous silicon and amorphous germanium. J. Non-Cryst. Solids **210**, 249–253 (1997)
59. C. Shin, S.M. Iftiquar, J. Park, Y. Kim, S. Baek, J. Jang, M. Kim, J. Jung, Y. Lee, S. Kim, J. Yi, Optimization of intrinsic hydrogenated amorphous silicon deposited by very high-frequency plasma-enhanced chemical vapor deposition using the relationship between Urbach energy and silane depletion fraction for solar cell application. Thin Solid Films **547**, 256–262 (2013)
60. S. Ilican, M. Caglar, Y. Caglar, Sn doping effects on the electro-optical properties of sol gel derived transparent ZnO films. Appl. Surf. Sci. **256**, 7204–7210 (2010)
61. A. Santhosh Kumar, K.K. Nagaraja, H.S. Nagaraja, Effect of Sn doping on structural, optical, electrical and wettability properties of oriented ZnO nanorod arrays. J. Mater. Sci.: Mater. Electron. **24**, 3812–3822 (2013)

62. R.-D. Sun, A. Nakajima, A. Fujishima, T. Watanabe, K. Hashimoto, Photoinduced surface wettability conversion of ZnO and TiO_2 thin films. J. Phys. Chem. B **105**, 1984–1990 (2001)
63. F.J. Sheini, D.S. Joag, M.A. More, Electrochemical synthesis of Sn doped ZnO nanowires on zinc foil and their field emission studies. Thin Solid Films **519**, 184–189 (2010)
64. A. Slassi, N. lakouari, Y. Ziat, Z. Zarhri, A. Fakhim Lamrani, E.K. Hlil, A. Benyoussef, Ab initio study on the electronic, optical and electrical properties of Ti-, Sn- and Zr-doped ZnO. Solid State Commun. **218**, 45–48 (2015)
65. S. Salam, M. Islam, A. Akram, Sol–gel synthesis of intrinsic and aluminum-doped zinc oxide thin films as transparent conducting oxides for thin film solar cells. Thin Solid Films **529**, 242–247 (2013)
66. A. Yildiz, S. Uzun, N. Serin, T. Serin, Influence of grain boundaries on the figure of merit of undoped and Al, In, Sn doped ZnO thin films for photovoltaic applications. Scr. Mater. **113**, 23–26 (2016)
67. V. Shelke, B.K. Sonawane, M.P. Bhole, D.S. Patil, Electrical and optical properties of transparent conducting tin doped ZnO thin films. J. Mater. Sci.: Mater. Electron. **23**, 451–456 (2012)
68. N.D. Md Sin, M.H. Mamat, M.F. Malek, M. Rusop, Fabrication of nanocubic ZnO/SnO2 film-based humidity sensor with high sensitivity by ultrasonic-assisted solution growth method at different Zn:Sn precursor ratios. Appl. Nanosci. **4**, 829–838 (2014)
69. N. Ye, J. Qi, Z. Qi, X. Zhang, Y. Yang, J. Liu, Y. Zhang, Improvement of the performance of dye-sensitized solar cells using Sn-doped ZnO nanoparticles. J. Power Sources **195**, 5806–5809 (2010)
70. C. Lai, X. Wang, Y. Zhao, H. Fong, Z. Zhu, Effects of humidity on the ultraviolet nanosensors of aligned electrospun ZnO nanofibers. RSC Adv. **3**, 6640–6645 (2013)
71. C.-L. Hsu, K.-C. Chen, T.-Y. Tsai, T.-J. Hsueh, Fabrication of gas sensor based on p-type ZnO nanoparticles and n-type ZnO nanowires. Sens. Actuator B-Chem. **182**, 190–196 (2013)
72. C.-L. Hsu, H.-H. Li, T.-J. Hsueh, Water- and humidity-enhanced UV detector by using p-type La-doped ZnO nanowires on flexible polyimide substrate. ACS Appl. Mater. Interfaces **5**, 11142–11151 (2013)
73. G.H. Zhang, P.Y. Wang, X.Y. Deng, Y. Chen, D.J. Gengzang, X.L. Wang, W.J. Chen, CTAB-assisted synthesis of 3D Sn doped ZnO nanostructures with enhanced acetone sensing performance. Mater. Lett. **162**, 265–268 (2016)
74. W. Zang, W. Wang, D. Zhu, L. Xing, X. Xue, Humidity-dependent piezoelectric output of Al-ZnO nanowire nanogenerator and its applications as a self-powered active humidity sensor. RSC Adv. **4**, 56211–56215 (2014)
75. S. Jagtap, K.R. Priolkar, Evaluation of ZnO nanoparticles and study of ZnO–TiO2 composites for lead free humidity sensors. Sens. Actuator B-Chem. **183**, 411–418 (2013)
76. P.M. Faia, J. Libardi, C.S. Louro, Effect of V_2O_5 doping on p- to n-conduction type transition of TiO_2:WO_3 composite humidity sensors. Sens. Actuator B-Chem. **222**, 952–964 (2016)

Mitochondrial miRNAs in Diabetes: Just the Tip of the Iceberg

Rohini Baradan[1, 2], John M. Hollander[3], and Samarjit Das[1, *]

[1]Department of Pathology, Johns Hopkins University, Baltimore, MD.
[2]School of Life Sciences, B.S. Abdur Rahman University, Tamilnadu, India.
[3]Division of Exercise Physiology, West Virginia University School of Medicine, Morgantown, WV.

Running Title: Mitochondrial miRNA in mitochondrial metabolism.

Word Count: 4634

*** Correspondence:** Samarjit Das, Ph.D.
Dept. of Pathology, Cardiovascular Division
Johns Hopkins University
Baltimore, MD 21205, USA
Tel: (410) 502-6921
Fax: (410) 502-5862
Email:sdas11@jhmi.edu

ABSTRACT

Over the last two decades mi(cro)RNAs have emerged as one of the key regulators of metabolic homeostasis. Most of the studies have highlighted that in the cytoplasm, miRNAs directly bind to the 3'-UTR (untranslated region) of a mRNA. Conventional RISC (RNA Inducing Silencing Complex) formation results in the post-transcriptional inhibition. This process is known to contribute to the development of metabolic diseases, including diabetes mellitus. Recent advancements with small RNA detection technologies have enabled us to identify miRNAs in the mitochondrial compartment of the cells. We have termed these miRNAs, which translocate into the mitochondria as mitochondrial miRNA, MitomiR. It has been demonstrated that MitomiRs can regulate gene expression, with some evidence even suggesting that after translocation, MitomiRs can bind to the 3'-end of a mitochondrial gene, altering its regulation. Our main focus in this review is to highlight the potential role of MitomiR in the pathogenesis of metabolic disorders such as diabetes mellitus.

Keywords: Mitochondria, Mitochondrial microRNA, MitomiR, Diabetes, Metabolism

INTRODUCTION

Diabetes mellitus, a metabolic disorder, is a condition in which either the insulin secretion of pancreatic β islet cells is impaired (Type-1), there is a defect in insulin action (Type 2), or a combination of the two (Kharroubi and Darwish 2015). Type 2 diabetes (T2D) is one of the most common causes of morbidity and disability (Villard et al. 2015), and it is influenced by environmental and genetic factors (Villard et al. 2015). T2D leads to vascular complications such as neuropathy, nephropathy, retinopathy [microvascular]; ischaemic heart disease and peripheral vasculopathy [macrovascular] (Villard et al. 2015). The number of affected patients with T2D complications is increasing at an alarming rate. Based on a recent American Diabetic Association's report, it was estimated that the economic burden diabetes poses is about $132 million in the United States alone (Cade 2008). It is estimated that the number of affected individuals will reach 592 million by the year 2035, with a global prevalence of 10.1% (Kharroubi and Darwish 2015).

A continuous relation exists between chronic hyperglycemia and the incidence and progression of vascular complications. These vascular complications lead to tissue and organ damage in approximately one-third to one-half of diabetic patients, and are a major cause of morbidity and mortality (Cade 2008). Some of the known molecular mechanisms that are involved in the etiology of micro- and macro-vascular complications include, advanced glycation end products (AGE), aberrant activation of protein kinase C (PKC), increased reactive oxygen species (ROS) production, and abnormal stimulation of hemodynamic regulation systems (Cade 2008; Fong et al. 2004). According to a recent report, adults with diabetes have an annual mortality of about 5.4% (double the rate for non-diabetic adults), and their life expectancy is decreased on average by 5-10 years (Donnelly et al. 2000). Even though the primary cause of death due to diabetes is cardiovascular defects, deaths from non-cardiovascular causes are also increased.

One of the most common microvascular complications of T2D is neuropathy. It has been estimated that about half of people with diabetes are affected by neuropathy (Cade 2008). The pathogenesis of diabetic neuropathy includes the symptoms of peripheral nerve dysfunction where all other causes of peripheral nerve dysfunction have been ruled out (Bansal et al. 2006). The molecular mechanism involves a decrease in angiogenic and neurotropic factors such as VEGF, IGFs, NGFs and angiopoietins with the progression of T2D. This condition alters the blood supply in the nerves and impairs neural function. This leads to changes in the nerve structure, ultimately resulting in neuropathy (Tahergorabi and Khazaei 2012).

Derangement of angiogenesis has also been identified as one of the factors contributing to vascular complications. Angiogenesis is a process in which new blood vessels arise from pre-existing ones. Neovascularization is achieved by maintaining a balance between the angiogenic (VEGF, FGF2, TGF-β) and anti-angiogenic factors (angiostatin, endostatin and thrombospondins) (Tahergorabi and Khazaei 2012). Angiogenesis in the eye due to diabetic retinopathy elevates reactive oxygen species (ROS) production, which directly or indirectly activates HIF-1α (hypoxia inducible factor-1α) (Tahergorabi and Khazaei 2012). ROS production coupled with activated HIF-1α signalling stimulates VEGF expression (Tahergorabi and Khazaei 2012). Diabetic retinopathy affects the peripheral retina, macula or both, eventually leading to blindness (Cade 2008). Diabetic retinopathy is one of the prime consequences of angiogenesis. Harris et al., (Harris 1993) has demonstrated that onset of diabetic retinopathy can begin seven years before a patient is even diagnosed with T2D. Each year, greater than 10,000 diabetic patients in the US develop blindness due to diabetic retinopathy, despite many medical advancements (Fong et al. 2004; Moore et al. 2009).

Diabetic nephropathy is characterized by the presence of albumin in urine (albuminuria), which is indicative of renal dysfunction (Cade 2008). Nephropathy leads to

end stage renal disease that requires dialysis and ultimately, a kidney transplant (Moore et al. 2009). "Proteinuria", also known as albuminuria or urine albumin, is a pathological condition where urine contains an abnormal amount of protein, mainly albumin. Proteinuria is a sign of chronic kidney disease (CKD), which can arise from chronic hyperglycemia. Approximately 15-40% patients with T1D, and 5-20% patients with T2D are affected by proteinuria (Chawla et al. 2016). It has been estimated that a quarter of patients with T2D develop microalbuminuria within 10 years of the diagnosis of diabetes (Adler et al. 2003). Unlike diabetic neuropathy, elevated angiogenesis is observed in diabetic nephropathy. It has been shown that the factors leading to enhanced angiogenesis are overexpression of VEGF, tumor growth factors (TGFs) and glomerular hypertension (Tahergorabi and Khazaei 2012).

The macrovascular complications like coronary artery disease, stroke and peripheral vascular disease contribute greatly to morbidity and mortality associated with diabetes (Moore et al. 2009). In 2013, cardiovascular disease due to diabetes accounted for 30.8% of deaths in the United States (Writing Group et al. 2016). The risk of developing stroke increases 2 to 5 fold in diabetic patients (Cade 2008). About 14% of peripheral artery disease prevalence is due to diabetes (Criqui and Aboyans 2015). In addition, several myocardial abnormalities such as cardiomyopathy, myocardial hypertrophy, fibrosis, and myofibril defects, result from hyperglycemia (Dhalla et al. 2014; Joshi et al. 2014). One of the major T2D-induced complications is diabetic cardiomyopathy. Diabetic cardiomyopathy, a major cause of mortality in T2D patients, may be defined as alterations in the structure and function of the left ventricular myocardium that is not directly attributable to coronary artery disease or hypertension (Boudina and Abel 2010). It has been described that there are several molecular factors contributing to the development of diabetic cardiomyopathy, which include hyperglycemia, lipotoxicity, ROS, mitochondrial dysfunction, impaired calcium metabolism,

renin angiotensin system (RAS) activation, altered substrate metabolism, and endothelial dysfunction (Joshi et al. 2014).

ROLE OF MITOCHONDRIA IN DIABETIC CARDIOMYOPATHY

Mitochondria, a cellular organelle, are the major site for energy production. Multiple energy pathways, such as the electron transport chain (ETC) which occurs in the inter membrane space of the mitochondria, and the Tricarboxylic acid cycle (TCA cycle) which occurs in the mitochondrial matrix, generate ATP as a source of energy (Steenbergen et al. 2009). In addition, parts of amino acid and nucleic acid metabolism also occur inside the mitochondria (Duncan 2011). It has been reported that T2D can affect mitochondrial function in various ways. Fatty acid and β-oxidation are the major sources of energy in the heart. The substrate choice (fatty acid or glucose) of a normal heart is usually dynamic and balanced, with approximately 70% of the energy obtained from fatty acid oxidation (FAO). Mitochondrial function in T2D-hearts has been altered due to changes in the rate of both FAO and glucose oxidation (GO) (Duncan 2011). Under diabetic conditions, FAO is the only source of energy for the heart. T2D impairs the ability of the heart to switch its substrate from glucose to fatty acid, which results in mitochondrial dysfunction (Duncan 2011). With T2D, targeting heart-mitochondria may lead to alterations in the rate of GO over FAO, which may ultimately lead to a therapeutic intervention in diabetic cardiomyopathy.

It has been demonstrated that hyperglycemic conditions induce cardiac mitochondrial swelling, reducing the number of cardiac-mitochondria (Joshi et al. 2014). Impaired cardiac insulin signalling leads to mitochondrial dysfunction (Boudina et al. 2009; Dhalla et al. 2014). Additionally, oxidative stress plays an important role in cardiac insulin signalling dysfunction during T2D stress (Boudina et al. 2009). Apart from hyperglycemia, an increase in free radical production can stimulate glucose oxidation, protein glycation, and subsequent

degradation of glycated proteins, which are involved in the pathogenesis of diabetic complications (Gillery et al. 1988; Hunt et al. 1990; Wolff and Dean 1987). Oxidative stress is one of the key regulators of sub-cellular abnormalities, including sarcoplasmic reticular and sarcolemmal functions (Dhalla et al. 1998). The excessive utilization of long-chain fatty acids for prolonged periods during the hyperglycemic condition results in the excessive production of free radicals. Thus, altered mitochondrial function can influence other sub-cellular organelles such as the sarcolemma, sarcoplasmic reticulum, and myofibrils in the progression of cardiac dysfunction.

In addition to oxidative stress, alterations in mitochondrial function with diabetic complications can lead to Ca^{2+}-handling abnormalities. Chronic diabetes has been associated with abnormalities in the sarcoplasmic reticular and sarcolemmal Ca^{2+}-transport processes (Dhalla et al. 1998; Dhalla et al. 2014; Machackova et al. 2005). Cardiac dysfunction in diabetes is associated with poor myofibrillar function due to inferior sarcoplasmic reticular and sarcolemmal Ca^{2+}-handling (Dhalla et al. 1998; Dhalla et al. 2014; Machackova et al. 2005). Long-term diabetes can lead to myofibrillar remodelling by altering the contractile and regulatory proteins in myofibrillar assembly. This alteration can be adaptive or maladaptive, based on the functional and metabolic demands of the heart (Machackova et al. 2005). On the basis of these observations, it is clear that mitochondria play an important role in the pathogenesis of cardiac dysfunction during the development of diabetic cardiomyopathy. Recently, it has been described that miRNAs can translocate into the mitochondrial compartment of cardiomyocytes, and play an important role in mitochondrial energy production by targeting mitochondrial genes (mito-mRNAs) or nuclear genes (mRNAs) in the mitochondrial matrix (Das et al. 2014; Das et al. 2012; Jagannathan et al. 2015; Srinivasan and Das 2015).

MITOCHONDRIAL miRNAs IN DIABETIC CARDIOMYOPATHY

miRNAs are a group of small, 19-25 nucleotides long, non-coding RNAs (Bartel 2004). These evolutionally conserved miRNAs have the ability to negatively regulate the expression of various genes by the degradation of target mRNA or by inhibiting the translational process (Bartel 2004). The biogenesis of a miRNA includes formation of a primary-miRNA transcript (pri-miRNA) from the nuclear genome. The pri-miRNA then gets digested by a RNA polymerase II, DROSHA/DGCR8, into a premature miRNA transcript (pre-miRNA), which is then translocated to the cytoplasm by exportin 5. Pre-miRNA in the cytoplasm then gets cleaved by another RNase III enzyme, DICER, into double-stranded mature miRNA (Srinivasan and Das 2015). In the cytoplasm, Ago2, an RNA binding protein, first binds to miRNA. This Ago2 bound miRNA transcript then finds the miRNA target mRNA (Kawamata and Tomari 2010). The Ago2 bound miRNA forms a ribonucleoprotein complex, the RNA induced silencing complex (RISC), by binding to the 3'-untranslated region (3'-UTR) of the mRNA. The RISC also includes other RNA binding proteins such as GW182, TRBP1, and TRBP2 (Srinivasan and Das 2015). The involvement of Dicer as one of the RISC components is still controversial (Gregory et al. 2005; Kawamata and Tomari 2010; Kim and Kim 2012; MacRae et al. 2008; Rivas et al. 2005). Usually, the formation of the RISC complex occurs in the cytoplasmic compartment of a cell; however, recent studies have shown that miRNAs are also found in mitochondrial (Barrey et al. 2011; Das et al. 2014; Das et al. 2012; Dasgupta et al. 2015; Jagannathan et al. 2015; Srinivasan and Das 2015; Zhang et al. 2014), nuclear (Hwang et al. 2007), and endoplasmic reticulum (ER) (Li et al. 2013; Montgomery and Ruvkun 2013) components of the cell.

Ago2 has been found to act as a carrier protein, transporting a miRNA such as miR-1 (Zhang et al. 2014) or miR-181c (Das et al. 2012), into the mitochondria after the miRNAs mature in the cytoplasm. In addition, Barrey et al. have suggested that both miRNAs and pre-

miRNAs are encoded within the mitochondrial genome (Barrey et al. 2011). However, the biogenesis of these mitochondrial genomic miRNAs is not known. Nevertheless, the functional aspects of these mitochondrial miRNAs are not well studied. Thus, in this article, we focus on the miRNAs which have been found in the mitochondrial compartment, and target either mitochondrial or nuclear genes, leading to an alteration of mitochondrial function during T2D. We term this subset of miRNAs as MitomiRs. MitomiRs can influence various metabolic pathways such as the TCA, electron transport chain, lipid metabolism, and amino acid metabolism. These mitochondrial metabolic pathways are actively involved in energy metabolism during T2D.

miRNA INFLUENCES THE TRICARBOXYLIC ACID CYCLE

The TCA cycle is a key metabolic pathway involved in glucose oxidation. It is a series of biochemical reactions that oxidizes acetyl co-A to release energy in the form of ATP. Glucose oxidation occurs in multiple steps, starting from glycolysis in the cytoplasm followed by pyruvate decarboxylation to acetyl co-A (An and Rodrigues 2006). Acetyl co-A, then enters into the TCA cycle. Since the TCA cycle is an indispensable process for GO, any alterations in the TCA cycle may lead to altered energy metabolism in the heart. Recently, miRNAs have been found to regulate the TCA cycle by targeting key enzymes in the pathway.

Pyruvate dehydrogenase (PDH) is an enzyme which links glycolysis to the TCA cycle by converting pyruvate into acetyl Co-A. It has been shown that miR-26a targets PDH subunit X (PDHX), a non-catalytic component of PDH (Chen et al. 2014). By targeting PDHX, miR-26a reduces PDH enzyme activity, leading to accumulation of pyruvate and decreased levels of acetyl-coA in the mitochondria (Chen et al. 2014).

Several miRNAs, such as miR-152, miR-148a, miR-148b, miR-299-5p, miR-19a-3p, miR-19b-3p, miR-122a, miR-421, and miR-494, target citrate synthase. By modulating the expression of citrate synthase, these miRNAs affect roughly 78 pathways that are involved in lipid, nucleotide, carbon, and amino acid metabolism (Tibiche et al. 2008).

Succinate co-A ligase GDP forming beta Subunit (SUCLG2) catalyses the conversion of succinate to succinyl co-A. In a study, miR-124 was found to downregulate the expression of SUCLG2 (Wang and Wang 2006).

miRNAS INFLUENCE THE ELECTRON TRANSPORT CHAIN

The electron transport chain (ETC) is a redox pathway carried out by ETC complexes; I, II, III, IV and V (ATP synthase), which is located in the inner membrane of the mitochondria. The ETC complexes I, III and IV generate a proton gradient by oxidizing NADH/NADPH. This proton gradient is then utilized by ATP synthase to produce ATP. Oxidative stress has been implicated in the etiology of diabetic cardiomyopathy. Mitochondrial ETC complexes I and III generate ROS as a by-product of their respiratory function. Generation of ROS has been found to have deleterious effects on mitochondria and eventually leads to mitochondrial dysfunction (Das et al. 2014; Das et al. 2012).

Iron-sulfur clusters (Fe-S) are essential cofactors for the transfer of electrons in oxidative phosphorylation (OXPHOS) (Tong and Rouault 2000). Thus, the function of Complex I and Complex IV is highly dependent on (Fe-S). The Fe-S assembly enzyme (ISCU) plays an important role in the synthesis of these Fe-S clusters (Tong and Rouault 2000). Under hypoxic conditions, it has been demonstrated that miR-210-5p can directly target the ISCU (Chan et al. 2009; Chen et al. 2010). Succinate dehydrogenase subunit D (SDHD), a subunit of Complex II, has been identified as a target of miR-210 (Puissegur et al. 2011). The authors have concluded that miR-210 can ultimately alter complex II activity

(Puissegur et al. 2011). COX10, another nuclear encoded subunit of complex IV has been reported as a target of miR-210-5p (Chen et al. 2010). Nuclear encoded, cytochrome c oxidase subunit IV (COXIV), one of the complex IV subunits, plays a vital role during the assembling process of complex IV and in its respiratory function (Li et al. 2006). *In vitro* studies on neuronal cells showed miR-338-5p alters complex IV activity by targeting the 3′-UTR of COXIV mRNA (Aschrafi et al. 2008).

Complex IV of the ETC has three subunits which are encoded in the mitochondrial genome - mt-COX1, mt-COX2, and mt-COX3. The remaining subunits; IV, Va, Vb, VIa, VIb, VIc, VIIa, VIIb, VIIc and VIII are encoded by the nuclear genome, and are translocated into the mitochondria after their maturation. In two independent studies, it has been shown that the mitochondrial genomic subunit of complex IV, mt-COX1, can be targeted by two different miRNAs, miR-181c (Das et al. 2014; Das et al. 2012), and miR-1 (Zhang et al. 2014). Mitochondrial transcripts are polycistronic in nature, and thus, the effects of miRNA binding to the 3'-UTR of mt-mRNA are still not fully understood. On the one hand, it has been shown that by binding to a miRNA, mt-mRNA expression is downregulated (Das et al. 2014; Das et al. 2012; Jagannathan et al. 2015). Conversely, it has been shown that miRNA acts as an activator of post-translational processes when it binds to a mitochondrial encoded-mRNA (Li et al. 2016; Zhang et al. 2014). Chronic overexpression of a miRNA that targets mitochondrial mRNA confirmed this observation (Das et al. 2014; Li et al. 2016).

Zheng et al. reported that miR-101-3p negatively regulates the expression of ATP synthase subunit β (ATP5B) (Zheng et al. 2011). In another study, miR-127-5p was also shown to target the 3'-UTR of the ATP5B transcript, and alters protein content (Willers et al. 2012). Additionally, miR-338-5p has been found to target ATP5G1, which ultimately augments ATP synthase activity (Aschrafi et al. 2008). Finally, miR-378 has been shown to target and bind to the mitochondrial transcriptome at the ATP6 locus, causing down-

regulation of the protein in the type 1 diabetic heart (Jagannathan et al. 2015). ATP6 is a subunit of the F0 complex of the ATP synthase, and its repression impacts ATP generating capacity.

EFFECT OF miRNA ON FATTY ACID METABOLISM

In the heart, energy in the form of ATP is obtained from various sources including fatty acids, glucose, lactate and ketone bodies (Rodrigues et al. 1998). The major source of energy is obtained by oxidation of fatty acids. During diabetes, FAO in the heart is augmented, and GO is reduced. This altered state leads to contractile dysfunction that initially begins with diastolic dysfunction, eventually developing into systolic dysfunction. This ultimately leads to diabetic cardiomyopathy (An and Rodrigues 2006). In several studies, miRNAs have been shown to target key components of the FAO pathway. A peroxisomal enzyme, Carnitine Octanoyl Transferase (CROT), allows short fatty acid chains to enter into the mitochondria by coupling them with carnitine. CPT1A converts acyl-CoA to acylcarnitine, thereby allowing fatty acids to enter the mitochondria where they are oxidized (Bonnefont et al. 2004). miR-33 has been found to target both CROT and CPT1A, which eventually affects fatty acid β oxidation (Gerin et al. 2010). miR-33a-5p and miR-33b-5p is encoded from the intronic region of SREBP2 (Bommer and MacDougald 2011), and SREBP1 (Xu et al. 2013) genes, respectively. By targeting important enzymes like CROT, CPT1A, and 3-Ketoacyl-CoA thiolase, the two miRNAs, miR-33a and miR-33b, affect fatty acid metabolism (Rottiers and Naar 2012). Interestingly, the complementary strand of miR-33a-5p is miR-33a-3p, which has been found to play an important role in FAO by targeting the same targets as miR-33a: CROT and CPT1A (Goedeke et al. 2013). In another study, miR-370 has been shown to reduce FAO by targeting the 3'-UTR of CPT1A transcript (Iliopoulos et al. 2010). Peroxisome proliferator activated receptor δ (PPARδ) plays an

important role in energy metabolism by switching the metabolism from FAO to glycolysis (Burkart et al. 2007). miR-199a-5p has been found to decrease the FAO by targeting PPARδ in both the heart and liver mitochondria (el Azzouzi et al. 2013). Azzouzi et al. (el Azzouzi et al. 2013) also concluded that by targeting PPARδ, miR-199a alters mitochondrial content and increases lipid deposition in the heart and liver cells. Another miRNA, miR-29a-3p, also has been found to target PPARδ and affects FAO (Kurtz et al. 2014). It has been demonstrated that in liver miR-122 affects lipid metabolism (Esau et al. 2006). The mRNA level of aldolase-A has been found to be reduced upon transfecting miR-122 in the hepatocellular carcinoma cell line, AML2 (Esau et al. 2006). Pantothenate kinase 1 (PANK) is an enzyme which is involved in the synthesis of coenzyme A (Leonardi and Jackowski 2007). Coenzyme A is a key cofactor involved in lipid metabolism. miR-107 and miR-103, located in the intronic sequence of the PANK1α gene, can influence lipid metabolism (Wilfred et al. 2007). miR-224-5p inhibits translation of acyl-CoA synthetase long chain family (ACSL4) (Wilfred et al. 2007). Acyl Co-A ester is an intermediate complex of lipid synthesis. ACSL4 regulates the synthesis of Acyl Co-A from free long chain fatty acids (Peng et al. 2013). Peng et al. (Peng et al. 2013) demonstrated that miR-224-5p alters FAO by regulating the mRNA of ACSL4.

ROLE OF miRNA IN AMINO ACID METABOLISM

Amino acid metabolism refers to the synthesis and breakdown of amino acids, and it mainly occurs within the mitochondria. Diabetic cardiomyopathy has been shown to alter amino acid metabolic pathways. The amino acid levels within the heart not only alters the energy stores of the heart, but also influences numerous contractile proteins that are essential for proper contractile function of the heart (Avogaro et al. 2004). Recently, multiple miRNAs have been implicated in the regulation of amino acid metabolism. For example, in a recent

study, miR-193b has been found to bind to the 3'-UTR of Serine Hydroxyl transferase (SHMT2) (Leivonen et al. 2011), which is responsible for converting serine to glycine. Glutaminase (GLS) is an enzyme that converts glutamine to glutamate by deamination. In human neuronal progenitor cells (NPCs), GLS was found to play an important role in cell proliferation and cell death (Wang et al. 2014). The lower stand component of the miR-23 family, miR-23a-3p and miR-23b-3p, have been found to inhibit GLS by binding to the 3'UTR of GLS (Gao et al. 2009). In another study, miR-29b was found to target the dihydrolipoyl branched chain acyltransferase (DBT). DBT is a component of branched chain α-ketoacid dehydrogenase (BCKD). BCKD plays an important role in the catabolism of branched chain amino acids leucine, isoleucine and valine (Mersey et al. 2005).

ROLE OF miRNA IN NUCLEOTIDE METABOLISM

The synthesis and the breakdown of nucleotides is referred to as nucleotide metabolism. Some parts of nucleotide metabolism occur inside the mitochondria, and it has been shown that various miRNAs can influence this process by regulating mRNAs in multiple nucleotide metabolism pathways (Desler et al. 2010). Three miRNAs, miR-149 (Wu et al. 2013), miR-125 (Stone et al. 2011), and miR-22 (Stone et al. 2011), have been found to target the Methylenetetrahydrofolate (MTHFR) transcript. By negatively regulating MTHFR, all three miRNAs have been shown to slow the process of the conversion of homocysteine to methionine. Mitochondrial dihydroorotate dehydrogenase enzyme (DHODH) is an enzyme that plays an important role in the de-novo pathway of pyrimidine biosynthesis (Rawls et al. 2000). Zhai et al. showed that miR-502 decreases both protein levels and mRNA expression of DHODH (Zhai et al. 2013). Thus, miR-502 negatively regulates nucleotide metabolism by attenuating pyrimidine biosynthesis (Zhai et al. 2013).

MITOCHONDRIAL TRANSPORT

The mitochondrial genome only has 37 genes, 13 of which are the major subunits of mitochondrial ETC complexes (Pearce et al. 2013). A major portion of the proteins responsible for proper mitochondrial functions are encoded within the nuclear genome. These proteins, after being translated, are imported into the mitochondria through translocases such as translocase of outer membrane (TOM) and translocase of inner membrane (TIM) (Neupert and Herrmann 2007). Mitochondrial transport of proteins is therefore essential for the proper functioning of the organelle. Impaired mitochondrial transport leads to cardiac mitochondrial dysfunction and eventually cardiomyopathy. By targeting the proteins responsible for transporting mitochondrial proteins, miRNAs are able to influence mitochondrial function. Slc25a3 is a mitochondrial phosphate carrier which carries inorganic phosphate from cytosol into the mitochondrial matrix. Slc25a3 supplies phosphate for the process of ATP synthesis by the ETC. In the myoblast cell line, HL-1, Slc25a3 has been found to be the target of miR-141 (Baseler et al. 2012). Consequently, overexpression of miR-141 can reduce ATP synthase. Baseler et al., demonstrated that in T1D, the expression of miR-141 goes up, influencing the ATP level in the heart (Baseler et al. 2012). It has been shown that in pancreatic β cells, miR-184 reduces insulin secretion by targeting Slc25a22 (Morita et al. 2013). Slc25a22 is a mitochondrial glutamate carrier. Consistent with the fact that glutamate can induce insulin secretion, repression of Slc25a22 by miR-184 resulted in a reduction in glucose-induced insulin secretion (Morita et al. 2013). Carnitine-acylcarnitine translocase (CACT) transports long-chain acyl carnitines into the mitochondria for GO. Two miRNAs, miR-212 and miR-132, can directly bind to the 3'-UTR of the CACT gene (Soni et al. 2014). By post-translational regulation of CACT, overexpression of both miR-212 and miR-132 can result in the accumulation of fatty acids in the cytoplasm and reduction in FAO (Soni et al. 2014). Arl2 is an interacting protein of adenine nucleotide transporter 1 (ANT1). Arl2 alters

adenine nucleotide transport by binding to the region on ANT1 called binder of Arl2 (BART) (Sharer et al. 2002). In another study by Nishi et al., it has been shown that the miR-15/16 cluster, miR-15b, miR-16, miR-195, and miR-424, target the 3'-UTR of Arl2 in the heart (Nishi et al. 2010). Furthermore, the authors described that overexpression of miR-15b results in decreased Arl2 protein and mRNA levels; resulting in reduced cellular ATP levels (Nishi et al. 2010). The role of the miR-15 family has been further evaluated in the context of multiple cardiac disorders, and the indispensable role of Arl2 has been highlighted in these studies (Hullinger et al. 2012; Porrello et al. 2011; Porrello et al. 2013).

CONCLUSIONS AND FUTURE DIRECTIONS

Multiple studies have clearly demonstrated the influence of miRNAs on numerous metabolic pathways, see table 1. A growing amount of evidence suggests a direct influence of miRNAs on the function of mitochondria. By targeting mitochondrial transcripts, miRNAs are able to influence various aspects of mitochondrial metabolism, resulting in the alteration of mitochondrial function. This alteration ultimately leads to mitochondrial dysfunction, which plays an important role in the development of diabetic cardiomyopathy. Targeting these miRNAs may lead to therapeutic options for patients with diabetic cardiomyopathy. The discovery of miRNAs in the mitochondrial compartment is possibly due to recent advancements in technologies. RNA-sequencing platforms are more sensitive. As methodologies improve, more and more researchers are attempting to isolate other subcellular fractions, such as sarcolemma and sarcoplasmic reticulum. Encouragingly, it has been shown that miRNAs can be found in the sarcoplasmic reticulum fraction of plant cells. More studies are necessary to explore the existence of miRNAs in various subcellular organelles. More importantly, the functional consequences of miRNAs isolated in these subcellular compartments needs to be well characterized.

As this field continues to expand, a number of pertinent questions are critical for understanding how miRNAs contribute to the regulation of mitochondrial proteins. In general, the continued identification of miRNAs that regulate mitochondrial proteins is of great interest. Further, identification of mechanisms and participants responsible for the import of miRNAs into the mitochondria as well as the cellular cues influencing their actions in extra-mitochondrial locales are of great interest. Finally, because the diabetic phenotype influences the cellular milieu, understanding whether these changes precipitate miRNA regulation of mitochondrial proteins as well as the impact to mitochondria located at different subcellular fractions is essential. The answers to these questions will facilitate the development of miRNA-based therapeutic options for the diabetic patient suffering from cardiac-related morbidities.

ACKNOWLEDGMENTS

This work was supported by a Scientist Development Grant from the American Heart Association 14SDG18890049 (S.D.). This work was supported by the National Institutes of Health from the National Heart, Lung and Blood Institute; R56 HL128485 (J.M.H.).

REFERENCES

Adler, A.I., Stevens, R.J., Manley, S.E., Bilous, R.W., Cull, C.A., Holman, R.R., and Ukpds, G. 2003. Development and progression of nephropathy in type 2 diabetes: the United Kingdom Prospective Diabetes Study (UKPDS 64). Kidney Int. **63**(1): 225-232. doi: 10.1046/j.1523-1755.2003.00712.x.

An, D., and Rodrigues, B. 2006. Role of changes in cardiac metabolism in development of diabetic cardiomyopathy. Am. J. Physiol. Heart Circ. Physiol. **291**(4): H1489-1506. doi: 10.1152/ajpheart.00278.2006.

Aschrafi, A., Schwechter, A.D., Mameza, M.G., Natera-Naranjo, O., Gioio, A.E., and Kaplan, B.B. 2008. MicroRNA-338 regulates local cytochrome c oxidase IV mRNA levels and oxidative phosphorylation in the axons of sympathetic neurons. J. Neurosci. **28**(47): 12581-12590. doi: 10.1523/JNEUROSCI.3338-08.2008.

Avogaro, A., Vigili de Kreutzenberg, S., Negut, C., Tiengo, A., and Scognamiglio, R. 2004. Diabetic cardiomyopathy: a metabolic perspective. Am. J. Cardiol. **93**(8A): 13A-16A. doi: 10.1016/j.amjcard.2003.11.003.

Bansal, V., Kalita, J., and Misra, U.K. 2006. Diabetic neuropathy. Postgrad. Med. J. **82**(964): 95-100. doi: 10.1136/pgmj.2005.036137.

Barrey, E., Saint-Auret, G., Bonnamy, B., Damas, D., Boyer, O., and Gidrol, X. 2011. Pre-microRNA and mature microRNA in human mitochondria. PLoS One, **6**(5): e20220. doi: 10.1371/journal.pone.0020220.

Bartel, D.P. 2004. MicroRNAs: genomics, biogenesis, mechanism, and function. Cell, **116**(2): 281-297.

Baseler, W.A., Thapa, D., Jagannathan, R., Dabkowski, E.R., Croston, T.L., and Hollander, J.M. 2012. miR-141 as a regulator of the mitochondrial phosphate carrier (Slc25a3) in the type 1 diabetic heart. Am. J. Physiol. Cell Physiol. **303**(12): C1244-1251. doi: 10.1152/ajpcell.00137.2012.

Bommer, G.T., and MacDougald, O.A. 2011. Regulation of lipid homeostasis by the bifunctional SREBF2-miR33a locus. Cell Metab. **13**(3): 241-247. doi: 10.1016/j.cmet.2011.02.004.

Bonnefont, J.P., Djouadi, F., Prip-Buus, C., Gobin, S., Munnich, A., and Bastin, J. 2004. Carnitine palmitoyltransferases 1 and 2: biochemical, molecular and medical aspects. Mol. Aspects Med. **25**(5-6): 495-520. doi: 10.1016/j.mam.2004.06.004.

Boudina, S., and Abel, E.D. 2010. Diabetic cardiomyopathy, causes and effects. Rev. Endocr. Metab. Disord. **11**(1): 31-39. doi: 10.1007/s11154-010-9131-7.

Boudina, S., Bugger, H., Sena, S., O'Neill, B.T., Zaha, V.G., Ilkun, O., Wright, J.J., Mazumder, P.K., Palfreyman, E., Tidwell, T.J., Theobald, H., Khalimonchuk, O., Wayment, B., Sheng, X., Rodnick, K.J., Centini, R., Chen, D., Litwin, S.E., Weimer, B.E., and Abel, E.D. 2009. Contribution of impaired myocardial insulin signaling to mitochondrial dysfunction and oxidative stress in the heart. Circulation, **119**(9): 1272-1283. doi: 10.1161/CIRCULATIONAHA.108.792101.

Burkart, E.M., Sambandam, N., Han, X., Gross, R.W., Courtois, M., Gierasch, C.M., Shoghi, K., Welch, M.J., and Kelly, D.P. 2007. Nuclear receptors PPARbeta/delta and PPARalpha direct distinct metabolic regulatory programs in the mouse heart. J. Clin. Invest. **117**(12): 3930-3939. doi: 10.1172/JCI32578.

Cade, W.T. 2008. Diabetes-related microvascular and macrovascular diseases in the physical therapy setting. Phys. Ther. **88**(11): 1322-1335. doi: 10.2522/ptj.20080008.

Chan, S.Y., Zhang, Y.Y., Hemann, C., Mahoney, C.E., Zweier, J.L., and Loscalzo, J. 2009. MicroRNA-210 controls mitochondrial metabolism during hypoxia by repressing the iron-sulfur cluster assembly proteins ISCU1/2. Cell Metab. **10**(4): 273-284. doi: 10.1016/j.cmet.2009.08.015.

Chawla, A., Chawla, R., and Jaggi, S. 2016. Microvasular and macrovascular complications in diabetes mellitus: Distinct or continuum? Indian J. Endocrinol. Metab. **20**(4): 546-551. doi: 10.4103/2230-8210.183480.

Chen, B., Liu, Y., Jin, X., Lu, W., Liu, J., Xia, Z., Yuan, Q., Zhao, X., Xu, N., and Liang, S. 2014. MicroRNA-26a regulates glucose metabolism by direct targeting PDHX in colorectal cancer cells. BMC Cancer, **14**: 443. doi: 10.1186/1471-2407-14-443.

Chen, Z., Li, Y., Zhang, H., Huang, P., and Luthra, R. 2010. Hypoxia-regulated microRNA-210 modulates mitochondrial function and decreases ISCU and COX10 expression. Oncogene, **29**(30): 4362-4368. doi: 10.1038/onc.2010.193.

Criqui, M.H., and Aboyans, V. 2015. Epidemiology of peripheral artery disease. Circ. Res. **116**(9): 1509-1526. doi: 10.1161/CIRCRESAHA.116.303849.

Das, S., Bedja, D., Campbell, N., Dunkerly, B., Chenna, V., Maitra, A., and Steenbergen, C. 2014. miR-181c regulates the mitochondrial genome, bioenergetics, and propensity for heart failure in vivo. PLoS One, **9**(5): e96820. doi: 10.1371/journal.pone.0096820.

Das, S., Ferlito, M., Kent, O.A., Fox-Talbot, K., Wang, R., Liu, D., Raghavachari, N., Yang, Y., Wheelan, S.J., Murphy, E., and Steenbergen, C. 2012. Nuclear miRNA regulates the mitochondrial genome in the heart. Circ. Res. **110**(12): 1596-1603. doi: 10.1161/CIRCRESAHA.112.267732.

Dasgupta, N., Peng, Y., Tan, Z., Ciraolo, G., Wang, D., and Li, R. 2015. miRNAs in mtDNA-less cell mitochondria. Cell Death Discov. **1**: 15004. doi: 10.1038/cddiscovery.2015.4.

Desler, C., Lykke, A., and Rasmussen, L.J. 2010. The effect of mitochondrial dysfunction on cytosolic nucleotide metabolism. J. Nucleic Acids, **2010**. doi: 10.4061/2010/701518.

Dhalla, N.S., Liu, X., Panagia, V., and Takeda, N. 1998. Subcellular remodeling and heart dysfunction in chronic diabetes. Cardiovasc. Res. **40**(2): 239-247.

Dhalla, N.S., Takeda, N., Rodriguez-Leyva, D., and Elimban, V. 2014. Mechanisms of subcellular remodeling in heart failure due to diabetes. Heart Fail. Rev. **19**(1): 87-99. doi: 10.1007/s10741-013-9385-8.

Donnelly, R., Emslie-Smith, A.M., Gardner, I.D., and Morris, A.D. 2000. ABC of arterial and venous disease: vascular complications of diabetes. BMJ **320**(7241): 1062-1066.

Duncan, J.G. 2011. Mitochondrial dysfunction in diabetic cardiomyopathy. Biochim. Biophys. Acta, **1813**(7): 1351-1359. doi: 10.1016/j.bbamcr.2011.01.014.

el Azzouzi, H., Leptidis, S., Dirkx, E., Hoeks, J., van Bree, B., Brand, K., McClellan, E.A., Poels, E., Sluimer, J.C., van den Hoogenhof, M.M., Armand, A.S., Yin, X., Langley, S., Bourajjaj, M., Olieslagers, S., Krishnan, J., Vooijs, M., Kurihara, H., Stubbs, A., Pinto, Y.M., Krek, W., Mayr, M., da Costa Martins, P.A., Schrauwen, P., and De Windt, L.J. 2013. The hypoxia-inducible microRNA cluster miR-199a approximately 214 targets myocardial PPARdelta and impairs mitochondrial fatty acid oxidation. Cell Metab. **18**(3): 341-354. doi: 10.1016/j.cmet.2013.08.009.

Esau, C., Davis, S., Murray, S.F., Yu, X.X., Pandey, S.K., Pear, M., Watts, L., Booten, S.L., Graham, M., McKay, R., Subramaniam, A., Propp, S., Lollo, B.A., Freier, S., Bennett, C.F., Bhanot, S., and Monia, B.P. 2006. miR-122 regulation of lipid metabolism revealed by in vivo antisense targeting. Cell Metab. **3**(2): 87-98. doi: 10.1016/j.cmet.2006.01.005.

Fong, D.S., Aiello, L.P., Ferris, F.L., 3rd, and Klein, R. 2004. Diabetic retinopathy. Diabetes Care, **27**(10): 2540-2553.

Gao, P., Tchernyshyov, I., Chang, T.C., Lee, Y.S., Kita, K., Ochi, T., Zeller, K.I., De Marzo, A.M., Van Eyk, J.E., Mendell, J.T., and Dang, C.V. 2009. c-Myc suppression of miR-23a/b enhances mitochondrial glutaminase expression and glutamine metabolism. Nature, **458**(7239): 762-765. doi: 10.1038/nature07823.

Gerin, I., Clerbaux, L.A., Haumont, O., Lanthier, N., Das, A.K., Burant, C.F., Leclercq, I.A., MacDougald, O.A., and Bommer, G.T. 2010. Expression of miR-33 from an SREBP2 intron inhibits cholesterol export and fatty acid oxidation. J. Biol. Chem. **285**(44): 33652-33661. doi: 10.1074/jbc.M110.152090.

Gillery, P., Monboisse, J.C., Maquart, F.X., and Borel, J.P. 1988. Glycation of proteins as a source of superoxide. Diabete Metab. **14**(1): 25-30.

Goedeke, L., Vales-Lara, F.M., Fenstermaker, M., Cirera-Salinas, D., Chamorro-Jorganes, A., Ramirez, C.M., Mattison, J.A., de Cabo, R., Suarez, Y., and Fernandez-Hernando, C. 2013. A regulatory role for microRNA 33* in controlling lipid metabolism gene expression. Mol. Cell. Biol. **33**(11): 2339-2352. doi: 10.1128/MCB.01714-12.

Gregory, R.I., Chendrimada, T.P., Cooch, N., and Shiekhattar, R. 2005. Human RISC couples microRNA biogenesis and posttranscriptional gene silencing. Cell, **123**(4): 631-640. doi: 10.1016/j.cell.2005.10.022.

Harris, M.I. 1993. Undiagnosed NIDDM: clinical and public health issues. Diabetes Care, **16**(4): 642-652.

Hullinger, T.G., Montgomery, R.L., Seto, A.G., Dickinson, B.A., Semus, H.M., Lynch, J.M., Dalby, C.M., Robinson, K., Stack, C., Latimer, P.A., Hare, J.M., Olson, E.N., and van Rooij, E. 2012. Inhibition of miR-15 protects against cardiac ischemic injury. Circ. Res. **110**(1): 71-81. doi: 10.1161/CIRCRESAHA.111.244442.

Hunt, J.V., Smith, C.C., and Wolff, S.P. 1990. Autoxidative glycosylation and possible involvement of peroxides and free radicals in LDL modification by glucose. Diabetes, **39**(11): 1420-1424.

Hwang, H.W., Wentzel, E.A., and Mendell, J.T. 2007. A hexanucleotide element directs microRNA nuclear import. Science, **315**(5808): 97-100. doi: 10.1126/science.1136235.

Iliopoulos, D., Drosatos, K., Hiyama, Y., Goldberg, I.J., and Zannis, V.I. 2010. MicroRNA-370 controls the expression of microRNA-122 and Cpt1alpha and affects lipid metabolism. J/ Lipid Res. **51**(6): 1513-1523. doi: 10.1194/jlr.M004812.

Jagannathan, R., Thapa, D., Nichols, C.E., Shepherd, D.L., Stricker, J.C., Croston, T.L., Baseler, W.A., Lewis, S.E., Martinez, I., and Hollander, J.M. 2015. Translational Regulation of the Mitochondrial Genome Following Redistribution of Mitochondrial MicroRNA in the Diabetic Heart. Circ. Cardiovasc. Genet. **8**(6): 785-802. doi: 10.1161/CIRCGENETICS.115.001067.

Joshi, M., Kotha, S.R., Malireddy, S., Selvaraju, V., Satoskar, A.R., Palesty, A., McFadden, D.W., Parinandi, N.L., and Maulik, N. 2014. Conundrum of pathogenesis of diabetic cardiomyopathy: role of vascular endothelial dysfunction, reactive oxygen species, and mitochondria. Mol. Cell. Biochem. **386**(1-2): 233-249. doi: 10.1007/s11010-013-1861-x.

Kawamata, T., and Tomari, Y. 2010. Making RISC. Trends Biochem. Sci. **35**(7): 368-376. doi: 10.1016/j.tibs.2010.03.009.

Kharroubi, A.T., and Darwish, H.M. 2015. Diabetes mellitus: The epidemic of the century. World J. Diabetes, **6**(6): 850-867. doi: 10.4239/wjd.v6.i6.850.

Kim, Y., and Kim, V.N. 2012. MicroRNA factory: RISC assembly from precursor microRNAs. Mol. Cell, **46**(4): 384-386. doi: 10.1016/j.molcel.2012.05.012.

Kurtz, C.L., Peck, B.C., Fannin, E.E., Beysen, C., Miao, J., Landstreet, S.R., Ding, S., Turaga, V., Lund, P.K., Turner, S., Biddinger, S.B., Vickers, K.C., and Sethupathy, P. 2014. MicroRNA-29 fine-tunes the expression of key FOXA2-activated lipid metabolism genes and is dysregulated in animal models of insulin resistance and diabetes. Diabetes, **63**(9): 3141-3148. doi: 10.2337/db13-1015.

Leivonen, S.K., Rokka, A., Ostling, P., Kohonen, P., Corthals, G.L., Kallioniemi, O., and Perala, M. 2011. Identification of miR-193b targets in breast cancer cells and systems biological analysis of their functional impact. Mol. Cell. Proteomics, **10**(7): M110 005322. doi: 10.1074/mcp.M110.005322.

Leonardi, R., and Jackowski, S. 2007. Biosynthesis of Pantothenic Acid and Coenzyme A. EcoSal Plus, **2**(2). doi: 10.1128/ecosalplus.3.6.3.4.

Li, H., Zhang, X., Wang, F., Zhou, L., Yin, Z., Fan, J., Nie, X., Wang, P., Fu, X.D., Chen, C., and Wang, D.W. 2016. MicroRNA-21 Lowers Blood Pressure in Spontaneous Hypertensive Rats by Upregulating Mitochondrial Translation. Circulation, **134**(10): 734-751. doi: 10.1161/CIRCULATIONAHA.116.023926.

Li, S., Liu, L., Zhuang, X., Yu, Y., Liu, X., Cui, X., Ji, L., Pan, Z., Cao, X., Mo, B., Zhang, F., Raikhel, N., Jiang, L., and Chen, X. 2013. MicroRNAs inhibit the translation of target mRNAs on the endoplasmic reticulum in Arabidopsis. Cell, **153**(3): 562-574. doi: 10.1016/j.cell.2013.04.005.

Li, Y., Park, J.S., Deng, J.H., and Bai, Y. 2006. Cytochrome c oxidase subunit IV is essential for assembly and respiratory function of the enzyme complex. J. Bioenerg. Biomembr. **38**(5-6): 283-291. doi: 10.1007/s10863-006-9052-z.

Machackova, J., Barta, J., and Dhalla, N.S. 2005. Molecular defects in cardiac myofibrillar proteins due to thyroid hormone imbalance and diabetes. Can. J. Physiol. Pharmacol. **83**(12): 1071-1091. doi: 10.1139/y05-121.

MacRae, I.J., Ma, E., Zhou, M., Robinson, C.V., and Doudna, J.A. 2008. In vitro reconstitution of the human RISC-loading complex. Proc. Natl. Acad. Sci. U. S. A. **105**(2): 512-517. doi: 10.1073/pnas.0710869105.

Mersey, B.D., Jin, P., and Danner, D.J. 2005. Human microRNA (miR29b) expression controls the amount of branched chain alpha-ketoacid dehydrogenase complex in a cell. Hum. Mol. Genet. **14**(22): 3371-3377. doi: 10.1093/hmg/ddi368.

Montgomery, T.A., and Ruvkun, G. 2013. MicroRNAs visit the ER. Cell, **153**(3): 511-512. doi: 10.1016/j.cell.2013.04.014.

Moore, D.J., Gregory, J.M., Kumah-Crystal, Y.A., and Simmons, J.H. 2009. Mitigating micro-and macro-vascular complications of diabetes beginning in adolescence. Vasc. Health Risk Manag. **5**: 1015-1031.

Morita, S., Horii, T., Kimura, M., and Hatada, I. 2013. MiR-184 regulates insulin secretion through repression of Slc25a22. PeerJ, **1**: e162. doi: 10.7717/peerj.162.

Neupert, W., and Herrmann, J.M. 2007. Translocation of proteins into mitochondria. Annu. Rev. Biochem. **76**: 723-749. doi: 10.1146/annurev.biochem.76.052705.163409.

Nishi, H., Ono, K., Iwanaga, Y., Horie, T., Nagao, K., Takemura, G., Kinoshita, M., Kuwabara, Y., Mori, R.T., Hasegawa, K., Kita, T., and Kimura, T. 2010. MicroRNA-15b modulates cellular ATP levels and degenerates mitochondria via Arl2 in neonatal rat cardiac myocytes. J. Biol. Chem. **285**(7): 4920-4930. doi: 10.1074/jbc.M109.082610.

Pearce, S., Nezich, C.L., and Spinazzola, A. 2013. Mitochondrial diseases: translation matters. Mol. Cell. Neurosci. **55**: 1-12. doi: 10.1016/j.mcn.2012.08.013.

Peng, Y., Xiang, H., Chen, C., Zheng, R., Chai, J., Peng, J., and Jiang, S. 2013. MiR-224 impairs adipocyte early differentiation and regulates fatty acid metabolism. Int. J. Biochem. Cell Biol. **45**(8): 1585-1593. doi: 10.1016/j.biocel.2013.04.029.

Porrello, E.R., Johnson, B.A., Aurora, A.B., Simpson, E., Nam, Y.J., Matkovich, S.J., Dorn, G.W., 2nd, van Rooij, E., and Olson, E.N. 2011. MiR-15 family regulates postnatal mitotic arrest of cardiomyocytes. Circ. Res. **109**(6): 670-679. doi: 10.1161/CIRCRESAHA.111.248880.

Porrello, E.R., Mahmoud, A.I., Simpson, E., Johnson, B.A., Grinsfelder, D., Canseco, D., Mammen, P.P., Rothermel, B.A., Olson, E.N., and Sadek, H.A. 2013. Regulation of neonatal and adult mammalian heart regeneration by the miR-15 family. Proc. Natl. Acad. Sci. U. S. A. **110**(1): 187-192. doi: 10.1073/pnas.1208863110.

Puissegur, M.P., Mazure, N.M., Bertero, T., Pradelli, L., Grosso, S., Robbe-Sermesant, K., Maurin, T., Lebrigand, K., Cardinaud, B., Hofman, V., Fourre, S., Magnone, V., Ricci, J.E., Pouyssegur, J., Gounon, P., Hofman, P., Barbry, P., and Mari, B. 2011. miR-210 is overexpressed in late stages of lung cancer and mediates mitochondrial alterations associated with modulation of HIF-1 activity. Cell Death Differ. **18**(3): 465-478. doi: 10.1038/cdd.2010.119.

Rawls, J., Knecht, W., Diekert, K., Lill, R., and Loffler, M. 2000. Requirements for the mitochondrial import and localization of dihydroorotate dehydrogenase. Eur. J. Biochem. **267**(7): 2079-2087.

Rivas, F.V., Tolia, N.H., Song, J.J., Aragon, J.P., Liu, J., Hannon, G.J., and Joshua-Tor, L. 2005. Purified Argonaute2 and an siRNA form recombinant human RISC. Nat. Struct. Mol. Biol. **12**(4): 340-349. doi: 10.1038/nsmb918.

Rodrigues, B., Cam, M.C., and McNeill, J.H. 1998. Metabolic disturbances in diabetic cardiomyopathy. Mol. Cell. Biochem. **180**(1-2): 53-57.

Rottiers, V., and Naar, A.M. 2012. MicroRNAs in metabolism and metabolic disorders. Nat. Rev. Mol. Cell Biol. **13**(4): 239-250. doi: 10.1038/nrm3313.

Sharer, J.D., Shern, J.F., Van Valkenburgh, H., Wallace, D.C., and Kahn, R.A. 2002. ARL2 and BART enter mitochondria and bind the adenine nucleotide transporter. Mol. Biol. Cell, **13**(1): 71-83. doi: 10.1091/mbc.01-05-0245.

Soni, M.S., Rabaglia, M.E., Bhatnagar, S., Shang, J., Ilkayeva, O., Mynatt, R., Zhou, Y.P., Schadt, E.E., Thornberry, N.A., Muoio, D.M., Keller, M.P., and Attie, A.D. 2014. Downregulation of carnitine acyl-carnitine translocase by miRNAs 132 and 212 amplifies glucose-stimulated insulin secretion. Diabetes, **63**(11): 3805-3814. doi: 10.2337/db13-1677.

Srinivasan, H., and Das, S. 2015. Mitochondrial miRNA (MitomiR): a new player in cardiovascular health. Can. J. Physiol. Pharmacol. **93**(10): 855-861. doi: 10.1139/cjpp-2014-0500.

Steenbergen, C., Das, S., Su, J., Wong, R., and Murphy, E. 2009. Cardioprotection and altered mitochondrial adenine nucleotide transport. Basic Res. Cardiol. **104**(2): 149-156. doi: 10.1007/s00395-009-0002-x.

Stone, N., Pangilinan, F., Molloy, A.M., Shane, B., Scott, J.M., Ueland, P.M., Mills, J.L., Kirke, P.N., Sethupathy, P., and Brody, L.C. 2011. Bioinformatic and genetic association analysis of microRNA target sites in one-carbon metabolism genes. PLoS One, **6**(7): e21851. doi: 10.1371/journal.pone.0021851.

Tahergorabi, Z., and Khazaei, M. 2012. Imbalance of angiogenesis in diabetic complications: the mechanisms. Int. J. Prev. Med. **3**(12): 827-838.

Tong, W.H., and Rouault, T. 2000. Distinct iron-sulfur cluster assembly complexes exist in the cytosol and mitochondria of human cells. EMBO J. **19**(21): 5692-5700. doi: 10.1093/emboj/19.21.5692.

Villard, A., Marchand, L., Thivolet, C., and Rome, S. 2015. Diagnostic Value of Cell-free Circulating MicroRNAs for Obesity and Type 2 Diabetes: A Meta-analysis. J. Mol. Biomark. Diagn. **6**(6). doi: 10.4172/2155-9929.1000251.

Wang, X., and Wang, X. 2006. Systematic identification of microRNA functions by combining target prediction and expression profiling. Nucleic Acids Res. **34**(5): 1646-1652. doi: 10.1093/nar/gkl068.

Wang, Y., Huang, Y., Zhao, L., Li, Y., and Zheng, J. 2014. Glutaminase 1 is essential for the differentiation, proliferation, and survival of human neural progenitor cells. Stem Cells Dev. **23**(22): 2782-2790. doi: 10.1089/scd.2014.0022.

Wilfred, B.R., Wang, W.X., and Nelson, P.T. 2007. Energizing miRNA research: a review of the role of miRNAs in lipid metabolism, with a prediction that miR-103/107 regulates human metabolic pathways. Mol. Genet. Metab. **91**(3): 209-217. doi: 10.1016/j.ymgme.2007.03.011.

Willers, I.M., Martinez-Reyes, I., Martinez-Diez, M., and Cuezva, J.M. 2012. miR-127-5p targets the 3'UTR of human beta-F1-ATPase mRNA and inhibits its translation. Biochim. Biophys. Acta, **1817**(5): 838-848. doi: 10.1016/j.bbabio.2012.03.005.

Wolff, S.P., and Dean, R.T. 1987. Glucose autoxidation and protein modification. The potential role of 'autoxidative glycosylation' in diabetes. Biochem. J. **245**(1): 243-250.

Writing Group, M., Mozaffarian, D., Benjamin, E.J., Go, A.S., Arnett, D.K., Blaha, M.J., Cushman, M., Das, S.R., de Ferranti, S., Despres, J.P., Fullerton, H.J., Howard, V.J., Huffman, M.D., Isasi, C.R., Jimenez, M.C., Judd, S.E., Kissela, B.M., Lichtman, J.H., Lisabeth, L.D., Liu, S., Mackey, R.H., Magid, D.J., McGuire, D.K., Mohler, E.R., 3rd, Moy, C.S., Muntner, P., Mussolino, M.E., Nasir, K., Neumar, R.W., Nichol, G., Palaniappan, L., Pandey, D.K., Reeves, M.J., Rodriguez, C.J., Rosamond, W., Sorlie, P.D., Stein, J., Towfighi, A., Turan, T.N., Virani, S.S., Woo, D., Yeh, R.W., Turner, M.B., American Heart Association Statistics, C., and Stroke Statistics, S. 2016. Heart Disease and Stroke Statistics-2016 Update: A Report From the American Heart Association. Circulation, **133**(4): e38-360. doi: 10.1161/CIR.0000000000000350.

Wu, C., Gong, Y., Sun, A., Zhang, Y., Zhang, C., Zhang, W., Zhao, G., Zou, Y., and Ge, J. 2013. The human MTHFR rs4846049 polymorphism increases coronary heart disease risk through modifying miRNA binding. Nutr. Metab. Cardiovasc. Dis. **23**(7): 693-698. doi: 10.1016/j.numecd.2012.02.009.

Xu, X., So, J.S., Park, J.G., and Lee, A.H. 2013. Transcriptional control of hepatic lipid metabolism by SREBP and ChREBP. Semin. Liver Dis. **33**(4): 301-311. doi: 10.1055/s-0033-1358523.

Zhai, H., Song, B., Xu, X., Zhu, W., and Ju, J. 2013. Inhibition of autophagy and tumor growth in colon cancer by miR-502. Oncogene, **32**(12): 1570-1579. doi: 10.1038/onc.2012.167.

Zhang, X., Zuo, X., Yang, B., Li, Z., Xue, Y., Zhou, Y., Huang, J., Zhao, X., Zhou, J., Yan, Y., Zhang, H., Guo, P., Sun, H., Guo, L., Zhang, Y., and Fu, X.D. 2014. MicroRNA directly enhances mitochondrial translation during muscle differentiation. Cell, **158**(3): 607-619. doi: 10.1016/j.cell.2014.05.047.

Zheng, S.Q., Li, Y.X., Zhang, Y., Li, X., and Tang, H. 2011. MiR-101 regulates HSV-1 replication by targeting ATP5B. Antiviral Res. **89**(3): 219-226. doi: 10.1016/j.antiviral.2011.01.008.

Table 1: Influence of MitomiRs on Metabolic Pathways

Pathway	miRNA	Target	References
TCA	miR-26a	PDHX	(Chen et al. 2014)
	miR-152-3p	Citrate synthase	(Tibiche et al. 2008)
	miR-148a-3p	Citrate synthase	(Tibiche et al. 2008)
	miR-148b-3p		
	miR-299-5p		
	miR-19a-3p		
	miR-19b-3p		
	miR-122a		
	miR-421		
	miR-494-3p		
	miR-124	SUCLG2	(Wang and Wang 2006)
ETC	miR-210-5p	ISCU, SDHD, COX10	(Chan et al. 2009; Chen et al. 2010; Puissegur et al. 2011)
	miR-338-5p	COX IV, ATP5G1	(Aschrafi et al. 2008)
	miR-181c	COX 1	(Das et al. 2014; Das et al. 2012)
	miR-1	COX 1	(Zhang et al. 2014)
	miR-101-3p	ATP5β	(Zheng et al. 2011)
	miR-127-5p	ATP5β	(Willers et al. 2012)
	miR-378	ATP6	(Jagannathan et al. 2015)
Fatty Acid Metabolism	miR-33	CROT, CPT1A	(Gerin et al. 2010)
	miR-370	CPT1A	(Iliopoulos et al. 2010)
	miR-199a	PPARδ	(el Azzouzi et al. 2013)
	miR-29a-3p	PPARδ	(Kurtz et al. 2014)
	miR-122	Aldolase A	(Esau et al. 2006)
	miR-224-5p	ACSL4	(Peng et al. 2013)
	miR-193b	SHMT2	(Leivonen et al. 2011)
Amino acid metabolism	miR-23-3p	GLS	(Gao et al. 2009)
	miR-23b-3p	GLS, DBT	(Gao et al. 2009; Mersey et al. 2005)
	miR-29b	GLS, DBT	(Gao et al. 2009; Mersey et al. 2005)
	miR-149	MTHFR	(Wu et al. 2013)
Nucleotide metabolism	miR-125	MTHFR, DHODH	(Stone et al. 2011)
	miR-22	MTHFR, DHODH	(Stone et al. 2011; Zhai et al. 2013)
	miR-502		(Stone et al. 2011; Zhai et al. 2013)
	miR-141	Slc25a3	(Baseler et al. 2012)
Mitochondrial transport	miR-184	Slc25a22	(Morita et al. 2013)
	miR-132	CACT	(Soni et al. 2014)
	miR-212	CACT, Arl2	(Nishi et al. 2010; Soni et al. 2014)
	miR-15b	CACT, Arl2	(Nishi et al. 2010; Soni et al. 2014)
	miR-16		
	miR-195	Arl2	(Nishi et al. 2010)

SPER Publications and Solutions Pvt. Ltd.

Original Article

Novel anticancerous compounds from *Sargassum wightii: In silico* and *in vitro* approaches to test the antiproliferative efficacy

S. M. Fazeela Mahaboob Begum[1], S. Priya[1,2], Raji Sundararajan[3], S. Hemalatha[1]

[1]School of Life Sciences, B.S. Abdur Rahman University, Chennai, Tamil Nadu, India, [2]Xinovem, Golden Jubilee Biotech Park, Chennai, India, [3]School of Engineering Technology, Purdue University, West Lafayette, IN 47907, USA

Correspondence: S. Hemalatha, School of Life Sciences, B.S. Abdur Rahman University, Chennai, Tamil Nadu, India. E-mail: hemalatha.sls@bsauniv.ac.in

ABSTRACT

Non-small cell lung cancer (NSCLC) contributes to 80% of lung cancer death. The poor survival rate is contributed by the uncontrolled proliferation, evasion of apoptosis, ubiquitous expression of cell survival genes, and resistance to anticancer therapies. This prompts the search for novel and potent drugs for the effective treatment and management of NSCLC. Marine seaweeds are rich in novel bioactives widely employed in pharma, medical, cosmetic, and food industries. For the current study, the ethyl acetate extract of *Sargassum wightii* is utilized to test antiproliferative efficacy against the NSCLC cell line A549. From ethyl acetate extract, two compounds, namely, n-hexadecanoic acid and l-(+)-ascorbic acid 2,6 dihexadecanoate were identified by mass spectrometry analysis. These compounds interacted with the cell survival protein PI3K which is upregulated in most of human cancers. The *in silico* results demonstrated that the algal compounds interacted with the target PI3K with a C score of 5. The *in vitro* antiproliferative activity of the ethyl acetate extract was analyzed by MTT assay. The apoptotic hallmarks including fragmentation of nuclei and DNA were observed in treated cells. The real-time polymerase chain reaction analysis of gene encoding PI3K showed the downregulation of the gene. The current results suggest that the compounds of *S. wightii* have antiproliferative activity and can control lung cancer through induction of apoptosis.

Keywords: Non-small cell lung cancer, *Sargassum wightii,* antiproliferative property, n-hexadecanoic acid, l–(+)-ascorbic acid 2, 6 dihexadecanoate

Introduction

Lung cancer is the major cause of cancer mortality worldwide accounting for 1.5 million deaths in 2012.[1] It constitutes 13% of the newly diagnosed cancer cases in 2015.[2] Among the major two types of lung cancer, the non-small cell lung cancer (NSCLC) contributes to 80% of lung cancer deaths, which urges the need for novel therapies in the effective treatment and management of NSCLC.[3]

Access this article online	
Website: www.japer.in	**E-ISSN:** 2249-3379

How to cite this article: Begum SMFM, Priya S, Sundararajan R, Hemalatha S. Novel anticancerous compounds from *Sargassum wightii*: In silico and *in vitro* approaches to test the antiproliferative efficacy. J Adv Pharm Edu Res 2017;7(3):272-277.

Source of Support: Nil, **Conflict of Interest:** None declared.

Apoptosis or programed cell death maintains the balance between cell proliferation and cell death. Uncontrolled proliferation results in oncogenesis. In NSCLC cell lines, the deletion or inactivation of the tumor suppressor genes directly contributes to the uncontrolled proliferation and prolonged survival of cancer cells.[4] Hence, drugs that can inhibit uncontrolled proliferation and induce apoptosis may be effective in the management and treatment of cancer.

A number of FDA-approved anticancer drugs are derived from the sea, including cytarabine, eribulin mesylate, and trabectedin. This has triggered the pharmaceutical industries to focus on marine natural products, and many marine bioactives have entered into the pre-clinical and clinical trials.[5] Marine seaweeds are a rich source in novel bioactives, which are widely employed in pharma, medical, cosmetic, and food industries. The marine brown algae of genus *Sargassum* is reported to possess antithrombotic, antiplatelet, antiviral, and anticancer properties.[6-8] In the current study, the marine brown algae *Sargassum wightii* was extracted, and the phytoconstituents were analyzed for the antiproliferative efficacy against the NSCLC cell line

A549. The outcomes of the study showed that the algal bioactives inhibited cancer cell proliferation through the induction of apoptosis in A549 cells. The results thus suggested that the algal bioactives can be utilized for the development of novel anticancer agents in the treatment of NSCLC.

Materials and Methods

Collection and identification of marine algae

The marine brown algae *S. wightii* was collected from the Mandapam coast of Tamil Nadu, India. The algae were identified and authenticated by Dr. Saravanan, Scientist, CMFRI, Mandapam, Tamil Nadu, India. The algae were washed in water to remove debris, shade dried, powdered, and were used for further studies.

Extraction and characterization of the algal extract

The dried algal powder was subjected to sequential extraction.[9] The phytoconstituents analysis was carried out in the extracts for detection of alkaloids, flavonoids, saponins, tannins, glycosides, carbohydrates, proteins, fats, and oils.[10] The total polyphenol content was estimated.[11] Gallic acid was used as a standard. The experiment was done in triplicate and the data were recorded as mean ±standard deviation (SD). Based on the phytochemical analysis, the ethyl acetate extract (SEA) was subjected to Fourier-transform infrared (FTIR) analysis in JASCO spectrometer, and the spectra in the range 400–4000 cm^{-1} were recorded.[12] The SEA (5 mg) was filtered in 0.45 µm filter and subjected to high-performance liquid chromatography (HPLC) analysis in Shimadzu HPLC 9A fitted with LC 20AD binary gradient pump, SPD-M20A Diode array detector, and RF-fluorescence detector. The separation was carried out in Enable C18 G column of 250 × 4.6 mm fitted with a C-18 guard column using acetonitrile and water as the mobile phase in the ratio of 70:30. The flow rate was maintained as 1 ml/min. The injection volume was 20 µl. The total running time was 25 min. The retention time (RT) of the compounds in all extract was recorded.[13] The advanced mass spectroscopy (Shimadzu GC-MS QP2010 ultra) with direct injection port was used for the mass spectrometry analysis of SEA. The sample was directly sent to mass spectra using the direct injection port (200°C), and the emerging fragment ions were collected. The ion source was maintained at 200°C and interface at 250°C. The detector voltage was maintained at 0.7kV throughout the analysis. The probable structure based on the ion fragmentation pattern was derived from the National Institute of Standards and Technologies 14 library search.

Molecular docking analysis

The structures of the compound n-hexadecanoic acid (PubchemCID:985) and l-(+)- ascorbic acid 2,6 dihexadecanoate (PubchemCID:54686917) identified in SEA by MS analysis were obtained from PubChem database (www.ncbi.nlm.nih.gov/pubchem), and the X-ray crystal structures of the target receptor (PI3K) of humans were retrieved from protein data bank (http//www.rscb.org/pdb). The compounds for docking were prepared as per the ligand preparation program, and Dock suite program of the SYBYL- × 1.3 was utilized. The prepared ligands were docked with the target protein PI3k based on the induced fit docking protocol. The interaction of the algal compounds with the target was visualized in Pymol, a python-based visualization tool (www.Pymol.org).

In vitro cell viability assay

The human adenocarcinoma cell line (A549) procured from NCCS, Pune, India, was used to test the antiproliferative efficacy of SEA. The cells were cultured in Dulbecco's modified Eagle's Medium (HiMedia) supplemented with 10% fetal bovine serum (HiMedia) and 1% antibiotic cocktail (Himedia). The cells were seeded in 96-well plate (1.5×10^5 cells) and treated with different concentrations of SEA (1, 500, 1000, 1500, and 2000 µg/ml) for 24 h to analyze the cell viability and determine the inhibitory concentration (IC_{50}) by MTT assay.[14] A549 cells treated with 1500 µg/ml of SEA for 24 h were analyzed for the hallmarks of apoptosis by staining with DAPI and acridine orange and ethidium bromide (1:1) mixture under fluorescent microscope (Zeiss Axio). DNA was isolated from the SEA-treated and control cells by Trizol method (Takaraa) and separated by electrophoresis (1.5% Agarose) at 75V for 40 min (BioRad) and observed in ChemiDoc (Eppendorf). The control was represented by ethyl acetate-treated cells, and the experiment was performed in triplicate.

Analysis of PI3K by real-time polymerase chain reaction (PCR)

Total RNA was isolated from control and SEA-treated cells by trizol method, followed by cDNA synthesis using the high capacity cDNA reverse transcription kit (Applied Biosystem) as per manufacturer's instruction. The cDNA synthesized was used for real-time PCR analysis of cell survival gene (PI3K) using SYBR Green PCR master mix (Bio-Rad). The analysis was done in triplicate, the fold change in gene expression was calculated based on $2^{-\Delta\Delta ct}$, and the expression was normalized with the housekeeping gene β actin. The primers used are PIK3CA (F) TGCAAAGAATCAGAACAATGCC: PI3KCA (R) CACGGAGGCATTCTAAAGTCA. βActin (F) TAGAAGCCTCTTCATGGACAAC: β Actin (R) GTATCAGGCATGCAACACAAG.

Results and Discussion

The phytochemical analysis of *S. wightii* revealed the presence of flavonoids, tannins, glycosides, terpenoids, carbohydrates, fats, resins, and phytosterols in the ethyl acetate, ethanol and methanol extracts; however, terpenoids, saponins, carbohydrates, proteins, and resins were not detected in hexane and DCM extracts [Table 1]. The abundance of phytoconstituents in *S. wightii* ethyl acetate extract (SEA) may be attributed to the mid-polar nature of the solvent. In previous studies, the non-polar solvents such as benzene, chloroform, and petroleum ether were used for extracting *S. wightii*,[15] but extraction with ethyl acetate increased the concentration of the phytoconstituents than the non-polar solvents.

Table 1 shows the results of preliminary phytochemical analysis of *S. wightii* by sequential extraction method. The phytoconstituents were found in different concentration in each extract.

The quantification of polyphenols [Figure 1a] in the algal extracts showed the highest concentration (266.6 µg/100 mg) in SEA, followed by ethanol (215 µg/100 mg), DCM (159 µg/100 mg), methanol (148 µg/100 mg), and hexane (122 µg/100 mg) extracts. As SEA showed the highest concentration of polyphenols which has various biological properties, it was utilized for further studies. Polyphenols form the major group of natural antioxidants. The polyphenol phlorotannin in brown algae is found to confer protection from ultraviolet radiation. Further, polyphenols are reported to possess various therapeutic properties such as antibacterial, antiviral, anticancer, and antidiabetic activities.[16] The HPLC analysis [Figure 1b] showed the presence of five major compounds in the SEA with RT 16.742, 18.907, 19.989, 21.539, and 22.684 min, respectively. The results of FTIR analysis [Figure 1c and Table 2] enabled the identification of functional groups such as alcohol, alkenes, and aliphatics in the extract at varying concentration. The presence of these functional groups may account for the biological properties of *S. wightii*.

The FTIR analysis showed many peaks which represent the functional groups that are present in the ethyl acetate extract of *S. wightii*.

The mass chromatogram of SEA revealed the presence of two major compounds. Based on the ion pattern, the two components were identified, namely, n-hexadecanoic acid with the molecular formula $C_{16}H_{32}O_2$ and molecular weight 256.4 [Figure 2a] and l-(+)-ascorbic acid 2,6-dihexadecanoate with the molecular formula $C_{38}H_{68}O_8$ and molecular weight 652.9 [Figure 2b]. Based on the ion pattern and the mass of parent peak, the following structures are proposed [Figure 2c and d]. The presence of strong peak at 3272 cm^{-1} in FTIR correlates with the carboxylic groups in both these compounds, and further, the peaks at 1654 cm^{-1}, 1086^{-1}, and 1044^{-1} coincide with the C=C, C-O-C, and C-OH stretching in l-(+)-ascorbic acid 2,6-dihexadecanoate. Hence, the results of FTIR support the MS data and the proposed structures of both compounds. These results correlate well with the previous

Table 1: Preliminary phytochemical screening of crude extracts of *S. wightii*

Phytoconstituent	Hexane	DCM	Ethyl acetate	Ethanol	Methanol
Tannins	++	++	+++	++	+
Flavonoids	++	++	+++	++	+++
Terpenoids	-	-	+++	++	+++
Saponins	-	-	-	-	-
Glycosides	+	+	+++	+++	+++
Carbohydrates	-	-	++	+++	+++
Fats and oils	-	-	++	+++	+++
Resins	-	-	+++	++	+
Phytosterols	++	++	+++	++	+
Protein	-	-	++	+	+

+: Presence, ++ and +++: Abundance, -: Absence, *S. wightii: Sargassum wightii*

Table 2: FTIR spectra of *S. wightii* ethyl acetate extract

Absorbance (cm^{-1})	Functional groups	Compounds
3272	O-H stretching of carboxylic acid or enolic OH or alcohol	Polysaccharides/alcohols
2970.5	C-H stretching of CH3, CH2/N-H stretching	Aliphatic compounds
1654.2	C=C	Alkene
1086	C-O-C stretch	Starch polysaccharides
1044	C-OH stretch	Alcohol

S. wightii: Sargassum wightii, FTIR: Fourier-transform infrared

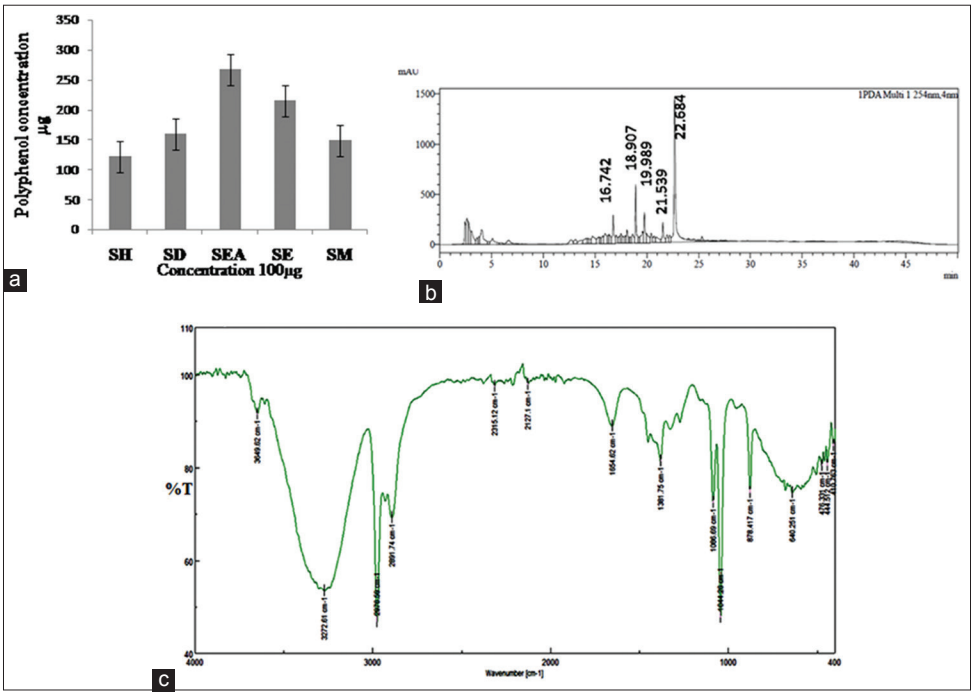

Figure 1: (a) Estimation of total phenolic content. The crude extracts of *Sargassum wightii* were analyzed for their total phenolic content. The ethyl acetate extract showed more polyphenol content than the other extracts, (b) high-performance liquid chromatography chromatogram of ethyl acetate extract, (c) Fourier-transform infrared spectra of ethyl acetate extract

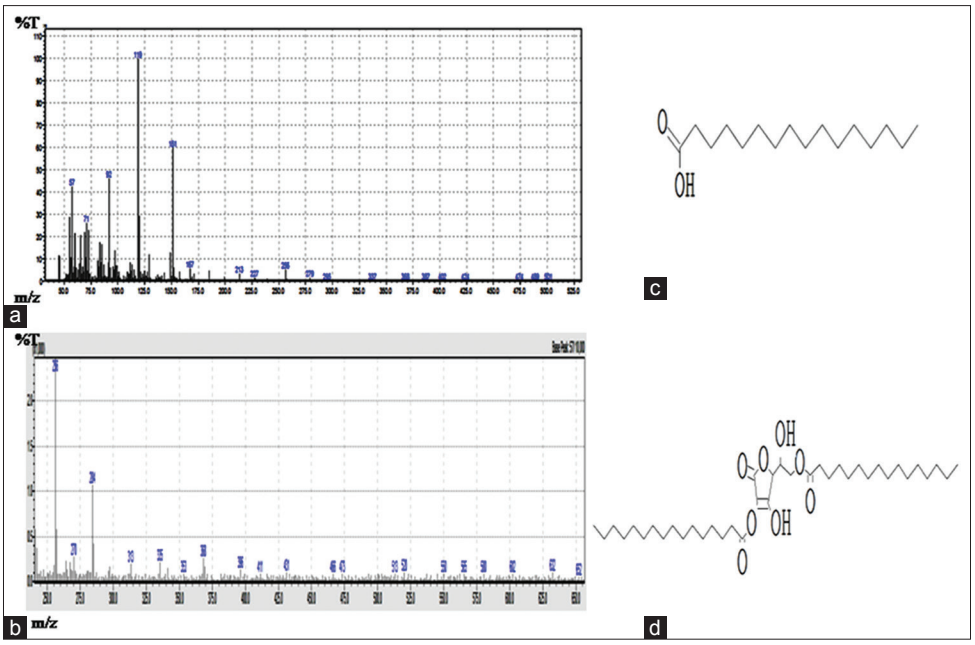

Figure 2: Mass spectrometry analysis of SEA. (a) Mass chromatogram of n-hexadecanoic acid, (b) mass chromatogram of l-(+)-ascorbic acid 2, 6 dihexadecanoate, (c) structure of n-hexadecanoic acid, (d) structure of l-(+)-ascorbic acid 2, 6 dihexadecanoate

studies of *S. wightii*.[12] These compounds were previously reported in macroalgae.[17]

However, this is the first study to report the occurrence of l-(+)-ascorbic acid 2, 6 dihexadecanoate in *S. wightii*. The compound n-hexadecanoic acid is used in the manufacture of artificial flavors and is reported to delay aerobic deterioration of silages.[18] Ascorbic acid is a natural hydrophilic antioxidant. The analogs of ascorbic acid formed by esterification and transesterification with fatty acids are shown to enhance the antioxidant, anti-inflammatory, and antitumor properties of ascorbic acid.[19] The presence of l-(+)-ascorbic acid 2, 6 dihexadecanoate in SEA which contains two hexadecanoates esterified with ascorbic acid may contribute to the enhanced antioxidant activity of *S. wightii*. l-(+)-ascorbic acid dihexadecanoate is reported to possess antibacterial,[20,21] antitumor,[22] and wound healing properties.[23]

The compounds identified by mass spectrometry were subjected to molecular docking study with the cell survival gene PI3K. The structure of the protein PI3K and SEA compounds identified by MS analysis are depicted in Figure 3. The interaction study revealed that n-hexadecanoic acid interacted with glutamate 563 of PI3K. Similarly, l-(+)-ascorbic acid 2, 6 dihexadecanoate interacted through threonine 560 and serine 535 of PI3K [Figure 3d and e]. Apart from these residues, the interaction was stabilized through many hydrophobic bonds. Table 3 shows the interacting residues and bond distance formed between the ligands and receptors. In one-third of human cancers, PI3K gene is aberrantly expressed which contributes to the uncontrolled proliferation and evasion of apoptosis in cancer cells.[24] The compounds interacted with the target protein with a consensus scoring (C score) of 5 which showed the specificity and stability of the interaction. As the algal compounds showed interaction with PI3K by *in silico*, *in vitro* studies were carried out in A549 cells.

Table 3: Interaction results of n-hexadecanoic acid and l-(+) - ascorbic acid 2, 6 dihexadecanoate with PI3K

Scores and residues	n-hexadecanoic acid with PI3K	-(+) - ascorbic acid 2, 6 dihexadecanoate with PI3K
Total score	54.3789	82.063
C score	5	5
Interacting residues and bond length	GLU563 3Å	THR 560 2.6Å SER 535 3.3Å

Table 3 shows the interaction results of n-hexadecanoic acid and l- (+)-ascorbic acid 2, 6, dihexadecanoate with PI3K. N-hexadecanoic acid interacted with glutamic acid in the receptor PI3K with a C score of 5. The bond distance was 3Å. The ligand l- (+)-ascorbic acid 2, 6, dihexadecanoate interacted with threonine 560 and serine 535 in PI3K with a C score of 5. The length of bond between the ligand and THR was 2.6Å and that of SER was 3.3Å.

The results of MTT assay [Figure 4a] showed the ability of SEA to induce cytotoxicity in A549 cells. The treatment with different concentrations of SEA showed an increase in the cytotoxicity with increasing concentration. The IC_{50} was determined as 1500 µg/ml. SEA inhibited the proliferation of A549 cells in a dose-dependent manner. The highest inhibition (77.84%) was observed at 2000 µg/ml.

The fluorescent microscopy analysis [Figure 4b] by DAPI staining detected the sublobe formation and fragmentation and blebbing of nuclei. To differentiate the live and apoptotic cells, acridine orange and ethidium bromide staining were carried out. The live cells showed green fluorescence with an unaltered morphology, whereas the early and late apoptotic cells showed orange fluorescence with rounding of the cells. The DAPI staining showed the induction of nuclear fragmentation in A549 cells treated with SEA, whereas the control

cells showed intact nuclei. The results of agarose electrophoresis [Figure 4c] showed the fragmentation of DNA isolated from SEA-treated cells, whereas the control cells showed intact DNA. The real-time expression of gene encoding PI3K [Figure 4d] showed the downregulation in SEA-treated cells. The electrophoretic separation of the real-time product showed the absence of DNA band in the treated group [Figure 4e] compared to the control. The antiproliferative activity of SEA may be due to the presence of the newly identified

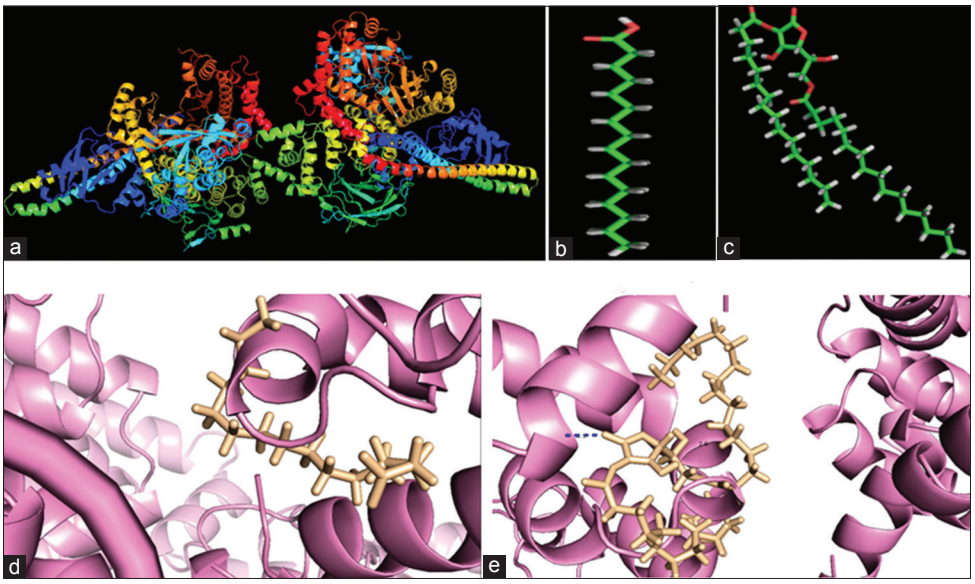

Figure 3: Molecular Docking analysis. (a) Structure of PI3K, (b) structure of n-hexadecanoic acid, (c) structure of l-(+)-ascorbic acid 2, 6 dihexadecanoate, (d) interaction of PI3K with n-hexanoic acid, (e) interaction of PI3K with l-(+)-ascorbic acid 2, 6 dihexadecanoate. The interaction studies were done using SYBL X 1.3

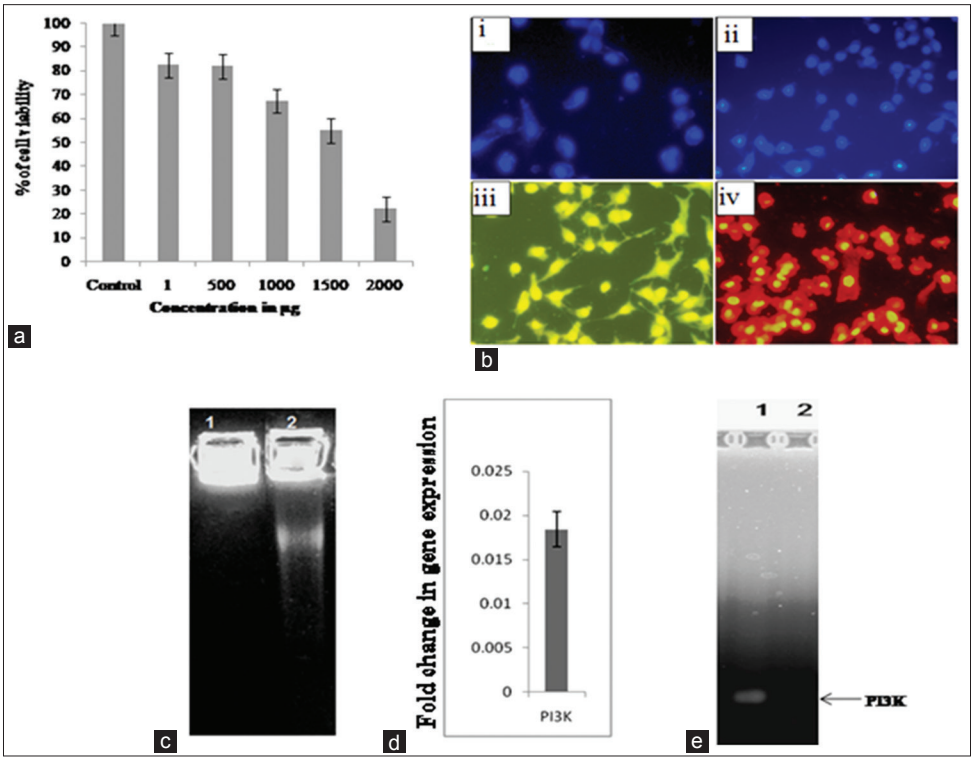

Figure 4: (a) Cytotoxic activity of SEA against A549 cells. The A549 cells were incubated with SEA at varying concentrations (1, 500, 1000, 1500, and 2000 µg/ml) for 24 h and the cytotoxicity was assessed by MTT assay. The IC50 was found as 1500 µg/ml. Control cells were treated with ethyl acetate. The data presented are mean±SD, (b) analysis of apoptosis by fluorescent microscopy. DAPI staining of control (i) and treated (ii) showing fragmented and lobbed nuclei. Acridine orange and ethidium bromide staining of control (iii) and treated (iv) showing live and apoptotic cells. The experiment was done in triplicate, (c) agarose gel electrophoresis showing intact DNA (lane 1) and fragmented DNA (lane 2), (d) fold change in PI3K gene expression in treated A549 cells, (e) agarose gel electrophoresis showing real-time polymerase chain reaction products

algal compounds l-(+)-ascorbic acid 2, 6 dihexadecanoate and n-hexadecanoate.

Conclusion

The inhibition of proliferation in cancer cells is an essential criterion for an anticancer drug. In the current study, SEA inhibited cell proliferation through the induction of apoptosis. This suggested that the algal bioactives possess anticancer activity which can be further studied for the development of effective anticancer drug in the management of NSCLC. The presence of polyphenols, flavonoids, and phytosterols and l-(+)-ascorbic acid dihexadecanoate in SEA may contribute to its antiproliferative nature. The identification of nuclear fragmentation, blebbing, and late apoptotic cells in SEA-treated cells by fluorescent microscopy confirmed the ability of SEA compounds to induce apoptosis. The real-time analysis of expression of gene PI3K showed that the inhibition of cell proliferation is mediated by the induction of apoptosis, through suppression of PI3K gene expression in the treated cells. The results of the *in vitro* study coincide with the *in silico* interaction study where the algal compounds showed good interaction with PI3K protein. As the outcomes of the current study highlight the downregulation of cell survival gene, the compounds in SEA may contribute to this effect. As marine natural products are gaining importance in the field of anticancer research, this study opens up a new avenue about marine algae which can be utilized effectively in the field of biomedical research.

References

1. Kumar R, Lu SK, Minchom A, Sharp A, Davidson M, Gunapala R, *et al.* A phase 1b trial of the combination of an all-oral regimen of capecitabine and erlotinib in advanced non-small cell lung cancer in Caucasian patients. Cancer Chemother Pharmacol 2016;77:375-83.
2. World Health Organization Cancer Mortality Database; 2015. Available from: http://www.Who.int/mediacenter/factsheets/fs/297/len. [last accessed on 2016 Oct 20].
3. American Cancer Society. Available from: http://www.cancer.org. [last accessed on 2016 Oct 22].
4. Perez-Ramirez C, Cañadas-Garre M, Jiménez-Varo E, Faus-Dáder MA, Calleja-Hernández MA. PTEN and PI3K/AKT in non-small-cell lung cancer. Pharmacogenomics J 2015;16:631-47.
5. Marine Pharmacology. Available from: http://www.marinepharmacology.midwestern.edu/clinPipeline.htm. [last accessed on 2016 Oct 22].
6. Jin W, Zhang W, Wang J, Yao J, Xie E, Liu D, *et al*. A study of neuroprotective and antioxidant activities of heteropolysaccharides from six *Sargassum* species. Int J Biol Macromol 2014;67:336-42.
7. Pathmanathan MK, Uthayarasa K, Jeyadevan JP, Jeyaseelan EC. *In vitro* antibacterial activity and phytochemical analysis of some selected medicinal plants. Int J Pharm Biol Arch 2010;1:291-9.
8. Harborne JB. Phytochemical methods. A Guide to Modern Techniques of Plant Analysis. 3rd ed. New York: Chapman and Hall; 1998. p. 1-150.
9. Singleton VL, Rossi JA. Colorimetry of total phenolics with phosphomolybdic-phosphotungstic acid reagents. Am J Enol Viticult 1965;16:144-58.
10. Kannan S. FT-IR and EDS analysis of the seaweeds *Sargassum wightii* (brown algae) and *Gracilaria corticata* (red algae). Int J Curr Microbiol App Sci 2014;3:341-51.
11. Gurav N, Kardani K, Solanki B, Patel B. Quantification of phenolic compound gallic acid in polyherbal ranger capsule by high performance chromatographic method. Int J Pharm Sci Res 2013;25:183-7.
12. Mosmann T. Rapid colorimetric assay for cellular growth and survival: Application to proliferation and cytotoxicity assays. J Immunol Methods 1983;65:55-63.
13. Marimuthu J, Essakimuthu P, Narayanan J, Anantham B, Tharmaraj RJ, Arumugam S. Phytochemical characterization of brown seaweed *Sargassum wightii*. Asian Pac J Trop Dis 2012;2:S109-13.
14. Machu L, Misurcova L, Ambrozova JV, Orsavova J, Mlcek J, Sochor J, *et al.* Phenolic content and antioxidant capacity in algal food products. Molecules 2015;20:1118-33.
15. Kumar P, Senthamilselvi S, Govindaraju M. GC-MS profiling and antibacterial activity of *Sargassum tenerrimum*. J Pharm Res 2012;6:88-92.
16. Al- saif S, Abdel Raouf N, El-Wazanani H and Aref I. Antibacterial substances from marine algae isolated from Jeddah coast of Red sea, Saudi Arabia. Saudi J BioSci 2014;21(1):57-64.
17. Kumar P, Selvi SS, Prabha AL, Kumar KP, Kumar RSG, Govindaraju M. Synthesis of silvernanoparticles from *Sargassum tenerrimum* and screening the phytochemicals for its antibacterial activity. Nano Biomed Eng 2012;4(1):12- 16.
18. Ohyama Y, Hara SI, Masaki S. The use of caproic acid to prevent aerobic deterioration of silages after opening, with special reference to the amounts and time of application. J Sci Food Agric 1977;28:369-74.
19. Mohamed R, Dharmappa KK, Tarannum S, Jameel NM, Kannum SA, Ashrafulla HS, *et al.* Chemical modification of ascorbic acid and evaluation of its lipophilic derivatives as inhibitors of secretory phospholipase A(2) with anti-inflammatory activity. Mol Cell Biochem 2010;345:69-76.
20. Arun K, Shrabani P, Pingalkumari S, Thirugnanasambandan S, Kathiresan K. Antibacterial and phytochemical assessment on various extracts of *Ipomoea pes-caprae* (l.) r. br through FTIR and GC-MS spectroscopic analysis. Asian J Pharm Clin Res 2104;7:134-8.
21. Soad M, El-Din M, El-Ahwany AM. Bioactivity and phytochemical constituents of marine red seaweeds (*Jania rubens*, *Corallina mediterranea* and *Pterocladia capillacea*). J Taibah Univ Sci 2016;10:471-84.
22. Botzki A, Rigden DJ, Braun S, Nukui M, Salmen S, Hoechstetter J, *et al.* L-Ascorbic acid 6-hexadecanoate, a potent hyaluronidase inhibitor. X-ray structure and molecular modeling of enzyme-inhibitor complexes. J Biol Chem 2004;279:45990-7.
23. Akinmoladun AC, Ibukun EO, Afor E, Akinsinlola BL, Onibon TR, Akinboboye AO, *et al*. Chemical constituents and antioxidant activity of Boonei Alstonia. Afr J Biotechnol 2007;6:1197.
24. Sun ZJ, Chen G, Hu X, Zhang W, Liu Y, Zhu LX, *et al.* Activation of PI3K/Akt/IKK-alpha/NF-kappaB signaling pathway is required for the apoptosis-evasion in human salivary adenoid cystic carcinoma: Its inhibition by quercetin. Apoptosis 2010;15:850-63.

NJC

Accepted Manuscript

ROYAL SOCIETY OF CHEMISTRY

rsc.li/njc

View Article Online
DOI: 10.1039/C7NJ04016D

Journal Name

ARTICLE

Hydrothermal synthesis, characterization and luminescence properties of $CaGd_2(MoO_4)_4$: Eu^{3+} ovoid like structures

Received 00th January 20xx,
Accepted 00th January 20xx

DOI: 10.1039/x0xx00000x

www.rsc.org/

Saravana Kumar Jaganathan,[a] Anthuvan John peter[b*], Venkatakrishnan Mahalingam[C] and Rajagopalan Krishnan[d]

Tetragonal phase $CaGd_2(MoO_4)_4$:Eu^{3+} with ovoid like hierarchical structures are prepared via employing ethylene diamine tetra acetic acid (EDTA) using hydrothermal route at 200°C for 24 h. X-ray diffraction patterns and Field emission scanning microscope images were used to characterize the crystal structure, phase, morphology and size of the nano samples. X-ray photo electron spectroscopy (XPS) and energy dispersive X-ray spectroscopy (Edax) confirmed the presence elements in phosphor samples. The PL properties of the phosphors were studied thoroughly. The photophysical properties of the samples were examined by Judd-Ofelt theory. The CIE coordinates of the prepared phosphor samples illustrate that red light emission can be realized from $CaGd_2(MoO_4)_4$: Eu^{3+} phosphor and it coexist very close to NTSC standard values. All these results show that ovoid like $CaGd_2(MoO_4)_4$: Eu^{3+} micro/nano phosphor is a promising material for display applications.

1. Introduction

Superior-controlled synthesis of self-aggregated three-dimensional (3D) hierarchical micro/nanostructures with uniform size distribution and structure is at a standstill demanding, and it is of much concern to the research community. Extremely homogeneous self-assembled three-dimensional (3D) micro/nanostructures have created a center of attention worldwide because of their prospective applications in high-performance display device, opto-electronics, biological, waste water treatment and photo catalyst applications derived from their novel electronic and optical properties.[1-4] The most suitable and promising approach to fabricate self-aggregated 3D architectures is to make use of a solution phase route which is a simple way to organize and influence the physical and chemical properties of materials.[5] In this regard, various shapes of 3D micro- and nano-structures have been synthesized and investigated through a number of wet chemistry-based techniques, including hydrothermal,[6] solvothermal,[7,8] microwave synthesis,[9] the Pechini process,[10,11] co-precipitation,[12] molten salt synthesis,[13] template-assisted methods.[14] Among these techniques, the hydrothermal method is a promising alternative technique for the large- area production of 3D hierarchical micro/nanostructures under feasible environments.[15] Recently, Lin et al prepared mono-disperse flower-like $NaY(MoO_4)_2$ architectures by hydrothermal route using polyvinylpyrrolidone (PVP) as the surfactant.[16] Li et al reported $NaLa(MoO_4)_2$ spindle- and flower-like architectures using the hydrothermal method.[17] Dumbbell-like orthorhombic $Gd_2(MoO_4)_3$:Eu^{3+} nanostructures[18] almond-like $(Na_{0.5}La_{0.5})MoO_4$, and bipyramid- like $(Na_{0.5}Gd_{0.5})MoO_4$ micro/- and nanostructures have all been demonstrated.[19] Zhang et al. synthesized pancake- like $Fe_2(MoO_4)_3$ microstructures by a rapid microwave- assisted hydrothermal method.[20] Huang et al reported 3D bowknot-like $Y_2(WO_4)_3$:Ln^{3+} hierarchical microstructures that were synthesized by a hydrothermal method.[21] Xu et al. successfully synthesized tetragonal $NaEu(MoO_4)_2$ with self-assembled rugby-like microstructures using a hydrothermal route.[22] Self-assembled flower-like $NaCe(MoO_4)_2$ architectures have been synthesized using a hydrothermal approach.[23] Chrysanthemum-flower like $Gd_2O(CO_3)_2.H_2O$ structures have been prepared by a modified urea-based homogeneous precipitation via a template free hydrothermal synthesis.[24] Among many parameters in hydro thermal process, the mixing of surfactants and reaction time parameters are key tools in regulating the formation of nuclei, the growth rate and oriented aggregation mechanism. The particle–particle interaction by steric effects is minimized by selecting suitable surfactant or chelating agent to afford a spacious class of nanostructures in the midst of proper size and structure by adsorbing the metal cations into the center and forming a complex molecule thereby greatly mobilizing the metal cations.[25]

[a] Department for Management of Science and Technology Development, Ton Duc Thang University, Ho Chi Minh City, Vietnam.
[a] Faculty of Applied Sciences, Ton Duc Thang University, Ho Chi Minh City, Vietnam.
[a]IJN-UTM Cardiovascular Engineering Center, Department of clinical sciences, Faculty of Biosciences and Medical Engineering, Universiti Teknologi Malaysia, Skudai 81300, Johor, Malaysia.
[b] Department of Physics, St. Anne's College of Engineering and Technology, Panruti, Tamilnadu, India.E-mail:quantajohn@gmail.com
[c] Department of Physics, B. S. Abdur Rahman University, Vandalur, Chennai, Tamilnadu, India.
[d] Department of Physics, Rajalakshmi Institute of Technology, Kuthambakkam Post, Chennai,Tamilnadu, India.

View Article Online
DOI: 10.1039/C7NJ04016D

To have a morphological modifications in the crystallographic surfaces of inorganic micro structures, many organic additives were utilized often. Among the many types of surface complex agents, ethylene diamine tetra acetic acid (EDTA) is the multidentate chelating ligand extensively studied as a capping agent. EDTA is a polydentate ligand that simultaneously forms more than one bond with the same metal atom/ion, and it complexes with numerous doubly, triply and quadruply charged cations. With this view, we chose EDTA as a selective chelating agent for the fabrication of micro/nanostructures.[26] Recently, Rare earth molybdates of scheelitetype tetragonal structure have been widely used as a good host material for luminescent rare earth elements due to their interesting physical and chemical properties and thus have technological application in the field of laser, fiber optics, and opto-electronics.[27-29] Scheelite type double molybdates with the general formula $MR(MoO_4)_2$ where M is the monovalent cation (Na^+ or K^+) and R is the trivalent rare earth ion (where R = La^{3+} or Gd^{3+} or Y^{3+}), have been synthesized by various techniques, sol–gel synthesis,[30] Pechini method,[31] etc. for up and down conversion luminescence applications. The compound $CaGd_2(MoO_4)_4$ (CGM) have a scheelite-type crystal structure in which Mo^{6+} populates the center of tetrahedral symmetry and Ca^+ and R^{3+} (La^{3+}, Gd^{3+}) populate the dodecahedral sites .[32-34] Liao et al prepared $CaLa_2(MoO_4)_4:Eu^{3+}$ phosphors with different doping concentrations by sol-gel method and investigated their luminescent properties in detail.[35]

Therefore, in this paper for the first time, we report on time dependent self assembly of ovoid like 3D architectures of (CGM):Eu^{3+} prepared by an EDTA-assisted hydrothermal route at 200^0C. By changing reaction parameters such as the reaction time and the molar ratio of EDTA, the 3D surface morphology of the particles were well controlled. In such a way that homogenous ovoid like micro structures were prepared. Their structural and luminescence properties were investigated using X-ray diffraction (XRD) pattern, FESEM and PL analysis. Photoluminescence properities of $CaGd_2(MoO_4)_4$ (CGM):xEu^{3+} of ovoid like nanostructured phosphors were studied in detail. All these results show that $CaGd_2(MoO_4)_4$ (CGM):Eu^{3+} micro structures found to be novel candidates for to produce high-quality luminescence devices.

2. Experimental details

2.1 Synthesis of $CaGd_2(MoO_4)_4:xEu^{3+}$ ovoid like structure

Appropriate stoichiometric amounts of $Ca(NO_3)_2$ (99 %,Sigma-Aldrich, USA), $Gd(NO_3)_3{\cdot}6H_2O$ (99 %, Sigma-Aldrich,USA), $Na_2MoO_4.2H_2O$ (99 %, Alfa Aesar, USA), $Eu(NO_3)_3{\cdot}6H_2O$ (99.9 %, Sigma-Aldrich, USA), NaOH (A.R.), EDTA (A.R.) and double distilled water were used to prepare $CaGd_2(MoO_4)_4:Eu^{3+}$, compounds. Initially ,the stoichiometric ratio of 1 mol of $Ca(NO_3)_2$, 1.96 mol of $Gd(NO_3)_3{\cdot}6H_2O$ and 0.06 mol of $Eu(NO_3)_3{\cdot}6H_2O$ were dissolved in double distilled water by vigorous stirring. On the other hand , 4 mol of Na_2MoO_4 was dissolved in 25 ml double distilled water by vigorous stirring. The rare earth nitrate solution was carefully added drop wise to the Na_2MoO_4 solution and a white colloidal precipitate was obtained. At the measure of 1.5 mM, EDTA was dissolved in 20 ml of double distilled water. It is added to the resultant colloidal solution. By adding NaOH solution, the pH value of the solution is maintained to a value of 7 to 8. Then, the solution is adjusted for 30 minutes. The resultant solution was transferred to 100 ml Teflon autoclave, sealed in a stainless steel vessel. The autoclave was maintained at 200^0C for 3-48 h. During the reaction the solution was stirred by a stainless steel stirrer with a rotational speed of 200 rpm. Then, the autoclave was allowed to cool to room temperature naturally. The final product was collected and washed with double distilled water and ethanol several times then dried at 60^0C in air for 4 hrs.[36]

2.2 Charcterization

X – ray powder diffraction (XRD) analysis was done using Pan Analytical X'pert pro x- ray diffractometer with Cu K-alpha radiation (λ = 1.5406 Å) at a scanning rate of 0.02^o per second. The XRD patterns were received in the range of $0^\circ \le 2\theta \le 70^\circ$ and were compared with the standard JCPDS data. The morphology and elemental composition of the product were investigated by field emission scanning electron microscope (FESEM JSM-7600F). X-ray photo electron spectroscopy (XPS) analysis was carried out using LAS-3000 surface analysis system (RIBER, France) with Al Kα X-rays (1489.6eV, width0.5eV).The measurements of PL and photoluminescence excitation (PLE) spectra were performed by a Jobin Yuvon Flurolog-3-11 Spectroflurometer at room temperature with 450W xenon lamp. All spectroscopic measurements of the phosphors were carried out at room temperature.

3. Results and discussion

3.1 Morphological evolution and the growth mechanism of oviod like $CaGd_2(MoO_4)_4:xEu^{3+}$ structures

The crystal structure and phase purity of the product were identified using powder XRD analysis. Fig. 1 shows the XRD pattern of the self-assembled ovoid like hierarchical structures of $CaGd_2(MoO_4)_4:xEu^{3+}$ obtained at different time intervals with 1mM of EDTA. All the diffraction peaks are in good agreement with the crystallographic data of $CaMoO_4$ (JCPDS-No. 29-0351). It is clearly seen from the XRD pattern that, well crystalline products of $CaGd_2(MoO_4)_4:xEu^{3+}$ were successfully prepared. No other impurity peaks related to starting materials were detected. The result implies that Eu^{3+} ions have been effectively doped into the host lattice without making considerable changes to the crystal structure of the host and thus also confirms that the crystalline nature of the material were not altered by employing host preparation for various reaction time interval.[37]

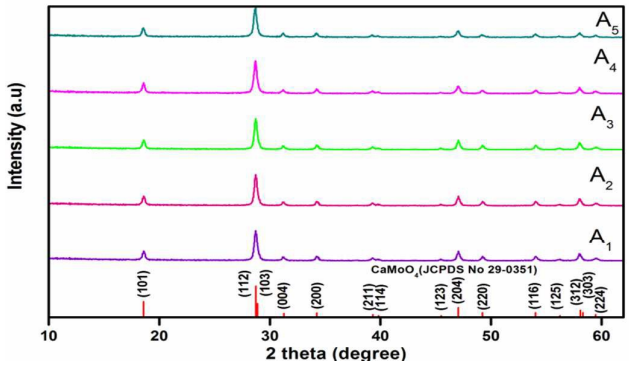

Fig.1 X-ray diffraction (XRD) pattern of the $CaGd_2(MoO_4)_4$: $0.06Eu^{3+}$ self assembled 3D hierarchical structures prepared with different time intervals, specifically 3h (A_1),5h (A_2),7h (A_3),12h (A_4),24h (A_5) using the hydrothermal method at 200^0c with fixed EDTA concentration (1 mM).

View Article Online
DOI: 10.1039/C7NJ04016D

Fig.2 exhibits the FESEM images of self aggregated 3D networks synthesized by hydrothermal method at various reaction time intervals (1.30h,3h,5h,7h,12h,24h and 36h) with fixed EDTA concentration (1 mM).It is observed that the dimension and morphology of the self assembled 3D networks of $CaGd_2(MoO_4)_4$: $0.06Eu^{3+}$ fully relates on the reaction time interval. From the literature, It is described that the origin for the growth of 3D hierarchical structures are initiating from it's constituents such as 0D nano particles,1D nano rods and 2 D nano sheets.

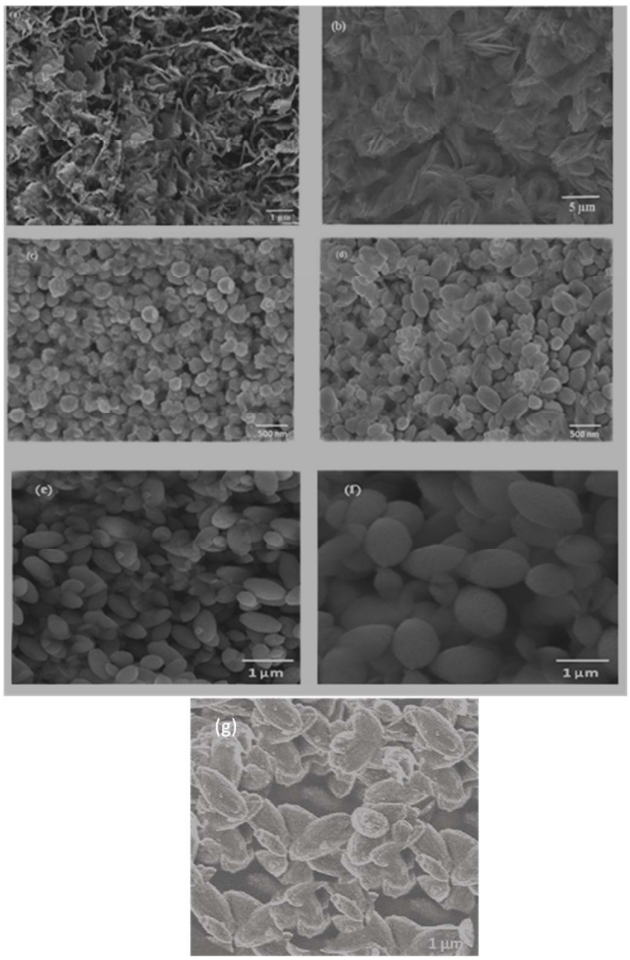

Fig.2 FESEM images of self aggregated 3D networks synthesized by hydrothermal method at various reaction time intervals i.e. (a) 1.30h, (b) 3h, (c) 5h, (d) 7h, (e) 12h, (f) 24h and (g) 36h and at 200°C

At the reaction time of 1.30h and 3h the SEM image (Fig .2(a&b)) exhibits 1D nano rods and 2D nanosheets with an average length of 150 nm and a thickness of few nm. It is monitored that if the reaction time consequently made greater than before to 5h and 7 h 2D nanosheets were began to form continuous manner through plane to plane combination and form sphere like morphology of an average diameter of 2.4 µm and then reach prolate sphere like structure with average diameter of 4.34 µm, respectively as shown in Figure 2(c&d).Particles with incomplete, inhomogenous ovoid like structures were seen once the reaction time is increased to 12h as shown in Figure 2(e).It indicates that the nanosheets fused further to form ovoid like structures. By increasing the reaction time to 24h,the improvement in the size distributions of the particles was observed with an average of 750 nm diameter thickness and 1.2µm length as shown in Figure. 2(f).It is well reported that the time dependent morphological formation of 3D networks are described as a process of dissolution- nucleation-Ostwald ripening. [38] In order to have a morphological modifications in the surfaces of the micro/nano particles various organic additives were employed recently. Herein, EDTA as one among the group of organic additives was used for the synthesis of $CaGd_2(MoO_4)_4:Eu^{3+}$ phosphors. The Influences of EDTA on the structural morphology of resultant powder is examined by adding different ratios EDTA. As the concentration of EDTA increases from 0.5mM to 2.0 mM in steps of 0.5mM at by maintaining other parameters constant, the particle sizes of the 3D networks gets reduced and thus due to increasing nature of chelating ability of surface capping agent EDTA as the concentration of EDTA increases in the host as seen in Figure. 3(a, b &c). The optimal concentration of EDTA is observed as 1.0mM. If the concentration of EDTA increases more than 2mM large, irregular agglomerated structures were formed. It is confirmed the analysis that the amount of chelating agent EDTA play a vital role in the self assembly of the ovoid like micro structures in the present system. Enlightened by our experimental results and the previous reports, a possible growth mechanism of the ovoid like structures is intended. Dissolution, adsorption, insitu transformation in acidic and basic media and the effective collision rates are the straight forward four processes explicitly describes the formation of mechanism of uniform homogenous $CaGd_2(MoO_4)_4$: $0.06Eu^{3+}$ ovoid like 3D hierarchical structures.

First, the dissolution process can be mentioned as,

$$4Na_2MoO_4.2H_2O \longrightarrow 8Na^{+}+4MoO_4^{2-}+2H_2O \quad (1)$$

$$Ca(NO_3)_2 \longrightarrow Ca^{2+}+(2)NO_3^{-}{}_{(aq)} \quad (2)$$

$$1.94\ Gd(NO_3)_3{\cdot}6H_2O \longrightarrow (1.94)\ Gd^{3+}{}_{(aq)}+(5.82)NO_3^{-}{}_{(aq)}+11.64\ H_2O$$
$$0.06\ Eu(NO_3)_3{\cdot}6H_2O \longrightarrow (0.06)\ Eu^{3+}{}_{(aq)}+(0.06)NO_3^{-}{}_{(aq)}+0.36H_2O \quad (3)$$

And then,

$$8\ Na^{+}+4\ MoO_4^{2-}{}_{+}\ Ca^{2+}{}_{(aq)}+(1.94)\ Gd^{3+}{}_{(aq)}+(0.06)\ Eu^{3+}{}_{(aq)}+(5.82)NO_3^{-}{}_{(aq)}+(0.06)NO_3^{-}{}_{(aq)}+(2)NO_3^{-}{}_{(aq)} \xrightarrow{200^{0}c-24\ hrs} Ca\ Gd_{1.96}\ Eu_{0.06}\ (MoO_4)_4+8Nano_3 \quad (4)$$

The molar concentration of capping agent EDTA present in the solution reasonably develops the metal ion absorption ability. When a molar concentration of EDTA is added in the system, it exclusively attracts the metal cations Ca^{2+},Gd^{3+}/ Eu^{3+} from MoO_4^{2-} and forms intermediate complex structure.

The reaction between the metal cations and EDTA is described as follows,

$$Ca^{2+}+(1.94)\ Gd^{3+}{}_{+}(0.06)\ Eu^{3+}{}_{+}[H_2L]^{2-} \longrightarrow Ca\ Gd_{1.94}\ Eu_{0.06}\ L+2H^{+} \quad (5)$$

The pH value was adjusted to have 7-8 during synthesis process as the role of pH is discussed in our previous works. While metal ions coordinate with EDTA and thus greatly affects the reaction to be slow and transfer rate which intern facilitate the oriented growth and self assembly of the system. The Ca^{2+},Gd^{3+}/ Eu^{3+} ions gradually released from the intermediate EDTA complexes and have reaction with MoO_4^{2-} once reaction temperature is increased to 200°C.

View Article Online
DOI: 10.1039/C7NJ04016D

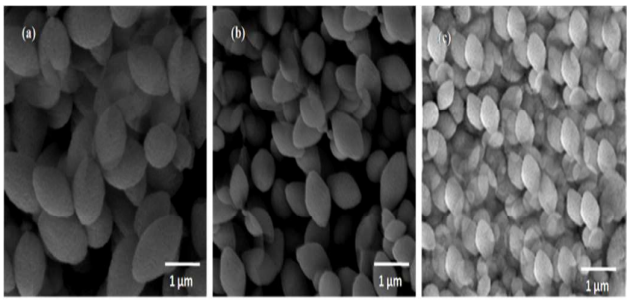

Fig. 3 FESEM images of ovoid like 3D hierarchical structures prepared with different molar concentration of EDTA i.e. (a) 0.5mM, (b) 1.0 mM and (c) 2.0 mM at 200^{0}C for 24h.

Fig. 4 shows representative XPS survey spectra of $CaGd_2(MoO_4)_4$: Eu^{3+} ovoid like 3D networks. Based on XPS analysis, It was confirmed that the presence of core levels of Ca,Gd,Mo,O and Eu were present in $CaGd_2(MoO_4)_4$: Eu^{3+} phosphors. In the range of 20–300 eV (Gd 5 s at 140 eV, Eu 5 s at 130 eV,Gd 4 s at 272 eV); 200–540 eV (Mo 3d5/2 at 228.5 eV, Mo $3d_{3/2}$ at 231 eV, Mo $3p_{3/2}$ at 394.5 eV, Mo $3p_{1/2}$ at 412 eV, Mo 3 s at 505.6 eV, O 1 s 531.5 eV, Ca $2p_{3/2}$ at 347 eV, Ca $2p_{1/2}$ at 352 eV,); and 750–1,150 eV (Gd $3d_{5/2}$ at 1,186 eV, Gd $3d_{3/2}$ at 1,219 eV, Eu $3d_{5/2}$ at1,126 eV, Eu $3d_{3/2}$ at 1,154 eV), respectively. It can be seen that the binding energy data (calibrated using C (1 s, 284.7 eV) as the reference) from $CaGd_2(MoO_4)_4$: Eu^{3+} self assembled 3D networks. All the peaks perfectly coincide with the literature.[39]

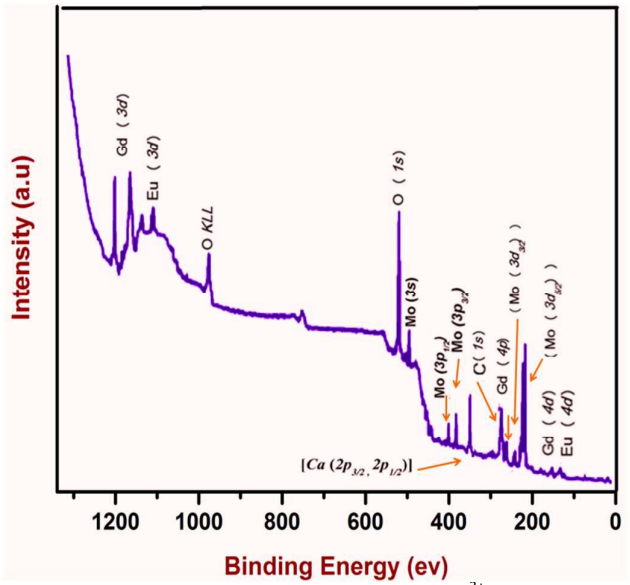

Fig. 4 XPS survey spectra of $CaGd_2(MoO_4)_4$: Eu^{3+} ovoid like 3D hierarchical structures at 200^{0}C for 24h with 1 mM of EDTA.

Figure 5 exhibits the energy dispersive X-ray spectroscopy patterns of the synthesized $CaGd_2(MoO_4)_4$: Eu^{3+} ovoid like 3D hierarchical structures. It indicates that $CaGd_2(MoO_4)_4$: Eu^{3+} phosphor is composed of Ca,Gd,Mo,O and Eu particles.

3.3 Photoluminescence behavior of $CaGd_2(MoO_4)_4$: Eu^{3+}

Figure 6 (a) depicts the room temperature PL excitation spectrum of the $CaGd_2(MoO_4)_4$: 0.06 Eu^{3+} phosphor in the emission wavelength of 615 nm.

The excitation spectrum exhibits two regions of an intense broad band and a series of sharp peaks. The broad band appears in the range from 230-350 nm and centered at 298 nm, assigned to the overlap of ligand to metal charge transfer transition (O - Mo and O- Eu^{3+}).[40] The sharp peaks at the wavelengths of 364 nm, 380 nm, 395 nm,416nm and 464 nm in the range of 350 – 500 nm are assigned to the characteristic intra-configurational f-f transitions ($^7F_0 \rightarrow {}^5D_4$, $^7F_0 \rightarrow {}^5G_3$, $^7F_0 \rightarrow {}^5L_6$, $^7F_0 \rightarrow {}^5D_3$ and $^7F_0 \rightarrow {}^5D_2$) of Eu^{3+} in the host.[41]

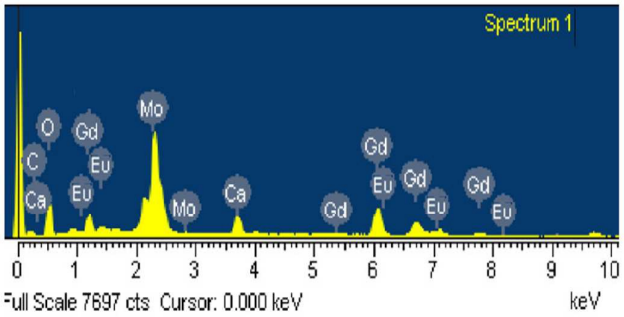

Fig. 5 Energy dispersive X-ray spectroscopy patterns of the synthesized $CaGd_2(MoO_4)_4$: Eu^{3+} ovoid like structures at 200^{0}C for 24h with 1 mM of EDTA

The room temperature PL emission spectra (λ_{exc}= 395 nm)of phosphors prepared at various intervals of time with 1mM of EDTA are shown in Fig. 6(b).

The emission spectra under the excitation wavelength of 395 nm for $CaGd_2(MoO_4)_4$: 0.06 Eu^{3+} exhibits a number of characteristic intra-configurational f-f transitions from 530 -710 nm, assigned to transitions of the excited Eu^{3+} ions from $^5D_0$ level to ^7F_J (J = 1, 2, 3, 4) levels of ground energy state. The intense emission peak is monitored at 615 nm and arises due to $^5D_0 \rightarrow {}^7F_2$ electric-dipole transition, which exhibits a parity-forbidden (ΔJ = 2) hypersensitive red emission and thus confirms that Eu^{3+} ions are located in the non inversion symmetry environment.[42]

The transition ($^5D_0 \rightarrow {}^7F_1$) at 590 nm due to magnetic dipole transition is fairly weak and shows an orange emission. The transitions at 656 nm ($^5D_0 \rightarrow {}^7F_3$) and 704 nm ($^5D_0 \rightarrow {}^7F_4$) are both relatively very weak. The PL emission intensity increases until the reaction time increases upto 24 h thus exhibits the crystallinity of phosphors improved as reaction time increases. A slight decrement in the PL intensity is observed at reaction time of 36 h (Fig 2(g)) thus the long time interval allows particles to get into disintegration.[43]

Figure. 6(c) exhibits the integrated areas of emission intensities due to $^5D_0 \rightarrow {}^7F_1$ at 590 nm (orange) and $^5D_0 \rightarrow {}^7F_2$ at 613 nm (red) as a function of the various reaction intervals.

Figure. 6(d) exhibits the ratio between red to orange emissions for different periods of reaction time. The maximum value of R/O ratio is 5.091 at the reaction time of 24h. It describes the nature of

View Article Online
DOI: 10.1039/C7NJ04016D

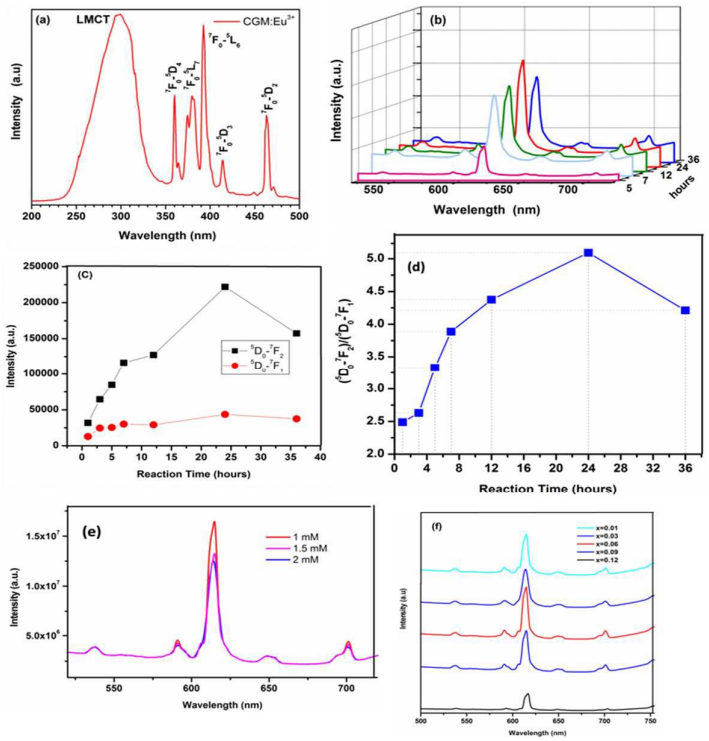

Fig. 6 (a) PL excitation spectrum of the $CaGd_2(MoO_4)_4$: 0.06 Eu^{3+} phosphor in the emission wavelength of 613 nm.
(b) The room temperature PL emission spectra (λ_{exc}= 395 nm)of phosphors prepared at various intervals of time with 1mM of EDTA.
(c) The integrated areas of emission intensities due to $^5D_0 \rightarrow {}^7F_1$ at 590 nm (orange) and $^5D_0 \rightarrow {}^7F_2$ at 613 nm (red) as a function of the various reaction times.
(d) Plot of R/O ratio versus various reaction time intervals.
(e) Emission spectra (λ_{exc}= 395 nm) of $CaGd_2(MoO_4)_4$: 0.06 Eu^{3+} phosphor prepared with different EDTA concentrations.
(f) Comparison of emission spectra of $CaGd_2(MoO_4)_4$: x Eu^{3+} phosphors for various doping concentrations of activators ((λ_{exc}= 395 nm) .

colour purity of the phosphor.[44] Figure. 6(e) illustrates emission spectra of $CaGd_2(MoO_4)_4$: 0.06 Eu^{3+} phosphor for different EDTA concentrations. It shows that characteristic red emission of phosphor decreases as the molar concentration of EDTA increases indicating that the surface area of the phosphor increases as their particle sizes gets decreased by increasing molar concentration of EDTA and thus leads to non radiative recombination of transitions and thus quenching phenomena is observed in the phosphor.[38]
As the Eu^{3+} ions concentration increases the emission intensity of the CaGd2(MoO4)4: x Eu^{3+} phosphors increases and thus emission intensity decreases beyond 0.06 mol of Eu^{3+} ions due to concentration quenching phenomena[45] as exhibited in Fig. 6(f) and the PL behaviour of the sample is in coexistence with the values calculated for quantum efficiency of phosphors with various dopant concentrations. The quantum efficiency measured value increases as the dopant concentration increases upto 0.06 mol and decreases due to increase of non radiative energy transfer among Eu^{3+} ions.[46] The calculated quantum efficiency of phosphor with 0.06 mol is the highest with the value of 85% as shown in Table (1).

3.4 Judd–Ofelt theory and spectroscopic properties

The PL emission spectra were taken as source for finding the Judd-Ofelt (J-O) intensity parameters. The J-O intensity parameters, Ω_J (J=2,4) presents insights into the bonding and local structure in the neighborhood of rare earth metal ions. [47-49] The investigation derived from Judd-Ofelt for the PL emission spectra could be utilized for calculating the electric dipole radiative transition rates with parity-forbidden between the different rare earth ions energy levels.The integrated emission intensities for the radiative emission transition between two different transitions $^5D_0$ and ^7F_J (J=2,4) were in relation to the radiative emission rates are given by,[38]

$$A_{0-J} = A_{0-1} \frac{I_{0-J}}{I_{0-1}} \frac{h\nu_{0-1}}{h\nu_{0-J}} \qquad (6)$$

Where I_{0-J} and $I_{0-1}$are integral intensities of $^5D_0$-^7F_J and $^5D_0$ – $^7F_1$ transitions and $h\nu_{0-1}$ and $h\nu_{0-J}$ are their corresponding energies,respectively. The rate of radiative emission due to magnetic dipole transition bears a value of 50 s^{-1}. [50] The radiative emission rates A_{0-J} could would be denoted as a function of the J–O intensity parameters as: [51]

$$A_{0-J} = \frac{64\,\pi^4 (\nu_{0-J})^3 e^2}{3hC^3} \frac{1}{4\pi\varepsilon_0} \chi \sum_{J=2,4} \Omega_J \left\langle\ 5D_0 \middle| U^{(J)} \middle| 7F_J \right\rangle^2 \qquad (7)$$

View Article Online
DOI: 10.1039/C7NJ04016D

Table 1: The Judd-Ofelt intensity parameters, radiative transition probability for $CaGd(MoO_4)_4$:x Eu^{3+} phosphors (x = 0.01,0.03,0.06,0.09 and 0.12)

Concentration of Eu^{3+} (moles)	J-O intensity parameters ($X10^{-20}$ cm^2)		Transitions	$A_{0\text{-}2,4}$ (s^{-1})	$A_{0\text{-}1}$ (s^{-1})	A_T (s^{-1})	A_{NR} (s^{-1})	β (%)	Quantum efficiency H (%)
	Ω_2	Ω_4							
0.01	5.70	5.56	$^5D_0$-$^7F_1$	-	50	744.00	454.78	5.72	62
			$^5D_0$-$^7F_2$	417.40	-			51.80	
			$^5D_0$-$^7F_4$	278.20	-			17.48	
0.03	10.20	9.18	$^5D_0$-$^7F_1$	-	50	996.80	324.00	4.04	75.5
			$^5D_0$-$^7F_2$	731.40	-			57.83	
			$^5D_0$-$^7F_4$	458.07	-			37.12	
0.06	7.71	6.54	$^5D_0$-$^7F_1$	-	50	1236.56	218.34	5.25	85
			$^5D_0$-$^7F_2$	554.20	-			58.41	
			$^5D_0$-$^7F_4$	344.11	-			37.34	
0.09	8.49	6.23	$^5D_0$-$^7F_1$	-	50	952.39	356.45	5.02	72.8
			$^5D_0$-$^7F_2$	610.23	-			62.33	
			$^5D_0$-$^7F_4$	337.26	-			34.65	
0.12	9.71	8.68	$^5D_0$-$^7F_1$	-	50	622.34	760.34	4.35	45
			$^5D_0$-$^7F_2$	656.30	-			57.81	
			$^5D_0$-$^7F_4$	445.56	-			35.84	

Using Eqs. (6) and (7). $\Omega_{2,4}$ values can be obtained. The calculated Judd-Ofelt parameters can be utilised to envisage radiative transition probability (A_{rad}) and lifetime (τ_{rad}) .[52]

unluckily, there is no systematic reports have been carried out in the literature in the evaluation of refractive index of $CaGd(MoO_4)_4$; however possessing the like structure of $CaMoO_4$, it is logical to make use of the refractive index $CaMoO_4$ (n=1.99) for added assessment of luminescence parameters.[53] The radiative transition probability (A_{rad}) could be obtained using the below equation as:[36]

$$A_{rad} = \sum_J A_{0-J} \qquad (8)$$

The radiative lifetime τ_{rad} for an excited state using A_{rad} , as given as:[42]

$$\tau_{rad} = \frac{1}{A_{rad}} \qquad (9)$$

The Judd-Ofelt intensity parameters, radiative transition probability for $CaGd(MoO_4)_4$:x Eu^{3+} phosphors are given in table1 for the prepared phosphor samples. In all the cases, $\Omega_2 > \Omega_4$ indicates that the hypersensitive electric dipole transition is pre-dominant. The luminescence quantum efficiency [54] is given by the relation,

$$\eta = \frac{A_T}{A_{T+A_{NR}}} \qquad (10)$$

The luminescence quantum efficiency (η) is presented in table 1.The luminescence quantum efficiencies values are satisfactory for all the concentrations. This indicates the suitability of the phosphor for the potential display applications.

3.5 Life time and CIE chromaticity measurements

Figure 7 exhibits the decay time profile of ovoid like structured $CaGd_2(MoO_4)_4$:xEu^{3+} (x= 0.01,0.03,0.06,0.09 and 0.12mol) phosphors prepared at 200°C for 24 h. The fluorescence life time in general is characterized as the time taken for the strongest emission intensity ($^5D_0 \rightarrow {}^7F_2$) of a peak to reduce to 1/e times than it's original emission intensity of that peak. It can be very well fitted by a single exponential function as [55]

$I(t) = I_o \exp(-t/\tau)$ (11)

Where I(t) is the luminescence intensity, t is the time after excitation, and τ is the decay constant.

It is observed that the decay time of $CaGd_2(MoO_4)_4$:xEu^{3+} phosphors exhibit approximately unchanged values for various dopant concentrations prepared at 200°C for 24 h as shown in table 2. It thus implies that the activators (Eu^{3+} ions) be positioned in the same coordination environment[56]. The fluorescence decay curve have similar behavior as the emission spectra (Fig 6(f)) thus confirms suitability of the phosphors for display applications.

Fig.8 exhibits the color chromaticity coordinates (x,y) for ovoid like phosphors. The CIE co-ordinates for $CaGd_2(MoO_4)_4$: x Eu^{3+} phosphors is found as given Table 2.These results may be important for the fabrication of red phosphors for lighting applications.

View Article Online
DOI: 10.1039/C7NJ04016D

Table 2: Luminescence lifetimes and CIE chromaticity coordinates (x,y) of $CaGd_2(MoO_4)_4:xEu^{3+}$ phosphors as a function of the concentration of Eu^{3+} ions.

Eu^{3+} concentrations (mol)	Life time (ms)	CIE chromaticity coordinates	
		x	y
0.01	0.312	0.601	0.364
0.03	0.378	0.617	0.352
0.06	0.436	0.626	0.328
0.09	0.382	0.620	0.338
0.12	0.341	0.618	0.342

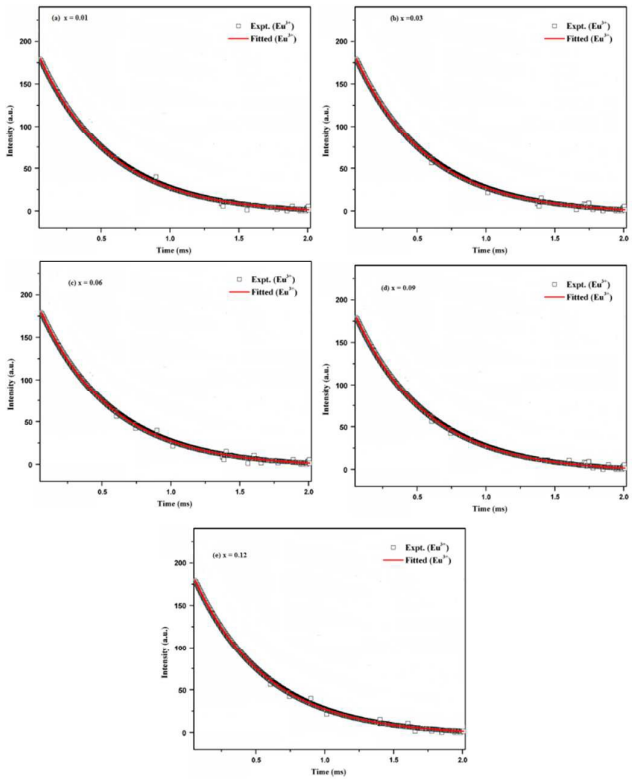

Figure 7 Fluorescent decay curve of $^5D_0 \rightarrow {}^7F_2$transitions in $CaGd_2(MoO_4)_4$: x Eu^{3+} phosphors.

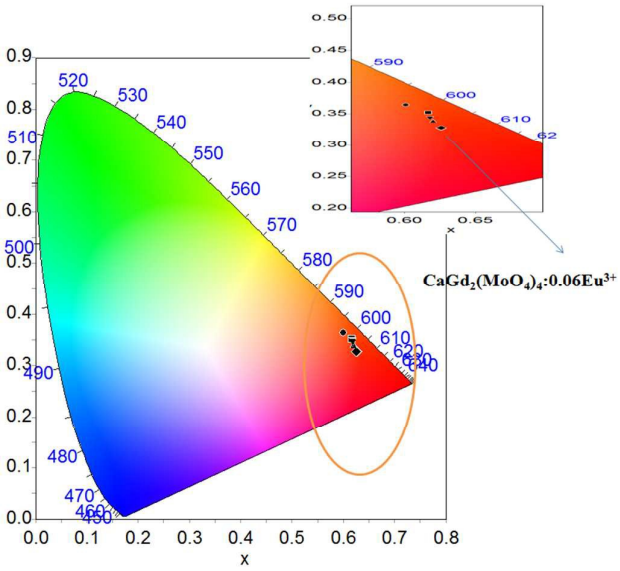

Figure 8 CIE (x, y) chromaticity diagram of $CaGd_2(MoO_4)_4$:x Eu^{3+} (x= 0.01,0.03,0.06,0.09 and 0.12mol) phosphor sample.

4. Conclusion

In summary,we have successfully synthesized oviod like rare-earth activated hierarchial structured phosphors using a EDTA-assisted hydrothermal method at 200°C for 24h. XRD patterns indicates the tetragonal distorted scheelite-type crystal structure of without any impurities. FESEM images show the uniform and homogenous ovoid like architectures for the synthesized powder phosphors at the concentration of 1mM of EDTA for 24h at 200°C. Further, the Photoluminescence properties of the self assembled 3D networks broadly studied. By the excitation at UV range, the $CaGd_2(MoO_4)_4$: 0.06 Eu^{3+} powder phosphor exhibits characteristic hypersensitive emissions in the red region. The photophysical parameters and luminescence quantum efficiency outcomes derived from the Judd–Ofelt theory description that the as-synthesised powder would provide as an efficient material for lighting and display applications.

References

1 H. Wang, Z. Yi, L. Rao, H. Liu and S. Zeng, *J. Mater. Chem. C,* 2013, **1**, 5520.
2 E. Wang, J. W. Y. Lam, R. Hu, C. Zhang, Y. S. Zhao and B. Z. Tang, *J. Mater. Chem. C*, 2014, **2**, 1801.
3 Q. Zhang, X. Wang and Y. Zhu, *J. Mater. Chem*., 2011, **21**, 12132.
4 Z. L. Fu, W. W. Xia, Q. S. Li, X. Y. Cui and W. H. Li, *CrystEngComm,* 2012, **14**, 4618.
5 X. Yu, Y. Shan, G. Li and K. Chen, *J. Mater. Chem*., 2011,**21**, 8104.
6 R. Krishnan and J. Thirumalai, *RSC Adv*., 2014, **4**, 64258.
7 J. Zhang, X. Wang, X. Zhang, X. Zhao, X. Liu and L. Peng, *Inorg. Chem. Commun*., 2011, **14**, 1723.

View Article Online
DOI: 10.1039/C7NJ04016D

8 T. D. Nguyen, C. T. Dinh, D. Nguyen and T. O. Do, *J. Phys.Chem. C*, 2009, **113**, 18584.
9 L. Zhang, X. F. Cao, Y. L. Ma, X. T. Chen, and Z. L. Xue, *New J. Chem*. 2010, **34**, 2027.
10 K. Zheng, Y. Liu, Z. Liu, Z. Chen and W. Qin, *Dalton Trans*., 2013, **42**, 5159.
11 Q. Chen, L. Qin, Z. Feng, R. GE, X. Zhao and H. Xu, *J. Rare Earths*, 2011, **29**, 843.
12 Y. Wang, L. Guo, Z. Zou, B. Wang, X. Guo, L. Han and W. Zeng, *J. Mater. Chem. C*, 2014, **2**, 2765.
13 M. Ding, C. Lu, L. Cao, W. Huang, Y. Nia and Z. Xu, *CrystEngComm,* 2013, **15**, 6015.
14 O. Ergen, D. J. Ruebusch, H. Fang, A. A. Rathore, R. Kapadia, Z. Fan, K. Takei, A. Jamshidi, M. Wu and A. Javey, *J. Am.Chem. Soc*., 2010, **132**, 13972.
15 V. Mahalingam, J. Thirumalai, R. Krishnan, and S. Mantha, *Spectrochim. Acta A*, 2016, **152**, 172.
16 H. Lin, X. Yan and X. Wang, *J. Solid State Chem*., 2013, **204**, 266.
17 G. Li, L. Li, M. Li, W. Bao, Y. Song, S. Gan, H. Zou, and X. Xu, *J. Alloy Compd*. 2013, **550**, 1.
18 J. Thirumalai, R. Krishnan, I. B. S. Banu, and R. Chandra-mohan, *J. Mater. Sci-Mater. El.* 2013, **24**, 253.
19 R. Krishnan, J. Thirumalai, S. Thomas, and M. Gowri, *J. Alloy Compd*., 2014, **604**, 20.
20 L. Zhang, X. F. Cao, Y. L. Ma, X. T. Chen, and Z. L. Xue, *New J. Chem*., 2010, **34**, 2027.
21 S. Huang, X. Zhang, L. Wang, L. Bai, J. Xu, C. Li and P. Yang, *Dalton Trans*., 2012, **41**, 5634.
22 L. Xu, X. Yang, Z. Zhai, X. Chao, Z. Zhang and W. Hou, *CrystEngComm*, 2011, **13**, 4921.
23 L. Xu, X. Yang, Z. Zhai, D. Gu, H. Pang and W. Hou, *CrystEngComm*, 2012, **14**, 7330.
24 G. S. R. Raju, E. Pavitra and J. S. Yu, *Dalton Trans*., 2013, **42**, 11400.
25 R. Krishnan and J. Thirumalai, *New J. Chem*., 2014, **38**, 3480.
26 R. Krishnan, J. Thirumalai, and A. Kathiravan, *Electron. Mater. Lett*., 2015, **11**, 24.
27 S. Dutta, S. Som, J. Priya, S.K. Sharma, *Solid State Sci*. 2013, **18**, 114–122.
28 A.M. Kaczmareka, R.V. Deun, *Chem. Soc. Rev*. 2013, **42**, 8835–8848.
29 Y. Wang, P. Yang, P. Ma, F. Qu, S. Gai, N. Niu, F. He, J. Lin, *J. Mater. Chem*. B, 2013, **1,** 2056–2065.
30 F. Cao, L. Liao-Shaa, Y. Tianb, X. Wu, *Opt. Laser Technol*. 2014, **55**, 6–10.
31 Q. Chen, L. Qin, Z. Feng, R. Ge, X. Zhao, H. Xu, *J. Rare Earths* .,2011, **29**, 843–848.
32 C.F. Guo, H.K. Yang, J.H. Jeong, *J. Lumin*. 2010, **130**, 1390.
33 V.V. Vakulyuk, A.A. Evdokimov, G.P. Khomchenko, *Russ. J. Inorg. Chem*. 1982, **27**, 1016.
34 M.M. Haque, D.K. Kim, *Mater. Lett.* 2009, **63**, 793.
35 J.Liao,D.zhou,B.Yang,R.Liu,Q.Zhang and Q.Zhou, *J.Lumin*. 2013,**134**, 533-538
36 V. Mahalingam and J.Thirumalai, *New J.Chem*., 2017,**41**,493.
37 V. Mahalingam, J. Thirumalai, R. Krishnan and R. Chandra mohan, *Electron. Mater. Lett*., 2016,**12**,32.
38 V. Mahalingam and J.Thirumalai, *RSC Adv*., 2016, **6**, 80390.
39 Hand-book of X-ray Photoelectron Spectroscopy, ed. J. Chastain, Perkin-Elmer Corporation, Eden Prairie, 1992.
40 A. J. Peter, I. B. Shameem Banu, *J. Mater Sci: Mater Electron*. 2015, **26**, 2045
41 A. J. Peter, I. B. Shameem Banu, *J. Mater Sci: Mater Electron*. 2014, **25**, 2771
42 A. Li, D. Xu, H. Lin, S. Yang, Y. Shao and Y. Zhang., *Scientific Reports,* 2016, **6**, 31366.
43 D. Xu, Y. Zhang, D. Zhang and S. Yang., *CrystEngComm,* 2015,**17**,1106.
44 Y. Zhou, B. Yan and X-H He., *J. Mater. Chem. C.* 2014, 2, 848.
45 V.Mahalingam,J.Thirumalai,R.KrishnanandS.Mantha, *Spectro chim. Acta,PartA*, 2016, **152**, 172–180.
46 S. K. Gupta, C. Reghukumar, R. M. Kadam., *RSC Adv.,* 2016,**6**, 53614.
47 B.R.Judd, *Phys. Rev.,* 1962, **127**, 750–761.
48 G.S.Ofelt, *J. Chem.Phys.,* 1962, **37**, 511–520.
49 M. P. Hehlen,M. G. Brikand, K. W. Kr¨amer, *J. Lumin*., 2013, **136**, 221–239.
50 L. Li,J. Zhang,W. Zi,S. Gan,G. Ji,H. Zouand,X. Xu, *Solid State Sci*., 2014, **29**, 58–65.
51 S. Som, S. Das, S. Dutta, H. G. Visser, M. K. Pandey, P. Kumar, R. K. Dubeynd S. K. Sharma, *RSC Adv.*, 2015, **5**, 70887–70898.
52 S. Dutta,S.SomandS.K.Sharma, *RSC Adv*., 2015, **5**, 7380– 7387.
53 W. L. Bond.,*Journal of Applied Physics*., 1965, **36**, 1674.
54 S. K. Gupta, M. Sahu, P. S. Ghosh, D. Tyagi, M. K. Saxena and R. M. Kadam, *Dalton Trans*., 2015, **44**, 18957–18969.
55 J. Zhang, L. Li, W. Zi,N. Guo, L. Zou,S. Ganand G. Ji, *J. Phys. Chem. Solid*., 2014, 75, 878.
56 A. Xie, X.M. Yuan, F. X. Wang, Y. Shi, J. Li, L. Liu, Z. F. Mu, *J. Alloys Compd.* 2010, **501**,124.

View Article Online
DOI: 10.1039/C7NJ04016D

Table of contents entry

Hydrothermal synthesis, characterization and luminescence properties of $CaGd_2(MoO_4)_4$: Eu^{3+} ovoid like structures

Saravana Kumar Jaganathan,[a] Anthuvan John peter[b*], Venkatakrishnan Mahalingam[C] and Rajagopalan Krishnan[d]

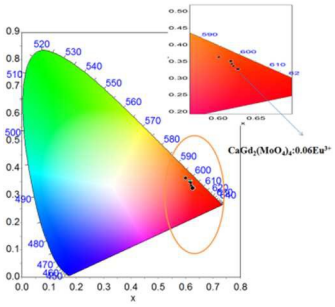

The red light emission color from $CaGd_2(MoO_4)_4$: 0.06 Eu^{3+} phosphor by EDTA assisted hydrothermal route at 200°C for 24 h.

ISSN: 2229-6956(ONLINE)
DOI: 10.21917/ijsc.2015.0141

BIG DATA VISUALISATION IN IMMERSIVE VIRTUAL REALITY ENVIRONMENTS: EMBODIED PHENOMENOLOGICAL PERSPECTIVES TO INTERACTION

Marko Teras[1] and Shriram Raghunathan[2]
[1]*School of Information Systems, Curtin University, Australia*
E-mail: marko.teras@postgrad.curtin.edu.au
[2]*School of Computer, Information and Mathematical Sciences, B. S. Abdur Rahman University, India*
E-mail: shriram@bsauniv.ac.in

Abstract

Ever-increasing human-computer interactions with various tracking technologies are creating unprecedented amounts of data. The amount and complexity of this 'big data' creates various challenges for its storage, analysis and presentation, but at the same time, big data is suggested to open up opportunities for those who can leverage it. This paper will discuss using immersive virtual reality environments for visualising, interacting and making sense of big data. It reveals that many of the developed applications do not justify their approaches to presentation or interaction. A phenomenological perspective of embodied perception and interaction is discussed to ground future developments.

Keywords:

Human-Computer Interaction, Software Development, Visualisation, Big Data, Immersive Virtual Environment, Phenomenology, Embodiment

1. INTRODUCTION

Several authors have proclaimed that the time of big data is upon us. More ubiquitous mobile devices and applications, social networks, faster Internet speeds, and increasing and free cloud storage generate a digital ecosystem that allow users to generate unprecedented amounts of data [13]. Various forms of sensors and other tracking technologies contribute to the data flux, creating a complex Internet of Things [2]. Everything from mouse clicks, uploaded images, written messages to geographical data are stored in ever-growing databases and waiting to be explored further.

Big data is suggested to provide better insights of human behaviour and the world in general, and to lead to better segmenting of users and decision-making in various sectors of life from business to education. Murdoch and Detsky (2013) proclaimed in the area of healthcare that information is one of the primary inputs of modern industries. Because of this, the application of big data is inevitable, and it has the power to change and improve an industry. In the education sector, data mining and student cognitive modelling has been proposed to predict students' undesired behaviour and performance, assist in better grouping, and in giving automated feedback to both students and instructors [27]. Big data has been argued to give a better overall picture of company's supply chain, and lead to better understanding of customers, new innovations [32], and supply chain optimisation [19]. Dumbill (2012) argued that big data and its potential analytical insights are transferring information systems from the periphery of organisational development to the fore of it. Contemporary organizations are an informational loop where customer interactions with products and services can be analysed and inform further development. Organisations that effectively employ big data managing and analysis methods are suggested to gain a competitive advantage.

Meanwhile, big data poses also practical challenges. How to store, manage, retrieve, analyse and present this fast, varied and ever-increasing amount of data [28]? How to do it faster when for example bandwidth or processing power might be limiting factors? Also the lack of experienced experts and well-established software creates a barrier for the efficient use. Questions in ethics and privacy have also been raised. Some fear big data might be misused to control people [7], or that the underlying assumptions of the usefulness of big data might actually be misleading [8]. Various human contexts have randomness in their interactions. Does it make sense to trust such seemingly imprecise environments? There is potential to draw wrong conclusions as much as right conclusions.

Also, what does it mean when product users become research objects, perhaps sometimes even against their own better judgment [26]? As customers' purchase and interact with various products and services, what are the ethical implications of selling and profiting from customer data? This raises a question of who has access to the data: researchers, private companies or even governments?

Some question the underlying assumptions and the promise of big data, including how it might reinforce existing inequalities in the world. Does its premise, "more is more", reduce the accepted definitions of what is knowledge and valuable research, and have unjustifiably big effect in decision-making? How are big data samples formed and analysed, based on what questions, and how to ensure the data really reflect a certain population? [15], [25].

Varying definitions leave open questions about what exactly is big data. Eg. Dumbill (2012) defined it as,

> …data that exceeds the processing capacity of conventional database systems. The data is too big, moves too fast, or doesn't fit the strictures of your database architectures. To gain value from this data, you must choose an alternative way to process it. [13].

Fosso Wamba et al. (2015) examined big data in the use of state emergency services in New South Wales Australia. From several earlier definitions, they proposed an integrated definition of big data as

> …a holistic approach to manage, process and analyse 5 Vs (i.e. volume, variety, velocity, veracity and value) in order to create actionable insights for sustained value

> delivery, measuring performance and establishing competitive advantages [19].

Boyd and Crawford (2012) argued that big data might be a misleading term from the beginning as some current data, easily analysed with just desktop computers, could be considered much 'smaller' than for example past census data. It is not just the question of quantity that creates the phenomenon of big data, but how to "search, aggregate, and cross-reference large data sets" [8] to make it meaningful. As understanding of the impacts of big data is still in the making, it is important to make explicit the underlying assumptions that might govern judging it to one way or another.

Big data has landed also in the education sector in the form of learning analytics and educational data mining. Better analytics are proposed to reduce costs, advise performance assessments of staff and learning units, and to improve the delivery of education in general [15], [16]. The annual speculative Horizon Report Higher Education Edition [21] noted in 2014 that the time to adaptation of learning analytics in a wider scale in higher education is year or less. According to the authors, "sophisticated web-tracking tools are already being used by leading institutions to capture precise student behaviours in online courses, recording not only simple variables such as time spent on a topic, but also much more nuanced information that can provide evidence of critical thinking, synthesis, and the depth of retention of concepts over time" (p. 39). Learning analytics are predicted to capture in what contexts and how students interact with learning content and software to "improve student engagement and provide high-quality, personalized experience for learners" [21]. The benefits of this are suggested to be more personalized support, adapting to students' need and giving personalized assistance to learners based on their level. Fernández-Gallego, Lama, Vidal and Mucientes (2013) proposed new algorithms for educational data mining to assess student's learning in educational 3D virtual worlds. They argued that analyzing student system logs would expose their level of learning. Such monitoring could help the instructor to make relevant changes to the learning flow in real time. Serrano-Laguna, Torrente, Moreno-Ger and Fernández-Manjón (2014) reported an initial work in developing a learning analytics model for game-based learning. Their work indicated that the complexity of different videogame approaches forces to simplify the development of generally applicable analytics models. As also in other sectors, not only the complexity of data, but also the complexity of usage situations creates development challenges.

Eynon (2012) observed several important areas for further discussion of the role of big data in education. First is ethical. What are the indications for privacy, what sort of data should be used and analysed, for what should it be used, and how might it direct behaviour?

> What happens to students who are most likely to drop out? Do we tell them, support them (which has economic implications), or let them sign up and take their money, knowing they will probably fail? What happens to serendipity in a system where all educational choices are based on recommender systems? What kinds of learning can a student truly keep 'private'? [15].

Secondly, how the pre-determined data-driven shape might form the outcomes of the research inquiry? As Eynon (2012) points out, data that inform what actions people have taken is valuable, but does not give out the whole truth nor the meaning people might assign to their actions, behaviour and social connections. The author points out that although big data might appear impressive, various research approaches are needed to understand what constitute phenomena around us. The author also notes that practical issues such as data storing, managing and processing are similar challenges in education as in other sectors. Eynon (2012) calls for a balanced discussion around big data that will include both barriers of use as how it can assist various stakeholders in the field.

One of the challenges big data poses is how much data are enough and what of it to model? For example in an educational analytics environment, are data about the students' past enough? Given that the students' learning is a product of their interaction with content and peers in a specific context, how to model this messy real life that lead to the students' state of learning?

The objective of this paper is to acknowledge these big questions, but not to try to find answers to all of them. Instead, the aim is to examine the use of big data through a specific area where it is increasingly applied, namely visualising it in immersive virtual environment (IVE) or virtual reality (VR). Many of the developed applications do not clearly justify their choices of presenting data or user interaction possibilities with it. The connection of the types of data presented and modes of interaction is not often well defined. The paper will describe big data visualisation and interaction in these applications and aims to better ground them in known aspects of human perception and cognition through a phenomenological perspective. It will also critically examine and vision how understanding human perception and interaction as embodied might advise the development of big data VR visualising applications.

2. BIG DATA VISUALISATION APPLICATIONS

This section will present developments of using immersive virtual environments to make sense of big data. It will ground the discussion of big data visualisation in developed applications and prototypes.

Visualisation has been suggested to be a valuable tool to disseminate big data. As the basic premise goes, visualisation of big data could help people to spot meanings that machines are not able to notice, to detect hidden patterns and correlations [35], and to make numbers more understandable for both general audience and scientists [7], [24], [33].

Although the current status of big data might push the recent developments of visualisation applications, using virtual reality for visualisation and manipulation of data has been well in the development for over 25 years, and some of the old libraries are still in use [36]. Also the aims, technologies and arguments for potential use have existed before the big data trend came to fore. In 1993, Cruz-Neira et al. (1993) reported collaboration with scientists from various fields to use an immersive virtual reality CAVE system to visualise and interact with presented research data in various areas such as living spaces, the Universe and galaxies, and brain structure. Their system used real architectural

data to model a part of Chicago in the VR system, and allowed users to walk or fly through the environment and observe and manipulate specific objects of interest. Also some of the technologies that are currently receiving lots of media visibility have long roots. For example Sutherland (1968) introduced the first head-mounted display design already in the 1960's, and Cox, Patterson and Thiebaux (2000) filed a patent claim in 1997 for voice and gesture manipulation of data in an immersive 3D environment. As an example for the aims of visualisation, Beck (2003) reported the use of virtual reality based geographical systems (VRGIS) in the visualisation of landscapes, cities and whole geographical areas. New application developments were proposed to result in faster rendering rates and possibility to stream even complex and highly realistic models over the Internet. Beck (2003) visioned that VRGIS applications could be used for real-time visualisation of weather conditions, and in the tourism sector to present local sites and services.

Childs, Geveci and Schroeder (2013) identified several challenges in the development of new visualisation for handling big data, namely "massive parallelization, processor architectures and programming models, application architecture and data management, data models, rendering, and interaction" (p. 35). They also discussed what might be the suitable role and use for VR visualisation applications. According to them, aims and methods of data analysis should determine what sort of interaction methods should be used to interact with data. If visualisation is to be used to confirm hypotheses, quick simulations might not need complex interaction. On the other hand, if the aim is to use various parameters to view and explore results through simulations, interaction might be very important. The authors note that although new and cheaper input-output and tracking technologies from Microsoft Kinect to various mobile devices might make VR visualisation techniques more readily available and more acceptable in the eyes of the users, the wider acceptance for scientific data analysis is still open for scrutiny.

Donalek et al. (2014) were more hopeful that the benefits of visualising big data in immersive virtual environments would drive a positive development for a wider application. According to the authors, discovery of hidden patterns through the data is the most promising aspect of developments in using big data. The authors argued that,

> Visualization is the main bridge between the quantitative content of the data and human intuition, and it can be argued that we cannot really understand or intuitively comprehend anything (including mathematical constructs) that we cannot visualize in some way. Humans have a remarkable pattern recognition system in our heads, and the ability for knowledge discovery in data-driven science depends critically on our ability to perform effective and flexible visual exploration. This may be one of the key methodological challenges for the data-rich science in the 21st century. (p. 609)

Instead of applying various algorithms based on existing assumption of what data might be important and how, the authors argued that our natural spatial way of understanding the world as three-dimensional should drive the development of visualisation methods. Finding connections, patterns and anomalies in the data might lead to interesting new outcomes. In contrast to large and immovable VR systems, Donalek et al. (2014) aimed to develop easy to use, affordable and portable visualisation applications that would employ state of the art commercially available VR input and output technologies and sensors. They have connected these devices with environments such as Second Life and Open Simulator to test the fit of the combination for scientific collaboration. Their preliminary tests are a beginning for using Unity 3D to develop a multiuser scientific data visualisation platform, called the iViz.

Arsiwalla et al. (2015) reported a prototype environment for visualising and interacting with brain data [1]. The authors asked a question, how can visualising the ever-increasing data from neurobiological databases support our understanding of the brain? Neuroscience regards the brain as a "complex dynamical network of neurons" [1]. It is important to see the different parts in action in the context of the whole to understand how they work together. This need initiated the development of BrainX3 environment, which aims to both visualisation and analysis of brain activity. The immersive virtual environment is projected 360 degrees in a specific room with various sensors supporting interaction. The authors suggest that the development of the environment is based on "a natural user interaction paradigm (including user immersion and gesture based inputs)" [1]. The immersive virtual environment allows the user to navigate through neural networks by walking. It also allows the use of hand gestures and body positioning for bookmark data and manipulate the brain by stimulating regions and performing virtual surgeries. The initial observations are that the chosen interaction approach resulted in better understanding of the data in question, and also lead to a more enjoyable user experience [5].

Possible applications for making sense of big data have also been explored by teams in the entertainment sector. For example recently Maddix (2015) reported an early VR prototype. As part of a VR and big data development challenge, the team had to innovate how to transfer a large data set of lifestyle and biological sample data for visualisation in a virtual environment developed with the Unreal engine. The team experimented with using gaze recognition and new input devices such as the Razor Hydra 3D mouse to allow the user to search, examine, filter and manipulate data accurately in 3D. The user is visioned to stand in the middle of revolving spheres that visualise data queries in the VR environment. They also trialled using heat maps to signify important sections in the data. In the future, the team also aims to experiment with voice recognition to make navigation and the overall user experience even faster.

As can be seen from this introduction, various VR visualisation applications that report users interacting with data in 3D environments rarely justify the selected modes of interaction. Some do not ground them at all, and some refer to concepts such as 'natural gestures' and 'embodied interaction' without discussing more in-depth what they might mean. The next section will explore this are through phenomenology and embodied interaction.

3. EMBODIED INTERACTION AND PERCEPTION

This section will introduce a phenomenological perspective to how we perceive and interact with the world, and try to lay a more theoretically sound basis to understand some of the

introduced forms of presentation and user interaction in VR environments for big data visualisation. As not the focus of this paper, deeper philosophical aspects of phenomenology will not be discussed in-depth. The section will concentrate on the concept of embodiment and how it has been perceived in the context of information systems and human-computer interaction [11], [31]. For those who wish to explore further the philosophical underpinnings of phenomenology in connection to human-computer interaction, accounts by Svanæs (2014) and Gallagher (2014) provide a good starting point.

Boland (1986) argued that understanding information systems as communicative acts by conscious and intentional human actors would lead to better outcomes in design and development. For this, phenomenological approach holds a great promise. He based on this argument on the notion that, "data becomes information in the consciousness of a human subject" (p. 200). According to Boland (1986), "Organizational actors never just react to situations, but first enact them and then make sense of what they have enacted" (p. 198). Human organisations are constituted through language and dialogue. He observed that some developments in information systems might fail before they even begin because of underlying assumptions of what constitutes information, how information is structured [12], and how organisational decision-making takes place. The value of phenomenology begins from the rigorous and systematic process of setting aside one's taken for granted suppositions. This is never entirely possible, but even partially done it can open new venues for understanding and development. The proceeding process of rigorous phenomenological analysis tries to uncover the essence of things and what constitutes them. According to Boland (1986), this allows better access to the everyday life where intentional actors are constantly bombarded with information and trying to cope with various meanings and communication situations. Studying actors and language in context can support more effective design of information systems to better support various organisational processes.

In contrast to existing positivist models of developing human-computer interaction and information systems, Dourish (2001) proposed an alternative perspective to developing human-computer interaction. According to Dourish (2004), positivist view presupposes that complex human behaviour can in general be reduced into mathematical models to find and analyse underlying patterns. Relying only to this view might inhibit HCI development and research because of the wrong underlying assumptions of what is context.

> …the idea that context consists of a set of features of the environment surrounding generic activities, and that these features can be encoded and made available to a software system alongside an encoding of the activity itself, is a common assumption in many systems. It is inherent in the notion that our systems will "capture", "represent" or "model" context—the normal and appropriate concerns of positivist design. (p. 22)

He presented a phenomenological view where instead of being information, context is considered to be a relation between objects and activity. Instead of pre-defined context, contextual features are dynamically defined. Context is not stable, but relevant to specific settings, actions and users. Context and content cannot be separated, but context is produced through activity (see also [34]).

Dourish proposed an alternative base for human-computer interaction and information systems through the concept of embodied interaction. Context does not mean only physical location, objects or other features that can be detached and coded individually. It is "the creation, manipulation, and sharing of meaning through engaged interaction with artifacts" [11]. Instead of being independent from user interaction, context is enacted by users. It is to allow "users to negotiate and evolve systems of practice and meaning in the course of their interaction with information systems" [11]. Meaning in the world is found through interaction: "embodiment is a participative status" [12]. Action creates new understanding. Instead of inhibiting action, information systems should make everyday practical activities easier. Because of this, understanding interaction as embodied works as a valuable starting point for human-computer interaction and information systems development.

Svanæs (2013) discussed embodiment in interaction design as a bodily experience. To understand the ever-increasing presence and use of technology we need to "understand the physicality of its contexts of use, including physicality of its users" [31]. Svanæs (2013) focuses especially in the embodied nature of perception. For Svanæs, our perception is embodied in a way that making sense of our surroundings is bodily and intentional: what we observe in the world is based on our goals and intentions. We make sense and meaning through bodily interaction with the world. He uses an interactive painting as an illustrative example of a user situation and the embodied nature of perception. In the example, the canvas of a painting is white. There is a button, "Touch me" that calls for action and changes the state of the painting to black if touched by the user. Svanæs (2013) explains:

> Without action, we are left simply with the visual appearance of a white canvas, missing out on the intended user experience of this work of art, which emerges through interaction… Experiencing the interactive artwork requires not only visual perception, but also an arm and a hand. Arm, hand, and eye movements are integrated parts of the perceptual process that leads to perception of the artwork's behavior. The interactive experience is thus both created by and mediated through the body. (p. 14).

Svanæs (2013) points out that technology can extend our perception. This allows us to proceed with our intentions in a way that well-designed and familiarized mediating technology might become transparent to our experience. Using an e-book reader's touch screen to turn a page or gaze-control to scroll are examples of interactions where our intention is to read, and our concentration is not on the technology itself. It is invisible to us. This can also be observed in the context of playing video games:

> In more complex interactions, such as when an experienced computer user plays the game World-of-Warcraft, the perceiving body extends into the game. When the player tries out a new sword that she has acquired for her game character, she perceives its behavior through the mouse and the part of the software that allows her to control her character [31].

Such perspectives of phenomenology and embodiment can provide a rigorous basis for designing meaningful interactions with immersive technologies. It can build a cornerstone for more robust and usable VR visualisation applications and interaction situations, make more explicit what sort of understandings might be possible through the use of VR visualisation applications, and also establish new research opportunities.

4. DISCUSSION: BRINGING EMBODIED PERCEPTION AND INTERACTION TO VR

Dourish (2004) argued that the way information is structured and presented affects the meaning people assign to it. On the level of giving 'better' knowledge, big data raises questions how do we come to know things, and what kinds of understandings might big data visualisation support? According to Eisner (1997), data presentation is closely connected to the nature of knowledge and how presented information can be considered as valid. He noted that different presenting methods (movies, stories or graphs) appeal differently to people. A movie with a plot might affect us differently than an academically accepted form of a research report consisting primarily of text, graphs and numbers. For example homeless people might appear to us differently through a movie than a research report presenting census data. In both of these cases, the object of presentation, homelessness, is given from a certain perspective. How information is presented directs perception. In a particular VR visualisation environment, someone has always developed it in a certain way. In the moment of doing so, the first step of tampering with the source data have already been taken. The question then is, does placing big data in a visualisation environment inherently mean it is already analysed at least on some level? Is any given approach to visualisation always already a perspective to the data in itself?

The fact that data visualisation environments are not only a medium for representation but also for interaction opens several questions about applying them for research. Does interaction with data in a visualisation environment alter it similarly to using qualitative and quantitative data analysis software? With the acting subject in some cases quite literally embodied in the centre of data, does it propose a new interactive medium for data analysis, presentation (which is what the word 'visualisation' might indicate) or both? If VR visualisation is a tool for analysis, does it afford transforming one kind of data to another kind of understanding (quantitative to qualitative), and how? What are its methods of analysis? Will there be VR-specific analysis methods one day, e.g. the 'VR ANOVA', or is using VR visualisation for data analysis based on premises that some might call more subjective? Technology always affords something, but at the same time, something else is restricted or left out. Statistics software can be used for quantitative analysis, but their application for qualitative analysis is limited or non-existent. This is because they have been designed to represent quantitative data, and support specific quantitative analysis methods. The developed software always directs user behaviour with what is possible in interaction, and it is always a design solution of the developer, affected by views of knowledge, needs and the world.

At the same time, phenomenological perspective of understanding our being in the world as the basis for the embodied human-computer interaction invites several new research and development opportunities. Many of the existing applications aim to enable interaction in ways that phenomenology has long since identified as important in human sense making. We understand the world by being in it with our body. We observe objects from different angles with moving our eyes in distinctive ways, touching things, rolling them in our hands, and testing what might happen to objects when we interact with them. Our understanding of the world is also contextual, active, intentional and social. As Svanæs (2013) observed, our personal backgrounds, intentions and tasks at hand affect our perception of things. Study by Vogt and Magnussen (as described in [31]) showed that artists and laypeople looking at the same artwork basically see a different painting. How might such insights advise how different end-users interact with different data and what kinds of knowledge do they find? Useful studies in this region could combine rich phenomenological descriptions of user experience with eye tracking data – now that some of the VR headsets are making it more available by starting to track users' gaze. This could give more valuable knowledge on the use of visualised big data in VR environments, and how tasks, roles and user interfaces affect interaction and knowledge.

On a level of what can big data inform us about, the work by Dourish (2004) proposes an important question, can everyday interactions and its meanings be captured and modelled? He argues that captured and re-presented data cannot give an authentic view to a context. Could visualisation and development of interactive situations based on big data add a new viewpoint to this comment or strengthen it? As a hypothetical example, let us presume big data in the form of opinions about a specific group of people is available. This opinion data would be fed to VR visualisation software, which then regenerated those attitudes to virtual agents who acted them. In the immersive virtual environment the user could engage in social interaction with the virtual agents who reacted based on the user avatar acting as a member of this studied group. How could this affect the user's understanding or feelings about this specific group? Some studies indicate that virtual experiences can affect our sense of self, our body and our opinions about other people. For example Banakou, Groten and Slater (2013) suggested that acting through another kind of body in VR could convey a new perspective to surroundings, and affect attitudes and behaviour. Also Fox, Bailenson and Tricase (2013) observed that wearing certain kinds of avatars affected real attitudes towards women.

Perhaps the connection of data visualisation and embodied interaction could be explored further in understanding our reactions and behaviour in everyday situations. A VR visualisation application could combine real traffic and map data to produce a computer-generated situational simulation where the user could sit in a car, in a traffic jam. The situation could be varied in multiple ways to determine how different conditions affected users' experience, and what decisions to get from A to B. Such experiments could guide the design of new applications to make a person's trip more enjoyable or safe. As it is done in an environment that allows various ways of data recording,

mixed research with user experience accounts could advise the development of real world solutions.

When designing presentations and interactions with visualisations, we should make transparent what do we mean by referring to modes such as 'natural interaction'. If we consider interaction from a phenomenological perspective, natural means our everyday being in the world, and how things are given to us in our interaction with the world. We experience with our body as we are in the world. As such, this might not be directly transferrable for navigating virtual brains and galaxies, as they are not our natural environments. We cannot perceive them 'naturally' as they are not part of our natural experience. As a spatial experience, they are not familiar to us to make sense of (although outer space is of course to astronauts). This is not to say that visualisation where data is presented through more abstract forms is meaningless. Our understanding of grouping, velocity, symmetry and others laws of perception are still operational and might be useful. But the relationship between data visualisation and interaction with it should be made explicit to for more robust development.

5. CONCLUSION

The meaning of big data is still in the making, and its promise, peril or forms of accommodation to existing information systems processes and technologies are still open for further research and practical applications. Immersive virtual reality visualisation applications are developed in order to make sense of big data. Such applications allow varied modes of presentation and interaction, but their design approaches are not always explicit. The project of this paper has been to ground the development of big data visualisation in immersive virtual reality environments to existing understandings of human perception and interaction through a phenomenological lens and the concepts of embodied interaction and perception. Examining applications from this perspective has raised open questions about what modes of big data visualisation and interaction might be useful for building knowledge. Application development through the principles of embodied interaction and perception has been discussed in this preliminary work on the topic. Using embodiment as the basis for understanding how we come to know and what is the role of interaction in it has revealed new avenues for research and development in big data VR visualisation applications.

REFERENCES

[1] Xerxes D. Arsiwalla, Riccardo Zucca, Alberto Betella, Enrique Martinez, David Dalmazzo, Pedro Omedas, Gustavo Deco and Paul F. M. J. Verschure, "Network dynamics with BrainX3: a large-scale simulation of the human brain network with real-time interaction", *Frontiers in Neuroinformatics*, Vol. 9, No. 02, pp. 1–14, 2015.

[2] Luigi Atzori, Antonio Iera and Giacomo Morabito, "The Internet of Things: A survey", *Computer Networks*, Vol. 54, No. 15, pp. 2787–2805, 2010.

[3] Domna Banakou, Raphaela Groten and Mel Slatera, "Illusory ownership of a virtual child body causes overestimation of object sizes and implicit attitude changes", *Proceedings of the National Academy of Sciences of the United States of America*, Vol. 110, No. 31, pp. 1246–12851, 2013.

[4] Michael Beck, "Real-Time Visualization of big 3D City Models", *International Archives of the Photogrammetry, Remote Sensing and Spatial Information Sciences*, Vol. XXXIV-5/W1, pp. 1–6, 2003.

[5] Alberto Betella, Enrique Martínez Bueno, Wipawee Kongsantad, Riccardo Zucca, Xerxes D. Arsiwalla, Pedro Omedas and Paul F. M. J. Verschure, "Understanding Large Network Datasets through Embodied Interaction in Virtual Reality", *Proceedings of the Virtual Reality International Conference*, 2014.

[6] R. J. Boland Jr, "*Phenomenology: a preferred approach to research on information systems*", in "Trends in Information Systems", pp. 341–349, Amsterdam: North-Holland Publishing Co., 1986.

[7] David Bollier, "*The promise and peril of big data*", Washington DC: The Aspen Institute, 2010.

[8] Danah Boyd and Kate Crawford, "*Critical Questions for Big Data*", Taylor & Francis, 2012.

[9] D.J. Cox, R.M. Patterson and M.L. Thiebaux Jr, (2000). "Virtual reality 3D interface system for data creation, viewing and editing, US patent No.6154723, 2000.

[10] C. Cruz-Neira et al., "Scientists in wonderland: A report on visualization applications in the CAVE virtual reality environment", *IEEE Symposium on Research Frontiers in Virtual Reality*, pp. 59–66, 2003.

[11] Paul Dourish, "What we talk about when we talk about context", *Personal and Ubiquitous Computing*, Vol. 8, No. 1, pp. 19–30, 2004.

[12] Paul Dourish, "*Where the Action Is: The Foundations of Embodied Interaction*", Cambridge, MA: The MIT Press, 2001.

[13] Edd Dumbill "Making Sense of Big Data", *Big Data*, Vol. 1, No. 1, pp. 1–2, 2013.

[14] Elliot W. Eisner, "The promise and perils of alternative forms of data representation", *Educational researcher*, Vol. 26, No. 6, pp. 4-10, 1997.

[15] Rebecca Eynon, "The rise of Big Data: what does it mean for education, technology, and media research?", *Learning, Media and Technology*, Vol. 38, No. 3, pp. 237–240, 2013.

[16] Rebecca Ferguson, "Learning analytics: drivers, developments and challenges", *International Journal of Technology Enhanced Learning*, Vol. 4, No. 5/6, pp. 304–317, 2012.

[17] Beatriz Fernández-Gallego, Manuel Lama, Juan C. Vidal and Manuel Mucientes, "Learning analytics framework for educational virtual worlds", *Procedia Computer Science*, Vol. 25, pp. 443–447, 2013.

[18] Jesse Fox, Jeremy N. Bailenson and Liz Tricase, "The embodiment of sexualized virtual selves: The Proteus effect and experiences of self-objectification via avatars", *Computers in Human Behavior*, Vol. 29, No. 3, pp. 930–938, 2013.

[19] Samuel Fosso Wamba, Shahriar Akter, Andrew Edwards, Geoffrey Chopin and Denis Gnanzou, "How "big data" can make big impact: Findings from a systematic review and a longitudinal case study", *International Journal of Production Economics*, Vol. 165, pp. 234–246, 2015.

[20] Dag Svanaes, "*Philosophy of Interaction*", Mads Soegaard and Rikke Friis Dam (Eds.), "The Encyclopedia of Human-Computer Interaction", 2nd Edition, Denmark: The Interaction Design Foundation, 2014. Available online at https://www.interaction-design.org/encyclopedia/philosophy_of_interaction.html

[21] L. Johnson, S.Adams Becker, V. Estrada, A. Freeman, "*NMC Horizon Report: 2014 Higher Education Edition*", Austin, Texas: The New Media Consortium, 2014

[22] Karl Maddix, "*Big Data VR Challenge*", Retrieved June 25, 2015, from http://www.mastersofpie.com/big-data-vr-challenge/

[23] Travis B Murdoch and Allan S Detsky, "The inevitable application of big data to health care", *Jama*, Vol. 309, No. 13, pp. 1351–1352, 2013.

[24] J.D. Mulder, R. van Liere and J.J. van Wijk, "Computational steering in the CAVE", *Future Generation Computer Systems*, Vol. 14, No. 3, pp. 199–207, 1998.

[25] Lisa Portmess and Sara Tower, "Data barns, ambient intelligence and cloud computing: the tacit epistemology and linguistic representation of Big Data", *Ethics and Information Technology*, Vol. 17, No. 1, pp. 1–9, 2015.

[26] Ryan H Purcell and Karen S Rommelfanger, "Internet-Based Brain Training Games, Citizen Scientists, and Big Data: Ethical Issues in Unprecedented Virtual Territories", *Neuron*, Vol. 86, No. 2, pp. 356–359, 2015.

[27] C. Romero, and S. Ventura, "Educational Data Mining: A Review of the State of the Art", *IEEE Transactions on Systems, Man, and Cybernetics, Part C (Applications and Reviews)*, Vol. 40, No. 6, pp. 601–618, 2010.

[28] S. Sagiroglu and D. Sinanc, "Big data: A review", *Proceedings of International Conference on Collaboration Technologies and Systems*, pp. 42–47, 2013.

[29] Ángel Serrano-Laguna, Javier Torrente, Pablo Moreno Ger and Baltasar Fernández-Manjón, "Application of Learning Analytics in Educational Videogames", *Entertainment Computing*, Vol. 5, No. 4, pp. 313–322, 2014.

[30] Ivan E. Sutherland, "A head-mounted three dimensional display", *Proceedings of the Fall Joint Computer Conference, Part I on – AFIPS*, pp. 757–764, 1968.

[31] Dag Svanæs, "Interaction Design for and with the Lived Body: Some Implications of Merleau-Ponty's Phenomenology", *ACM Transactions on Computer-Human Interaction (TOCHI) - Special issue on the theory and practice of embodied interaction in HCI and interaction design*, Vol. 20, No. 1, 2013.

[32] Kim Hua Tan, YuanZhu Zhan, Guojun Ji, Fei Ye and Chingter Chang, "Harvesting big data to enhance supply chain innovation capabilities: An analytic infrastructure based on deduction graph", *International Journal of Production Economics*, Vol. 165, pp. 223–233, 2015.

[33] Andries Van Dam, David H. Laidlaw, Rosemary Michelle Simpson and Rosemary Michelle Simpson, "Experiments in Immersive Virtual Reality for Scientific Visualization", *Computers & Graphics*, Vol. 26, pp. 535–555, 2002.

[34] Janet Vertesi and Paul Dourish, "The Value of Data: Considering the Context of Production in Data Economies", *Proceedings of the ACM Conference on Computer supported cooperative work*, pp. 533-542, 2011.

[35] Ciro Donalek, S. G. Djorgovski, Alex Cioc, Anwell Wang, Jerry Zhang, Elizabeth Lawler, Stacy Yeh, et al., "Immersive and Collaborative Data Visualization Using Virtual Reality Platforms", *IEEE International Conference on Big Data*, pp. 609–614, 2014.

[36] H. Childs, B. Geveci, W. Schroeder, J. Meredith, K. Moreland, C. Sewell, T. Kuhlen and E.W. Bethel, "Research Challenges for Visualization Software", *Computer*, Vol. 46, No. 05, pp. 34–42, 2013.

7

An *in vitro* study of electroporation of leukemia and cervical cancer cells

Raja Prabu Ramachandran, S. Madhivanan, Raji Sundararajan, Cindy Wan-Ying Lin and Kavitha Sankaranarayanan

DOI: 10.1533/9781908818294.161

Abstract: Cancer therapies mainly target the uncontrolled proliferation of the cancerous cells. A translational therapy for inoperable, chemo- and radio-resistant tumors is electroporation-based chemotherapy, known as electrochemotherapy, a physical means of using electrical pulses in conjunction with minimal doses of the chemo drug to achieve proliferation control. It is applicable to all histologies of tumors and its efficacy depends on a variety of factors, including the electric field intensity, the pulse duration and the number of pulses. In this chapter, we describe the optimization of pulse parameters for effective electroporation of leukemic and cervical cancer cell lines. Human promyelocytic leukemia (HL60), human acute myeloid leukemia (KG1) and human cervical (ME180) cancer cell lines were subjected to electroporation in the presence of various doses of FDA approved chemo drug, Bleomycin. The effect of curcumin and electroporation is also tested for HL60 cells. The results indicate that by using electroporation, chemo drug molecules could be uploaded into these cells to control proliferation. This promises to be a very useful tool for treating patients suffering from chemo-refractive tumors.

Key words: Leukemia, cervical cancer, HL60 cell line, KG1 cell line, ME180 cell line, Bleomycin, curcumin, dose curve, voltage pulses, viability.

7.1 Introduction

About every four minutes, two people are diagnosed with a blood cancer and about every ten minutes, two die due to a blood cancer, in the US [1]. Leukemia is one of the blood cancers that affects the bone marrow, which is the source of blood cells and occurs at all ages. It is characterized by a rapid increase in the number of immature blood cells in the blood stream, thereby affecting regular functions. In addition, the disease is subdivided based on the type of blood cells affected – lymphoblastic (cancer of lymphocyte forming cells) and myeloid leukemia (cancer of cells that become red blood corpuscles (RBCs)), some types of white blood corpuscles (WBCs) and platelets. Leukemia is one of the leading causes of mortality around the world, as evidenced by the global statistics conducted by the Leukemia and Lymphoma Society [2]. Table 7.1 shows the incidence of the disease and the death rate for various ages [3]. Figure 7.1 shows the 5-year survival rate for the periods, from 1960–63 versus 1975–77 versus 2001–07 [1]. Leukemia accounts for about 30% of cancer cases in children aged 0–14 years. There are more than 232 000 people in the US living with leukemia and approximately 44 000 new cases were diagnosed in 2011 [4]. The standard of care currently used is radiotherapy and chemotherapy. With the current poor cure rate, the need for alternate therapies cannot be overstated.

While leukemia affects both genders and at all ages, cervical cancer is a gynecologic cancer (any cancer that starts in a woman's reproductive

Table 7.1 Leukemia statistics – incidence and death rate at various ages [3]

Age	% Diagnosed	% Died
<20	11.4	3.3
20–34	5.2	3.5
35–44	5.9	3.9
45–54	9.7	6.7
55–64	13.9	11.8
65–74	20.5	23.4
75–84	23.2	31.1
85 and above	10.1	16.4

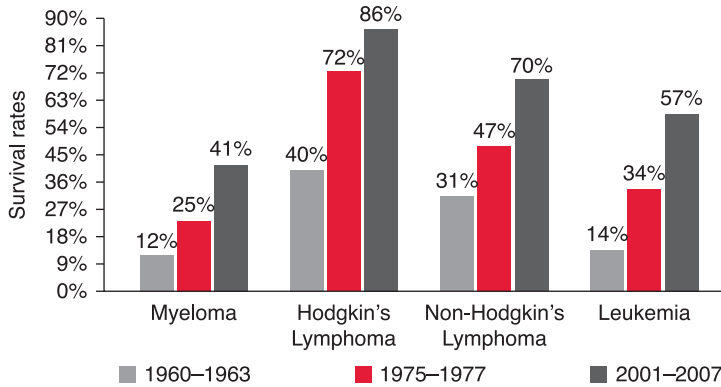

Figure 7.1 **Five-year relative survival rate for the periods, from 1960–63 vs. 1975–77 vs. 2001–07 [1]**

organs). It is the cancer that begins in the cervix, the lower part of the uterus [5]. It is almost always caused by human papilloma virus (HPV) infection [6], with virtually all cervical cancer cases (99%) being linked to infection with the HPV. The E6 and E7 genes present in the genome of HPV suppress the activity of two tumor suppressor genes, Rb and p53, thereby triggering uncontrolled proliferation of the same [7].

All women are at risk and it occurs most often in women over age 30. In the US each year, it affects about 12 000 women. Worldwide, it is the third most commonly diagnosed cancer and the fourth leading cause of cancer death in women, accounting for 9% (529 800) of the total new cancer cases and 8% (275 100) of the total cancer deaths among females in 2008 (Figure 7.2 [8]). More than 85% of these cases (453 300/529 800) and deaths (242 000/275 100) occur in developing countries. India, the second most populous country in the world, accounts for 27% (77 100) of the total cervical cancer deaths. Worldwide, the highest incidence rates are in Eastern, Western and Southern Africa, as well as South-Central Asia and South America. Rates are lowest in Western Asia, Australia/New Zealand and North America. The high incidence rate of cervical cancer in developing countries could be attributed to the lack of screening, its awareness and the socio-economical status, lacking resources and infrastructure, and the culture. The health care infrastructure in these countries does not support Papanicolaou testing or other types of screening tests. In addition, the vaccines do not provide protection for 30% of chronic infections by HPV types, other than HPV 16, 18, 6 and

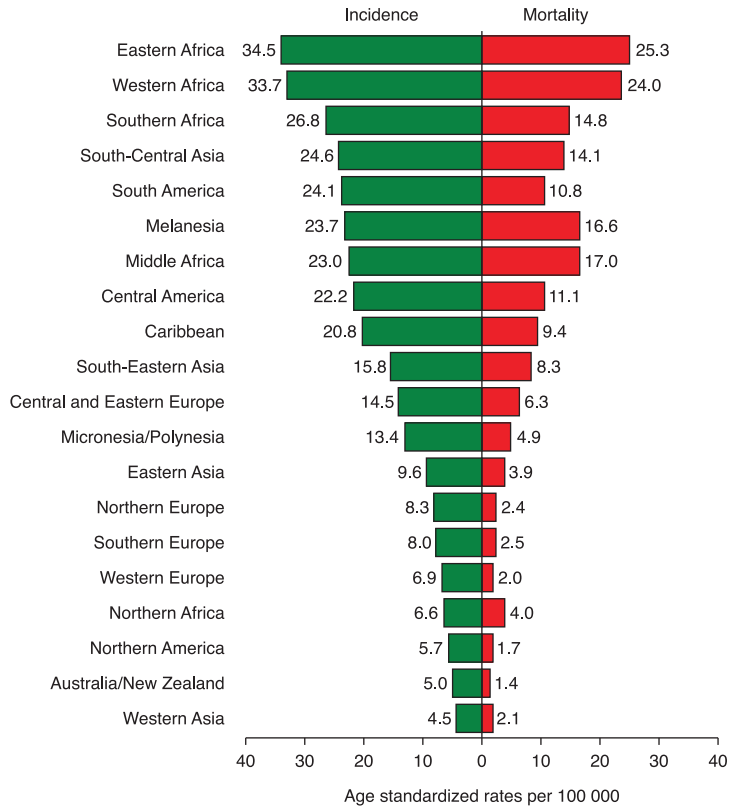

Figure 7.2 **Age-standardized cervical cancer incidence and mortality in various countries [8]**

11 that cause cervical cancer [8–10]. Normally, they are treated with surgery, chemotherapy, radiotherapy and hormonal therapy. However, these do not work well for all patients, as seen from the high death rate. Hence, additional/alternate, efficient and economical therapies are critical to save these women.

Cancerous cells such as HL60 develop resistance to a variety of cytotoxic drugs, making treatment of such types of cancers difficult. The drug, which by itself is relatively less permeable to the cell membrane, is not retained in the cancerous cell as a result of an enhanced drug efflux mechanism acquired by these cancerous cells [11–13]. This has been demonstrated to be due to the over-expression of a specific type of membrane phosphoglycoprotein and a drug resistance associated ATP binding protein on the cell surface. It has been demonstrated that

as HL60 cells divide and 'age', there is an increase in the cell cholesterol content, which in turn modulates a decrease in membrane lipid dynamics [14].

Most leukemia and lymphoma cells grown as suspension culture are resistant to most gene transfer methods, thereby making electroporation the method of choice. The cell membrane, comprising a lipid bilayer, is interspersed with protein molecules – some of the transmembrane spanning the entire lipid bilayer (i.e. ion channels, H^+ pumps, etc.) are only partially embedded in the cell membrane and are exposed only at either end. In addition to the lipids and proteins, carbohydrates are also present in the cell membrane, as either glycoproteins or glycolipids. The lipid and protein compositions of the cell membrane vary from cell to cell and this bestows unique membrane properties to different types of cells, based on their function. Although, in previous research, the efficiency of electroporation for the hematopoietic cells was reported to be roughly just 1% [15], with a variety of low voltage, long duration and high voltage and short duration pulses, it is possible to identify the optimal pulse parameters. This is because of the mechanical property of the membrane as a major determinant in the efficiency of application of electrical pulses to a cell for electroporation-based methods for gene/molecule/drug transfer. It is largely determined by the cytoskeletal architecture of a cell, which is a variant in cancerous cells [16]. Electrodeformation, or the mechanical response of the cell to electrical fields, vary from cell to cell [17] and would account for the necessity for different parameters while working with various types of cells. It has been reported that there is a change in the membrane properties of the myeloid cells during maturation as well as differentiation [18]. Whether the changes in membrane properties affect the parameters required for electrochemotherapy of the different type of cells is what was probed into by this study.

Professor McConnel's group in Stanford had demonstrated that weak non-uniform external electric fields have disruptive effects on biological membranes [19]. This effect is primarily due to the effect of the fields on the lipid layer of the cell membranes, thereby affecting the membrane proteins impregnated on the same, which in turn results in abnormal cellular function. The size of the pores thus formed remains a function of the duration of the electric field pulse. Nanosecond pulses have been shown to result in a temporary externalization of the phosphatidyl serine residues [20], a release of intracellular calcium [21,22] and induction of apoptosis [23,24].

In the presence of a strong electric field, there is a significant increase in permeability and conductance of the lipid membrane. If the applied electrical field is of not too high an amplitude and time duration, then the cell membrane is capable of returning to its previous state, as in reversible electroporation. At higher amplitudes or time durations, the membrane loses its ability to reseal and self-destructs, as in the process of irreversible electroporation. Initially it was not understood as to where these pores were formed in the lipid bilayer – the lipid matrix, integral membrane protein region or the contact region between the two. However, studies on human erythrocytes and lymphocytes along with an artificial bilayer revealed that the electrical breakdown of the membrane arises in its lipid matrices [25].

A study of tumor treating fields (TTFs) of low intensity, intermediate frequency, alternating current on a variety of human and rodent tumor cell lines exhibit varying rates of reduction of cell proliferation, both *in vitro* and *in vivo*. This could be due to the difference in the property of the cell membrane, though the basic lipid matrix largely remains the same [26]. The study demonstrated a specific intensity and frequency dependence of the TTF inhibition on different types of cancerous cells. It also revealed that the electric fields disturbed the normal polymerization-depolymerization processes of the microtubules of the mitotic spindle during mitosis and hence arrests the proliferation of actively dividing cells such as cancer cells.

Large cells have been shown to be more susceptible to electrical breakdown, which might hint at a higher risk of breakdown with an increase in the membrane surface area. Hence the parameters for successful electroporation may not only be dependent on the type of cellular lipids and the other membrane components, but also its size. In this connection we have probed into the parameters for pulsing HL60, KG1 and ME180, which are of different cellular origins for increased uptake of chemo drugs [27–33]. This method of treatment could be a very economical palliative treatment strategy, owing to the absence of any rigorous time-consuming procedures, as well as a significant reduction in the dose of the drug required and could be out-patient-based, ideally suited for developing countries. The process is simpler for tumors on the skin and for other surface lesions, while endoscopic ECT procedures need to be used for deep tumors. It is safe and the entire process can be completed in a few minutes per nodule. The side effects of the drug are also drastically reduced, since the concentration of the chemo drug used is also minimal, with up to 1000 times the efficacy for the same dose [29].

7.2 Materials and methods

7.2.1 Cell lines

HL60 (human promyelocytic leukemia cell line)

HL60 is a human caucasian promyelocytic leukemia cell line (Figure 7.3(a)), derived from a 36-year-old woman with acute PML at the National Cancer Institute. HL60 cells are predominantly a neutrophilic promyelocyte, used for laboratory research on how certain kinds of blood cells are formed. PML, or a cancer of the blood forming tissue viz. the bone marrow, is caused due to a non-inherited (or somatic) mutation in the PML gene. The disease is characterized by an accumulation of immature white blood cells (promyelocytes) in the bone marrow. The PML gene codes for a tumor suppressor, which prevents uncontrolled proliferation of cells and induces apoptosis in such cells, providing a check point for healthy cell division. Mutations in this gene results in an uncontrolled proliferation of the white blood cells leading to PML [34, 35]. HL60 proliferates continuously in suspension culture in a RPMI medium supplemented with fetal bovine serum, L-glutamine, HEPES and antibiotics [36]. A hemocytometer was used to obtain a final concentration of 1×10^6 cells/ml.

KG1 (human acute myeloid leukemia cell line)

The KG1 cell line was derived from a bone marrow aspirate of a 59-year-old man with acute myelogenous leukemia, which developed from

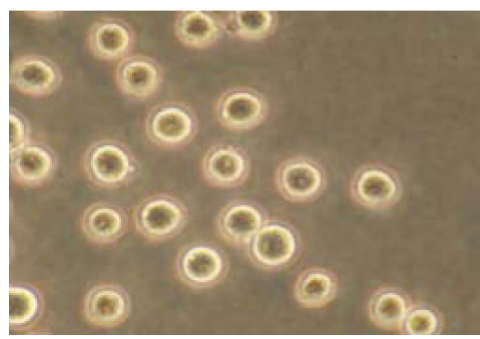

Figure 7.3 (a) Microscopic view of HL 60 cell line

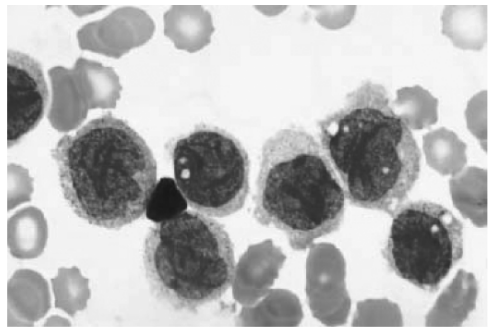

Figure 7.3 (b) Microscopic view of KG1 cell line

erythroleukemia (Figure 7.3(b)) [37]. In medical terms, 'acute' refers to a sudden onset, rapidly progressing disease that could turn fatal if not treated, as is a typical of KG1. Myeloid leukemias refer to leukemias in non-lymphocyte white blood cells, red blood cells or platelet-making cells [38]. Acute myeloid leukemia refers to a malignant disorder where there is a maturational arrest of bone marrow cells at early stages of differentiation [39]. Chromosomal abnormalities and other genetic translocations are involved in the onset of this disease. The production of normal blood cells, including RBCs, neutrophils and thrombocytes, are affected (reduced) resulting in anemia, neutropenia and thrombocytopenia (blood conditions involving lower than normal numbers of these cells). The presence of thrombocytopenia or a reduction in the count of platelets explains the abnormal bleeding which is one of the symptoms of the disease. The cells lose their ability to undergo apoptosis and this culminates in them accumulating in the spleen, bone marrow, liver and in the blood. These cells are responsive to the colony stimulating factor (CSF). The cells are rounded and myeloblast in nature and grow in suspension culture. They are capable of spontaneous differentiation into granulocytes and macrophages and represent an early stage of hematopoietic differentiation.

The cells were cultured in RPMI 1640 media with 10% fetal bovine serum (ATCC) and incubated in a 5% CO_2 atmosphere at 37°C. A hemocytometer was used to obtain a final concentration of 1×10^6 cells/mL.

ME180 (human cervical cancer cell line)

ME180, the human cervix-derived epithelial cell line (Figure 7.3(c)), is used as the model for studying cervical cancer characteristics. Isolated

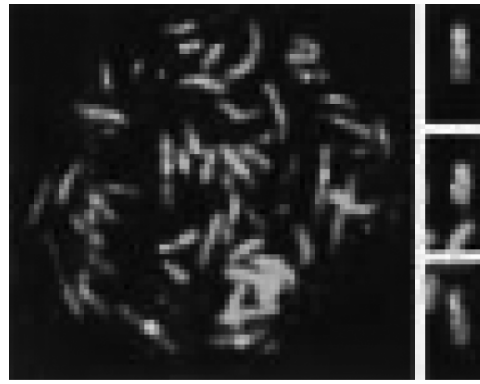

Figure 7.3 (c) Microscopic view of ME180 human cervical cancer cell line

from an omental metastasis of a spreading cervical carcinoma of a 66-year-old Caucasian female, this line was derived from a highly invasive squamous cell carcinoma with irregular cell clusters and no significant keratinization. The cells contain HPV DNA, with greater homology to HPV-39 than HPV-18 [40]. The cells were cultured RPMI 1640 media with 10% fetal bovine serum (ATCC) and incubated in a 5% CO_2 atmosphere at 37°C. A hemocytometer was used to obtain a final concentration of 1×10^6 cells/mL.

7.2.2 Anticancer drugs

Bleomycin

Bleomycin (C55H84N17O21S3) is FDA approved in the US and by the respective agencies in other countries as an anti-cancer chemotherapy drug. It is classified as an 'antitumor antibiotic'. Bleomycin can be used in combination with surgery or radiotherapy, or in the palliative treatment of a number of cancers. It is used in the treatment of squamous cell cancers, melanoma, sarcoma, testicular cancer, Hodgkin's and non-Hodgkin's lymphoma [28]. Figure 7.4 shows the chemical structure of Bleomycin.

Bleomycin inflicts direct damage to the DNA [41]. It is a powerful drug and its administration causes a number of side effects such as skin rash, hives, changes in skin sensation, hyper-pigmentation (darkening of skin and nails), hair loss, mouth ulcers, hard patches on skin [42], etc. Thus

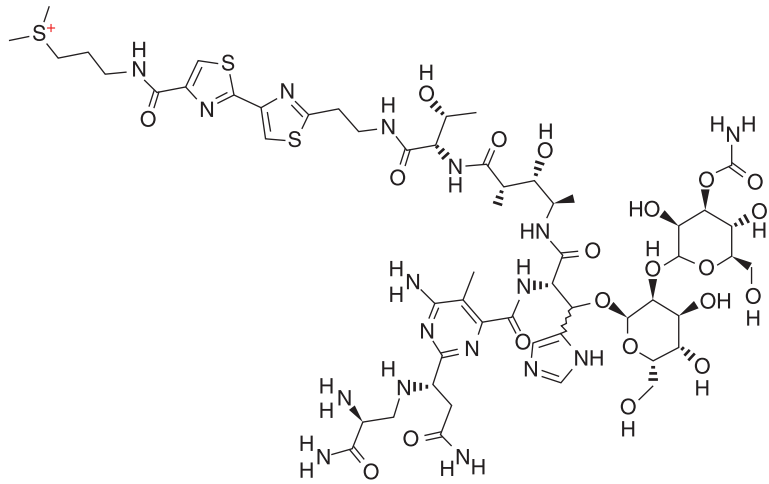

Figure 7.4 Chemical structure of Bleomycin

the dose should always be optimal and determined based on the patient's response. In our study, we aim to examine the effect of reducing the concentration of the drug so as to reduce the side effects and alleviate the pain suffered by cancer victims.

Curcumin

Curcumin, the yellow pigment of turmeric, is a hydrophobic phytochemical exerting a number of therapeutic effects, including the inhibition of cancer cell proliferation. It also has both anti-inflammatory and antioxidant effects. It inhibits production of the free radicals H_2O_2 and NO by macrophages [43, 44] and astrocytes [45] *in vitro*. The pharmacological safety and efficacy of curcumin makes it a potential compound for treatment and prevention of a wide variety of human diseases.

In spite of its efficacy and safety, curcumin has not yet been approved as a therapeutic agent, and the relative bioavailability of curcumin has been highlighted as a major problem [46]. For this purpose, we intend to upload it using electrical pulses and study its efficacy under these conditions in the HL60 cells.

Curcumin (diferuloylmethane) with a purity of more than 98% was purchased from Sigma-Aldrich Corporation (St Louis, MO), and was dissolved in dimethyl sulfoxide (DMSO) as a 10 mM stock solution and stored at –20 °C.

7.2.3 Electroporation

Using Bleomycin and HL60, KG1, and ME180 cell lines

Both high intensity, short duration (1200 V/cm, 100 μs) [27–33] and low intensity, long duration pulses (200 V/cm, 40 ms) [47] were used. In addition, medium intensity, 450 V/cm, 25 ms pulses were also used [48]. These pulses were chosen based on previous research and our experience. The choice of pulse parameters is critical as, if the pulse intensity is too high and/or too long, it kills the cells, and if it is too low and/or too short, pores will not open up to allow the drug to enter into the cells [49–52]. A BTX ECM 830 (Genetronics, Inc., San Diego, CA), square wave electroporator with 0.4 cm (electrode gap) cuvettes was used to conduct the study (Figure 7.5).

The electroporation buffer used was RPMI 1640 media with 10% fetal bovine serum (ATCC). The sample to be electroporated was taken in the cuvette and generally fixed at a total volume of 200 μL. For those experiments requiring electroporation without any drug, 100 μL of the cell suspension is used along with 100 μL of media and electroporated. For electroporation with the drug, 100 μL of cell suspension, 50 μL of appropriate drug stock and 50 μL of media was used. The drug is made up to required concentration by serial dilution technique.

The pulse parameters used are given in Table 7.2 and the doses used were 0.1, 1 and 10 μM of Bleomycin, very small compared to the conventional amount used in the clinics. In each case, 8 pulses at 1 second intervals (1 Hz) between pulses were used.

Figure 7.5 Electroporation apparatus and cuvettes

Table 7.2 Pulse parameters studied

Electric Field intensity, V/cm	Pulse width
1200	100 μs
450	25 ms
200	40 ms

Using curcumin and HL60

In the case of curcumin, 400 μL cells were used with 5 μL of curcumin at a concentration of 100 μM. Table 7.3 shows the various pulse parameters studied.

7.2.4 Cell counting and viability

After electroporation, cells are counted to determine the viability. Trypan Blue assay was used to count the cells [53].

For curcumin tests, iNcyto, disposable hemocytometer was used. For other tests, an Olympus CKX41, Phase contrast, inverted florescent microscope was used to image and count the cells. Images were captured using Motix software.

Table 7.3 Curcumin pulse parameters for HL60 cells

Sample No.	Description	Electric field intensity, V/cm	Pulse Duration	Number of pulses
1	Control	–	–	–
2	Drug only	–	–	–
3	Drug + Pulse	1200 V/cm	100 μs	8
4	Drug + Pulse	1000 V/cm	100 μs	8
5	Drug + Pulse	200 V/cm	5 ms	4
6	Drug + Pulse	500 V/cm	20 ms	2

7.3 Results and analysis

7.3.1 Dose curve

In order to prescribe the optimal amount of drug, so as to achieve maximum cell death without causing harmful side effects on the patient, a proper drug dose is required. There is only a thin line of seperation between optimal dose and drug overdose. In the case of drugs such as Bleomycin, this becomes even more vital, as the patient is only allowed to take a lifetime dose of 400 units.

In this study, the viability was studied for the doses of 0.1, 1.0 and 10.0 μM, for all 3 cell lines and for all the 3 pulse parameters. The cell viability decreases as the drug concentration increases, which is shown in Figure 7.6. While very low doses such as 0.1 μM can also be effective, the 1 μM dose was much more effective as we moved from one pulse parameter to the other in all the 3 cell lines. When the dose was changed from 1–10 and 1–0.1 μM, there was a nonlinear swing of 15–20% viability on both sides. Figure 7.6 shows the drug dosage curve for the HL60 cell line. Similar data were obtained for other cell lines too.

7.3.2 Viability study

Figure 7.7 shows the microscopic pictures illustrating the viability of control (no treatment), 450 V/cm, 25 ms and 1200 V/cm, 100 μs samples

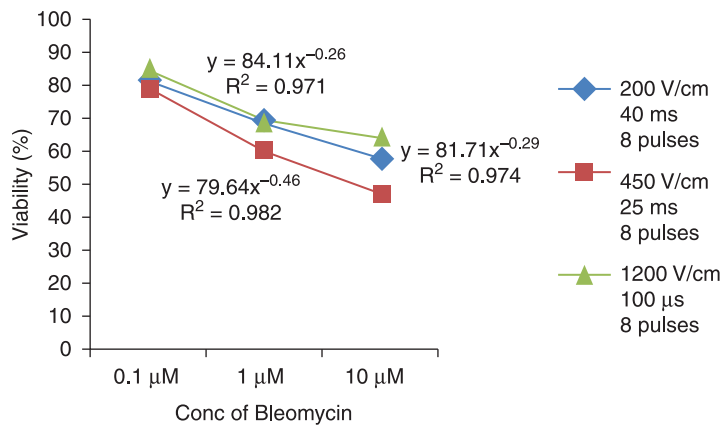

Figure 7.6 Bleomycin dose curve for HL60 cell line

of ME180 cervical cancer cells. There is reduction in the number of live cells due to electroporation compared to control cells. Similar results were also obtained for other cells (data not shown). Table 7.4 shows the mortality of the 3 types of cells studied. Figure 7.8 shows a comparison of the viability of the 3 cell lines for various pulse parameters at 1 μM dose.

The results indicate that among the various electroporation parameters, the cell mortality is found to be the highest at 450 V/cm, 25 ms, 8 pulses condition for all the 3 concentrations of Bleomycin for all the 3 cell

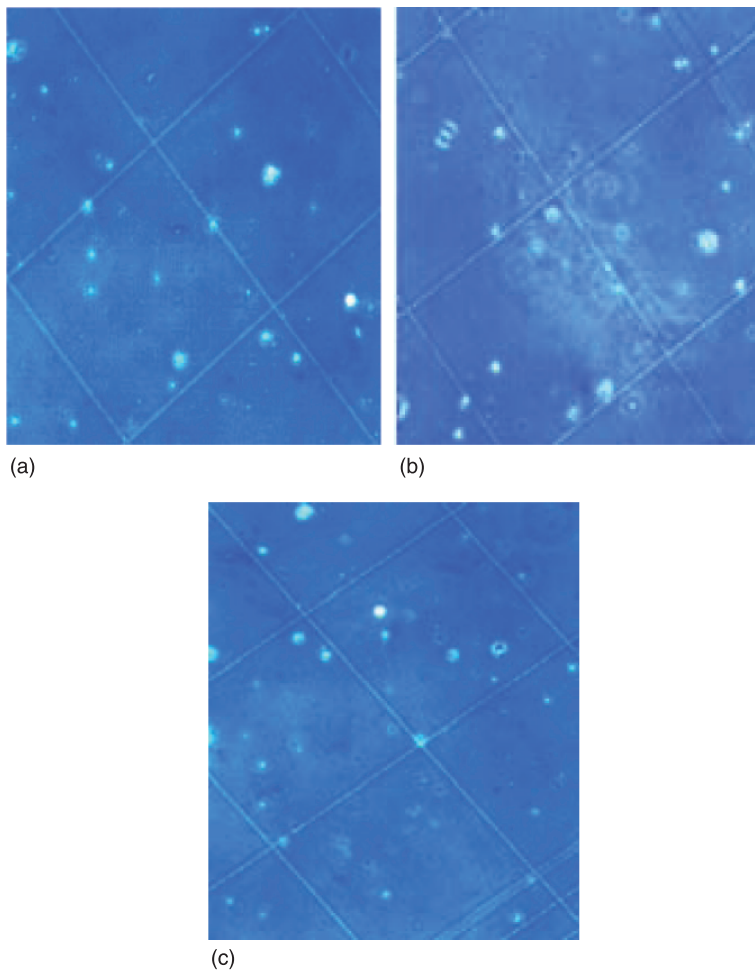

Figure 7.7 **Viability of ME180 cervical cancer cells – control, 450 V/cm, and 1200 V/cm samples respectively from left to right**

Table 7.4 Viability study of the three cell lines

Electric Field Intensity V/cm	Pulse Width	Bleomycin Dose	HL60	KG1	ME180
			Mortality, %		
Control	–	–	11.0	12.0	7.7
Bleomycin only	–	1.0 μM	14.8	14.7	13.4
EP only 200	40 ms	–	18.0	14.8	14.2
EP only 450	25 ms	–	18.8	17.3	20.0
EP only 1200	100 μs	–	14.2	13.7	10.0
200	40 ms	0.1 μM	26.4	19.2	18.8
450	25 ms	0.1 μM	30.0	21.5	20.6
1200	100 μs	0.1 μM	20.6	15.0	18.0
200	40 ms	1.0 μM	34.0	31.4	30.0
450	25 ms	1.0 μM	38.2	40.0	35.0
1200	100 μs	1.0 μM	23.0	31.8	26.9
200	40 ms	10.0 μM	42.9	42.1	42.2
450	25 ms	10.0 μM	56.5	53.4	53.0
1200	100 μs	10.0 μM	39.2	35.8	35.5

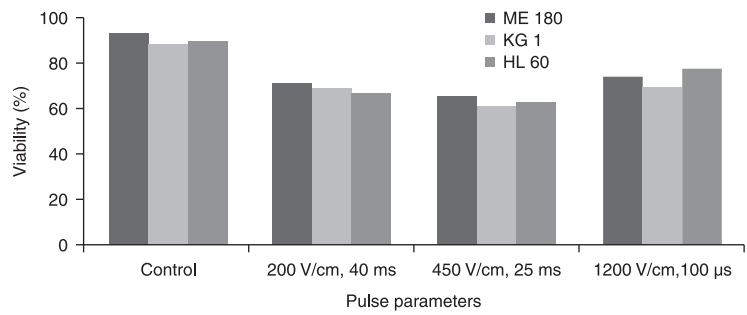

Figure 7.8 Viabilities of the three cell lines at various pulse parameters for 1 μM concentration of Bleomycin for ME180 (left), KG1 (middle) and HL60 (right) cells at various conditions

lines. Comparatively 200 V/cm, 40 ms shows a lower cell mortality and 1200 V/cm, 100 μs mortality values were even smaller. At 10 μM concentration, the viability decreased to around 56.5% for 450 V/cm pulses in HL60 cell line, which is almost a 50% decrease compared to control, whose viability is 89.0%.

Table 7.4 shows the pulse parameters studied for curcumin at 100 μM concentration using HL 60 cells and Figure 7.9 shows the corresponding viabilities at various periods, including immediately after pulsing (0 h), after 24 hours and 48 hours. The results show that with electrical pulses, the efficacy of curcumin is felt immediately compared to the control (with no treatment) and with drug only (no pulses). In general, all of the pulse parameters are effective after 24 and 48 hours, including the drug-only sample. Considering that the bioavilability of the turmeric is rapid and it is metabolized quickly, the use of electrical pulses is a viable option for enhancing the efficacy of targeted locoregional delivery.

Sample 1-control (no treatment), 2-drug only, 3–1200 V/cm, 100 μs, 8 pulses, 4–1000 V/cm, 100 μs, 8 pulses, 5–200 V/cm, 5 ms, 4 pulses and 6–500 V/cm, 20 ms, 2 pulses. All at 1 second interval

7.3.3 Equivalent energy and charge

In the absence of the measurement of the resistance or the current values, the energy applied during each pulse application could be computed as V^2TN J/Ω, where V is the applied voltage in V (E V/cm*0.4 cm), T is the

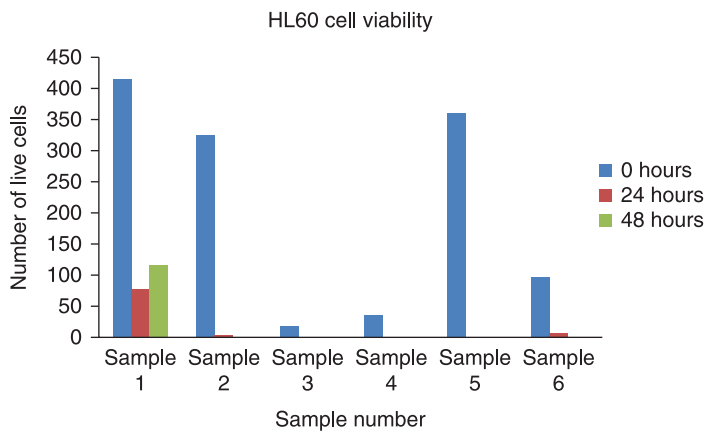

Figure 7.9 **Viabilities of the HL60 cell line at various pulse parameters for 100 μM concentration of curcumin. Sample 1-control (no treatment), 2-drug only, 3–1200 V/cm, 100 μs, 8 pulses, 4–1000 V/cm, 100 μs, 8 pulses, 5–200 V/cm, 5 ms, 4 pulses and 6–500 V/cm, 20 ms, 2 pulses. All at 1 second intervals**

pulse width in s, and N is the number of pulses. The equivalent of charge is calculated as ETN C/Ω. Energy and charge are indicators of the current applied and hence the duration for which the voltage is applied. The higher the energy, the lower the viability and vice versa. Thus a negative linear relationship is obtained for each of the pulse parameters studied in all the three cell lines. Use of energy as a parameter also has an attractive serendipity, in that the medical community would understand the terminology and the technique easily, since energy in joules is used for defibrillation and other techniques. Figures 7.10(a) and (b) show the energy and charge applied and the corresponding viability for the various samples for the HL60 and KG1 cell lines. A comparison of previously published results indicates good qualitative correlation in trends (Figures 7.11(a) and (b)) [54, 55].

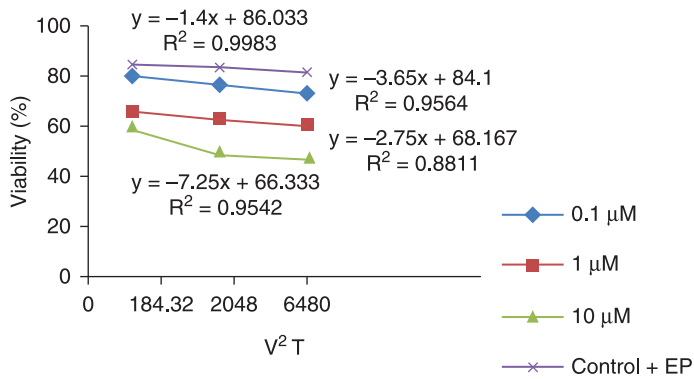

Figure 7.10 (a) Energy (J/Ω) vs. viability plot for HL60 cell line

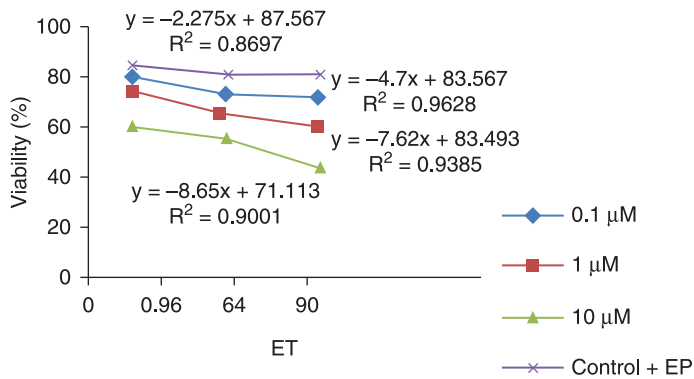

Figure 7.10 (b) Charge equivalent (Q/Ω) vs. viability plot for KG1 cell line

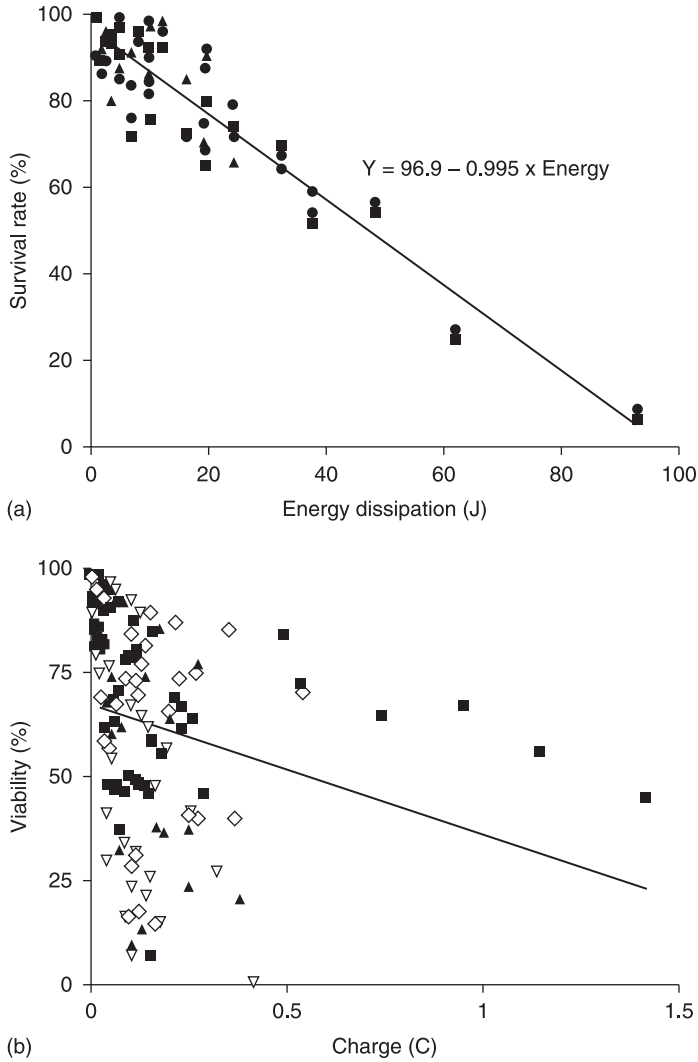

Figure 7.11 **Negative linear relationship between viability vs. electroporation energy applied (a) [54] and charge delivered (b) [55]**

7.4 Conclusions

Electrochemotherapy is an extremely effective, physical technique that enables cytotoxic drugs to have direct access to the cytosol [56]. This

budding mode of therapy uses electrical pulses and chemo drugs to trigger cell death in cancerous cells. The efficacy of this technique depends on a variety of factors, including electric field intensity, pulse duration and the number of pulses. In this study, HL60, KG1 and ME180 cancerous cell lines were subjected to electroporation in the presence of 1 μM Bleomycin at 1200 V/cm, 100 μs; 450 V/cm, 25 ms; and 200 V/cm, 40 ms.

HL60 cells were also studied at 100 μM curcumin concentration for their efficacy in preventing proliferation of the HL60 leukemia cells. The results indicate the promise of using electro-curcumin therapy for the proliferation control of HL60 leukemia cell lines. Electrical pulse intensities, as low as 200 V/cm, but long duration (40 ms) and 450 V/cm, 25 ms offer lower viability, indicating the efficacy of electrochemotherapy using Bleomycin chemodrug.

The dose curve helps to optimize the dose levels for a given viability (and hence cell death) of the tumors to be treated. The energy applied and the charge accumulated with each pulse is also calculated. The energy calculations indicate that the higher the energy value, the lower is the viability or with increase in energy delivered, there is increase in cell death. It is possible to use a single, simple, key parameter, such as energy to describe the efficacy of optimization of electrical parameters.

It is interesting to observe that when using Bleomycin, the viabilities of the three cell lines at various pulses parameters are almost similar. This could indicate that the properties and composition of the cell membrane of these three types of cells may be similar. It may be noteworthy that KG1 and HL60 are cancers of myeloid origin and hence arise from the same precursor. This means that the overall membrane composition of these blood-forming cells would be similar, which can account for the similarity seen in the electroporation viability values. With similar viability also observed in the cervical cancer cell line, we may conclude that the membrane properties of these three cancer cells, in general, may be similar with particular respect to amenability to these parameters of electroporation at these doses.

Considering that 20 million people were living with cancer in 2010 [10] and the trend seems to rise every year, and that the currently administered doses of chemo drugs are costly with severe side effects, not just from chemo drugs but also from other drugs given for coping with the chemo and surgery, there is a critical need for effective, safe, physical and affordable alternative treatments. Since this method allows specific entry of poorly permanent chemotherapeutic drugs into cells at specific tissue locations without affecting neighboring regions, electrochemotherapy

has the potential to be a viable tool for the treatment of patients suffering from chemo-refractive tumors.

7.5 Acknowledgments

The authors are very grateful to M Sriram Kumar, V Madan Kumar, S Vignesh and P Sadasivam of BS Abdur Rahman University (Crescent Engineering College), Chennai, India for conducting the experiments and to Frontier Lifeline scientists for their help with the technical details and acquiring cell lines during the course of experiments.

7.6 References

[1] Facts 2012 (2012), Leukemia & Lymphoma Society – fighting blood cancers.
[2] *www.lls.org*. 2012.
[3] Leukemia Statistics (2012). Available at: *http://leukemia.emedtv.com/leukemia/leukemia-statistics.html*
[4] Leukemia stages and survival rates (2012). Available at: *http://www.thesurvivorsclub.org/health/surviving-cancer/leukemia-stages-and-survival-rates*, June.
[5] Basic information about gynecologic cancers. Available at: *www.Cdc.gov/cancer/gynecologic/basic_info/index.htm*
[6] Schiffman M, Castle P J, Jeronimo J J, Rodriguez, A and Wacholder C S (2007), 'Human papillomavirus and cervical cancer', *Lancet*, **370(9590)**: 890–907.
[7] Massimi P and Banks L (1997), 'Repression of p53 transcriptional activity by the HPV E7 proteins', *Virology*, **227(1)**: 255–9.
[8] Globocan (2008), Cervical cancer incidence and mortality worldwide in 2008, Summary.
[9] Ferlay J, Shin H R, Bray F, Forman D, Mathers C, and Parkin D M (2010), 'Estimates of worldwide burden of cancer in 2008: Globocan 2008', *Int J Cancer*, **127(12)**: 2893–917.
[10] *http://www.who.int/whosis/whostat/2010/en/index.html*
[11] Inaba M, Kobayashi H, Sakurai V and Johnson R K (1979), 'Active efflux of Daunorubicin and Adriamycin in sensitive and resistant sub-lines of P388 leukemia', *Cancer Res*, **39**: 2200–3.
[12] Skovsgaard T M (1978), 'Mechanisms of resistance to Daunorubicin in Ehrlich ascites tumor cells', *Cancer Res*, **38**: 1785–91.
[13] McGrath T and Center M S (1988), 'Mechanisms of multidrug resistance in HL60 cells: evidence that a surface membrane protein distinct from p-glycoprotein contributes to reduced cellular accumulation of drug', *Cancer Res*, **48**: 3959–63.

[14] Levi M, et al. (1997), 'K562 and HL60 cells membrane ageing during cell growth is associated with changes in cholesterol concentration', *Mech Age Devel*, **97**(**2**): 109–19.
[15] Pachernick J, et al. (2002), 'Conditions for gene transfection into the HL60 human leukemia cell line by electroporation', *Folia Biologica* (*Praha*), **48**: 154–6.
[16] Cross S E, Jin Y S, Rao J and Gimzewski J K (2007), 'Nanomechanical analysis of cells from cancer patients', *Nat Nanotechnol*, **2**: 780–3.
[17] Chen J, et al. (2011), 'Electrodeformation for single cell mechanical characterization', *J Micromech Microeng*, **21**: 054012 (11 pager).
[18] Meng X, Riordan N H, Riordan H D, Mikirova J, Jackson J, et al. (2004), 'Cell membrane fatty acid composition differs between normal and malignant cell lines', *PRHSJ*, **2**(**June**): 103–6.
[19] *news.stanford.edu/pr/94/940201Arc4464.html*
[20] Vernier P T, Sun Y H, Marcu L, Craft C M and Gundersen M A (2004), 'Nanosecond pulsed electric fields perturb membrane phospholipids in T lymphoblasts', *FEBS Lett*, **572**: 103–8.
[21] Buescher E S and Schoenbach K H (2003), 'Effects of submicrosecond, high intensity pulsed electric fields on living cells – intracellular electromanipulation', *IEEE Transactions on Dielectrics and Electrical Insulation*, **10**: 788–94.
[22] White J A, Blackmore P F, Schoenbach K H and Beebe S J (2004), 'Stimulation of capacitative calcium entry in HL-60 cells by nanosecond pulsed electric fields', *J Biol Chem*, **279**: 22964–72.
[23] Beebe S J, Fox P M, Rec L J, Somers K, Stark R H and Schoenbach K H (2002), 'Nanosecond pulsed electric field (nsPEF) effects on cells and tissues: apoptosis induction and tumor growth inhibition', *IEEE Transactions on Plasma Science*, **30**: 286–92.
[24] Beebe S J, Fox P M, Rec L J, Willis E L and Schoenbach L H (2003), 'Nanosecond, high-intensity pulsed electric fields induce apoptosis in human cells', *FASEB J*, **17**: 1493–5.
[25] Chernomordik L V, Sukharev S I, Popov S V, Pastushenko V F, Sokirko A V, et al. (1987), 'The electrical breakdown of cell and lipid membranes: the similarity of phenomenologies', *Biochimica et Biophysica Acta*, **902**: 360–73.
[26] Kirson E D, Gurvich Z, Schneiderman R, Dekel E, Itzhaki A, et al. (2004), 'Disruption of cancer cell replication by alternating electric fields', *Cancer Res*, **64**: 3288–95.
[27] Sersa G, Cemazar M and Rudolf Z (2003), 'Electrochemotherapy: advantages and drawbacks in treatment of cancer patients', *Cancer Thera*, **1**: 133–42.
[28] Gothelf A, Mir L M and Gehl J (2003), 'Electrochemotherapy: results of cancer treatment using enhanced delivery of Bleomycin by electroporation', *Cancer Treat Rev*, **29**(**5**): 371–87.
[29] Heller R, Gilbert R and Jaroszeski M J (2000), 'Clinical trials for solid tumors using electrochemotherapy', in: *Electrochemotherapy, Electrogenetherapy, and Transdermal Delivery*, Jaroszeski, M, Heller R and Gilbert R (eds), New Jersey: Humana Press, 137–56.

[30] Dev S B, Rabussay D P, Widera G and Hofmann G A (2000), 'Medical applications of electroporation', *IEEE Transactions on Plasma Science*, **28(1)**: 206–23.
[31] Campana L G, Valpione S, Mocellin S, Sundararajan R, Granziera E, et al. (2012), 'Superficial disease control in melanoma patients treated with electrochemotherapy in a palliative setting', *Brit J Surg*, **99**: 821–30.
[32] Campana L G, Mocellin S, Basso M, Puccetti O, De Salvo G L, et al. (2009), 'Bleomycin-based electrochemotherapy: clinical outcome from a single Institution's experience with 52 patients', *Ann Surg Oncol*, **16**: 191–9.
[33] Larkin J O, et al. (2007), 'Electrochemotherapy: aspects of practical development and early clinical experience', *Ann Surg*, **245(3)**: 465–79.
[34] *http://omim.org/entry/102578*
[35] Salomoni P and Pandolfi P P (2002), 'The role of PML in tumor suppression', *Cell*, **108(2)**: 165–70.
[36] *http://bioinformatics.istge.it/hypercldb/cl3022.html*
[37] *http://bioinformatics.istge.it/hypercldb/cl1694.html*
[38] *http://www.cancer.org/Cancer/LeukemiaAcuteMyeloidAML/DetailedGuide/leukemia-acute-myeloid-myelogenous-what-is-aml*
[39] *http://emedicine.medscape.com/article/197802-overview#a0101*
[40] *http://www.atcc.org/ATCCAdvancedCatalogSearch/ProductDetails/tabid/452/Default.aspx?ATCCNum=HTB- 33&Template=cellBiology*
[41] Branner K W and Sonntag R W (1975), 'Bleomycin in testicular teratomas', *J Cancer Res Clin Oncol*, **84(3)**: 291–7.
[42] Cancer Drug Manual (the Manual) (1994), British Columbia Cancer Agency (BCCA) & Compendium of Pharmaceuticals and Specialties, 2006. Blenoxane®. Canadian Pharmacists Association.
[43] Joe B and Lokesh B R (1994), 'Role of capsaicin, curcumin and dietary n-3 fatty acids in lowering the generation of reactive oxygen species in rat peritoneal macrophages', *Biochim Biophys Acta*, **1224**: 255–63.
[44] van Meeteren M E, Hendriks J J, Dijkstra C D, van Tol E A (2004), 'Dietary compounds prevent oxidative damage and nitric oxide production by cells involved in demyelinating disease', *Biochem Pharmacol*, **67**: 967–75.
[45] Soliman K F and Mazzio E A (1998), '*In vitro* attenuation of nitric oxide production in C6 astrocyte cell culture by various dietary compounds', *Proc Soc Exp Biol Med*, **218**: 390–7.
[46] Anand P, Kunnumakkara A B, Newman R A and Aggarwal B (2007), 'Bioavailability of curcumin: problems and promises', *Mol Pharm*, **4(6)**: 807–18.
[47] Xiao F, et al. (2009), 'Electrically-enhanced chemodrug delivery to human breast cancer cells', *Electrostatic Society of America Annual Meeting*, Boston, June.
[48] Cutrera J, Torrero M, Shiomitsu K, Mauldin N and Li S (2008), 'Intratumoral Bleomycin and IL-12 electrochemotherapy for treating head and neck cancer tumors in dogs', *Methods in Mol Biol*, **423**: 319–25.
[49] Neumann E, Sowers A E and Jordan C A (eds) (1989), *Electroporation and Electrofusion in Cell Biology*. New York: Plenum.
[50] Zimmermann U and Neil G A (eds) (1996), *Electromanipulation of Cells*. Boca Raton, FL: CRC Press.

[51] Lynch P T and Davey M R (eds) (1996), *Electrical Manipulation of Cells*. New York: Chapman & Hall.
[52] Okino M and Mohri H (1987), 'Effects of a high-voltage electrical impulse and an anticancer drug on *in vivo* growing tumors', *Jpn J Cancer Res*, **78**: 1319–21.
[53] *http://www.protocolonline.org./prot/Cell_Biology/Cell_Culture/Generalprocedures/CellCountingandViabilityAssay/index.html*
[54] Chen G Y, Conner A J, Wang J, Fautrier A G and Field R J (1998), 'Energy dissipation as a key factor for electroporation of protoblasts', *Mol Biotech*, **10**: 209–16.
[55] Cantella P J, Karr J F, Petros J A and Prausnitz M R (2001), 'Quantitative study of electroporation-mediated molecular uptake and cell viability', *Biophysical J*, **80**: 755–64.
[56] Rols M-P, Golzio M and Delteil C (2000), '*In vitro* delivery of drugs and other molecules to cells', in: *Electrochemotherapy, Electrogenetherapy, and Transdermal Drug Delivery*, Jaroszeski M J, Heller R, and Gilbert R (eds), New Jersey: Humana Press.

7

An *in vitro* study of electroporation of leukemia and cervical cancer cells

Raja Prabu Ramachandran, S. Madhivanan, Raji Sundararajan, Cindy Wan-Ying Lin and Kavitha Sankaranarayanan

DOI: 10.1533/9781908818294.161

Abstract: Cancer therapies mainly target the uncontrolled proliferation of the cancerous cells. A translational therapy for inoperable, chemo- and radio-resistant tumors is electroporation-based chemotherapy, known as electrochemotherapy, a physical means of using electrical pulses in conjunction with minimal doses of the chemo drug to achieve proliferation control. It is applicable to all histologies of tumors and its efficacy depends on a variety of factors, including the electric field intensity, the pulse duration and the number of pulses. In this chapter, we describe the optimization of pulse parameters for effective electroporation of leukemic and cervical cancer cell lines. Human promyelocytic leukemia (HL60), human acute myeloid leukemia (KG1) and human cervical (ME180) cancer cell lines were subjected to electroporation in the presence of various doses of FDA approved chemo drug, Bleomycin. The effect of curcumin and electroporation is also tested for HL60 cells. The results indicate that by using electroporation, chemo drug molecules could be uploaded into these cells to control proliferation. This promises to be a very useful tool for treating patients suffering from chemo-refractive tumors.

Key words: Leukemia, cervical cancer, HL60 cell line, KG1 cell line, ME180 cell line, Bleomycin, curcumin, dose curve, voltage pulses, viability.

7.1 Introduction

About every four minutes, two people are diagnosed with a blood cancer and about every ten minutes, two die due to a blood cancer, in the US [1]. Leukemia is one of the blood cancers that affects the bone marrow, which is the source of blood cells and occurs at all ages. It is characterized by a rapid increase in the number of immature blood cells in the blood stream, thereby affecting regular functions. In addition, the disease is subdivided based on the type of blood cells affected – lymphoblastic (cancer of lymphocyte forming cells) and myeloid leukemia (cancer of cells that become red blood corpuscles (RBCs)), some types of white blood corpuscles (WBCs) and platelets. Leukemia is one of the leading causes of mortality around the world, as evidenced by the global statistics conducted by the Leukemia and Lymphoma Society [2]. Table 7.1 shows the incidence of the disease and the death rate for various ages [3]. Figure 7.1 shows the 5-year survival rate for the periods, from 1960–63 versus 1975–77 versus 2001–07 [1]. Leukemia accounts for about 30% of cancer cases in children aged 0–14 years. There are more than 232 000 people in the US living with leukemia and approximately 44 000 new cases were diagnosed in 2011 [4]. The standard of care currently used is radiotherapy and chemotherapy. With the current poor cure rate, the need for alternate therapies cannot be overstated.

While leukemia affects both genders and at all ages, cervical cancer is a gynecologic cancer (any cancer that starts in a woman's reproductive

Table 7.1 Leukemia statistics – incidence and death rate at various ages [3]

Age	% Diagnosed	% Died
<20	11.4	3.3
20–34	5.2	3.5
35–44	5.9	3.9
45–54	9.7	6.7
55–64	13.9	11.8
65–74	20.5	23.4
75–84	23.2	31.1
85 and above	10.1	16.4

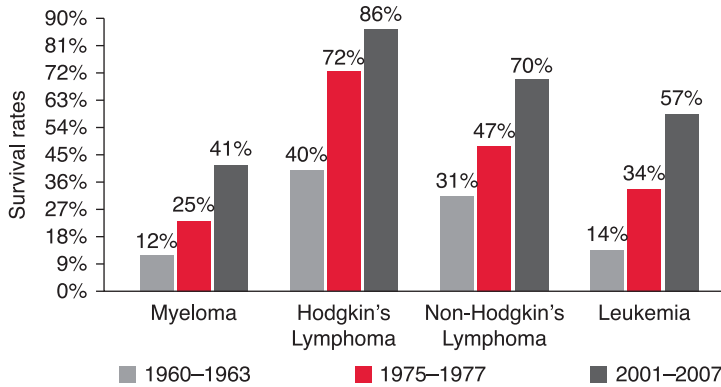

Figure 7.1 **Five-year relative survival rate for the periods, from 1960–63 vs. 1975–77 vs. 2001–07 [1]**

organs). It is the cancer that begins in the cervix, the lower part of the uterus [5]. It is almost always caused by human papilloma virus (HPV) infection [6], with virtually all cervical cancer cases (99%) being linked to infection with the HPV. The E6 and E7 genes present in the genome of HPV suppress the activity of two tumor suppressor genes, Rb and p53, thereby triggering uncontrolled proliferation of the same [7].

All women are at risk and it occurs most often in women over age 30. In the US each year, it affects about 12 000 women. Worldwide, it is the third most commonly diagnosed cancer and the fourth leading cause of cancer death in women, accounting for 9% (529 800) of the total new cancer cases and 8% (275 100) of the total cancer deaths among females in 2008 (Figure 7.2 [8]). More than 85% of these cases (453 300/529 800) and deaths (242 000/275 100) occur in developing countries. India, the second most populous country in the world, accounts for 27% (77 100) of the total cervical cancer deaths. Worldwide, the highest incidence rates are in Eastern, Western and Southern Africa, as well as South-Central Asia and South America. Rates are lowest in Western Asia, Australia/New Zealand and North America. The high incidence rate of cervical cancer in developing countries could be attributed to the lack of screening, its awareness and the socio-economical status, lacking resources and infrastructure, and the culture. The health care infrastructure in these countries does not support Papanicolaou testing or other types of screening tests. In addition, the vaccines do not provide protection for 30% of chronic infections by HPV types, other than HPV 16, 18, 6 and

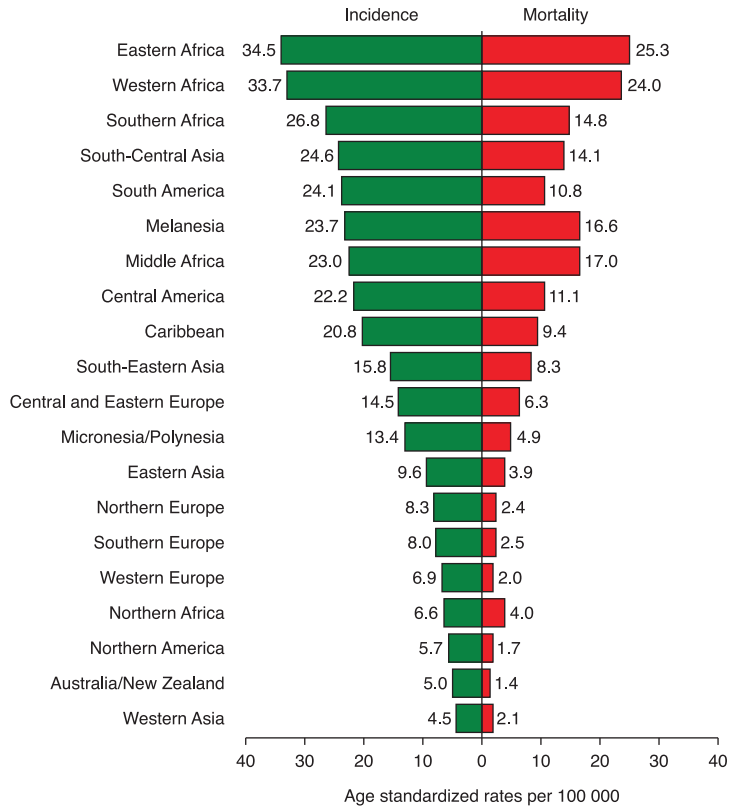

Figure 7.2 **Age-standardized cervical cancer incidence and mortality in various countries [8]**

11 that cause cervical cancer [8–10]. Normally, they are treated with surgery, chemotherapy, radiotherapy and hormonal therapy. However, these do not work well for all patients, as seen from the high death rate. Hence, additional/alternate, efficient and economical therapies are critical to save these women.

Cancerous cells such as HL60 develop resistance to a variety of cytotoxic drugs, making treatment of such types of cancers difficult. The drug, which by itself is relatively less permeable to the cell membrane, is not retained in the cancerous cell as a result of an enhanced drug efflux mechanism acquired by these cancerous cells [11–13]. This has been demonstrated to be due to the over-expression of a specific type of membrane phosphoglycoprotein and a drug resistance associated ATP binding protein on the cell surface. It has been demonstrated that

as HL60 cells divide and 'age', there is an increase in the cell cholesterol content, which in turn modulates a decrease in membrane lipid dynamics [14].

Most leukemia and lymphoma cells grown as suspension culture are resistant to most gene transfer methods, thereby making electroporation the method of choice. The cell membrane, comprising a lipid bilayer, is interspersed with protein molecules – some of the transmembrane spanning the entire lipid bilayer (i.e. ion channels, H^+ pumps, etc.) are only partially embedded in the cell membrane and are exposed only at either end. In addition to the lipids and proteins, carbohydrates are also present in the cell membrane, as either glycoproteins or glycolipids. The lipid and protein compositions of the cell membrane vary from cell to cell and this bestows unique membrane properties to different types of cells, based on their function. Although, in previous research, the efficiency of electroporation for the hematopoietic cells was reported to be roughly just 1% [15], with a variety of low voltage, long duration and high voltage and short duration pulses, it is possible to identify the optimal pulse parameters. This is because of the mechanical property of the membrane as a major determinant in the efficiency of application of electrical pulses to a cell for electroporation-based methods for gene/molecule/drug transfer. It is largely determined by the cytoskeletal architecture of a cell, which is a variant in cancerous cells [16]. Electrodeformation, or the mechanical response of the cell to electrical fields, vary from cell to cell [17] and would account for the necessity for different parameters while working with various types of cells. It has been reported that there is a change in the membrane properties of the myeloid cells during maturation as well as differentiation [18]. Whether the changes in membrane properties affect the parameters required for electrochemotherapy of the different type of cells is what was probed into by this study.

Professor McConnel's group in Stanford had demonstrated that weak non-uniform external electric fields have disruptive effects on biological membranes [19]. This effect is primarily due to the effect of the fields on the lipid layer of the cell membranes, thereby affecting the membrane proteins impregnated on the same, which in turn results in abnormal cellular function. The size of the pores thus formed remains a function of the duration of the electric field pulse. Nanosecond pulses have been shown to result in a temporary externalization of the phosphatidyl serine residues [20], a release of intracellular calcium [21,22] and induction of apoptosis [23,24].

In the presence of a strong electric field, there is a significant increase in permeability and conductance of the lipid membrane. If the applied electrical field is of not too high an amplitude and time duration, then the cell membrane is capable of returning to its previous state, as in reversible electroporation. At higher amplitudes or time durations, the membrane loses its ability to reseal and self-destructs, as in the process of irreversible electroporation. Initially it was not understood as to where these pores were formed in the lipid bilayer – the lipid matrix, integral membrane protein region or the contact region between the two. However, studies on human erythrocytes and lymphocytes along with an artificial bilayer revealed that the electrical breakdown of the membrane arises in its lipid matrices [25].

A study of tumor treating fields (TTFs) of low intensity, intermediate frequency, alternating current on a variety of human and rodent tumor cell lines exhibit varying rates of reduction of cell proliferation, both *in vitro* and *in vivo*. This could be due to the difference in the property of the cell membrane, though the basic lipid matrix largely remains the same [26]. The study demonstrated a specific intensity and frequency dependence of the TTF inhibition on different types of cancerous cells. It also revealed that the electric fields disturbed the normal polymerization-depolymerization processes of the microtubules of the mitotic spindle during mitosis and hence arrests the proliferation of actively dividing cells such as cancer cells.

Large cells have been shown to be more susceptible to electrical breakdown, which might hint at a higher risk of breakdown with an increase in the membrane surface area. Hence the parameters for successful electroporation may not only be dependent on the type of cellular lipids and the other membrane components, but also its size. In this connection we have probed into the parameters for pulsing HL60, KG1 and ME180, which are of different cellular origins for increased uptake of chemo drugs [27–33]. This method of treatment could be a very economical palliative treatment strategy, owing to the absence of any rigorous time-consuming procedures, as well as a significant reduction in the dose of the drug required and could be out-patient-based, ideally suited for developing countries. The process is simpler for tumors on the skin and for other surface lesions, while endoscopic ECT procedures need to be used for deep tumors. It is safe and the entire process can be completed in a few minutes per nodule. The side effects of the drug are also drastically reduced, since the concentration of the chemo drug used is also minimal, with up to 1000 times the efficacy for the same dose [29].

7.2 Materials and methods

7.2.1 Cell lines

HL60 (human promyelocytic leukemia cell line)

HL60 is a human caucasian promyelocytic leukemia cell line (Figure 7.3(a)), derived from a 36-year-old woman with acute PML at the National Cancer Institute. HL60 cells are predominantly a neutrophilic promyelocyte, used for laboratory research on how certain kinds of blood cells are formed. PML, or a cancer of the blood forming tissue viz. the bone marrow, is caused due to a non-inherited (or somatic) mutation in the PML gene. The disease is characterized by an accumulation of immature white blood cells (promyelocytes) in the bone marrow. The PML gene codes for a tumor suppressor, which prevents uncontrolled proliferation of cells and induces apoptosis in such cells, providing a check point for healthy cell division. Mutations in this gene results in an uncontrolled proliferation of the white blood cells leading to PML [34, 35]. HL60 proliferates continuously in suspension culture in a RPMI medium supplemented with fetal bovine serum, L-glutamine, HEPES and antibiotics [36]. A hemocytometer was used to obtain a final concentration of 1×10^6 cells/ml.

KG1 (human acute myeloid leukemia cell line)

The KG1 cell line was derived from a bone marrow aspirate of a 59-year-old man with acute myelogenous leukemia, which developed from

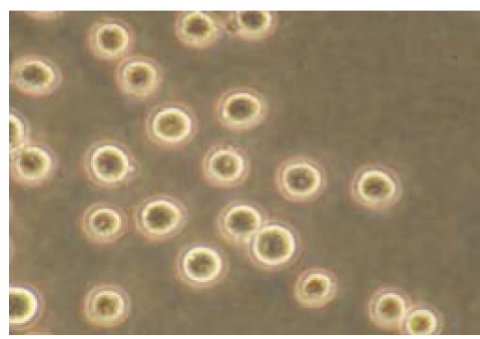

Figure 7.3 (a) Microscopic view of HL 60 cell line

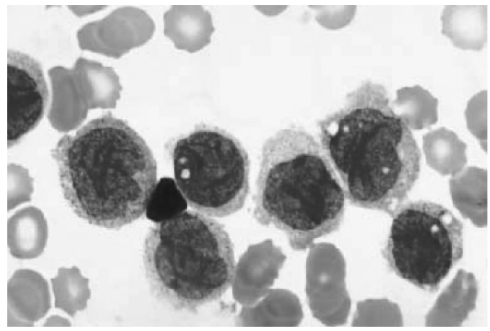

Figure 7.3 (b) Microscopic view of KG1 cell line

erythroleukemia (Figure 7.3(b)) [37]. In medical terms, 'acute' refers to a sudden onset, rapidly progressing disease that could turn fatal if not treated, as is a typical of KG1. Myeloid leukemias refer to leukemias in non-lymphocyte white blood cells, red blood cells or platelet-making cells [38]. Acute myeloid leukemia refers to a malignant disorder where there is a maturational arrest of bone marrow cells at early stages of differentiation [39]. Chromosomal abnormalities and other genetic translocations are involved in the onset of this disease. The production of normal blood cells, including RBCs, neutrophils and thrombocytes, are affected (reduced) resulting in anemia, neutropenia and thrombocytopenia (blood conditions involving lower than normal numbers of these cells). The presence of thrombocytopenia or a reduction in the count of platelets explains the abnormal bleeding which is one of the symptoms of the disease. The cells lose their ability to undergo apoptosis and this culminates in them accumulating in the spleen, bone marrow, liver and in the blood. These cells are responsive to the colony stimulating factor (CSF). The cells are rounded and myeloblast in nature and grow in suspension culture. They are capable of spontaneous differentiation into granulocytes and macrophages and represent an early stage of hematopoietic differentiation.

The cells were cultured in RPMI 1640 media with 10% fetal bovine serum (ATCC) and incubated in a 5% CO_2 atmosphere at 37°C. A hemocytometer was used to obtain a final concentration of 1×10^6 cells/mL.

ME180 (human cervical cancer cell line)

ME180, the human cervix-derived epithelial cell line (Figure 7.3(c)), is used as the model for studying cervical cancer characteristics. Isolated

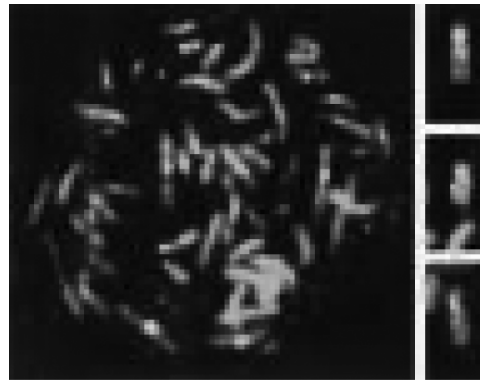

Figure 7.3 (c) Microscopic view of ME180 human cervical cancer cell line

from an omental metastasis of a spreading cervical carcinoma of a 66-year-old Caucasian female, this line was derived from a highly invasive squamous cell carcinoma with irregular cell clusters and no significant keratinization. The cells contain HPV DNA, with greater homology to HPV-39 than HPV-18 [40]. The cells were cultured RPMI 1640 media with 10% fetal bovine serum (ATCC) and incubated in a 5% CO_2 atmosphere at 37°C. A hemocytometer was used to obtain a final concentration of 1×10^6 cells/mL.

7.2.2 Anticancer drugs

Bleomycin

Bleomycin (C55H84N17O21S3) is FDA approved in the US and by the respective agencies in other countries as an anti-cancer chemotherapy drug. It is classified as an 'antitumor antibiotic'. Bleomycin can be used in combination with surgery or radiotherapy, or in the palliative treatment of a number of cancers. It is used in the treatment of squamous cell cancers, melanoma, sarcoma, testicular cancer, Hodgkin's and non-Hodgkin's lymphoma [28]. Figure 7.4 shows the chemical structure of Bleomycin.

Bleomycin inflicts direct damage to the DNA [41]. It is a powerful drug and its administration causes a number of side effects such as skin rash, hives, changes in skin sensation, hyper-pigmentation (darkening of skin and nails), hair loss, mouth ulcers, hard patches on skin [42], etc. Thus

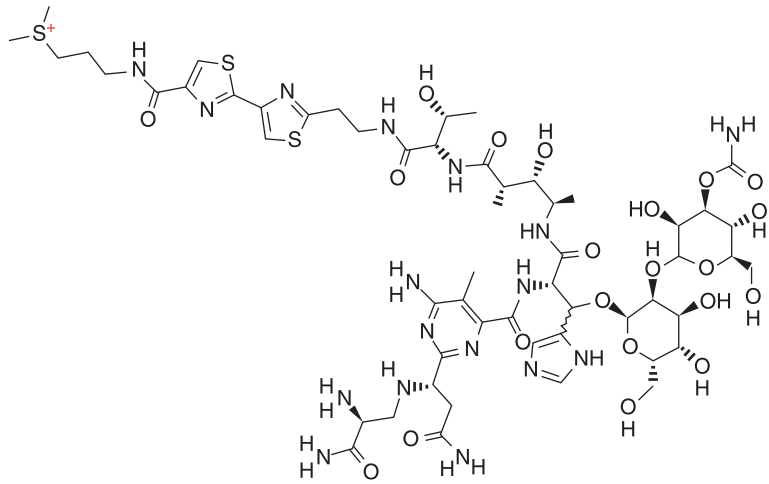

Figure 7.4 Chemical structure of Bleomycin

the dose should always be optimal and determined based on the patient's response. In our study, we aim to examine the effect of reducing the concentration of the drug so as to reduce the side effects and alleviate the pain suffered by cancer victims.

Curcumin

Curcumin, the yellow pigment of turmeric, is a hydrophobic phytochemical exerting a number of therapeutic effects, including the inhibition of cancer cell proliferation. It also has both anti-inflammatory and antioxidant effects. It inhibits production of the free radicals H_2O_2 and NO by macrophages [43, 44] and astrocytes [45] *in vitro*. The pharmacological safety and efficacy of curcumin makes it a potential compound for treatment and prevention of a wide variety of human diseases.

In spite of its efficacy and safety, curcumin has not yet been approved as a therapeutic agent, and the relative bioavailability of curcumin has been highlighted as a major problem [46]. For this purpose, we intend to upload it using electrical pulses and study its efficacy under these conditions in the HL60 cells.

Curcumin (diferuloylmethane) with a purity of more than 98% was purchased from Sigma-Aldrich Corporation (St Louis, MO), and was dissolved in dimethyl sulfoxide (DMSO) as a 10 mM stock solution and stored at –20 °C.

7.2.3 Electroporation

Using Bleomycin and HL60, KG1, and ME180 cell lines

Both high intensity, short duration (1200 V/cm, 100 μs) [27–33] and low intensity, long duration pulses (200 V/cm, 40 ms) [47] were used. In addition, medium intensity, 450 V/cm, 25 ms pulses were also used [48]. These pulses were chosen based on previous research and our experience. The choice of pulse parameters is critical as, if the pulse intensity is too high and/or too long, it kills the cells, and if it is too low and/or too short, pores will not open up to allow the drug to enter into the cells [49–52]. A BTX ECM 830 (Genetronics, Inc., San Diego, CA), square wave electroporator with 0.4 cm (electrode gap) cuvettes was used to conduct the study (Figure 7.5).

The electroporation buffer used was RPMI 1640 media with 10% fetal bovine serum (ATCC). The sample to be electroporated was taken in the cuvette and generally fixed at a total volume of 200 μL. For those experiments requiring electroporation without any drug, 100 μL of the cell suspension is used along with 100 μL of media and electroporated. For electroporation with the drug, 100 μL of cell suspension, 50 μL of appropriate drug stock and 50 μL of media was used. The drug is made up to required concentration by serial dilution technique.

The pulse parameters used are given in Table 7.2 and the doses used were 0.1, 1 and 10 μM of Bleomycin, very small compared to the conventional amount used in the clinics. In each case, 8 pulses at 1 second intervals (1 Hz) between pulses were used.

Figure 7.5 Electroporation apparatus and cuvettes

Table 7.2 Pulse parameters studied

Electric Field intensity, V/cm	Pulse width
1200	100 μs
450	25 ms
200	40 ms

Using curcumin and HL60

In the case of curcumin, 400 μL cells were used with 5 μL of curcumin at a concentration of 100 μM. Table 7.3 shows the various pulse parameters studied.

7.2.4 Cell counting and viability

After electroporation, cells are counted to determine the viability. Trypan Blue assay was used to count the cells [53].

For curcumin tests, iNcyto, disposable hemocytometer was used. For other tests, an Olympus CKX41, Phase contrast, inverted florescent microscope was used to image and count the cells. Images were captured using Motix software.

Table 7.3 Curcumin pulse parameters for HL60 cells

Sample No.	Description	Electric field intensity, V/cm	Pulse Duration	Number of pulses
1	Control	–	–	–
2	Drug only	–	–	–
3	Drug + Pulse	1200 V/cm	100 μs	8
4	Drug + Pulse	1000 V/cm	100 μs	8
5	Drug + Pulse	200 V/cm	5 ms	4
6	Drug + Pulse	500 V/cm	20 ms	2

7.3 Results and analysis

7.3.1 Dose curve

In order to prescribe the optimal amount of drug, so as to achieve maximum cell death without causing harmful side effects on the patient, a proper drug dose is required. There is only a thin line of seperation between optimal dose and drug overdose. In the case of drugs such as Bleomycin, this becomes even more vital, as the patient is only allowed to take a lifetime dose of 400 units.

In this study, the viability was studied for the doses of 0.1, 1.0 and 10.0 μM, for all 3 cell lines and for all the 3 pulse parameters. The cell viability decreases as the drug concentration increases, which is shown in Figure 7.6. While very low doses such as 0.1 μM can also be effective, the 1 μM dose was much more effective as we moved from one pulse parameter to the other in all the 3 cell lines. When the dose was changed from 1–10 and 1–0.1 μM, there was a nonlinear swing of 15–20% viability on both sides. Figure 7.6 shows the drug dosage curve for the HL60 cell line. Similar data were obtained for other cell lines too.

7.3.2 Viability study

Figure 7.7 shows the microscopic pictures illustrating the viability of control (no treatment), 450 V/cm, 25 ms and 1200 V/cm, 100 μs samples

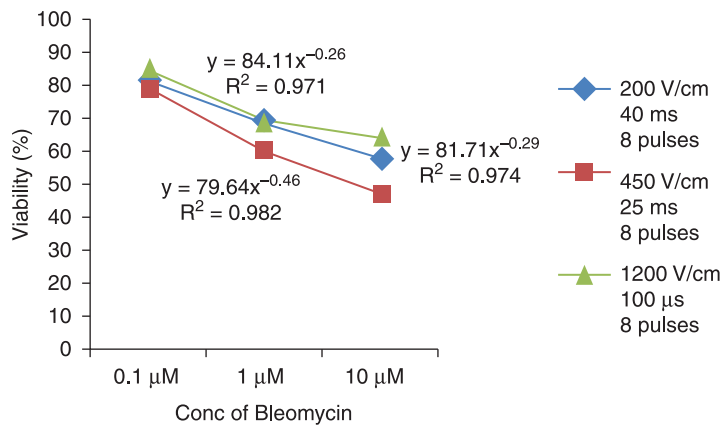

Figure 7.6 Bleomycin dose curve for HL60 cell line

of ME180 cervical cancer cells. There is reduction in the number of live cells due to electroporation compared to control cells. Similar results were also obtained for other cells (data not shown). Table 7.4 shows the mortality of the 3 types of cells studied. Figure 7.8 shows a comparison of the viability of the 3 cell lines for various pulse parameters at 1 μM dose.

The results indicate that among the various electroporation parameters, the cell mortality is found to be the highest at 450 V/cm, 25 ms, 8 pulses condition for all the 3 concentrations of Bleomycin for all the 3 cell

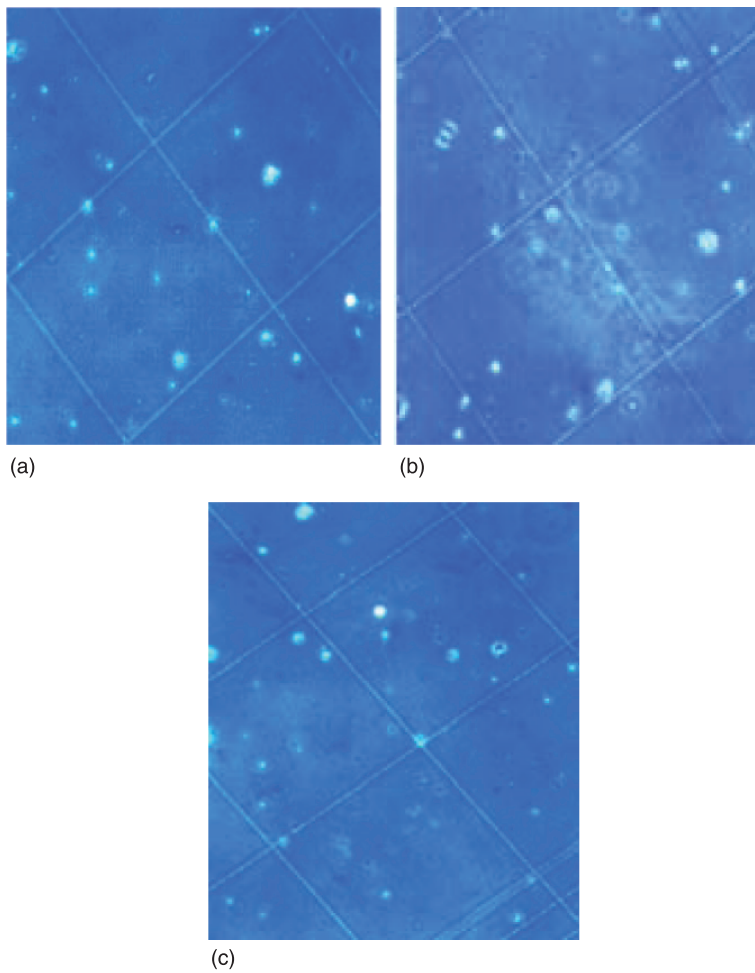

Figure 7.7 **Viability of ME180 cervical cancer cells – control, 450 V/cm, and 1200 V/cm samples respectively from left to right**

Table 7.4 Viability study of the three cell lines

Electric Field Intensity V/cm	Pulse Width	Bleomycin Dose	HL60	KG1	ME180
			Mortality, %		
Control	–	–	11.0	12.0	7.7
Bleomycin only	–	1.0 μM	14.8	14.7	13.4
EP only 200	40 ms	–	18.0	14.8	14.2
EP only 450	25 ms	–	18.8	17.3	20.0
EP only 1200	100 μs	–	14.2	13.7	10.0
200	40 ms	0.1 μM	26.4	19.2	18.8
450	25 ms	0.1 μM	30.0	21.5	20.6
1200	100 μs	0.1 μM	20.6	15.0	18.0
200	40 ms	1.0 μM	34.0	31.4	30.0
450	25 ms	1.0 μM	38.2	40.0	35.0
1200	100 μs	1.0 μM	23.0	31.8	26.9
200	40 ms	10.0 μM	42.9	42.1	42.2
450	25 ms	10.0 μM	56.5	53.4	53.0
1200	100 μs	10.0 μM	39.2	35.8	35.5

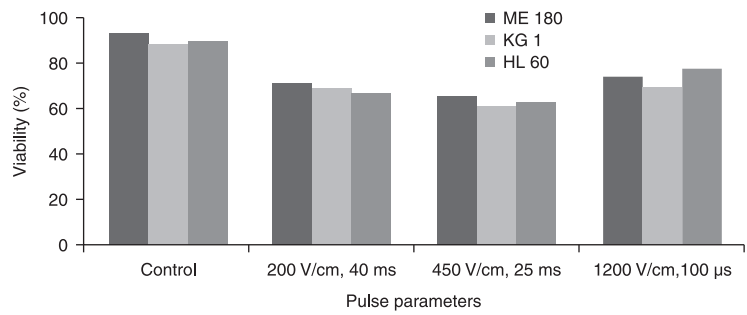

Figure 7.8 Viabilities of the three cell lines at various pulse parameters for 1 μM concentration of Bleomycin for ME180 (left), KG1 (middle) and HL60 (right) cells at various conditions

lines. Comparatively 200 V/cm, 40 ms shows a lower cell mortality and 1200 V/cm, 100 μs mortality values were even smaller. At 10 μM concentration, the viability decreased to around 56.5% for 450 V/cm pulses in HL60 cell line, which is almost a 50% decrease compared to control, whose viability is 89.0%.

Table 7.4 shows the pulse parameters studied for curcumin at 100 μM concentration using HL 60 cells and Figure 7.9 shows the corresponding viabilities at various periods, including immediately after pulsing (0 h), after 24 hours and 48 hours. The results show that with electrical pulses, the efficacy of curcumin is felt immediately compared to the control (with no treatment) and with drug only (no pulses). In general, all of the pulse parameters are effective after 24 and 48 hours, including the drug-only sample. Considering that the bioavilability of the turmeric is rapid and it is metabolized quickly, the use of electrical pulses is a viable option for enhancing the efficacy of targeted locoregional delivery.

Sample 1-control (no treatment), 2-drug only, 3–1200 V/cm, 100 μs, 8 pulses, 4–1000 V/cm, 100 μs, 8 pulses, 5–200 V/cm, 5 ms, 4 pulses and 6–500 V/cm, 20 ms, 2 pulses. All at 1 second interval

7.3.3 Equivalent energy and charge

In the absence of the measurement of the resistance or the current values, the energy applied during each pulse application could be computed as V^2TN J/Ω, where V is the applied voltage in V (E V/cm*0.4 cm), T is the

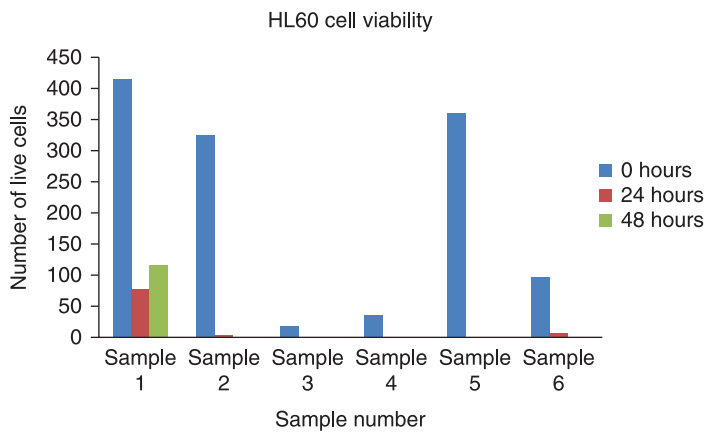

Figure 7.9 **Viabilities of the HL60 cell line at various pulse parameters for 100 μM concentration of curcumin. Sample 1-control (no treatment), 2-drug only, 3–1200 V/cm, 100 μs, 8 pulses, 4–1000 V/cm, 100 μs, 8 pulses, 5–200 V/cm, 5 ms, 4 pulses and 6–500 V/cm, 20 ms, 2 pulses. All at 1 second intervals**

pulse width in s, and N is the number of pulses. The equivalent of charge is calculated as ETN C/Ω. Energy and charge are indicators of the current applied and hence the duration for which the voltage is applied. The higher the energy, the lower the viability and vice versa. Thus a negative linear relationship is obtained for each of the pulse parameters studied in all the three cell lines. Use of energy as a parameter also has an attractive serendipity, in that the medical community would understand the terminology and the technique easily, since energy in joules is used for defibrillation and other techniques. Figures 7.10(a) and (b) show the energy and charge applied and the corresponding viability for the various samples for the HL60 and KG1 cell lines. A comparison of previously published results indicates good qualitative correlation in trends (Figures 7.11(a) and (b)) [54, 55].

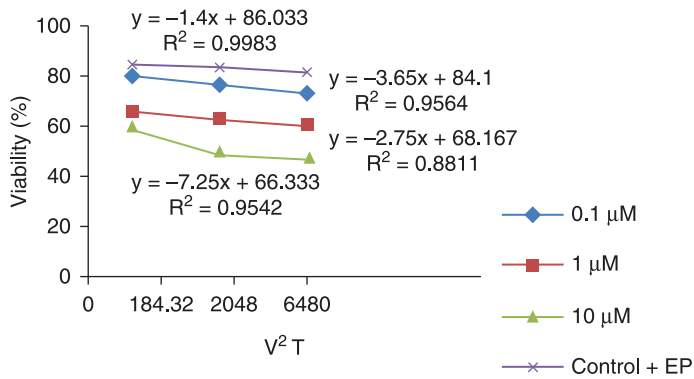

Figure 7.10 (a) Energy (J/Ω) vs. viability plot for HL60 cell line

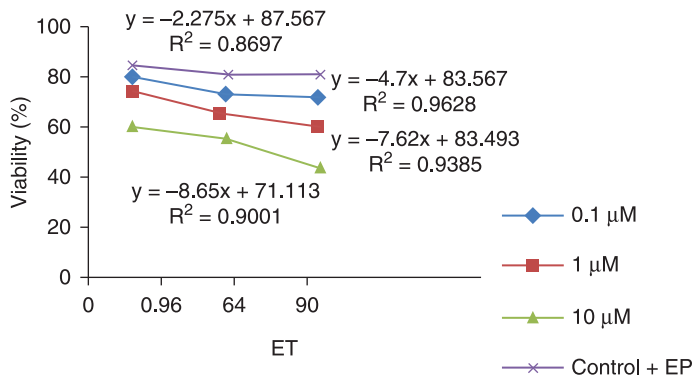

Figure 7.10 (b) Charge equivalent (Q/Ω) vs. viability plot for KG1 cell line

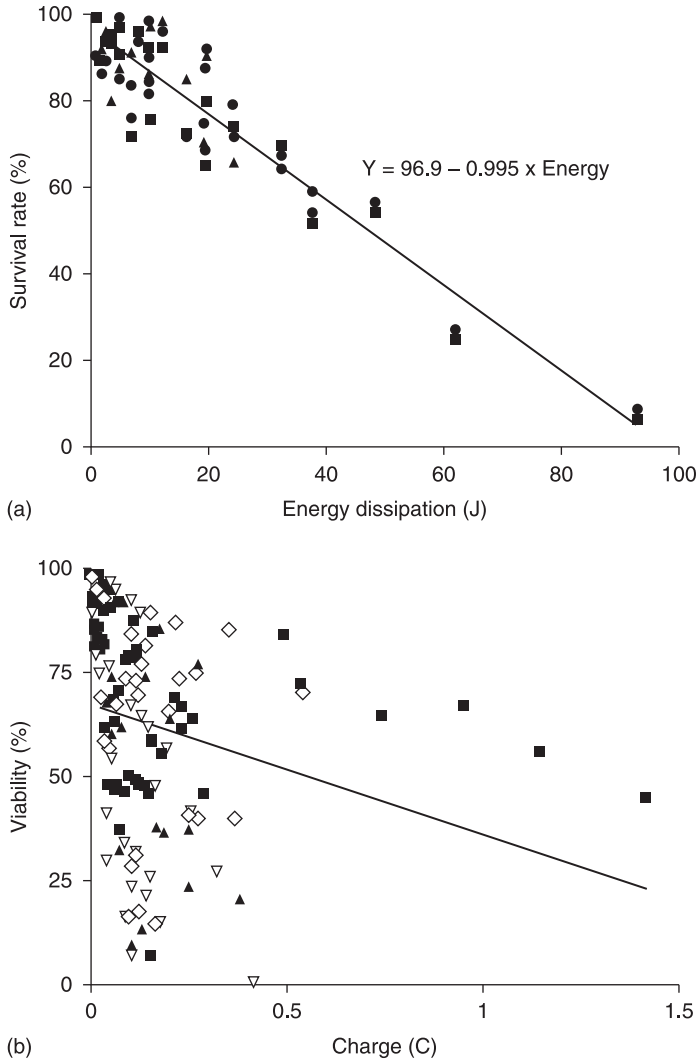

Figure 7.11 **Negative linear relationship between viability vs. electroporation energy applied (a) [54] and charge delivered (b) [55]**

7.4 Conclusions

Electrochemotherapy is an extremely effective, physical technique that enables cytotoxic drugs to have direct access to the cytosol [56]. This

budding mode of therapy uses electrical pulses and chemo drugs to trigger cell death in cancerous cells. The efficacy of this technique depends on a variety of factors, including electric field intensity, pulse duration and the number of pulses. In this study, HL60, KG1 and ME180 cancerous cell lines were subjected to electroporation in the presence of 1 μM Bleomycin at 1200 V/cm, 100 μs; 450 V/cm, 25 ms; and 200 V/cm, 40 ms.

HL60 cells were also studied at 100 μM curcumin concentration for their efficacy in preventing proliferation of the HL60 leukemia cells. The results indicate the promise of using electro-curcumin therapy for the proliferation control of HL60 leukemia cell lines. Electrical pulse intensities, as low as 200 V/cm, but long duration (40 ms) and 450 V/cm, 25 ms offer lower viability, indicating the efficacy of electrochemotherapy using Bleomycin chemodrug.

The dose curve helps to optimize the dose levels for a given viability (and hence cell death) of the tumors to be treated. The energy applied and the charge accumulated with each pulse is also calculated. The energy calculations indicate that the higher the energy value, the lower is the viability or with increase in energy delivered, there is increase in cell death. It is possible to use a single, simple, key parameter, such as energy to describe the efficacy of optimization of electrical parameters.

It is interesting to observe that when using Bleomycin, the viabilities of the three cell lines at various pulses parameters are almost similar. This could indicate that the properties and composition of the cell membrane of these three types of cells may be similar. It may be noteworthy that KG1 and HL60 are cancers of myeloid origin and hence arise from the same precursor. This means that the overall membrane composition of these blood-forming cells would be similar, which can account for the similarity seen in the electroporation viability values. With similar viability also observed in the cervical cancer cell line, we may conclude that the membrane properties of these three cancer cells, in general, may be similar with particular respect to amenability to these parameters of electroporation at these doses.

Considering that 20 million people were living with cancer in 2010 [10] and the trend seems to rise every year, and that the currently administered doses of chemo drugs are costly with severe side effects, not just from chemo drugs but also from other drugs given for coping with the chemo and surgery, there is a critical need for effective, safe, physical and affordable alternative treatments. Since this method allows specific entry of poorly permanent chemotherapeutic drugs into cells at specific tissue locations without affecting neighboring regions, electrochemotherapy

has the potential to be a viable tool for the treatment of patients suffering from chemo-refractive tumors.

7.5 Acknowledgments

The authors are very grateful to M Sriram Kumar, V Madan Kumar, S Vignesh and P Sadasivam of BS Abdur Rahman University (Crescent Engineering College), Chennai, India for conducting the experiments and to Frontier Lifeline scientists for their help with the technical details and acquiring cell lines during the course of experiments.

7.6 References

[1] Facts 2012 (2012), Leukemia & Lymphoma Society – fighting blood cancers.
[2] *www.lls.org*. 2012.
[3] Leukemia Statistics (2012). Available at: *http://leukemia.emedtv.com/leukemia/leukemia-statistics.html*
[4] Leukemia stages and survival rates (2012). Available at: *http://www.thesurvivorsclub.org/health/surviving-cancer/leukemia-stages-and-survival-rates*, June.
[5] Basic information about gynecologic cancers. Available at: *www.Cdc.gov/cancer/gynecologic/basic_info/index.htm*
[6] Schiffman M, Castle P J, Jeronimo J J, Rodriguez, A and Wacholder C S (2007), 'Human papillomavirus and cervical cancer', *Lancet*, **370(9590)**: 890–907.
[7] Massimi P and Banks L (1997), 'Repression of p53 transcriptional activity by the HPV E7 proteins', *Virology*, **227(1)**: 255–9.
[8] Globocan (2008), Cervical cancer incidence and mortality worldwide in 2008, Summary.
[9] Ferlay J, Shin H R, Bray F, Forman D, Mathers C, and Parkin D M (2010), 'Estimates of worldwide burden of cancer in 2008: Globocan 2008', *Int J Cancer*, **127(12)**: 2893–917.
[10] *http://www.who.int/whosis/whostat/2010/en/index.html*
[11] Inaba M, Kobayashi H, Sakurai V and Johnson R K (1979), 'Active efflux of Daunorubicin and Adriamycin in sensitive and resistant sub-lines of P388 leukemia', *Cancer Res*, **39**: 2200–3.
[12] Skovsgaard T M (1978), 'Mechanisms of resistance to Daunorubicin in Ehrlich ascites tumor cells', *Cancer Res*, **38**: 1785–91.
[13] McGrath T and Center M S (1988), 'Mechanisms of multidrug resistance in HL60 cells: evidence that a surface membrane protein distinct from p-glycoprotein contributes to reduced cellular accumulation of drug', *Cancer Res*, **48**: 3959–63.

[14] Levi M, et al. (1997), 'K562 and HL60 cells membrane ageing during cell growth is associated with changes in cholesterol concentration', *Mech Age Devel*, **97**(**2**): 109–19.
[15] Pachernick J, et al. (2002), 'Conditions for gene transfection into the HL60 human leukemia cell line by electroporation', *Folia Biologica* (*Praha*), **48**: 154–6.
[16] Cross S E, Jin Y S, Rao J and Gimzewski J K (2007), 'Nanomechanical analysis of cells from cancer patients', *Nat Nanotechnol*, **2**: 780–3.
[17] Chen J, et al. (2011), 'Electrodeformation for single cell mechanical characterization', *J Micromech Microeng*, **21**: 054012 (11 pager).
[18] Meng X, Riordan N H, Riordan H D, Mikirova J, Jackson J, et al. (2004), 'Cell membrane fatty acid composition differs between normal and malignant cell lines', *PRHSJ*, **2**(**June**): 103–6.
[19] *news.stanford.edu/pr/94/940201Arc4464.html*
[20] Vernier P T, Sun Y H, Marcu L, Craft C M and Gundersen M A (2004), 'Nanosecond pulsed electric fields perturb membrane phospholipids in T lymphoblasts', *FEBS Lett*, **572**: 103–8.
[21] Buescher E S and Schoenbach K H (2003), 'Effects of submicrosecond, high intensity pulsed electric fields on living cells – intracellular electromanipulation', *IEEE Transactions on Dielectrics and Electrical Insulation*, **10**: 788–94.
[22] White J A, Blackmore P F, Schoenbach K H and Beebe S J (2004), 'Stimulation of capacitative calcium entry in HL-60 cells by nanosecond pulsed electric fields', *J Biol Chem*, **279**: 22964–72.
[23] Beebe S J, Fox P M, Rec L J, Somers K, Stark R H and Schoenbach K H (2002), 'Nanosecond pulsed electric field (nsPEF) effects on cells and tissues: apoptosis induction and tumor growth inhibition', *IEEE Transactions on Plasma Science*, **30**: 286–92.
[24] Beebe S J, Fox P M, Rec L J, Willis E L and Schoenbach L H (2003), 'Nanosecond, high-intensity pulsed electric fields induce apoptosis in human cells', *FASEB J*, **17**: 1493–5.
[25] Chernomordik L V, Sukharev S I, Popov S V, Pastushenko V F, Sokirko A V, et al. (1987), 'The electrical breakdown of cell and lipid membranes: the similarity of phenomenologies', *Biochimica et Biophysica Acta*, **902**: 360–73.
[26] Kirson E D, Gurvich Z, Schneiderman R, Dekel E, Itzhaki A, et al. (2004), 'Disruption of cancer cell replication by alternating electric fields', *Cancer Res*, **64**: 3288–95.
[27] Sersa G, Cemazar M and Rudolf Z (2003), 'Electrochemotherapy: advantages and drawbacks in treatment of cancer patients', *Cancer Thera*, **1**: 133–42.
[28] Gothelf A, Mir L M and Gehl J (2003), 'Electrochemotherapy: results of cancer treatment using enhanced delivery of Bleomycin by electroporation', *Cancer Treat Rev*, **29**(**5**): 371–87.
[29] Heller R, Gilbert R and Jaroszeski M J (2000), 'Clinical trials for solid tumors using electrochemotherapy', in: *Electrochemotherapy, Electrogenetherapy, and Transdermal Delivery*, Jaroszeski, M, Heller R and Gilbert R (eds), New Jersey: Humana Press, 137–56.

[30] Dev S B, Rabussay D P, Widera G and Hofmann G A (2000), 'Medical applications of electroporation', *IEEE Transactions on Plasma Science*, **28(1)**: 206–23.
[31] Campana L G, Valpione S, Mocellin S, Sundararajan R, Granziera E, et al. (2012), 'Superficial disease control in melanoma patients treated with electrochemotherapy in a palliative setting', *Brit J Surg*, **99**: 821–30.
[32] Campana L G, Mocellin S, Basso M, Puccetti O, De Salvo G L, et al. (2009), 'Bleomycin-based electrochemotherapy: clinical outcome from a single Institution's experience with 52 patients', *Ann Surg Oncol*, **16**: 191–9.
[33] Larkin J O, et al. (2007), 'Electrochemotherapy: aspects of practical development and early clinical experience', *Ann Surg*, **245(3)**: 465–79.
[34] *http://omim.org/entry/102578*
[35] Salomoni P and Pandolfi P P (2002), 'The role of PML in tumor suppression', *Cell*, **108(2)**: 165–70.
[36] *http://bioinformatics.istge.it/hypercldb/cl3022.html*
[37] *http://bioinformatics.istge.it/hypercldb/cl1694.html*
[38] *http://www.cancer.org/Cancer/LeukemiaAcuteMyeloidAML/DetailedGuide/leukemia-acute-myeloid-myelogenous-what-is-aml*
[39] *http://emedicine.medscape.com/article/197802-overview#a0101*
[40] *http://www.atcc.org/ATCCAdvancedCatalogSearch/ProductDetails/tabid/452/Default.aspx?ATCCNum=HTB- 33&Template=cellBiology*
[41] Branner K W and Sonntag R W (1975), 'Bleomycin in testicular teratomas', *J Cancer Res Clin Oncol*, **84(3)**: 291–7.
[42] Cancer Drug Manual (the Manual) (1994), British Columbia Cancer Agency (BCCA) & Compendium of Pharmaceuticals and Specialties, 2006. Blenoxane®. Canadian Pharmacists Association.
[43] Joe B and Lokesh B R (1994), 'Role of capsaicin, curcumin and dietary n-3 fatty acids in lowering the generation of reactive oxygen species in rat peritoneal macrophages', *Biochim Biophys Acta*, **1224**: 255–63.
[44] van Meeteren M E, Hendriks J J, Dijkstra C D, van Tol E A (2004), 'Dietary compounds prevent oxidative damage and nitric oxide production by cells involved in demyelinating disease', *Biochem Pharmacol*, **67**: 967–75.
[45] Soliman K F and Mazzio E A (1998), '*In vitro* attenuation of nitric oxide production in C6 astrocyte cell culture by various dietary compounds', *Proc Soc Exp Biol Med*, **218**: 390–7.
[46] Anand P, Kunnumakkara A B, Newman R A and Aggarwal B (2007), 'Bioavailability of curcumin: problems and promises', *Mol Pharm*, **4(6)**: 807–18.
[47] Xiao F, et al. (2009), 'Electrically-enhanced chemodrug delivery to human breast cancer cells', *Electrostatic Society of America Annual Meeting*, Boston, June.
[48] Cutrera J, Torrero M, Shiomitsu K, Mauldin N and Li S (2008), 'Intratumoral Bleomycin and IL-12 electrochemotherapy for treating head and neck cancer tumors in dogs', *Methods in Mol Biol*, **423**: 319–25.
[49] Neumann E, Sowers A E and Jordan C A (eds) (1989), *Electroporation and Electrofusion in Cell Biology*. New York: Plenum.
[50] Zimmermann U and Neil G A (eds) (1996), *Electromanipulation of Cells*. Boca Raton, FL: CRC Press.

[51] Lynch P T and Davey M R (eds) (1996), *Electrical Manipulation of Cells*. New York: Chapman & Hall.
[52] Okino M and Mohri H (1987), 'Effects of a high-voltage electrical impulse and an anticancer drug on *in vivo* growing tumors', *Jpn J Cancer Res*, **78**: 1319–21.
[53] *http://www.protocolonline.org./prot/Cell_Biology/Cell_Culture/Generalprocedures/CellCountingandViabilityAssay/index.html*
[54] Chen G Y, Conner A J, Wang J, Fautrier A G and Field R J (1998), 'Energy dissipation as a key factor for electroporation of protoblasts', *Mol Biotech*, **10**: 209–16.
[55] Cantella P J, Karr J F, Petros J A and Prausnitz M R (2001), 'Quantitative study of electroporation-mediated molecular uptake and cell viability', *Biophysical J*, **80**: 755–64.
[56] Rols M-P, Golzio M and Delteil C (2000), '*In vitro* delivery of drugs and other molecules to cells', in: *Electrochemotherapy, Electrogenetherapy, and Transdermal Drug Delivery*, Jaroszeski M J, Heller R, and Gilbert R (eds), New Jersey: Humana Press.